DYNAMICS, ALLOSTERY, AND SIGNALLING BIAS IN G PROTEIN–COUPLED RECEPTORS

by

Özge Duman

B.S., Chemical Engineering, Boğaziçi University, 2018

M.S., Chemical Engineering, Boğaziçi University, 2020

Submitted to the Institute for Graduate Studies in
Science and Engineering in partial fulfillment of
the requirements for the degree of
Doctor of Philosophy

Graduate Program in Chemical Engineering

Boğaziçi University

2025

ACKNOWLEDGEMENTS

First, I would like to express my deepest gratitude to my advisor, Prof. Türkan Haliloğlu, for her invaluable guidance, knowledge, and encouragement throughout my doctoral journey. I am sincerely thankful to the members of my thesis jury committee, Assoc. Prof. Betül Uralcan Kılavuz and Asst. Prof. Hasan Demirci, whose thoughtful insights and constructive feedback have significantly enriched the quality of this research. I also extend my appreciation to Assoc. Prof. Hilal Taymaz Nikerel and Prof. Özlem Keskin for serving as defense committee members and contributing to the evaluation of my thesis.

I gratefully acknowledge the collaborative contributions of Assoc. Prof. Oded Lewinson and Prof. Nir Ben-Tal. It has been a privilege to work with such esteemed scientists. I would also like to express my heartfelt thanks to Prof. Dr. Reyhan Küçükkaya, with whom I had the chance to collaborate during my PhD. She has been my physician since I was 12 years old, and having the opportunity to work with her during my doctoral studies was both an honor and a deeply meaningful experience for me.

I am especially grateful to Yiğit Kutlu, with whom I shared the PhD journey. Thank you for your unwavering support, your brilliant ideas during our brainstorming sessions, and above all, your friendship. I would also like to thank my lab mates Dr. Burçin Acar, Dr. Erge Akbaş Buz, Bengi Altıntel, Dr. Handan Akülker, and Büşra Özgüney for the enjoyable times we spent together. Special thanks to Yüksel Gülten, the source of joy in the PRC group.

I would like to thank my dear friends Dr. Seymen İlke Kaykanat, Dr. Sercan Altundemir, Duygu Kaya, and Ayşe Korkut. Having such supportive friends during the PhD journey has been truly invaluable. İlke, you have become one of the most precious friends I've gained in recent years. Thank you for always being there—through laughter

and through tears. Despite all of life's lemons, I believe we've made some pretty good lemonade together. Your constant support throughout my graduate life means the world to me. Sercan, thank you for bringing joy and fresh perspective to my academic life. Duygu and Ayşe, thank you for your patience during the days I kept bothering you—you always made me feel supported.

I would also like to thank my friends from the university mountaineering club, Fatmanur Tiryaki, Cansu Büyükbalcı, Hatice Gökbaraz, and Dr. Çağla Ergün, who have been by my side for over 12 years. Your presence throughout both my undergraduate and graduate years has been a consistent source of strength. I am truly grateful for all the unforgettable adventures we've shared. Your adventurous spirits and unwavering friendship helped keep me going, even through the toughest moments. You have always inspired me, believed in me, and helped me believe in myself.

To my dear friend from undergraduate years, Şebnem Or, thank you for always being there for me. During the thesis writing process, I often remembered the sleepless nights we worked through together. Your support in both academic matters and real life has meant a lot to me.

I am also thankful for one of the most entertaining activities of this period: Kangoo Jumping, and to my trainer Öner Çankaya for keeping me energized and motivated.

This thesis is dedicated to my grandfather, Necati Duman. In our last phone call, I told him I had been accepted into the PhD program, and he was overjoyed. I wish he could have lived to see this day. Grandpa, thank you for always believing in me.

Finally, I would like to thank my family, who has stood by me unconditionally: my grandmother (Gülsevim Duman), my mother (Dr. Melike Şavk), my father (Kenan Duman), my uncle (Kemal Duman), my grandfather (İsmail Şavk), and my grandmother (Ülkü Şavk). Their endless love, patience, and unwavering belief in me

have been the foundation of my strength throughout this journey. I am truly grateful for your constant encouragement and support. Grandma, you have played just as important a role in this diploma as I have—thank you for everything.

This work was supported by NATO Science for Peace Multi-Year Project G5685, TÜSEB Project 24218, and TÜBİTAK Projects 118Z915 and 119F392.

ABSTRACT

DYNAMICS, ALLOSTERY, AND SIGNALLING BIAS IN G PROTEIN–COUPLED RECEPTORS

G protein-coupled receptors (GPCRs) are central to cellular signal transduction and represent the most intensively targeted protein family in pharmacology. This thesis presents a comprehensive computational analysis of Class A GPCR dynamics, with a focus on activation mechanisms, biased signaling, and allosteric regulation. Conventional MD simulations struggle to capture large-scale, long-timescale motions. To address these limitations, we employed the Anisotropic Network Model–Langevin Dynamics (ANM-LD) framework to model 30 conformational transitions across 25 GPCRs, including dual activation pathways for five receptors. These simulations generated dynamic ensembles of intermediate states, validated using hallmark collective variables such as TM6 tilt and TM7 shift. Covibrational mode analysis revealed distinct dynamical signatures for G protein– and β-arrestin–bound states, highlighting pathway-specific encoding of collective motions. Mechanistic insights into biased signaling revealed that key hinge residues, including the DRY and NPxxY motifs, were identified as critical mediators of pathway-selective transitions. GNM-based transfer entropy (GNM-TE) analysis demonstrated strong receptor-driven information flow from the orthosteric binding site in both signaling states. A newly developed metric, the Differential Coupling Score, captured structural segments involved in signaling bias. Additionally, ensemble-level comparisons across 300 structures revealed conserved allosteric scaffolds and dynamic diversity associated with ligand type and signaling partner. In particular, Helix 8 and TM7-IC emerged as flexible hubs modulating pathway-specific communication. These findings provide a unified and generalizable framework for decoding GPCR dynamics and guiding the design of biased ligands and allosteric modulators.

ÖZET

G PROTEİN–BAĞLI RESEPTÖRLERDE DİNAMİKLER, ALOSTERİ VE SİNYAL YANLILIĞI

G protein-bağlı reseptörler (GPCR'ler), hücresel sinyal iletiminde merkezi rol oynayan ve farmakolojide en çok hedeflenen protein ailesidir. Bu tez, Sınıf A GPCR'lerin aktivasyon mekanizmaları, yanlı sinyal iletimi ve alosterik düzenlemelerini inceleyen kapsamlı bir hesaplamalı analiz sunmaktadır. Klasik Moleküler Dinamik (MD) simülasyonları, uzun zaman ölçekli ve büyük ölçekli yapısal değişimleri yakalamakta yetersiz kaldığından, bu çalışmada 25 GPCR için 30 konformasyonel geçiş Anizotropik Ağ Modeli–Langevin Dinamiği (ANM-LD) yöntemi ile modellenmiştir. Beş reseptör için hem G proteini hem de β-arrestin'e yönelik çift aktivasyon yolakları oluşturulmuştur. Elde edilen ara yapılar, TM6 eğimi ve TM7 hareketi gibi kolektif değişkenlerle doğrulanmıştır. Kovibrasyonel mod analizi, G proteini ve β-arrestin ile bağlanmış durumlar için ayırt edici dinamik imzalar belirleyerek, her bir yolakta kolektif hareketlerin yolak-özgül kodlamasını ortaya koymuştur. Yanlı sinyal iletimine ilişkin mekanistik içgörüler, DRY ve NPxxY motifleri gibi temel menteşe rezidülerinin yolak-seçici geçişlerde kritik düzenleyiciler olduğunu ortaya koymuştur. GNM tabanlı Transfer Entropi (GNM-TE) analizi, her iki sinyal durumunda da ortosterik bağlanma bölgesinden reseptör kaynaklı güçlü bir bilgi akışını göstermiştir. Yeni geliştirilen bir metrik olan Diferansiyel Bağlanma Skoru, yanlı sinyallemede rol oynayan yapısal segmentleri ortaya koymuştur. Ayrıca, 300 yapıyı kapsayan topluluk düzeyindeki karşılaştırmalar, ligand tipi ve sinyal ortağı ile ilişkili olarak korunan alosterik çerçeveleri ve dinamik çeşitliliği ortaya koymuştur. Özellikle Heliks 8 ve TM7-IC, yolak-özgül iletişimi düzenleyen merkezler olarak öne çıkmıştır. Bu bulgular, GPCR dinamiklerini çözümlemek ve yanlı ligandlar ile alosterik modülatörlerin tasarımına rehberlik etmek için birleşik ve genellenebilir bir çerçeve sunmaktadır.

TABLE OF CONTENTS

ACKNOWLEDGEMENTS iii
ABSTRACT vi
ÖZET vii
LIST OF FIGURES xii
LIST OF TABLES xxiii
LIST OF SYMBOLS xxvi
LIST OF ACRONYMS/ABBREVIATIONS xxvii
1. INTRODUCTION 1
2. LITERATURE REVIEW 5
2.1. Structural Insights into Class A GPCRs 5
2.2. Mechanisms of GPCR Activation 6
2.3. Functional Selectivity and Biased Signaling in GPCRs 9
2.4. GPCR Dynamics in Drug Development Research 13
2.5. Computational Approaches for Class A GPCR Analysis 14
2.6. Literature Review of Selected Class A GPCRs 17
2.6.1. M2 Muscarinic Acetylcholine Receptor (ACM2) 17
2.6.2. Serotonin Receptor 2B (5HT2B) 17
2.6.3. β_1-adrenergic receptor (ADRB1) 18
2.6.4. β_2-adrenergic receptor (ADRB2) 19
2.6.5. Dopamine D3 receptor (DRD3) 19
2.6.6. Neurotensin receptor 1 (NTR1) 20
2.6.7. Vasopressin V2 receptor (V2R) 21
2.6.8. Angiotensin II Type 1 Receptor (AGTR1) 21
2.6.9. K-Opioid Receptor (OPRK) 22
2.6.10. μ-opioid receptor (OPRM) 22
2.6.11. Adenosine A1 Receptor (AA1R) 23
2.6.12. Adenosine A2A receptor (AA2AR) 23
2.6.13. Adenosine A2B receptor (AA2BR) 24

2.6.14. Purinergic Receptor 1 (P2RY1) 24
2.6.15. Purinergic Receptor 12 (P2Y12) 25
2.6.16. Cannabinoid Receptor 1 (CNR1) 25
2.6.17. Prostaglandin D_2 Receptor 2 (PD2R2) 26
2.6.18. Thromboxane A_2 Receptor TA2R 26
2.6.19. Lysophosphatidic Acid Receptor 1 (LPAR1) 26
2.6.20. Sphingosine-1-phosphate receptor 1 (S1PR1) 27
2.6.21. C-C chemokine receptor 1 (CCR1) 27
2.6.22. C-C chemokine receptor 5 (CCR5) 28
2.6.23. C-C Chemokine Receptor 8 (CCR8) 28
2.6.24. C-X-C Chemokine Receptor 2 (CXCR2) 29
2.6.25. C-X-C Chemokine Receptor 4 (CXCR4) 29
3. MATERIALS AND METHODS 31
3.1. Dataset Generation 31
3.2. Elastic Network Models 37
3.2.1. Anisotropic Network Model 38
3.2.2. Co-vibrational Modes 39
3.2.3. Gaussian Network Model (GNM) 40
3.2.4. Signature Dynamic Analysis 42
3.2.5. GNM-Transfer Entropy (GNM-TE) 43
3.2.6. Statistical Analysis 45
3.3. Molecular Dynamics (MD) Simulations 46
3.4. ANM Driven Langevin Dynamics (ANM-LD) 48
3.5. Time-Independent and Time-Delayed Correlations 50
3.6. Differential Coupling Score 50
4. RESULTS AND DISCUSSIONS 52
4.1. Modeling Conformational Transitions of GPCRs via ANM-LD Simulations 53
4.1.1. M2 Muscarinic Acetylcholine Receptor (ACM2) 69
4.1.2. Serotonin Receptor 2B (5HT2B) 71
4.1.3. β_1-adrenergic receptor (ADRB1) 72
4.1.4. β_2-adrenergic receptor (ADRB2) 76

4.1.5. Dopamine D3 receptor (DRD3) 79
4.1.6. Neurotensin receptor 1 (NTR1) 80
4.1.7. Vasopressin V2 receptor (V2R) 82
4.1.8. Angiotensin II Type 1 Receptor (AGTR1) 84
4.1.9. K-Opioid Receptor (OPRK) 85
4.1.10. μ-opioid receptor (OPRM) 87
4.1.11. Adenosine A1 Receptor (AA1R) 88
4.1.12. Adenosine A2A receptor (AA2AR) 92
4.1.13. Adenosine A2B receptor (AA2BR) 93
4.1.14. Purinergic Receptor 1 (P2RY1) 95
4.1.15. Purinergic Receptor 12 (P2Y12) 95
4.1.16. Cannabinoid Receptor 1 (CNR1) 97
4.1.17. Prostaglandin D_2 Receptor 2 (PD2R2) 99
4.1.18. Thromboxane A_2 Receptor TA2R 99
4.1.19. Lysophosphatidic Acid Receptor 1 (LPAR1) 101
4.1.20. Sphingosine-1-phosphate receptor 1 (S1PR1) 103
4.1.21. C-C chemokine receptor 1 (CCR1) 103
4.1.22. C-C chemokine receptor 5 (CCR5) 105
4.1.23. C-C Chemokine Receptor 8 (CCR8) 106
4.1.24. C-X-C Chemokine Receptor 2 (CXCR2) 109
4.1.25. C-X-C Chemokine Receptor 4 (CXCR4) 110
4.1.26. Evaluating Transition Pathways via Allosteric Co-Vibrational ANM Modes 112
4.2. Switching Signals: Conformational transitions pathway underly dynamic communication bias in GPCRs 120
4.2.1. Key Modes of Motion 121
4.2.2. The Allosteric Interactions of 5HT2B 131
4.2.3. Temporal order of allosteric communication 142
4.2.4. Information Flow and Allosteric Communication 151
4.2.5. Differential Coupling Score for Identifying Key Differential Couplings 172

4.3. Allostery and Activation in Class A GPCRs: Conserved and Divergent Features from Comparative Ensemble Analysis 177
4.3.1. Overall Dynamics from Ensemble Analysis 177
4.3.2. State-Specific Dynamics 186
4.3.3. Ligand-Specific Dynamics 196
4.3.4. Differential Dynamics Driven by G proteins and β-Arrestins . . 206
4.4. Additional Works 209
4.4.1. Computational and experimental mapping of the allosteric network of two manganese ABC transporters 209
4.4.2. ANM-LD Path Web Server: A Framework for Predicting Conformational Transitions and Allosteric Interactions 216
4.4.2.1. Adenylate kinase (ADK) 217
4.4.2.2. The Sarcoplasmic / Endoplasmic Reticulum Calcium ATPase (SERCA) 218
4.4.2.3. Calmodulin (CaM) 220
4.4.2.4. Human Transferrin 221
4.4.2.5. D-Ribose-Binding Protein 223
4.4.3. Understanding the Role of Factor V in the Coagulation Cascade and the Impact of Mutations on Its Dynamics 224
5. CONCLUSIONS AND RECOMMENDATIONS 232
5.1. Conclusion 232
5.2. Recommandation 235
REFERENCES 236
APPENDIX A: FIGURE PERMISSION 263

LIST OF FIGURES

Figure 2.1. Demonstration of A2A receptor. 6

Figure 2.2. Functionally important regions of the A2A receptor a) motifs b) distances. 7

Figure 2.3. Biased signaling mechanism in GPCRs 11

Figure 3.1. A schematic overview of the ANM-LD methodology. 49

Figure 4.1. ANM-LD simulation results for the conformational transition of ACM2 from the inactive state to the G protein-bound active state. 70

Figure 4.2. ANM-LD simulation results for the conformational transition of ACM2 from the inactive state to the β-arrestin-bound active state. 71

Figure 4.3. ANM-LD simulation results for the conformational transition of 5HT2B from the inactive state to the G protein-bound active state. 73

Figure 4.4. ANM-LD simulation results for the conformational transition of 5HT2B from the inactive state to the β-arrestin-bound active state. 74

Figure 4.5. ANM-LD simulation results for the conformational transition of ADRB1 from the inactive state to the G protein-bound active state. 75

Figure 4.6. ANM-LD simulation results for the conformational transition of ADRB2 from the inactive state to the active state. 76

Figure 4.7. ANM-LD simulation results for the conformational transition of ADRB2 from the inactive state to the active state. 78

Figure 4.8. Comparison of conformational intermediates generated by ANM-LD simulations with time-resolved cryo-EM structures of the ADRB2 receptor–Gs complex. 79

Figure 4.9. ANM-LD simulation results for the conformational transition of DRD3 from the inactive state to the active state. 80

Figure 4.10. ANM-LD simulation results for the conformational transition of NTR1 from the inactive state to the G protein-bound active state. 81

Figure 4.11. ANM-LD simulation results for the conformational transition of NTR1 from the inactive state to the β-arrestin-bound active state. 82

Figure 4.12. ANM-LD simulation results for the conformational transition of V2R from the inactive state to the G protein-bound active state. . 83

Figure 4.13. ANM-LD simulation results for the conformational transition of V2R from the inactive state to the β-arrestin-bound active state. . 84

Figure 4.14. ANM-LD simulation results for the conformational transition of AT1R from the inactive state to the active state. 85

Figure 4.15. ANM-LD simulation results for the conformational transition of OPRK from the inactive state to the active state. 86

Figure 4.16. ANM-LD simulation results for the conformational transition of OPRM from the inactive state to the active state. 87

Figure 4.17. ANM-LD simulation results for the conformational transition of AA1R from the inactive state to the active state. 90

Figure 4.18. Comparison of ANM-LD and AlphaFlow Sampling on A1R 91

Figure 4.19. Projection of ANM-LD–generated intermediate structures onto the free energy landscape (FEL) of adenosine A1 receptor (A1R) activation, adapted from metadynamics simulations. 92

Figure 4.20. [ANM-LD simulation results for the conformational transition of AA2AR from the inactive state to the active state. 93

Figure 4.21. ANM-LD simulation results for the conformational transition of AA2BR from the inactive state to the active state. 94

Figure 4.22. ANM-LD simulation results for the conformational transition of P2RY1 from the inactive state to the active state. 96

Figure 4.23. ANM-LD simulation results for the conformational transition of P2Y12 from the inactive state to the active state. 97

Figure 4.24. ANM-LD simulation results for the conformational transition of CNR1 from the inactive state to the active state. 98

Figure 4.25. ANM-LD simulation results for the conformational transition of PD2R2 from the inactive state to the active state. 100

Figure 4.26. ANM-LD simulation results for the conformational transition of TA2R from the inactive state to the active state. 101

Figure 4.27. ANM-LD simulation results for the conformational transition of LPAR1 from the inactive state to the active state. 102

Figure 4.28. ANM-LD simulation results for the conformational transition of S1PR1 from the inactive state to the active state. 104

Figure 4.29. ANM-LD simulation results for the conformational transition of CCR1 from the inactive state to the active state. 105

Figure 4.30. ANM-LD simulation results for the conformational transition of CCR5 from the inactive state to the active state. 107

Figure 4.31. Comparison of ANM-LD and MD sampling for the CCR5 receptor. 108

Figure 4.32. ANM-LD simulation results for the conformational transition of CCR8 from the inactive state to the active state. 109

Figure 4.33. ANM-LD simulation results for the conformational transition of CXCR2 from the inactive state to the active state. 111

Figure 4.34. ANM-LD simulation results for the conformational transition of CXCR4 from the inactive state to the active state. 112

Figure 4.35. Overlap analysis between co-vibrational ANM modes and structural difference vectors for aminergic-bound receptors. 115

Figure 4.36. Overlap analysis between co-vibrational ANM modes and structural difference vectors for peptide-bound receptors. 116

Figure 4.37. Overlap analysis between co-vibrational ANM modes and structural difference vectors for nucleotide-bound receptors. 117

Figure 4.38. Overlap analysis between co-vibrational ANM modes and structural difference vectors for lipid-bound receptors. 118

Figure 4.39. Overlap analysis between co-vibrational ANM modes and structural difference vectors for protein-bound receptors. 119

Figure 4.40. Comparison of difference vectors and cumulative ANM mode shapes for 5HT2B activation pathways. 122

Figure 4.41. Cumulative ANM mode shapes and identification of hinge regions in 5HT2B activation pathways. 124

Figure 4.42. Cumulative ANM mode shapes and identification of hinge regions in ADRB1 activation pathways. 128

Figure 4.43. Cumulative ANM mode shapes and identification of hinge regions in ACM2 activation pathways. 129

Figure 4.44. Cumulative ANM mode shapes and identification of hinge regions in V2R activation pathways. 130

Figure 4.45. Cumulative ANM mode shapes and identification of hinge regions in NTR1 activation pathways. 131

Figure 4.46. Segment-level cross-correlation analysis for the G protein–targeted activation pathway of 5HT2B receptor. 135

Figure 4.47. Segment-level cross-correlation analysis for the β-arrestin–targeted activation pathway of 5HT2B receptor. 136

Figure 4.48. Segment-level cross-correlation difference analysis for the G portein- and β-arrestin–targeted activation pathway of 5HT2B receptor. . . 137

Figure 4.49. Segment-level cross-correlation difference networks for distinct receptor activation pathways for (A) ADRB1 and (B) ACM2. 138

Figure 4.50. Segment-level cross-correlation difference networks for distinct receptor activation pathways for (A) V2R and (B) NTR1. 139

Figure 4.51. Segment-level correlation difference networks for for (A) ADRB1 and (B) ACM2 receptor activation pathways. 140

Figure 4.52. Segment-level correlation difference networks for (A) V2R and (B) NTR1 receptor activation pathways. 141

Figure 4.53. Time-delayed dynamic cross-correlation maps at the residue level during the activation of the 5HT2B receptor. 145

Figure 4.54. Segment-level time-delayed dynamic cross-correlation analysis of 5HT2B receptor for the G protein–targeted activation pathway. . . 146

Figure 4.55. Segment-level time-delayed dynamic cross-correlation analysis of 5HT2B receptor for the β-arrestin–targeted activation pathway. . . 147

Figure 4.56. Segment-level time-delayed dynamic cross-correlation analysis of ADRB1. 149

Figure 4.57. Segment-level time-delayed dynamic cross-correlation analysis of ACM2 activation pathways. 150

Figure 4.58. Transfer Entropy (TE) Analysis of the 5HT2B Receptor Bound to G protein and β-arrestin in 1-10 modes. 153

Figure 4.59. Demonstration of TEcol scores across residue indices for the G protein-bound (A) and β-arrestin-bound (B) states. 154

Figure 4.60. Statistical validation of GNM-TE predicted allosteric hotspots through randomization analysis. 155

Figure 4.61. Chain-level net transfer entropy (Net TE) maps for G protein– and β-arrestin–bound states. 157

Figure 4.62. TEcol score profiles across residues for G protein—bound state. . . 158

Figure 4.63. TEcol score profiles across residues for β-arrestin–bound state. . . 159

Figure 4.64. Information transfer from the ligand-binding region to the receptor–signaling complex across different mode regimes. 160

Figure 4.65. Chain-level Net transfer entropy (Net TE) analysis of ADRB1 for G protein– (A) and β-arrestin–bound (B) states in 1-10 mode subset. 162

Figure 4.66. Chain-level Net transfer entropy (Net TE) analysis of ADRB1 for G protein– (A) and β-arrestin–bound (B) states in 2-10 mode subset. 163

Figure 4.67. Chain-level Net transfer entropy (Net TE) analysis of ADRB1 for G protein– (A) and β-arrestin–bound (B) states in 3-10 mode subset. 164

Figure 4.68. TEcol scores and structural mapping of information source residues for the G protein–bound state in ADRB1. 165

Figure 4.69. TEcol scores and structural mapping of information source residues for the β-arrestin state in ADRB1. 166

Figure 4.70. Chain-level Net transfer entropy (Net TE) analysis of ACM2 for G protein– (A) and β-arrestin–bound (B) states in 1-10 mode subset. 167

Figure 4.71. Chain-level Net transfer entropy (Net TE) analysis of ACM2 for G protein– (A) and β-arrestin–bound (B) states in 2-10 mode subset. 168

Figure 4.72. Chain-level Net transfer entropy (Net TE) analysis of ACM2 for G protein– (A) and β-arrestin–bound (B) states in 3-10 mode subset. 169

Figure 4.73. TEcol scores and structural mapping of information source residues for the G protein–bound state in ACM2. 170

Figure 4.74. TEcol scores and structural mapping of information source residues for the β-arrestin state in ACM2. 171

Figure 4.75. Segment-level differential Coupling in 5HT2B receptor between G protein- and β-arrestin-bound states. 173

Figure 4.76. Segment-level differential coupling in ADRB1 and ACM2 receptors between G protein- and β-arrestin-bound states. 174

Figure 4.77. Segment-level differential coupling in V2R and NTR1 receptors between G protein- and β-arrestin-bound states. 175

Figure 4.78. Mean squared fluctuation (MSF) analysis across the GPCR ensemble.179

Figure 4.79. Cross-correlation analysis of collective motions across the GPCR ensemble. 182

Figure 4.80. Segment-averaged cross-correlation networks derived from the global (A) and low-frequency (B) modes. 183

Figure 4.81. Variability in cross-correlation patterns across the GPCR ensemble. 185

Figure 4.82. Fluctuation profiles of state-specific GPCR ensembles. 187

Figure 4.83. Structural mapping of the average fluctuations onto the M2 muscarinic receptor (PDB ID: 5ZK3) for different mode regimes across different states. 188

Figure 4.84. Cross-correlation differences between receptor states in the global mode regime. 191

Figure 4.85. Segment-based average cross-correlation differences corresponding to dynamic shifts in global modes 192

Figure 4.86. Cross-correlation differences between receptor states in the low frequency regime. 194

Figure 4.87. Segment-based average cross-correlation differences corresponding to dynamic shifts in low frequency modes. 195

Figure 4.88. Fluctuation profiles of ligand-type–specific GPCR ensembles. . . . 197

Figure 4.89. Ligand-type–specific cross-correlation differences in the global mode regime. 199

Figure 4.90. Ligand-type–specific segment based correlation networks derived from global mode differences. 200

Figure 4.91. Ligand-type–specific cross-correlation differences in the low frequency mode regime. 201

Figure 4.92. Ligand-type–specific segment based correlation networks derived from low frequency mode differences. 202

Figure 4.93. Signal protein–specific cross-correlation differences across global and low-frequency mode regimes. 207

Figure 4.94. Signal protein–specific segment based correlation differences across global and low-frequency mode regimes. 208

Figure 4.95. Identification of allosteric hotspots in PsaBC. 213

Figure 4.96. Relative contribution in 1/Eigenvalue of the slow modes of PsaBC and MntBC to the overall dynamics as a function of mode number. 213

Figure 4.97. Allosteric peaks and collectivity across mode ranges in PsaBC. . . 215

Figure 4.98. Correlation between allosteric hotspots in MntBC and functionally essential residues. 216

Figure 4.99. ANM-LD simulation results for adenylate kinase (AdK). 218

Figure 4.100. ANM-LD simulation results for the SERCA protein. 220

Figure 4.101. ANM-LD simulation results for calmodulin. 221

Figure 4.102. ANM-LD simulation results for human transferrin. 222

Figure 4.103. ANM-LD simulation results for D-ribose-binding protein. 224

Figure 4.104. Representation of human Factor V with A) important sites B) mutation points. 226

Figure 4.105. RMSD analysis of Factor V wild-type and mutant variants over the course of 500 ns molecular dynamics simulations. 228

Figure 4.106. Residue correlations of seven slowest GNM modes in color-coded ribbon diagram of the factor V 229

Figure 4.107. Residue correlations of seven slowest GNM modes in color-coded ribbon diagram of the C1 and C2 region of factor V 229

Figure 4.108. Comparison of the dynamic behavior of wild-type and mutant Factor V, calculated using the average Kirchhoff matrix from snapshots taken between 250-500 ns, focusing on modes 1-10. 231

LIST OF TABLES

Table 2.1. Important distances and motifs 8

Table 3.1. Summary of GPCR family members analyzed in this study. 32

Table 4.1. ANM-LD simulation summary of ACM2 receptor. 54

Table 4.2. ANM-LD simulation summary of 5HT2B receptor. 55

Table 4.3. ANM-LD simulation summary of ADRB1 receptor. 56

Table 4.4. ANM-LD simulation summary of ADRB2 receptor. 57

Table 4.5. ANM-LD simulation summary of DRD3 receptor. 57

Table 4.6. ANM-LD simulation summary of NTR1 receptor. 58

Table 4.7. ANM-LD simulations of V2R 59

Table 4.8. ANM-LD simulation summary of AGTR1 receptor 60

Table 4.9. ANM-LD simulation summary of OPRK receptor. 60

Table 4.10. ANM-LD simulation summary of OPRM receptor. 61

Table 4.11. ANM-LD simulation summary of AA1R receptor. 61

Table 4.12. ANM-LD simulation summary of AA2AR receptor. 62

Table 4.13. ANM-LD simulation summary of AA2BR receptor. 62

Table 4.14. ANM-LD simulation summary of P2RY1 receptor. 63

Table 4.15. ANM-LD simulation summary of P2Y12 receptor 63

Table 4.16. ANM-LD simulation summary of CNR1 receptor. 64

Table 4.17. ANM-LD simulation summary of DP2 receptor. 64

Table 4.18. ANM-LD simulation summary of TA2R receptor. 65

Table 4.19. ANM-LD simulation summary of LPAR1 receptor. 65

Table 4.20. ANM-LD simulation summary of S1PR1 receptor. 66

Table 4.21. ANM-LD simulation summary of CCR1 receptor. 66

Table 4.22. ANM-LD simulation summary of CCR5 receptor. 67

Table 4.23. ANM-LD simulation summary of CCR8 receptor. 67

Table 4.24. ANM-LD simulation summary of CXCR2 receptor. 68

Table 4.25. ANM-LD simulation summary of CXCR4 receptor. 68

Table 4.26. Proximity analysis between functionally annotated residues and hinge residues, where residues within 7 $\AA$ are plotted for the G protein-bound case. 124

Table 4.27. Proximity analysis between functionally annotated residues and hinge residues, where residues within 7 $\mathring{A}$ are plotted for the β-arrestin-bound case. 126

LIST OF SYMBOLS

a_i	Acceleration of particle i
C	Cross Correlation
D_F	Deformation factor
d_i	Distance between the coordinates of atom i in two structures
D_i	Distance difference vector
F_i	Force exerted on particle i
H	Hessian matrix
k_B	Boltzmann constant
m_i	Mass of particle i
N	Number of atoms
O_{ij}	Overlap value of j^{th} eigenvector with the difference vector for cycle i
R_{cut}	Cut-off radius
R^0_{ij}	Equilibrium distance between residues i and j
R_i	Position vector of residue i
R_{ij}	Instantaneous distance between residues i and j
t	Time
T	Absolute temperature
u_k	k^{th} eigenvector
V	Potential function
γ_f	Force constant for harmonic spring
Γ	Kirchhoff matrix
$\triangle R_i$	Fluctuation of residue i
λ_k	k^{th} eigenvalue
ν_i	Velocity of atom i

LIST OF ACRONYMS/ABBREVIATIONS

ANM	Anisotropic Network Model
ANM-LD	Anisotropic Network Model Guided Langevin Dynamics
ECL	Extracellular Loop
ENM	Elastic Network Model
GNM	Gaussian Network Model
GNM-TE	GNM-Transfer Entropy
GPCRs	Guanine Binding Protein Coupled Receptors
ICL	Intracellular Loop
LD	Langevin Dynamics
MD	Molecular Dynamics
MSF	Mean Square Fluctuations
PDB	Protein Data Bank
RMSD	Root-Mean-Square Deviation
SF	Square Fluctuations
TM	Transmembrane

1. INTRODUCTION

G protein-coupled receptors (GPCRs) represent the largest and most pharmacologically significant family of membrane proteins in humans, comprising more than 800 members involved in diverse physiological processes, including sensory perception, immune regulation, cardiovascular control, and neurotransmission [1–7]. Owing to their central role in signal transduction, nearly one-third of all FDA-approved drugs target GPCRs. Among the six major GPCR classes, Class A is the most structurally and functionally characterized, accounting for approximately 85% of all GPCRs [8]. These receptors share a conserved seven-transmembrane (7TM) architecture yet exhibit remarkable variability in ligand binding mechanisms, activation pathways, and signaling outcomes.

A major conceptual breakthrough in GPCR research has been the discovery of biased signaling, wherein different ligands stabilize distinct receptor conformations that preferentially engage either G proteins or β-arrestins. This phenomenon enables selective modulation of downstream pathways and opens the door to the design of safer and more effective therapeutics [9–13]. However, the molecular mechanisms underlying biased signaling remain incompletely understood, partly because conventional experimental techniques capture only a limited number of stable receptor conformations and fail to resolve the transient intermediate states that drive activation and signal propagation.

Ligand selectivity in GPCRs is governed by multiple structural features, including ligand size, binding location, and the extent of interaction with the transmembrane domain and extracellular loops (ECLs) [14]. Small aminergic ligands typically bind deep within the TM core with minimal ECL engagement, whereas larger peptide or protein ligands interact more extensively with extracellular regions, inducing broader rearrangements in the TM helices [15]. Lipid ligands, by contrast, embed laterally through the membrane and promote local flexibility without deep penetration into the

core [16]. These differences influence how ligands modulate receptor activation and determine signaling outcomes.

GPCRs can initiate signaling through multiple intracellular partners, most commonly G proteins and β-arrestins. G protein engagement typically requires an outward displacement of TM6 to expose a cytoplasmic cavity, while β-arrestin binding involves recognition of both phosphorylated receptor tails and the active receptor core. These interactions highlight the conformational plasticity that supports pathway-specific signaling [17–28].

Through this highly complex mechanism, different ligands can activate distinct intracellular signaling partners via the same GPCR, and conversely, different GPCRs can activate the same signaling proteins. Despite significant advances, the mechanistic foundations of GPCR activation, the nature of allosteric transitions, and the dynamic similarities and differences among receptor subtypes remain insufficiently understood [16, 29, 30].

In recent years, molecular dynamics (MD) simulations have been widely used to study the atomic-level dynamics of macromolecules, revealing that proteins often occupy multiple conformational substates and transition dynamically between them. GPCR activation typically occurs over tens of milliseconds to seconds under physiological conditions—except for rhodopsin, whose TM rearrangement occurs within one millisecond. However, MD simulations are generally limited to nanosecond-to-microsecond timescales, creating a mismatch between biological processes and accessible simulation durations [31–34]. This limitation highlights the need for alternative sampling methods capable of capturing long-timescale transitions and exploring functionally relevant intermediate conformations.

To address these challenges and provide a comprehensive mechanistic view of GPCR dynamics, this thesis presents an integrated investigation using Anisotropic Network Model driven Langevin Dynamics (ANM-LD) simulations [35–37] combined

with complementary computational techniques. The modeled intermediates generated by ANM-LD capture hallmark features of GPCR activation, such as the outward tilt of transmembrane TM6 [21], and serve as physically meaningful conformations along the activation pathway. These structures enable further investigation into the sequence of activation events and the identification of intrinsic dynamic elements that contribute to signal specificity and allosteric regulation across the GPCR family.

The major aim of this thesis is to uncover the dynamic basis of signaling selectivity in GPCRs through comparative analysis of the structural dynamics across family members. Specifically, we investigate how the intrinsic dynamics—encoded by sequence and structure—facilitate the conformational transitions required for function. Furthermore, we aim to decode the dynamic signatures that define signaling specificity by exploring how the structural and dynamic potential of GPCRs generalizes or differentiates transition pathways across diverse receptor states, ligand types, signaling partners, and family members. This work is organized into four main sections. The first section focuses on modeling activation transitions across 25 Class A GPCRs using ANM-LD simulations. Each pathway consists of a series of intermediate structures bridging inactive and active conformations, providing a foundation for identifying shared and receptor-specific features of activation. To enhance the physical relevance of the simulations, we apply the covibrational mode framework introduced by Kolossváry (2024) [38], which uses weighted combinations of low-frequency modes to better represent collective transitions underlying allosteric mechanisms.

The second section centers on five receptors with available structures in both G protein and β-arrestin bound active states, as well as their transition pathways modeled in Section 4.1. By integrating ANM mode analysis, conventional and time-delayed cross-correlation, and transfer entropy derived from the Gaussian Network Model, we explore the structural basis of biased signaling. We introduce a novel metric, the Differential Coupling Score, to quantify regions where information flow and correlation patterns diverge between signaling pathways, helping to pinpoint residues responsible for pathway-specific communication.

The third section extends the analysis to a comparative level across all 25 GPCRs using the SignDy tool [39, 40], which identifies signature dynamics from structural ensembles. This approach uncovers conserved and divergent dynamic signatures associated with receptor state, ligand type, and signaling partner. The ensemble-level view reveals both shared allosteric frameworks and subtype-specific adaptations that underlie functional diversity within the GPCR family.

The final section of the thesis demonstrates the generalizability of the developed framework through three complementary case studies: (i) an analysis of allosteric communication in transition-metal ABC transporters validated through mutagenesis data, (ii) the development and benchmarking of the ANM-LD Path server for dynamic pathway modeling, and (iii) an investigation of how disease-relevant mutations in Factor V alter long-range dynamic communication relevant to blood coagulation.

Together, these studies establish a unified computational framework for understanding GPCR activation, allosteric regulation, and selective signaling. By integrating pathway modeling, dynamic mode analysis, and information-theoretic measures, this work bridges static structural snapshots with functional dynamics and reveals how intrinsic motions shape receptor behavior across multiple biological contexts. The results not only illuminate the molecular underpinnings of biased signaling but also provide a scalable strategy for probing signaling specificity across Class A GPCRs. Taken together, the findings offer valuable insights for structure-based drug design, guide the interpretation of experimental data, and contribute to a deeper understanding of how proteins encode and transmit functional information through dynamics.

2. LITERATURE REVIEW

G protein-coupled receptors (GPCRs) constitute the largest family of membrane proteins in humans, with over 800 members involved in various physiological processes. These receptors play pivotal roles in numerous diseases, including cancer, sensory disorders, immunological conditions, viral infections, cardiovascular, and inflammatory diseases. Consequently, GPCRs have become prominent targets in drug discovery, with approximately one-third of marketed medications acting on these receptors [1–6].

Rhodopsin-like receptors (class A), secretin-like receptors (class B), metabotropic glutamate receptors (class C), fungal coupling pheromone receptors (class D), cAMP receptors (class E), and frizzled receptors (class F) are the classes used to categorize GPCRs [41]. Class A represents the most extensively studied group, accounting for about 85% of all GPCRs [8]. Their prominence in drug discovery is attributed to their involvement in critical physiological functions and high druggability.

2.1. Structural Insights into Class A GPCRs

Class A G protein-coupled receptors (GPCRs) share a conserved structural framework consisting of seven transmembrane (TM) helices (TM1-TM7), which are linked by three extracellular loops (ECL1–ECL3) and three intracellular loops (ICL1–ICL3), along with an extracellular N-terminal domain and an intracellular C-terminal domain [42] . These TM helices arrange into a compact bundle that forms an orthosteric binding site for ligands. Upon ligand engagement, notable conformational changes in intracellular side occur, promoting the recruitment of signal protein and initiating downstream signaling [21]. The structure and the corresponding regions of a representative case (A2A receptor) are shown in Figure 2.1.

The extracellular loops help to determine ligand selectivity and receptor activation. Notably, ECL2 frequently forms a conserved disulfide link with TM3, which

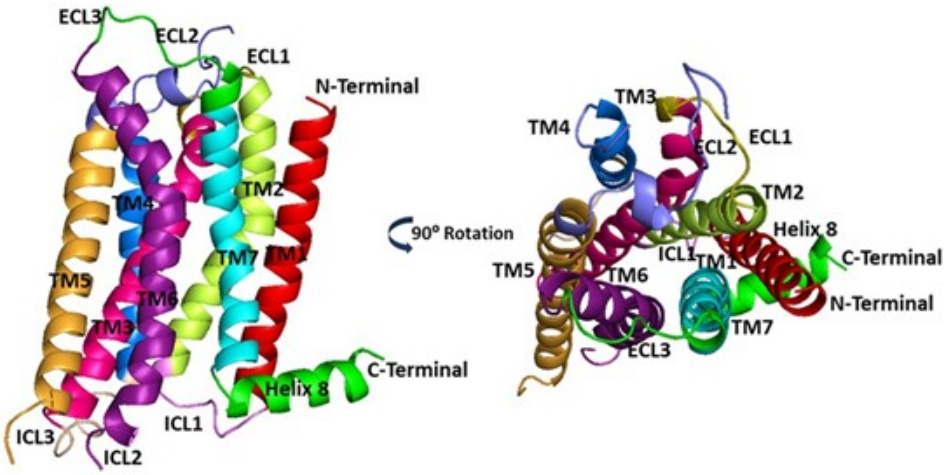

Figure 2.1. Demonstration of A2A receptor.

stabilizes the receptor structure and plays an important function in ligand recognition. Intracellular loops play an important role in transferring signals from activated receptors to intracellular effectors [17, 21, 24]. ICL2 and ICL3 play key roles in G protein coupling and receptor modulation. Many Class A GPCRs have an α-helix, H8, situated right after TM7 on the intracellular side [43]. Helix-8 helps to maintain receptor integrity, interacts with G proteins and β-arrestins, and is involved in receptor desensitization and internalization processes [44].

2.2. Mechanisms of GPCR Activation

GPCR activation involves an allosteric mechanism in which the binding of an extracellular ligand triggers the recruitment of intracellular partners. A key feature of this process is the outward movement of TM6, which creates space for G protein/β-arrestin engagement. Structural analyses have identified conserved "microswitches," such as the DRY, NPxxY, and PIF motifs, which undergo conformational changes during activation [1, 45, 46]. Table 2.1 summarizes the highly conserved residues and motifs, along with key inter-residue distances that are critical for activation across Class A GPCR family members [32] (Residues are annotated using the Ballesteros–Weinstein numbering scheme, in which the number before the decimal refers to the transmembrane helix, and the number after the decimal indicates the residue's position relative

to the most conserved site (designated as .50) within that helix [47]. These residues are demonstrated on the structure in Figure 2.2.

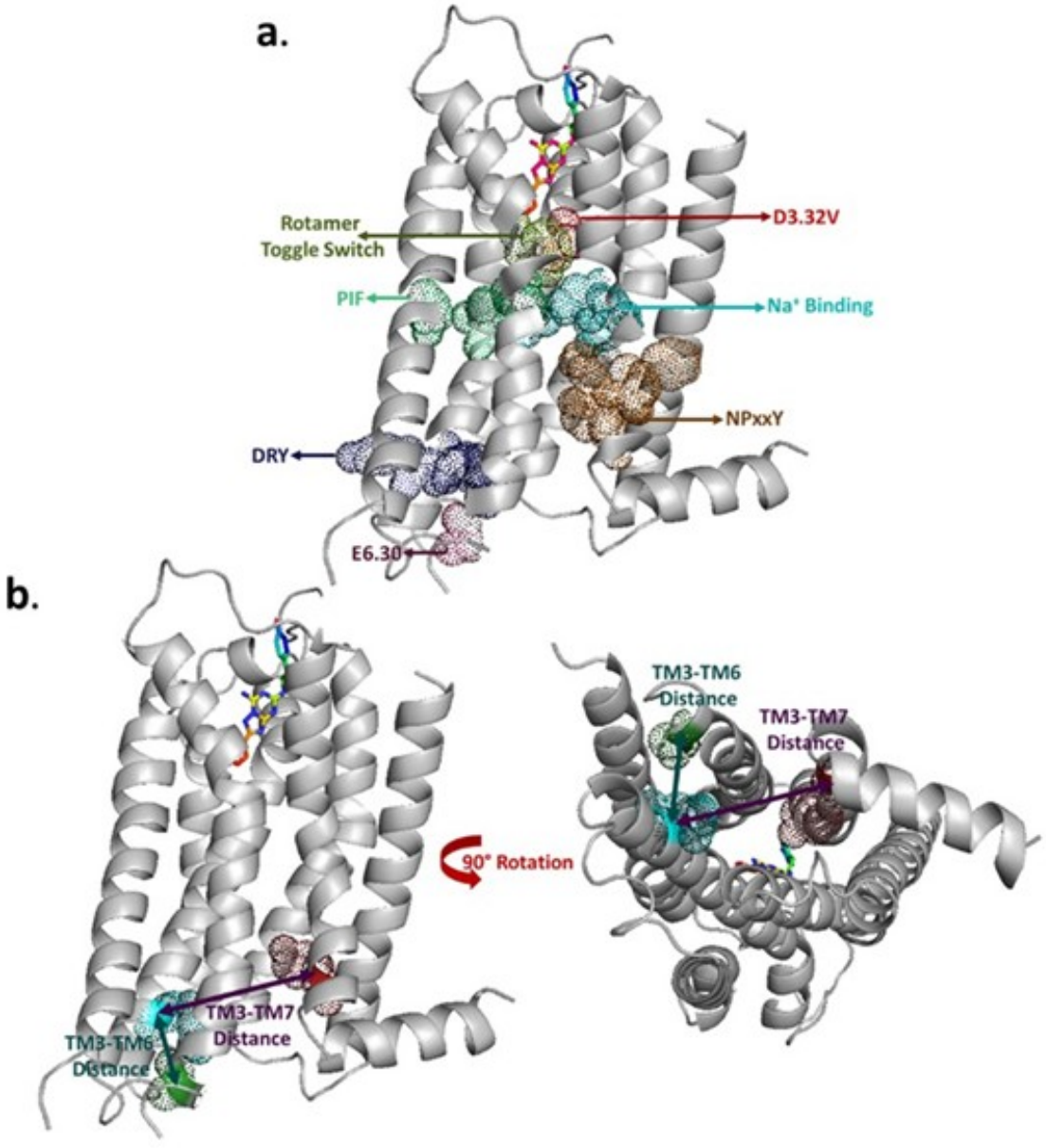

Figure 2.2. Functionally important regions of the A2A receptor a) motifs b) distances.

Table 2.1. Important distances and motifs with their residue names.

Important Distances and Motifs	**Residue Names**
TM3–TM6	$R^{3.50}$–$E^{6.30}$
TM3–TM7	$R^{3.50}$–$Y^{7.53}$
DRY Motif	$D^{3.49}$–$R^{3.50}$–$Y^{3.51}$
NPxxY Motif	$N^{7.49}$–$P^{7.50}$–$x^{7.51}$–$x^{7.52}$–$Y^{7.53}$
PIF Motif	$P^{5.50}$–$I^{3.40}$–$F^{6.44}$
Na^+ Binding Site	$D^{2.50}$–$S^{3.39}$–$N^{7.45}$–$S^{7.46}$
Rotamer Toggle Switch	$W^{6.48}$
Ionic Lock	$R^{3.50}$–$E^{6.30}$

The dynamic nature of GPCRs arises from a combination of their inherent structural flexibility and influences from external factors, leading to conformational changes that can span the entire receptor. Among the seven transmembrane helices, TM5 through TM7 play a central role in relaying activation signals across the membrane [17]. Rather than switching between just one active and one inactive form, GPCRs occupy a diverse ensemble of conformations, each linked to distinct signaling outcomes. Although the most prominent structural rearrangements occur on the intracellular side during activation, the extracellular regions also experience modest conformational adjustments. Ligand binding at the orthosteric site is tightly coupled to changes on the intracellular side, and the structural composition of extracellular ligand-binding pockets varies widely among receptors [29, 48]. Additionally, the regions responsible for G protein versus β-arrestin binding differ structurally, allowing the receptor to selectively activate different signaling pathways [30].

These conformational transitions are crucial for transmitting extracellular signals into intracellular responses. GPCR activation entails adopting specific conformational states that enable coupling with G proteins or β-arrestins. While substantial progress

has been made in identifying conserved structural motifs and their activation-associated rearrangements [21,49], the full mechanism linking the extracellular ligand-binding site to intracellular effector coupling remains only partially understood. One consistently observed hallmark of activation is the outward displacement of the cytoplasmic end of TM6. In a comprehensive analysis, Zhou et al. (2019) examined 234 structures across 45 Class A GPCRs using residue-residue contact scores to capture structural transitions during activation. Their findings support a four-layered model of activation: (1) changes in contacts between the CWxP and PIF motifs and the sodium-binding pocket; (2) disruption of the hydrophobic lock characteristic of the inactive state; (3) rearrangement of interactions involving the NPxxY motif; and (4) rewiring of contact patterns within the DRY motif. Together, these layers illustrate a sequential and coordinated pathway of structural changes that bridge ligand binding with intracellular signal transduction [21].

2.3. Functional Selectivity and Biased Signaling in GPCRs

The signaling mechanisms of GPCRs involve three main protein families: G proteins, GPCR kinases (GRKs), and β-arrestins. Upon agonist binding, GPCRs undergo conformational changes that enable the Gα subunit of the heterotrimeric G protein to exchange GDP for GTP, triggering dissociation of the Gα and G$\beta\gamma$ subunits. These subunits then modulate various downstream effectors [50]. β-arrestins, initially characterized for their role in desensitizing G protein signaling, have since been recognized as multifunctional scaffolding proteins that initiate distinct pathways such as MAPK, AKT, and SRC signaling [51]. The recruitment of β-arrestin typically requires phosphorylation of serine and threonine residues in the intracellular loops and C-terminal tail of GPCRs [50].

Structural studies of GPCRs bound to G proteins, GRKs, or β-arrestins suggest that biased signaling is unlikely to arise from a single, universal receptor conformation; rather, it may be driven by receptor-specific dynamics, fine-tuned residue interactions, or the absence of a broadly conserved bias-favoring structural state [13].

Biased signaling, or functional selectivity, refers to the phenomenon where different ligands stabilize distinct receptor conformations that preferentially promote either G protein or β-arrestin-mediated pathways, as demonstrated in Figure 2.3. This ligand-directed signaling preference enables modulation of downstream effects without uniformly activating all possible signaling routes. Although crystallographic structures of GPCRs often appear similar in active states, differences emerge in the dynamics and interacting protein complexes that underlie biased signaling. For instance, while typical active-state GPCRs can recruit both G proteins and β-arrestins, certain ligands can bias the receptor toward activating only one of these pathways—stimulating G protein signaling without engaging β-arrestins, or vice versa [52]. Additionally Thomsen et al. demonstrated that GPCRs can form stable "megaplexes" with both β-arrestin and G proteins simultaneously, revealing a structural basis for sustained G protein signaling from internalized receptors through combined biochemical, biophysical, and electron microscopy analyses [53].

Activation of GPCRs involves extensive conformational rearrangements on the intracellular surface, most prominently the outward displacement of transmembrane helix 6 (TM6), which opens a cavity for binding intracellular effectors such as G proteins and β-arrestins. Additional shifts in TM5, TM7, and helix 8 also contribute to selective transducer engagement and shape the resulting signaling bias. A hallmark of β-arrestin interaction is the insertion of its finger loop into a pocket formed by TM2, TM3, TM6, and TM7—though the depth, orientation, and stability of this insertion can vary substantially depending on the receptor and ligand, thereby influencing transducer preference and signaling outcomes [17–28].

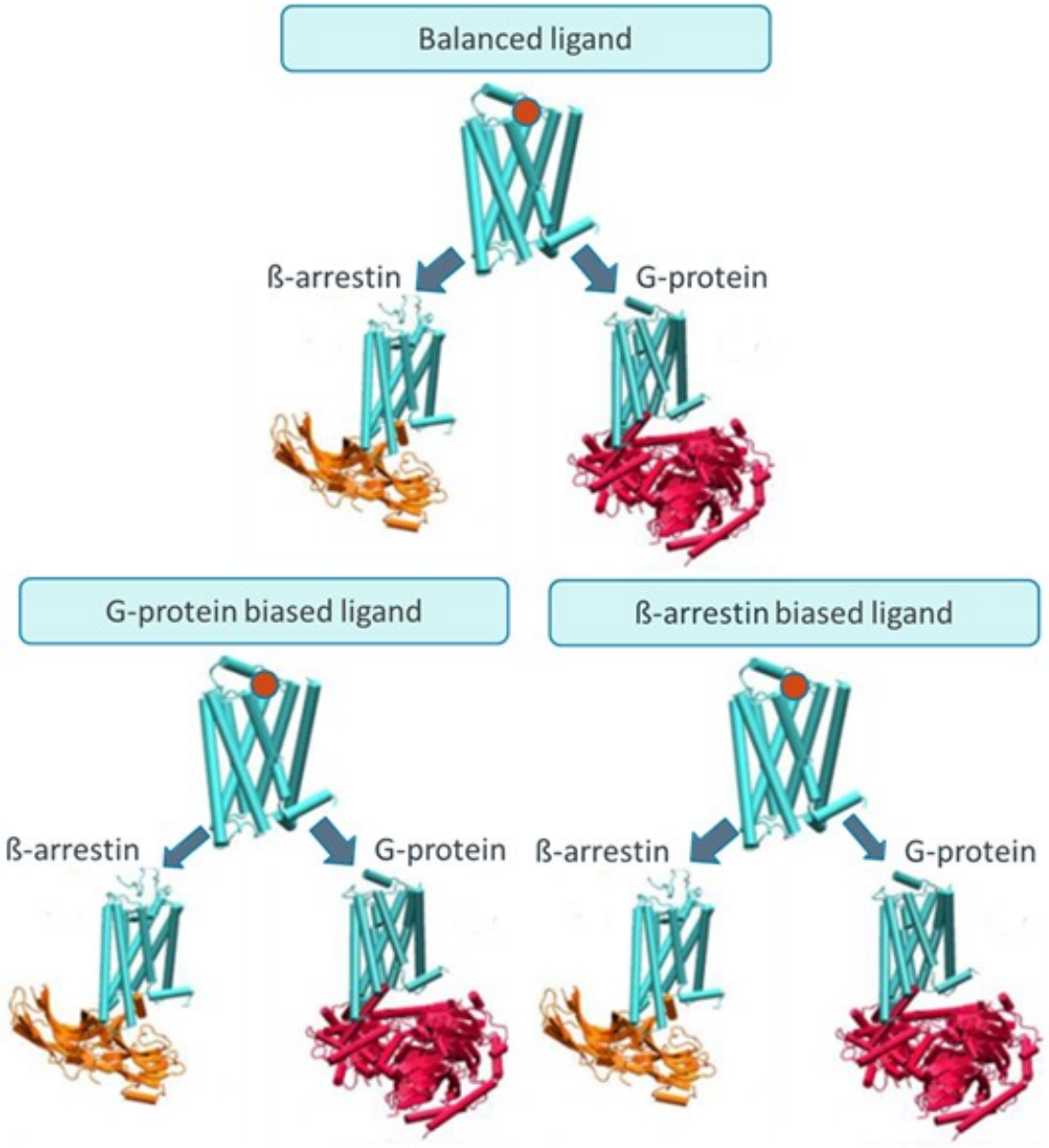

Figure 2.3. Biased signaling mechanism in GPCRs

Recent cryo-EM studies have shed light on the structural diversity of GPCR–β-arrestin complexes. For instance, in the M2R–β-arrestin 1 structure, β-arrestin engages both the phosphorylated receptor tail and the transmembrane core, with its finger loop mimicking G protein binding and its C-edge anchoring into the lipid bilayer to stabilize the complex [23]. In contrast, the neurotensin receptor 1 (NTS1) complexed with the β-arrestin-biased modulator SBI-553 exhibits a unique interaction mode, wherein β-

arrestin binds primarily to intracellular loop 3 (ICL3) rather than inserting deeply into the transmembrane core—indicating an alternative, arrestin-selective receptor conformation [54].

Biased allosteric modulators (BAMs) represent a promising strategy for selectively modulating GPCR signaling. By binding to allosteric sites outside the orthosteric pocket, BAMs stabilize receptor conformations that preferentially recruit either G proteins or β-arrestins [55]. SBI-553 exemplifies this mechanism by shifting NTS1 into a β-arrestin–favoring state through noncanonical intracellular loop engagement. This reconfiguration of the receptor-transducer interface, confirmed via cryo-EM and phosphomimetic receptor constructs, underscores how BAMs can finely tune signaling outcomes for therapeutic advantage [54].

The clinical implications of biased signaling—and by extension, BAMs—are particularly significant in neurological and psychiatric disorders. In the case of 5-HT_2AR, a key target for antipsychotic therapies, full receptor blockade can inadvertently downregulate mGlu2R expression, potentially worsening cognitive symptoms in schizophrenia. Instead, selective modulation of specific signaling arms (e.g., Gαq vs. β-arrestin) may offer a way to preserve therapeutic efficacy while minimizing detrimental effects [56–59]. BAMs targeting such pathways could avoid the pitfalls of global receptor inhibition.

In systemic disorders, biased signaling also provides therapeutic leverage. For example, μ-opioid receptor (μ-OR) agonists like enkephalin engage both G protein and β-arrestin pathways. However, β-arrestin recruitment by morphine has been associated with adverse outcomes such as tolerance, constipation, and respiratory depression. G protein-biased agonists like TRV130 (oliceridine) have shown preserved analgesic efficacy with reduced side effects, demonstrating the value of pathway-selective modulation [60, 61].

Beyond ligand bias, mutations in GPCR transducer-coupling motifs—such as the DRY motif or C-terminal phosphorylation clusters—can intrinsically skew signaling

bias, contributing to diseases such as nephrogenic diabetes insipidus (e.g., V2R mutations) or immune dysregulation (e.g., CXCR4 mutations) [62–64]. This underscores the therapeutic potential of bias-corrective allosteric drugs, which could restore balanced signaling even in genetically compromised receptors.

The ability to selectively modulate GPCR signaling through biased ligands presents significant potential for advancing next-generation drug development, offering a means to enhance therapeutic benefits while reducing adverse effects. Ongoing research into the molecular basis of biased signaling—especially the structural and dynamic changes triggered by different ligands—continues to drive progress in the field of precision pharmacology.

2.4. GPCR Dynamics in Drug Development Research

GPCRs have been widely investigated as pharmacological targets due to their central role in regulating diverse physiological processes and the accessibility of their druggable sites on the cell surface. Currently, drugs targeting GPCRs make up approximately 34% of the global therapeutic market, generating annual sales exceeding 180 billion USD [3, 65–67]. Their prominence as drug targets stems from both the broad spectrum of physiological functions governed by GPCR signaling and the structural diversity of their ligand-binding pockets.

Orthosteric ligands, which bind to the primary active site of GPCRs, are generally classified as agonists, partial agonists, inverse agonists, or antagonists. Full agonists mimic the action of endogenous ligands and fully activate the receptor, whereas partial agonists can activate the receptor but with lower efficacy. Inverse agonists, by contrast, suppress the receptor's basal activity in the absence of agonist stimulation. Antagonists block the action of both agonists and inverse agonists without triggering a response themselves. Biased ligands represent a distinct class, capable of selectively modulating specific signaling pathways—such as preferentially activating G protein- or β-arrestin-mediated signaling [68]. In addition to orthosteric ligands, allosteric lig-

ands bind to secondary sites on the receptor, distinct from the orthosteric pocket. Allosteric agonists can stabilize the receptor in an active conformation independently of orthosteric ligand binding, while allosteric antagonists inhibit receptor activation by interfering with orthosteric ligand efficacy [69, 70].

2.5. Computational Approaches for Class A GPCR Analysis

Advancements in computational biology have significantly deepened our understanding of Class A G protein-coupled receptors (GPCRs). A range of online platforms and computational strategies have been developed to model, visualize, and analyze the dynamic behavior of these receptors, offering valuable insights into their activation mechanisms and biased signaling.

Recent breakthroughs in protein structure prediction—such as AlphaFold2, and RoseTTAFold—have revolutionized structural biology by enabling highly accurate modeling of protein structures directly from amino acid sequences [71, 72]. However, these models typically represent a single, static conformation and are limited in their ability to reflect the dynamic conformational landscape crucial for GPCR function. To overcome this limitation, newer methods like AlphaFold3 have been introduced, which aim to predict structures of large molecular complexes and potentially sample multiple conformational states [73].

Among the most widely used platforms, GPCRdb serves as a comprehensive resource for the GPCR research community. It provides tools for structural visualization, experimental design, and ligand-receptor interaction analysis. To address the limitation of state-specific modeling, Pándy-Szekeres et al. developed over 800 refined GPCR models using AlphaFold-Multistate, enabling the prediction of both active and inactive conformations. This approach overcomes the static nature of conventional AlphaFold predictions, offering a more functionally relevant view of GPCR signaling states [42].

In parallel, understanding the dynamic nature of GPCRs is essential for elucidating their functional mechanisms. GPCRmd is an open-access, community-driven platform dedicated to molecular dynamics (MD) simulations of GPCRs. It enables researchers to observe the conformational flexibility of receptors in atomistic detail, facilitating investigations into activation processes and ligand-induced structural changes. By supporting the visualization, comparison, and sharing of MD simulation data, GPCRmd fosters interdisciplinary collaboration in GPCR research. The 2025 study by Aranda-García et al., offers an in-depth exploration of G protein-coupled receptors (GPCRs) using large-scale molecular dynamics simulations. In this research, the authors conducted MD simulations on 190 experimentally resolved GPCR structures. Each receptor system was simulated for a total of 1.5 microseconds (three simulations of 500 nanoseconds each). Analyzing approximately 60% of structurally characterized GPCRs, the authors uncovered novel allosteric sites and lateral gateways that are integral to receptor function [74].

A detailed investigation of the β2-adrenergic receptor (β2AR) in its active, ligand-bound form with norepinephrine and the stimulatory G protein (Gs), using multi-microsecond atomistic molecular dynamics (MD) simulations, provided critical insights into the energetic and structural determinants of receptor activation and G protein dissociation This study highlights that structural differences in non-conserved regions—especially ECL2 and ECL3—between β1AR and β2AR play a central role in norepinephrine (NE^+) selectivity, influencing both its entry and exit pathways. Through weighted ensemble (WE) simulations, the complete dissociation routes of NE^+ were characterized, revealing ECL3 as a critical differentiator between the two receptors. However, since WE simulations prioritize predefined pathways, they may overlook secondary binding sites, which were instead captured using conventional long-timescale MD and Gaussian accelerated MD (GaMD). The authors propose that combining WE with enhanced methods like GaMD could offer a more comprehensive view of ligand-receptor dynamics and recommend that future drug discovery efforts consider orthosteric, non-conserved, secondary, and allosteric binding regions to improve docking and screening accuracy [75].

Despite their strengths, conventional MD simulations face inherent limitations in capturing slow or large-scale conformational transitions, especially in systems with high atomic complexity like membrane-embedded GPCRs. These constraints hinder the exhaustive sampling of rare but functionally important intermediate states, such as those involved in receptor activation, allosteric modulation, or biased signaling. Anton supercomputers, developed by D. E. Shaw Research, have addressed these challenges by enabling millisecond-scale simulations that uncovered key processes such as spontaneous ligand binding and G protein coupling transitions in GPCR [17, 76]. However, the high computational demand of such platforms has led to the emergence of enhanced sampling techniques as more broadly accessible alternatives.

Intrinsic dynamics are essential for understanding complex GPCR signaling mechanism. Elastic Network Models (ENMs) reveal that global modes capture conserved cooperative motions, while intermediate-to-high frequency modes reflect subfamily-specific differences [39, 40]. Studies using SignDy [8], which analyzed structurally resolved Class A GPCRs, have shown that TM5, TM6, and loop regions such as ICL3 and ECL2 are major contributors to allosteric activation and ligand selectivity. In a separate study, Inan et al. integrated residue interaction network (RIN) analysis and SILCS-Hotspots to systematically identify and evaluate allosteric binding sites across Class A GPCRs using 105 structures. Their method demonstrated strong predictive performance for known binding sites and revealed novel, potentially druggable allosteric pockets, offering a promising computational strategy for modulator discovery [77].

To mitigate these challenges, several enhanced sampling techniques—such as adaptive sampling, accelerated MD, and metadynamics—have been developed [17, 78] These approaches efficiently explore conformational landscapes and facilitate the identification of transition states and low-population intermediates. Such techniques are particularly valuable for studying dynamic systems like GPCRs, where conformational diversity underpins function and signaling specificity.

2.6. Literature Review of Selected Class A GPCRs

2.6.1. M2 Muscarinic Acetylcholine Receptor (ACM2)

Muscarinic acetylcholine receptors (mAChRs) are Class A GPCRs that mediate essential functions in both the central and peripheral nervous systems. These receptors regulate numerous physiological processes, including cognition, memory, autonomic control, and smooth muscle contraction. There are five subtypes of mAChRs—M1R through M5R—each displaying high sequence similarity but distinct tissue distributions and signaling profiles. Among them, the M2 receptor (M2R) is of particular interest due to its coupling to Gi/o proteins, leading to inhibition of adenylate cyclase, reduction in intracellular cAMP levels, and modulation of potassium channels [19]. M2R is predominantly expressed in cardiac and neural tissues and is implicated in a variety of disorders, including Alzheimer's disease, Parkinson's disease, and schizophrenia [79]. Owing to their central role in neurotransmission, mAChRs remain significant targets for therapeutic intervention in neurodegenerative and neuropsychiatric diseases. In the case of the M2 receptor, β-arrestin engagement regulates signaling pathways that mediate cellular responses distinct from those triggered by G protein activation, highlighting its role in biased signaling [23].

2.6.2. Serotonin Receptor 2B (5HT2B)

The 5HT2B receptor is a Class A GPCR activated by serotonin, and it plays critical roles in both peripheral and central physiological processes. It is prominently expressed in cardiac tissue, gastrointestinal smooth muscle, and the central nervous system, particularly in microglia. Upon activation, 5HT2B receptors stimulate phospholipase C, leading to increased intracellular calcium levels and downstream activation of MAPK/ERK signaling pathways, which contribute to cell proliferation and differentiation [80].

Clinically, excessive 5HT2B receptor activation has been implicated in pathological cardiac remodeling and valvular heart disease, as observed with serotonergic drugs such as fenfluramine. Additionally, its activation has been associated with pulmonary fibrosis, systemic sclerosis, and certain cancers, making it a promising therapeutic target [81–83]. In the central nervous system, 5HT2B receptors are thought to modulate serotonergic tone and influence the efficacy of selective serotonin reuptake inhibitors (SSRIs), thereby contributing to mood regulation and the pathophysiology of depression. Due to its involvement in a wide range of disorders, 5HT2B continues to be the focus of drug discovery efforts aimed at developing selective antagonists for cardiovascular, fibrotic, and neuropsychiatric diseases.

2.6.3. β_1-adrenergic receptor (ADRB1)

The ADRB1 gene encodes the β_1-adrenergic receptor (β_1AR), a member of the Class A GPCR family predominantly expressed in cardiac tissue. ADRB1 plays a vital role in regulating heart rate, contractility, and conduction velocity, primarily mediating the body's "fight-or-flight" response. Upon binding of catecholamines such as norepinephrine or epinephrine, β_1AR couples to the stimulatory G protein (Gs), leading to the activation of adenylate cyclase. This cascade increases intracellular cyclic AMP (cAMP) levels, thereby activating protein kinase A (PKA). PKA subsequently phosphorylates downstream targets including L-type calcium channels, phospholamban, and troponin I, promoting enhanced calcium handling, accelerated relaxation, and increased cardiac output [84, 85].

In addition to G protein-mediated signaling, ADRB1 also engages β-arrestin-mediated pathways, which regulate receptor desensitization, internalization, and G protein-independent signaling, such as the activation of the MAPK cascade. This dual signaling capacity positions β_1AR as a critical node in both acute and chronic regulation of cardiac physiology and pharmacological intervention [22].

2.6.4. β_2-adrenergic receptor (ADRB2)

The β_2-adrenergic receptor (ADRB2) is one of the most thoroughly characterized members of the Class A GPCR family. It is activated by endogenous catecholamines such as epinephrine, as well as synthetic agonists like isoprenaline. β_2AR regulates smooth muscle relaxation, bronchodilation, vasodilation, and various metabolic processes, making it a critical pharmacological target for diseases such as asthma, chronic obstructive pulmonary disease (COPD), hypertension, and preterm labor [86].

Upon agonist binding, ADRB2 primarily couples with Gs proteins to activate adenylate cyclase, leading to increased intracellular cAMP levels. This elevation in cAMP activates protein kinase A (PKA), which in turn modulates a range of downstream targets, including L-type calcium channels. In addition to canonical Gs signaling, ADRB2 can also couple to Gi proteins and is subject to GPCR kinase (GRK)-mediated phosphorylation, promoting β-arrestin recruitment, receptor desensitization, and internalization [87]. These diverse signaling modes contribute to ADRB2's dual functionality in both G protein-dependent and β-arrestin-dependent pathways, positioning it as a central model in the study of biased signaling.

2.6.5. Dopamine D3 receptor (DRD3)

The dopamine D3 receptor (DRD3) is a Class A GPCR predominantly expressed in the limbic regions of the brain, where it plays a central role in regulating emotion, cognition, and reward-related behaviors [88, 89]. It has a high binding affinity for dopamine and primarily couples to Gi/o proteins, leading to inhibition of adenylate cyclase and decreased intracellular cAMP levels. DRD3 has been implicated in the pathophysiology of several neuropsychiatric disorders, including schizophrenia, Parkinson's disease, and substance use disorders, positioning it as a valuable therapeutic target.

In recent years, DRD3 has attracted attention due to its capacity for biased signaling—where specific ligands can preferentially activate either G protein-dependent

or β-arrestin-dependent pathways. This functional selectivity opens new opportunities for the development of drugs with improved therapeutic profiles and minimized adverse effects.

2.6.6. Neurotensin receptor 1 (NTR1)

Neurotensin receptors are members of the Class A GPCR family and are activated by neurotensin (NTS), a 13-amino acid neuropeptide that functions as a neuromodulator in both the central nervous system and peripheral tissues. Neurotensin is implicated in a variety of physiological processes, including dopamine signaling, pain modulation, appetite control, and thermoregulation. Additionally, it has been associated with the pathophysiology of psychiatric conditions such as schizophrenia and Parkinson's disease, as well as tumor progression in various cancers [90, 91].

Three neurotensin receptor subtypes have been identified: NTSR1, NTSR2, and NTSR3. Among them, NTSR1 is the most extensively studied and belongs to the Class A GPCR family. It primarily couples to Gq proteins, triggering activation of phospholipase C (PLC), calcium mobilization, and protein kinase C (PKC) signaling. NTR1 can also couple to Gi/o proteins to inhibit adenylate cyclase activity. Due to its role in cancer progression, NTR1 is actively being investigated as a therapeutic target in oncology [92].

β-arrestin mediates receptor desensitization, internalization, and initiates downstream β-arrestin-dependent signaling pathways in NTR1. Studies have shown that both neurotensin and the β-arrestin-biased allosteric modulator SBI-553 promote β-arrestin2 recruitment to NTR1, highlighting the receptor's ability to engage in arrestin-mediated signaling [93].

2.6.7. Vasopressin V2 receptor (V2R)

The vasopressin V2 receptor (V2R), encoded by the AVPR2 gene, is a Class A GPCR predominantly expressed on the basolateral membrane of principal cells in the kidney's collecting duct. V2R plays a vital physiological role in water balance by mediating the antidiuretic effects of arginine vasopressin (AVP), also known as antidiuretic hormone (ADH). Upon AVP binding, V2R couples to the stimulatory G protein (Gs), activating adenylate cyclase and elevating intracellular cyclic AMP (cAMP) levels. This cAMP signal activates protein kinase A (PKA), which phosphorylates the aquaporin-2 (AQP2) water channels. Phosphorylated AQP2 then translocates to the apical membrane, allowing water reabsorption from the urine back into the bloodstream and contributing to urine concentration and fluid homeostasis [94].

2.6.8. Angiotensin II Type 1 Receptor (AGTR1)

Angiotensin II receptors are members of the Class A GPCR family and play a central role in regulating cardiovascular homeostasis. Dysregulation of this system has been linked to a wide range of pathological conditions, including inflammation, hypertension, atherosclerosis, and heart failure [95,96]. There are two major subtypes: angiotensin II type 1 receptor (AT1R) and type 2 receptor (AT2R). Among these, AT1R is the principal mediator of the classical physiological actions of angiotensin II, including vasoconstriction, aldosterone release, and sodium reabsorption.

AT1R is known to couple with multiple G protein families, including Gq, Gi, G12, and G13, thereby activating a diverse array of downstream signaling pathways. These include the production of second messengers such as inositol trisphosphate (IP3), diacylglycerol (DAG), and reactive oxygen species (ROS), ultimately leading to the activation of intracellular kinase cascades. Due to its central role in cardiovascular physiology and disease, AT1R has been extensively targeted in the development of antihypertensive therapies, such as angiotensin receptor blockers (ARBs) [97].

2.6.9. K-Opioid Receptor (OPRK)

The K-opioid receptor (OPRK) is a Class A GPCR primarily expressed in the central and peripheral nervous systems, where it contributes to pain modulation, stress responses, and affective regulation. Like other opioid receptors, OPRK primarily couples to Gi/o proteins, inhibiting adenylate cyclase activity, reducing intracellular cAMP levels, and modulating various ion channels. This signaling mechanism leads to hyperpolarization of neurons and decreased neurotransmitter release.

OPRK is selectively activated by ligands such as ketazocine and salvinorin A, which produce analgesic effects without the high abuse potential associated with μ-opioid receptor agonists. However, OPRK activation is also associated with dysphoria, hallucinations, and cognitive disruption [98, 99]. These unique pharmacological effects make OPRK a subject of intense research interest, particularly for developing non-addictive analgesics and treatments for mood disorders.

2.6.10. μ-opioid receptor (OPRM)

The μ-opioid receptor (OPRM), a member of the Class A GPCR family, is the primary molecular target for widely used opioid painkillers, including morphine, fentanyl, and oxycodone. It is highly expressed in the brain, spinal cord, and peripheral sensory pathways, where it regulates key physiological processes such as pain relief, reward, respiratory control, and the development of tolerance [100]. When activated by agonists, OPRM primarily engages Gi/o proteins, leading to the suppression of adenylate cyclase activity, decreased intracellular cAMP levels, and modulation of ion channels (Ca^2+ and K^+), which together inhibit neuronal signaling.

Given its pivotal role in both analgesia and opioid dependence, OPRM has become a central focus in studies of biased signaling. These efforts aim to dissociate therapeutic effects from harmful side effects like addiction or respiratory depression [101]. As such, elucidating the structural basis of OPRM activation is of significant interest for the design of safer, more selective opioid therapies. OPRM plays a central role in both analgesic therapy and addiction research, making it a major focus in the study of biased signaling—an approach aimed at separating desired pain-relieving effects from undesirable outcomes like addiction and respiratory depression. Gaining insight into its activation mechanism at the structural level is essential for guiding the development of safer opioid medications.

2.6.11. Adenosine A1 Receptor (AA1R)

The adenosine A1 receptor (AA1R) is a Class A GPCR widely expressed in the brain and peripheral tissues, where it regulates numerous physiological functions including synaptic transmission, sleep, nociception, and cardiovascular control. Upon binding to extracellular adenosine, A1R couples to Gi proteins, which inhibits adenylate cyclase activity and lowers intracellular cAMP levels. Additionally, the G$\beta\gamma$ subunits can activate phospholipase C (PLC), contributing to secondary messenger production and signal amplification [102]. Due to its regulatory influence on neuronal excitability and neurotransmitter release, A1R remains an attractive target for therapeutic development in disorders such as epilepsy, ischemia, and chronic pain.

2.6.12. Adenosine A2A receptor (AA2AR)

The adenosine A2A receptor (A2AR) is another prominent subtype of the adenosine receptor family and exerts its physiological effects by coupling to Gs proteins, thereby activating adenylate cyclase and increasing intracellular cAMP levels [102]. A2AR is highly expressed in the basal ganglia and immune cells, where it plays important roles in neuromodulation and inflammation.

In the central nervous system, A2AR activation inhibits dopaminergic signaling, making it particularly relevant in the context of neurodegenerative diseases such as Parkinson's and Alzheimer's [103, 104]. Pharmacological targeting of A2AR has led to the development of both agonists and antagonists with therapeutic potential.

2.6.13. Adenosine A2B receptor (AA2BR)

The adenosine A2B receptor (AA2BR), a member of the Class A GPCR family, is activated by extracellular adenosine in both physiological and pathophysiological settings, including tissue injury, inflammation, and hypoxia. AA2BR is widely expressed in vascular endothelial cells, immune cells, and epithelial tissues, where it contributes to maintaining tissue homeostasis, regulating vascular tone, and modulating inflammatory responses [105].

Primarily coupling to Gs proteins, A2BR activation leads to stimulation of adenylate cyclase and elevated intracellular cAMP levels. In certain cell types, AA2BR can also engage Gq proteins, resulting in phospholipase C (PLC) activation, increased intracellular calcium, and subsequent activation of protein kinase C (PKC). These dual coupling capabilities position AA2BR as a versatile modulator of immune and vascular functions [106, 107]. Due to its roles in fibrotic disease, inflammatory disorders, and vascular remodeling, A2BR has emerged as a potential therapeutic target in both pulmonary and cardiovascular conditions.

2.6.14. Purinergic Receptor 1 (P2RY1)

The $P2Y_1$ receptor (P2RY1) belongs to the P2Y subfamily of Class A GPCRs and is selectively activated by extracellular adenosine diphosphate (ADP). While the broader P2Y receptor family responds to various nucleotides—including ATP, UTP, and UDP—P2RY1 specifically mediates critical physiological responses to ADP. This receptor plays a fundamental role in platelet aggregation, vascular tone regulation, and central nervous system signaling [108].

Upon activation by ADP, P2RY1 couples to Gq proteins, triggering phospholipase C (PLC) activation and subsequent intracellular calcium release. In platelets, this signaling cascade leads to shape change and activation, making P2RY1 a key player in thrombus formation [108]. Owing to its essential function in hemostasis, P2RY1 is a validated pharmacological target in the prevention and treatment of thrombosis, stroke, and related cardiovascular conditions.

2.6.15. Purinergic Receptor 12 (P2Y12)

The $P2Y_{12}$ receptor (P2Y12) is a Class A GPCR and a member of the P2Y receptor family, selectively activated by adenosine diphosphate (ADP). It plays an essential role in mediating platelet aggregation and thrombus stabilization, making it a critical regulator of hemostasis. Upon ADP binding, P2Y12 primarily couples to Gi proteins, leading to the inhibition of adenylate cyclase and subsequent downstream signaling events that reinforce platelet activation [108].

2.6.16. Cannabinoid Receptor 1 (CNR1)

Cannabinoid receptors are Class A GPCRs that mediate the diverse physiological functions of the endocannabinoid system. The two major subtypes, CNR1 and CNR2, differ in their tissue distribution and biological roles. CB1 receptors (CNR1) are highly expressed in the central nervous system—particularly in brain regions involved in memory, emotion, motor coordination, and sensory processing—as well as in peripheral nerve terminals. In contrast, CNR2 receptors are primarily found in immune cells and are involved in modulating inflammatory and immune responses [109].

CNR1 is the principal molecular target of THC, the psychoactive component of Cannabis sativa. Upon ligand binding, CNR1 undergoes conformational changes that enable coupling to Gi/o proteins, resulting in the inhibition of adenylate cyclase, reduced cAMP production, and regulation of ion channel activity. Depending on G protein subunit dissociation, CNR1 can inhibit calcium channels or activate potassium

channels, producing a wide range of effects including analgesia, appetite stimulation, mood regulation, and suppression of neurotransmitter release [110]

2.6.17. Prostaglandin D_2 Receptor 2 (PD2R2)

The prostaglandin D_2 receptor 2 (PD2R2), also known as CRTH2, is a Class A GPCR that binds to prostaglandin D_2—a lipid mediator produced during arachidonic acid metabolism. PD2R2 plays a critical role in regulating immune responses, particularly in allergic inflammation and Th2 cell-driven disorders [111]. It is predominantly expressed on Th2 cells, eosinophils, and basophils, key players in the pathogenesis of asthma, allergic rhinitis, and atopic dermatitis [112].

2.6.18. Thromboxane A_2 Receptor TA2R

The thromboxane A_2 receptor (TA2R), also known as the TP receptor, is a Class A GPCR that binds to thromboxane A_2 (TXA_2), a potent lipid mediator derived from arachidonic acid metabolism. TA2R plays a central role in regulating vascular tone, platelet aggregation, and inflammatory responses, making it a key participant in cardiovascular and thrombotic diseases [113].

2.6.19. Lysophosphatidic Acid Receptor 1 (LPAR1)

Lysophosphatidic acid receptor 1 (LPAR1) is a Class A GPCR that belongs to the lysophosphatidic acid receptor family and is activated by lysophosphatidic acid (LPA), a signaling lipid involved in regulating diverse cellular processes such as proliferation, migration, survival, and differentiation. LPAR1 is known to couple to several G protein subtypes—including Gi, Gq, and G12/13—activating a range of downstream pathways that modulate both physiological functions and pathological responses [114–116].

Given its wide expression and signaling versatility, LPAR1 plays a pivotal role in tissue development, wound healing, and immune cell trafficking. It has also been

implicated in various diseases, including cancer metastasis, pulmonary and hepatic fibrosis, and autoimmune conditions such as multiple sclerosis. These associations make LPAR1 an attractive target for therapeutic intervention, with ongoing efforts to develop selective antagonists and pathway-specific modulators [116].

2.6.20. Sphingosine-1-phosphate receptor 1 (S1PR1)

Sphingosine-1-phosphate receptor 1 (S1PR1) is a Class A GPCR activated by sphingosine-1-phosphate (S1P), a lipid signaling molecule that governs a variety of essential physiological functions, including immune cell migration, vascular permeability, and embryonic morphogenesis. S1PR1 is broadly expressed in endothelial cells, lymphoid tissues, and the central nervous system, where it serves as a key modulator of immune and vascular homeostasis [117].

Upon ligand binding, S1PR1 primarily couples to Gi proteins, leading to inhibition of adenylate cyclase and activation of downstream signaling pathways such as PI3K/Akt and MAPK. These cascades regulate processes ranging from lymphocyte egress to endothelial barrier function. Due to its critical roles in inflammation and vascular regulation, S1PR1 has been extensively investigated as a drug target in autoimmune diseases (e.g., multiple sclerosis), as well as in vascular pathologies. Several therapeutic agents, including fingolimod and ozanimod, act via functional modulation of S1PR1 signaling [118].

2.6.21. C-C chemokine receptor 1 (CCR1)

C-C chemokine receptor 1 (CCR1) is a Class A GPCR that plays a crucial role in orchestrating immune responses by mediating the chemotactic migration and activation of leukocytes. CCR1 binds to multiple CC chemokines, including CCL3 (MIP-1α), CCL5 (RANTES), and CCL7 (MCP-3), which act as signaling cues to direct immune cells to sites of infection, inflammation, or tissue damage. Upon ligand binding, CCR1 primarily couples to Gi proteins, leading to the inhibition of adenylate cyclase and

activation of downstream signaling pathways that influence immune cell trafficking and inflammatory cytokine production [119].

Due to its central role in immune cell recruitment and its involvement in chronic inflammation, CCR1 has been implicated in a range of pathologies, including autoimmune diseases such as multiple sclerosis and rheumatoid arthritis, as well as in cancer progression. These associations have made CCR1 a promising target for anti-inflammatory and immunomodulatory drug development [120].

2.6.22. C-C chemokine receptor 5 (CCR5)

C-C chemokine receptor 5 (CCR5) is a Class A GPCR that regulates immunological responses primarily by recruiting and activating T cells, macrophages, and dendritic cells. It is typically triggered by chemokines such as CCL3, CCL4, and CCL5 and plays a role in priming adaptive immune responses at sites of infection or inflammation. Beyond its immunological function, CCR5 has received special attention for its involvement as a significant co-receptor for HIV-1 entrance into host immune cells. The virus uses CCR5, together with CD4, to infect T cells, making CCR5 an important determinant of viral tropism and transmission. Understanding the conformational dynamics and signaling mechanisms of CCR5 is essential not only for elucidating immune regulation but also for developing anti-HIV therapies. Indeed, CCR5 antagonists, such as maraviroc, have been successfully developed to block viral entry, illustrating the receptor's importance as a therapeutic target in infectious disease and immunology [121].

2.6.23. C-C Chemokine Receptor 8 (CCR8)

C-C chemokine receptor 8 (CCR8) is a Class A GPCR predominantly expressed on immune cells such as regulatory T cells (Tregs), eosinophils, and macrophages. It plays an essential role in maintaining immune homeostasis and regulating inflammatory responses, as well as contributing to the immunosuppressive tumor microenvironment.

CCR8 is primarily activated by the chemokine CCL1, but can also respond to CCL8 and CCL18 under certain physiological and pathological conditions [122].Upon ligand binding, CCR8 primarily couples to Gi/o proteins, resulting in decreased cAMP production and activation of downstream signaling pathways that guide immune cell migration and activation. Given its role in tumor-infiltrating Tregs and its contribution to immune evasion, CCR8 has emerged as a promising therapeutic target in cancer immunotherapy [123].

2.6.24. C-X-C Chemokine Receptor 2 (CXCR2)

C-X-C chemokine receptor 2 (CXCR2) is a Class A GPCR that plays a pivotal role in immune cell trafficking, particularly during infection, inflammation, and tissue repair. CXCR2 acts as a primary chemoattractant receptor for neutrophils and other immune cells by binding to a range of CXC chemokines, including CXCL1 (GRO-α), CXCL2 (GRO-β), CXCL5 (ENA-78), and CXCL8 (IL-8). These ligand interactions enable CXCR2 to coordinate processes such as acute inflammation, wound healing, and angiogenesis. In pathological contexts, CXCR2 has been implicated in tumor progression, chronic inflammatory diseases, and autoimmune conditions [124, 125].

Upon chemokine binding, CXCR2 predominantly couples to Gi proteins, leading to the inhibition of adenylate cyclase and initiation of downstream signaling pathways that mediate chemotaxis, cellular activation, and immune modulation [126]. Due to its crucial role in immune regulation and inflammation, CXCR2 has emerged as a therapeutic target in diseases such as asthma, rheumatoid arthritis, and metastatic cancers.

2.6.25. C-X-C Chemokine Receptor 4 (CXCR4)

C-X-C chemokine receptor 4 (CXCR4) is a Class A G protein-coupled receptor (GPCR) with essential roles in both normal physiology and disease. It is critically involved in processes such as organ formation, immune cell migration, and the develop-

ment of cancer. Its primary natural ligand is stromal cell-derived factor-1 (SDF-1), also known as CXCL12. The CXCR4–CXCL12 signaling axis governs key biological functions including embryogenesis, the homing of hematopoietic stem cells, and immune system surveillance. This pathway has also been linked to a range of pathological conditions, such as HIV infection, chronic inflammation, and cancer metastasis [127, 128].

Upon binding to its ligand, CXCR4 typically engages Gi proteins, resulting in the suppression of adenylate cyclase activity and activation of downstream pathways that regulate cellular migration, growth, and survival [129]. In addition, CXCR4 recruits β-arrestins, which mediate receptor desensitization and alternative signaling routes [130]. Due to its involvement in diverse biological and pathological contexts, CXCR4 remains a prominent therapeutic target in areas including cancer treatment, antiviral therapy, and tissue regeneration.

3. MATERIALS AND METHODS

3.1. Dataset Generation

In this study, we analyzed 25 Class A GPCR families, categorized into five ligand-binding classes: aminergic, lipid, nucleotide, protein, and peptide. A central aim was to investigate how receptor dynamics vary across ligand types using the SignDy framework. To ensure balanced and statistically robust comparisons, the dataset was curated to include five representative receptors from each ligand-binding class. Among these, five receptors were selected to model dual activation pathways, as they are the only Class A GPCRs with experimentally resolved structures in both G protein-bound and β-arrestin-bound active states. To simulate conformational transitions, we applied ANM-LD simulations to generate 30 unique activation pathways across the dataset. Each pathway required an inactive and an active structure as endpoints. When experimental structures were not available in the Protein Data Bank (PDB) [131], AlphaFold2 models or AlphaFold Multistate predictions from GPCRdb were used as substitutes [42]. Additionally, when experimental active structures contained unresolved regions or missing segments, we used GPCRdb-refined structures to ensure completeness and consistency across simulations. This approach enabled the generation of intermediate conformations that enriched the dynamic ensemble, allowing for a systematic investigation of receptor-, ligand-, and signaling protein–specific features that contribute to GPCR activation, allosteric communication, and signaling specificity. The structures used in this thesis are summarized in the Table 3.1.For SignDy analysis, a total of 250 structures were compiled to construct the main GPCR ensemble. This dataset included 10 conformations per receptor—comprising the inactive and active states, along with 8 intermediate conformations generated via ANM-LD simulations—across 25 GPCRs. To explore biased signaling mechanisms, dual transition pathways were modeled for five receptors, each transitioning toward both G protein-bound and β-arrestin-bound active states. Two separate ensembles, each containing 50 structures, were generated to facilitate direct comparisons of signaling protein–specific

dynamics. All structures were structurally aligned to the M2 muscarinic receptor (PDB ID: 5ZK3) [132], which was used as the reference framework for downstream dynamic analysis. Alignment was performed using the buildPDBEnsemble() function from the ProDy software suite [40], ensuring a consistent spatial orientation across receptors for subsequent SignDy calculations [39].

Table 3.1. Summary of GPCR family members analyzed in this study.

Uni Prot	**IUP HAR**	**Receptor family**	**PDB**	**Species**	**State**	**Signal Protein**	**Ligand Type**
ACM2	M2	Acetylcholine (muscarinic)	5ZK3	Human	Inactive	-	Aminergic
			6OIK	Human	Active	G protein	
			6U1N	Human	Active	β-arrestin	
5HT2B	5-HT2B	5 Hydroxytryptamine	Alpha Fold2 Model	Human	Inactive	-	Aminergic
			7SRR	Human	Active	G protein	
			7SRS	Human	Active	β-arrestin	

Table 3.1 Summary of GPCR family members analyzed in this study (cont.)

Uni Prot	**IUP HAR**	**Receptor family**	**PDB**	**Species**	**State**	**Signal Protein**	**Ligand Type**
ADRB1	β_1	Adrenoceptors	4GPO	Wild Turkey	Inactive	-	Aminergic
			7JJO	Wild Turkey	Active	G protein	
			6TKO	Wild Turkey	Active	β-arrestin	
ADRB2	β_2	Adrenoceptors	2RH1	Human	Inactive	-	Aminergic
			3SN6	Human	Active	G protein	
DRD3	D3	Dopamine	3PBL	Human	Inactive	-	Aminergic
			8IRT	Human	Active	G protein	
NTR1	NTS1	Neurotensin	7UL2	Human	Inactive	-	Peptide
			6OSA	Human	Active	G protein	
			6PWC	Human	Active	β-arrestin	

Table 3.1 Summary of GPCR family members analyzed in this study (cont.)

Uni Prot	**IUPHAR**	**Receptor family**	**PDB**	**Species**	**State**	**Signal Protein**	**Ligand Type**
V2R	V2	Vasopressin and oxytocin	Alpha Fold2 Model	Human	Inactive	-	Peptide
			7DW9	Human	Active	G protein	
			7R0C	Human	Active	β-arrestin	
AGTR1	AT1	Angiotensin	4YAY	Human	Inactive	-	Peptide
			6DO1	Human	Active	-	
OPRK	κ	Opioid	4DJH	Human	Inactive	-	Peptide
			6B73	Human	Active	-	
OPRM	μ	Opioid	4DKL	Mouse	Inactive	-	Peptide
			5C1M	Mouse	Active	-	
AA1R	A1	Adenosine	5UEN	Human	Inactive	-	Nucleotide
			6D9H	Human	Active	G protein	
AA2AR	A2A	Adenosine	5MZP	Human	Inactive	-	Nucleotide
			5G53	Human	Active	G protein	

Table 3.1 Summary of GPCR family members analyzed in this study (cont.)

Uni Prot	**IUP HAR**	**Receptor family**	**PDB**	**Species**	**State**	**Signal Protein**	**Ligand Type**
AA2BR	A2B	Adenosine	Alpha Fold2 Model	Human	Inactive	-	Nucleotide
			8HDP	Human	Active	G protein	
P2RY1	P2Y1	P2Y	Alpha Fold MS Model	Human	Inactive	-	Nucleotide
			7XXH	Human	Active	-	
P2Y12	P2Y12	P2Y	Alpha Fold MS Model	Human	Inactive	-	Nucleotide
			7XXI	Human	Active	-	
CNR1	CB1	Cannabinoid	5TGZ	Human	Inactive	-	Lipid
			5XRA	Human	Active	-	
PD2R2	DP2	Prostanoid	7M8W	Human	Inactive	-	Lipid
			Alpha Fold MS Model	Human	Active	-	

Table 3.1 Summary of GPCR family members analyzed in this study (cont.)

Uni Prot	**IUPHAR**	**Receptor family**	**PDB**	**Species**	**State**	**Signal Protein**	**Ligand Type**
TA2R	TP	Prostanoid	6IIU	Human	Inactive	-	Lipid
			8XJO	Human	Active	G protein	
LPAR1	LPA1	Lysophospholipid(LPA)	4Z34	Human	Inactive	-	Lipid
			7YU3	Human	Active	G protein	
S1PR1	S1P1	Lysophospholipid(S1P)	Alpha Fold2 Model	Human	Inactive	-	Lipid
			8G94	Human	Active	G protein	
CCR1	CCR1	Chemokine	Alpha Fold2 Model	Human	Inactive	-	Protein
			7VLA	Human	Active	G protein	
CCR5	CCR5	Chemokine	6AKY	Human	Inactive	-	Protein
			7O7F	Human	Active	G protein	

Table 3.1 Summary of GPCR family members analyzed in this study (cont.)

Uni Prot	**IUP HAR**	**Receptor family**	**PDB**	**Species**	**State**	**Signal Protein**	**Ligand Type**
CCR8	CCR8	Chemokine	Alpha Fold2 Model	Human	Inactive	-	Protein
			8KFX	Human	Active	G protein	
CXCR2	CXCR2	Chemokine	6LFL	Human	Inactive	-	Protein
			6LFM	Human	Active	G protein	
CXCR4	CXCR4	Chemokine	Alpha Fold2 Model	Human	Inactive	-	Protein

3.2. Elastic Network Models

Proteins are inherently dynamic and do not remain fixed in a single conformation. Instead, they fluctuate around equilibrium states—corresponding to global energy minima—sampling a range of conformational substates. These fluctuations are primarily governed by collective, cooperative, and large-scale motions, which are tightly linked to the protein's biological function. Normal Mode Analysis (NMA) provides a powerful framework to predict these functionally relevant motions by analyzing the intrinsic vibrational modes of a protein structure [133]. Among these, low-frequency modes typically capture the most significant, functionally important movements. Elastic Network Models (ENMs) offer a coarse-grained approach to NMA by representing each residue as a node in a network, connected to neighboring residues via harmonic springs. Rather

than relying on detailed atomic potentials, ENMs focus on simplified harmonic interactions, enabling efficient computation of large-scale protein dynamics. This abstraction not only enhances computational tractability but also reveals the intrinsic dynamic signatures that underlie conformational changes critical for function [133–135]. In this thesis, both the Gaussian Network Model (GNM) and the Anisotropic Network Model (ANM)—two widely adopted ENM frameworks [136–138] - are employed to investigate protein dynamics.

3.2.1. Anisotropic Network Model

The Anisotropic Network Model (ANM) is a three-dimensional extension of Elastic Network Models that accounts for the directional nature of protein motions by incorporating anisotropic fluctuations observed in real biological systems [136, 138, 139]. Unlike the Gaussian Network Model (GNM), which assumes isotropic (direction–independent) fluctuations, ANM allows independent variations along each Cartesian coordinate of a residue's position vector. As a result, while GNM yields $N-1$ non-zero modes for a protein with N residues, ANM produces $3N-6$ non-trivial modes, reflecting its higher resolution in capturing motion directionality.

A key advantage of ANM lies in its ability to generate plausible alternative conformations in the vicinity of the native structure. These conformations are obtained by perturbing the original structure along the collective mode directions—also known as difference vectors—offering valuable insights into potential transition pathways and functional motions [134, 140]. The potential energy function of the ANM is defined as

$$V_{ANM} \;=\; \frac{1}{2}\sum_{ij}\gamma_{f,ij(R_{ij}-R^0_{ij})}. \tag{3.1}$$

The fluctuations in equilibrium positions between residue pairs i and j, represented as $\Delta R_{ij} = R_{ij} - R^0_{ij}$, and the correlations between these fluctuations are derived through the decomposition of the Hessian matrix $\mathbf{H}$, which characterizes the second derivatives of the system's potential energy. In ANM, this decomposition yields $3N-6$ non-zero

normal modes for a system of N residues, excluding global translations and rotations. To analyze correlated motions, the Hessian matrix is reconstructed using a subset or the full set of these modes. The resulting correlations between residue fluctuations are computed by perturbing the structure along mode k, and the pairwise directional correlations are evaluated using below equation

$$< \Delta R_i . \Delta R_j > = \frac{3k_B T}{\gamma} tr\lfloor H^{-1} \rfloor = \frac{3k_B T}{\gamma_f} \sum_{k=1}^{N} tr\lfloor \lambda_k^{-1} u_k u_k^T \rfloor_{ij}. \tag{3.2}$$

The elements of the Hessian matrix, which is central to the Anisotropic Network Model (ANM), are computed by taking the second derivatives of the potential energy function V_{ANM} with respect to the positions of the C_α atoms of residues i and j. Each off-diagonal block H_{ij} in the Hessian matrix, representing the interaction between residues i and j, is a 3×3 matrix given by

$$H_{ij} = \frac{\gamma}{R_{ij}^2} \begin{bmatrix} x_{ij}^2 & x_{ij}y_{ij} & x_{ij}z_{ij} \\ x_{ij}y_{ij} & y_{ij}^2 & y_{ij}z_{ij} \\ x_{ij}z_{ij} & y_{ij}z_{ij} & z_{ij}^2 \end{bmatrix} \quad (i \neq j). \tag{3.3}$$

3.2.2. Co-vibrational Modes

The concept of co-vibrational modes—also referred to as allosteric co-vibrational modes (covib)—describes the composite vibrational response of a protein to functional perturbations, such as ligand binding at an allosteric site [38]. These modes represent a linear combination of low-frequency normal modes and are instrumental in visualizing how protein structures might respond to allosteric events. This approach facilitates the interpretation of functional dynamics from static structures, such as those resolved by X-ray crystallography, by projecting observed conformational changes onto intrinsic modes of motion. Co-vibrational modes are particularly valuable for characterizing the dynamic coupling between two biologically relevant conformational states. The

co-vibrational mode vector s^f which captures the direction of motion consistent with a conformational transition vector f is defined as

$$\mathbf{s}^f = \sum_{j=1}^{M} \frac{\mathbf{f} \cdot \mathbf{v}_j}{\|\mathbf{f}\|} \mathbf{v}_j. \tag{3.4}$$

The equation quantifies the contribution of selected normal modes to the observed conformational change, where $\mathbf{f}$ is the displacement vector between the two conformations, $\|\mathbf{f}\|$ is its Euclidean norm, $\mathbf{v}_j$ is the jth normalized eigenvector (mode vector), and M is the number of modes included in the summation.

This weighted superposition of mode vectors provides a physically meaningful representation of the conformational transition, grounded in the intrinsic dynamic tendencies of the protein structure.

3.2.3. Gaussian Network Model (GNM)

The Gaussian Network Model (GNM) is a one-dimensional Elastic Network Model that characterizes protein dynamics based on isotropic fluctuations of residues around their equilibrium positions [137, 141, 142]. In GNM, each residue is represented by its Cα atom and is connected to neighboring residues within a predefined cutoff distance via harmonic springs. The entire interaction network is encoded in the Kirchhoff matrix γ, also known as the connectivity matrix, where non-zero off-diagonal elements indicate the presence of direct contacts between residues. In the Gaussian Network Model (GNM), each residue is represented by its C_α atom, which serves as a node in the network. Nodes are connected via harmonic springs if they fall within a predefined cutoff distance, representing physical proximity and potential interaction. These spring-based connections define the neighborhood of each node and reflect the protein's internal mechanical coupling. GNM assumes that fluctuations are isotropic—i.e., they occur equally in all directions—and captures the magnitudes of these fluctuations and the associated cross-correlations. The network of interactions is encoded in an $N \times N$ Kirchhoff (or connectivity) matrix, Γ, where N is the number of residues. The potential

energy function of GNM is expressed as

$$V_{\mathrm{GNM}} \;=\; \frac{1}{2}\sum_{i,j}\gamma_{ij}\big[\big(\mathbf{R}_{ij}-\mathbf{R}^{0}_{ij}\big)\cdot\big(\mathbf{R}_{ij}-\mathbf{R}^{0}_{ij}\big)\big]. \tag{3.5}$$

The Kirchhof matrix Γ_{ij} is defined as:

$$\Gamma_{ij}=\begin{cases}-1, & \text{if } R_{ij}\le r_c \text{ and } i\neq j,\\ 0, & \text{if } R_{ij}> r_c \text{ and } i\neq j,\\ -\displaystyle\sum_{k\neq i}\Gamma_{ik}, & \text{if } i=j.\end{cases} \tag{3.6}$$

Here, r_c denotes the cutoff distance for residue–residue interactions, and the diagonal elements of Γ are set so that each row (and column) sums to zero, reflecting the connectivity of each node to its neighbors. GNM assumes that residue fluctuations follow a Gaussian distribution, and the correlation between fluctuations of residue i and residue j, denoted by $\langle \Delta\mathbf{R}_i \cdot \Delta\mathbf{R}_j\rangle$, is calculated as

$$\big\langle \Delta\mathbf{R}_i \cdot \Delta\mathbf{R}_j\big\rangle \;=\; \frac{k_B T}{\gamma}\left(\Gamma^{-1}\right)_{ij}, \tag{3.7}$$

where k_B is Boltzmann's constant, T is the absolute temperature and γ is the uniform spring constant.

The overall fluctuation behavior of the protein can also be expressed as the superposition of $N-1$ non-zero eigenmodes derived from the eigen decomposition of the Kirchhoff matrix Γ, excluding the zero eigenvalue associated with global translation. This low-dimensional representation makes GNM particularly efficient and insightful for capturing the intrinsic dynamic behavior of proteins.

In the Gaussian Network Model, the dynamic behavior of a protein structure is described through the eigen decomposition of the Kirchhoff matrix Γ, such that

$$\Gamma^{-1} \;=\; \left[U\Lambda^{-1}U^{\mathsf{T}}\right]_{ij} \;=\; \left[\lambda_k^{-1}\,\mathbf{u}_k\mathbf{u}_k^{\mathsf{T}}\right]_{ij}, \tag{3.8}$$

where U is the matrix of eigenvectors $\mathbf{u}_k$, each corresponding to a mode k and describing the direction of residue displacements along that mode, and Λ is the diagonal matrix of eigenvalues λ_k, each proportional to the square of the frequency of the respective mode. The eigenvalues and eigenvectors collectively define the intrinsic dynamics of the structure.

The decomposition of fluctuations into $N-1$ nonzero modes (for a structure with N residues) allows the identification of dominant collective motions, particularly through the first few slow modes, which often correspond to the most cooperative, functionally relevant dynamics.

3.2.4. Signature Dynamic Analysis

The Gaussian Network Model (GNM) was employed to characterize the intrinsic dynamics of each structure within the GPCR ensemble [137, 141]. For consistency across receptors, GNM mode shapes were mapped onto a common reference structure, with non-alignable residues treated as environmental components using SignDy module [39, 40] of ProDy. Each GNM analysis was performed on the full structure of the receptor, incorporating both core residues shared across the family and variable residues specific to individual receptors.

To identify dynamic signatures, the mean and standard deviation of mean square fluctuations (MSFs) were computed across ensemble members. Residue-residue cross-correlation matrices were derived from the global modes using the SignDy framework, enabling the identification of conserved interaction patterns that underlie shared functional mechanisms.

The dynamic behavior of the system is described by the eigenvectors and eigenvalues of the Kirchhoff connectivity matrix Γ, which reflects the residue-level contact topology. The GNM covariance matrix $\mathbf{C}_{\mathrm{GNM}} \cdot \mathbf{C}_{\mathrm{GNM}}$, which encodes the extent of correlated fluctuations between residue pairs, is defined as

$$\mathbf{C}_{\mathrm{GNM}} \cdot \mathbf{C}_{\mathrm{GNM}} = \sum_{k=1}^{N} \left(\frac{1}{\lambda_k} \right) \mathbf{v}_k \mathbf{v}_k^{\mathsf{T}}, \tag{3.9}$$

where $\mathbf{v}_k$ represent eigenvectors and λ_k represent eigenvalues. The lower-frequency modes (with smaller λ_k) dominate the global motions and thus contribute more prominently to the covariance matrix.

3.2.5. GNM-Transfer Entropy (GNM-TE)

The integration of Transfer Entropy (TE) [143] into into the Gaussian Network Model (GNM) [137] framework enables the assessment of directional information flow between residue pairs during protein dynamics [37, 144, 145]. Specifically, transfer entropy (TE) quantifies how much the movement of residue i at a given time reduces the uncertainty about the future movement of residue j by introducing a time delay τ. The directional transfer entropy from residue i to residue j at time delay τ is formulated as

$$T_{i \to j}(\tau) = S(\Delta R_j(t+\tau) \mid \Delta R_i(t)) - S(\Delta R_j(t+\tau) \mid \Delta R_i(t), \Delta R_j(t)), \tag{3.10}$$

where $T_{i \to j}(\tau)$ measures the extent to which knowledge of the past dynamics of residue i improves the prediction of the future dynamics of residue j, beyond what is already predictable from the past dynamics of j itself. The S terms represent conditional entropies and are calculated as

$$S(\Delta R_j(t+\tau) \mid \Delta R_i(t)) = -\langle \ln p(\Delta R_i(0), \Delta R_j(\tau)) \rangle + \langle \ln p(\Delta R_i(0)) \rangle. \tag{3.11}$$

The net TE from residue i to residue j at a given time delay τ is described as

$$\Delta T_{i\to j}(\tau) = T_{i\to j}(\tau) - T_{j\to i}(\tau), \tag{3.12}$$

where $\Delta T_{i\to j}(\tau)$ determines the transfer entropy directionality between residues i and j. Positive net TE values identify entropy sources, meaning residue i disseminates information toward other residues. Conversely, negative net TE values designate entropy receivers, indicating that residue i primarily acquires information from the rest of the structure.

The time delay τ critically influences the detection of causal relationships, with an optimal $\tau \approx 3\tau_{\text{opt}}$—the time point maximizing total transfer entropy—providing the best balance between capturing local and long-range allosteric communication.

The degree of collectivity in information transfer measures how extensively a residue's motion influences the overall structure, reflecting the collective nature of allosteric communication. Inspired by Bruschweiler's framework [146], we computed collectivity values $K_{i,s}$ for each residue i engaged in information transfer using positive net TE values, providing insights into their collective impact on protein dynamics. The collectivity value was calculated as

$$K_{i,s} = \frac{1}{N} \exp\left(-\sum_{j=1}^{N} \alpha(\Delta T_{i\to j,s}(\tau))^2 \log\left[\alpha(\Delta T_{i\to j,s}(\tau))^2\right] \right), \tag{3.13}$$

where N is the total number of residues, s denotes the selected subset of slow GNM modes, and α is a normalization factor satisfying

$$\sum_{j=1}^{N} \alpha(\Delta T_{i\to j,s}(\tau))^2 = 1. \tag{3.14}$$

In this context, s refers to any chosen subset of slow modes, and the time delay τ was set to $3\tau_{\text{opt}}$, where τ_{opt} maximizes total transfer entropy [144]. To further integrate the

extent of information flow and its collectivity, we defined a TEcol score for each residue by multiplying the cumulative positive net TE by the collectivity value

$$\text{TEcolScore}_{i,s} = K_{i,s} \cdot \sum_{j=1}^{N} \Delta T_{i \to j,s}. \tag{3.15}$$

The TEcol score thus highlights residues that act as strong, globally collective sources of information flow, enabling the identification of functionally critical allosteric hubs within the protein.

In the present calculations, we initially focused on the ten slowest modes, as these contribute most significantly to overall protein dynamics, with allosteric interactions primarily embedded within them. However, averaging across all ten modes can cause the slowest (dominant) modes to overshadow the influence of other functionally important but less dominant modes. To mitigate this, we repeated the calculations by sequentially removing the slowest mode at each step, resulting in the use of mode subsets (1–10, 2–10, and 3–10), following previous strategies [37, 145].

3.2.6. Statistical Analysis

The subsequent spatial correlation analysis evaluated the frequency at which functionally essential residues aligned with predicted allosteric peaks, using a cutoff distance of 4 Å to define first-neighbor proximity. To assess the statistical significance of the spatial correlation between functionally essential residues and allosteric hotspots, we generated 100,000 sets of randomly placed entropy source residues and recorded how often they coincided with known functional sites. Z-scores were calculated using the formula

$$Z = \frac{X - \mu}{\sigma}, \tag{3.16}$$

where X represents the number of correct predictions, and μ and σ denote the mean and standard deviation of correct matches across the random sets, respectively. Based

on the Z-scores, p-values were then computed using a one-tailed hypothesis test, with a significance threshold set at 0.05.

3.3. Molecular Dynamics (MD) Simulations

Molecular Dynamics (MD) simulation is a computational method used to explore the time-dependent behavior of atoms and molecules. It involves numerically solving Newton's equations of motion to simulate how particles evolve over time under the influence of interatomic forces. The fundamental components required for MD simulations include the initial atomic coordinates—typically obtained from experimental techniques such as X-ray crystallography or NMR spectroscopy—and a well-defined energy function, or force field, that governs the interactions between atoms [147, 148]. The core of molecular dynamics (MD) is based on Newton's second law, which relates the force F acting on a particle to its mass m and acceleration a as

$$F_i \;=\; m_i a_i. \tag{3.17}$$

Acceleration is derived as the second derivative of the position vector with respect to time, while the force is expressed as the negative gradient of the potential energy surface

$$\frac{d^2 r_i}{dt^2} \;=\; \frac{F_i}{m_i}, \tag{3.18}$$

where r_i is the position of atom i.

By integrating Newton's equations iteratively over small time steps, new positions and velocities of atoms are computed, allowing the simulation to evolve and capture dynamic trajectories of biomolecular systems. This procedure is repeated until the system reaches a desired timescale or target conformation as explained in equations

$$F_i \;=\; -grad V_i \;=\; -\Delta V_i, \tag{3.19}$$

$$\frac{d^2 r_i}{dt^2} \;=\; -\frac{1}{m_i}\frac{\partial V(\; r_1,\; r_2, ...,\; r_N)}{\partial\; r_i} \;=\; a_i. \tag{3.20}$$

To initialize the system's dynamics, the Maxwell–Boltzmann distribution is employed to assign initial velocities based on temperature. The velocity of an atom in a particular direction is given by

$$p(v_{ix}) \;=\; (\frac{m_i}{2\pi k_B T})^{\frac{1}{2}} exp\lfloor -\frac{1}{2}\frac{m_i v_{ix}^2}{k_B T}\rfloor, \tag{3.21}$$

$$p \;=\; \sum_{i=1}^{N} m_i v_i \;=\; 0, \tag{3.22}$$

where T is the absolute temperature, m_i is the atomic mass of atom i, and k_B is Boltzmann's constant.

The relationship between temperature and kinetic energy is expressed as

$$T \;=\; \frac{2}{3N k_B}\sum_{i=1}^{N}\frac{1}{2} m_i < v_i^2 >, \tag{3.23}$$

where $\langle v^2 \rangle$ represents the mean squared velocity of particles, and N is the number of atoms in the system.

To more realistically model environmental effects such as solvent friction and stochastic collisions, the Langevin equation is incorporated. This stochastic differential equation introduces a friction term and a random force R to simulate the influence of a thermal bath as

$$m_i \frac{d^2 r_i}{dt^2} \;=\; -\frac{\partial v}{\partial r_i} - m_i \gamma \frac{dr_i}{dt} + R_i(t), \tag{3.24}$$

where γ is the friction coefficient, and $R(t)$ is a randomly fluctuating force with zero

mean and defined correlation. When $\gamma = 0$, the equation reduces to the classical MD form. Incorporating the Langevin equation thus enhances MD simulations by accounting for thermal noise and solvent interactions [149].

3.4. ANM Driven Langevin Dynamics (ANM-LD)

The Anisotropic Network Model–Langevin Dynamics (ANM-LD) method is a hybrid simulation approach designed to generate biologically relevant intermediate conformations between two known states of a protein. This method leverages the global, cooperative motions captured by ANM and incorporates the stochasticity of Langevin Dynamics (LD), enabling efficient exploration of large-scale conformational transitions [35–37]. To initiate ANM-LD simulations, both the initial and target structures of the protein must be specified. The method proceeds iteratively: at each cycle, a deformation is applied to the current structure along a selected ANM mode, resulting in a new intermediate conformation. RMSD (Root-Mean-Square Deviation) is calculated at every step to assess the proximity of the generated structure to the target as

$$RMSD \ = \ \sqrt{\frac{\sum_{i=1}^{N} d_i^2}{N}}, \tag{3.25}$$

where N is the total number of atoms and d is the distance between the formed structure and the target structure.

To determine the most effective direction of motion, the overlap score between the displacement vector and each global ANM mode is computed as

$$O_{i,j} \ = \frac{\mid u_j.D_i \mid}{\mid u_j \mid . \mid D_i \mid}. \tag{3.26}$$

ANM mode is selected as the mode with the highest overlap value. This structure is perturbated by the selected ANM mode and the deformation factor which is one of

the simulation parameters. The structure formed as a result of this procedure is used as the initial structure of the next step. This methodology continues until the RMSD converges between the iteratively created structure and the target structure. The procedure applied in the ANM-LD simulations is demonstrated in Figure 3.1.

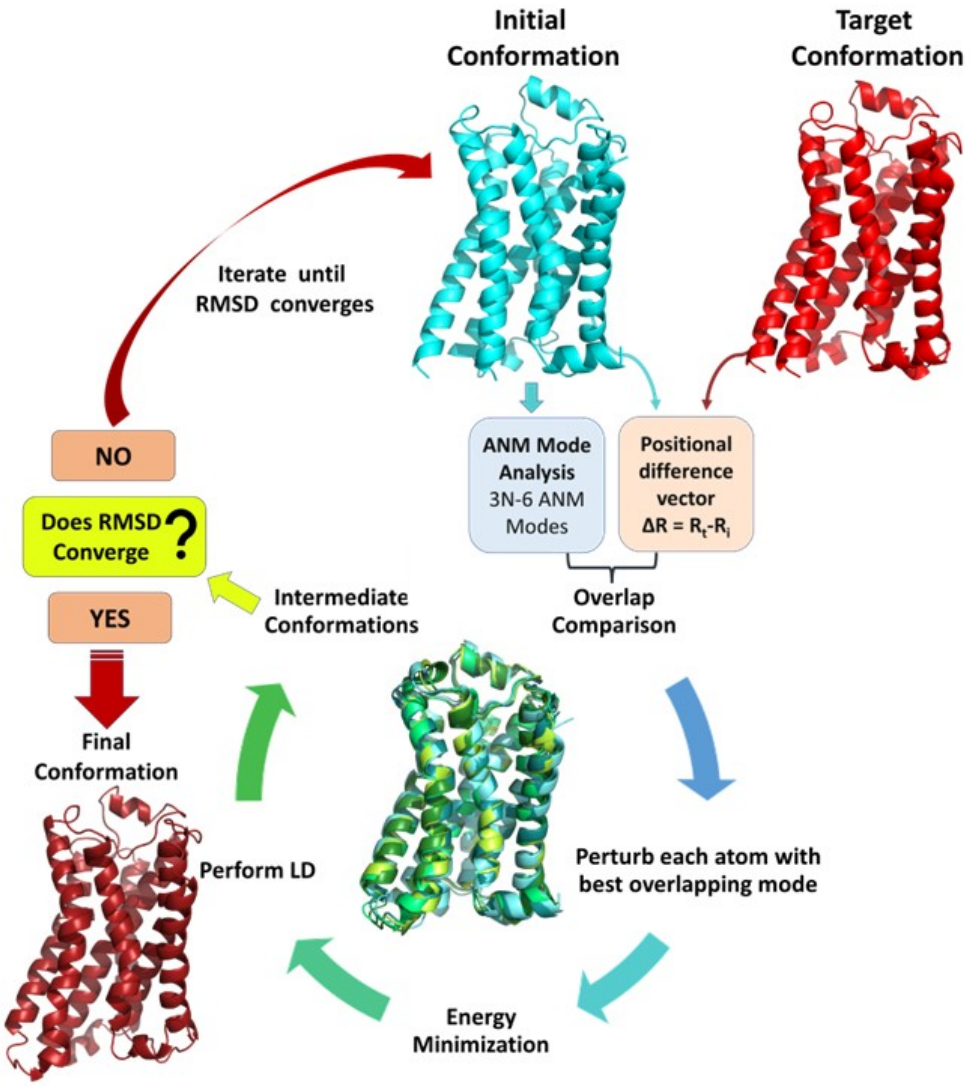

Figure 3.1. A schematic overview of the ANM-LD methodology.

3.5. Time-Independent and Time-Delayed Correlations

The positional fluctuation vectors ($\Delta\mathbf{R}$) of residues i and j were calculated by measuring the deviations of their C_α atoms from their respective mean positions within a specified time window during the ANM-LD transition pathway. Dynamic cross-correlations between the fluctuations of residues i ($\Delta\mathbf{R}_i$) and j ($\Delta\mathbf{R}_j$) were computed using the following equation as

$$C_{ij}(\tau) = \frac{\langle \Delta\mathbf{R}_i(t)\, \Delta\mathbf{R}_j(t+\tau)\rangle}{\sqrt{\langle (\Delta\mathbf{R}_i(t))^2\rangle}\sqrt{\langle (\Delta\mathbf{R}_j(t+\tau))^2\rangle}}, \tag{3.27}$$

where t represents a pseudo-time variable corresponding to the ANM-LD simulation cycles, and τ is the applied time delay. When $\tau = 0$, the formula simplifies to the standard equal-time cross-correlation, with values ranging from -1 (perfect anti-correlation) to $+1$ (perfect correlation). For $\tau > 0$, the equation evaluates delayed cross-correlations, capturing how fluctuations of residue i at time t influence fluctuations of residue j at a later time $t + \tau$. When $i = j$, the equation describes the autocorrelation of a residue at both current and delayed time points.

3.6. Differential Coupling Score

To quantify dynamic differences underlying biased signaling, we developed a Differential Coupling Score that integrates changes in dynamic correlations and allosteric information flow between G protein- and β-arrestin-bound activation pathways. First, normalized cross-correlation matrices were computed separately for G protein-targeting and β-arrestin-targeting simulations, and the element-wise differences between matrices were calculated. For each residue, the absolute differences were summed across all pairs to yield a Cross-Correlation Difference Score. TEcol scores were normalized to zero mean and unit variance for each regime, and the normalized difference between G protein and β-arrestin TEcol values was computed and averaged across the three regimes to produce a Normalized TEcol Difference for each residue. The final Differential Coupling Score (DCS) for each residue was defined as the sum of the absolute Normalized

TEcol Difference and the Cross-Correlation Difference Score. This combined metric ensures that both dynamic correlation changes and alterations in allosteric information flow contribute equally to the identification of key switching regions associated with biased signaling. DCS is formulated as

$$\begin{aligned} \mathrm{DCS}_i = \frac{1}{3}\sum_{k=1}^{3}\left|\mathrm{norm}\Big(\mathrm{TEcol}_{\text{G-prot}}^{(k\text{–}10)}(i)\Big) - \mathrm{norm}\Big(\mathrm{TEcol}_{\beta\text{-Arr}}^{(k\text{–}10)}(i)\Big)\right| \\ + \frac{1}{N}\sum_{j=1}^{N}\left|\mathrm{norm}(C_{\text{G-prot}}(i,j)) - \mathrm{norm}(C_{\beta\text{-Arr}}(i,j))\right|, \end{aligned} \tag{3.28}$$

where k indexes the three mode regimes (1–10, 2–10, and 3–10 modes), $\mathrm{TEcol}_{\text{G-protein}}^{(k\text{–}10\ \text{modes})}(i)$ and $\mathrm{TEcol}_{\beta\text{-arrestin}}^{(k\text{–}10\ \text{modes})}(i)$ are the normalized TEcol scores for residue i calculated within mode regime k for G protein- and β-arrestin-bound simulations, respectively.

N is the total number of residues, and $C_{\text{G-protein}}(i,j)$ and $C_{\beta\text{-arrestin}}(i,j)$ represent the cross-correlation values between residue i and residue j in the G protein- and β-arrestin-targeting simulations, respectively.

This formulation captures both changes in dynamic correlations and shifts in information flow between the two signaling states in a single residue-specific metric.

4. RESULTS AND DISCUSSIONS

This section presents a comprehensive investigation of the conformational dynamics and allosteric communication in Class A GPCRs using ANM-LD simulations and complementary computational analyses. We begin by modeling activation transitions across 25 GPCRs, capturing intermediate states along their conformational pathways. These ensembles form the basis for evaluating shared and receptor-specific features of activation. To enhance the interpretation of ANM results, we also applied the covibrational mode framework introduced by Kolossváry (2024) [38], constructing weighted combinations of low-frequency modes to better capture collective motions underlying allosteric transitions. Building on these modeled transitions, we then focus on a subset of five receptors with available structures in both G protein- and β-arrestin-bound active states. Through a combination of ANM mode analysis, conventional and time-delayed cross-correlation, and GNM-based transfer entropy (GNM-TE), we dissect the dynamic underpinnings of biased signaling. To systematically quantify regions with pathway-specific behavior, we introduce a novel metric—the Differential Coupling Score—which integrates changes in correlation and information flow to identify dynamic differential coupling regions that mediate signaling specificity. Expanding beyond individual case studies, we perform a comparative analysis across the 25 GPCRs to uncover conserved and divergent allosteric signatures linked to receptor state, ligand type, and signaling partner. This ensemble-level view highlights both shared scaffolding features and variations that enable functional diversity. Finally, we present complementary studies that demonstrate the generalizability of our methods: (i) an analysis of allosteric coupling in transition-metal ABC transporters validated through mutagenesis, (ii) development and benchmarking of the ANM-LD Path server using diverse protein systems, and (iii) an exploration of how mutations in Factor V alter dynamic communication relevant to coagulation. Together, these findings provide a mechanistic framework for understanding GPCR activation, signal bias, and functional evolution, with implications for drug discovery and broader protein dynamics research.

4.1. Modeling Conformational Transitions of GPCRs via ANM-LD Simulations

To assess the structural progression along the simulated pathways, root-mean-square deviation (RMSD) values were computed between the initial (inactive) and target (active) structures for each receptor. Initial RMSDs ranged from 1.9 Å to 3.8 Å, reflecting varying degrees of conformational rearrangement across the dataset. At the endpoint of each ANM-LD simulation, the RMSD between the generated structure and the experimental active conformation served as a metric of convergence accuracy. Final RMSD values as low as 0.8 Å were observed for some receptors, indicating highly accurate transitions (Tables 4.1–4.25). These results highlight both the structural diversity within Class A GPCRs and the robustness of the ANM-LD method in capturing activation-related conformational changes.

The resulting trajectories successfully captured key conformational features associated with GPCR activation, including outward displacement of TM6, reorganization of the TM3–TM7 interface, and subtle rearrangements in the extracellular loops. These results establish a dynamic framework that goes beyond static endpoint comparisons and enables systematic exploration of transition states and transient allosteric couplings in GPCRs.

To further evaluate the biological relevance of the simulated transitions, we examined two collective variables commonly associated with activation: the TM3–TM6 (R3.50-E6.30) distance and the TM3–TM7 (R3.50-Y7.53) distance [21, 32]. These respectively reflect the opening of the intracellular G protein/β-arrestin-binding cavity and the rearrangement of the NPxxY motif. The results for all transition pathways are presented in Figures 4.1-4.34, where pathways exhibiting physically and biologically compatible trends are emphasized. Simulations that most effectively converged toward the active structure—based on RMSD as well as TM3–TM6 and TM3–TM7 distance shifts—are highlighted as bold in Tables 4.1–4.25 and were selected as representative cases.

Table 4.1. ANM-LD simulation summary of ACM2 receptor.

Initial Structure	**Final Structure**	**Sim No**	**Simulation Parameter**	**Initial RMSD (Å)**	**Final RMSD (Å)**
5ZK3	6OIK	1	DF=0.40 Modemax=30 Rcut=8	2.1	1.0
		2	DF=0.40 Modemax=100 Rcut=8		1.0
		3	DF=0.50 Modemax=30 Rcut=8		1.1
		4	DF=0.50 Modemax=100 Rcut=8		1.0
		5	DF=0.60 Modemax=30 Rcut=8		1.1
		6	**DF=0.60 Modemax=100 Rcut=8**		1.0
5ZK3	6UIN	7	DF=0.40 Modemax=30 Rcut=8	2.4	1.3
		8	DF=0.40 Modemax=100 Rcut=8		1.3
		9	DF=0.50 Modemax=30 Rcut=8		1.3
		10	DF=0.50 Modemax=100 Rcut=8		1.3
		11	**DF=0.60 Modemax=30 Rcut=8**		1.4
		12	DF=0.60 Modemax=100 Rcut=8		1.3

Table 4.2. ANM-LD simulation summary of 5HT2B receptor.

Initial Structure	**Final Structure**	**Sim No**	**Simulation Parameter**	**Initial RMSD (Å)**	**Final RMSD (Å)**
AF2 Model	7SRR	13	DF=0.40 Modemax=30 Rcut=8	1.9	1.3
		14	DF=0.40 Modemax=100 Rcut=8		1.1
		15	DF=0.50 Modemax=30 Rcut=8		1.4
		16	**DF=0.50 Modemax=100 Rcut=8**		1.1
		17	DF=0.60 Modemax=30 Rcut=8		1.3
		18	DF=0.60 Modemax=100 Rcut=8		1.9
AF2 Model	7SRS	19	DF=0.40 Modemax=30 Rcut=8	2.5	1.2
		20	DF=0.40 Modemax=100 Rcut=8		1.1
		21	DF=0.50 Modemax=30 Rcut=8		1.2
		22	DF=0.50 Modemax=100 Rcut=8		1.4
		23	DF=0.60 Modemax=30 Rcut=8		1.3
		24	**DF=0.60 Modemax=100 Rcut=8**		1.0

Table 4.3. ANM-LD simulation summary of ADRB1 receptor.

Initial Structure	**Final Structure**	**Sim No**	**Simulation Parameter**	**Initial RMSD (Å)**	**Final RMSD (Å)**
4GPO	7JJO	25	**DF=0.40 Modemax=30 Rcut=8**	2.4	1.1
		26	DF=0.40 Modemax=100 Rcut=8		1.0
		27	DF=0.50 Modemax=30 Rcut=8		1.2
		28	DF=0.50 Modemax=100 Rcut=8		1.6
		29	DF=0.60 Modemax=30 Rcut=8		1.1
		30	DF=0.60 Modemax=100 Rcut=8		1.1
4GPO	6TKO	31	DF=0.40 Modemax=30 Rcut=8	2.0	1.2
		32	DF=0.40 Modemax=100 Rcut=8		1.0
		33	DF=0.50 Modemax=30 Rcut=8		1.2
		34	**DF=0.50 Modemax=100 Rcut=8**		1.0
		35	DF=0.60 Modemax=30 Rcut=8		1.2
		36	DF=0.60 Modemax=100 Rcut=8		1.1

Table 4.4. ANM-LD simulation summary of ADRB2 receptor.

Initial Structure	**Final Structure**	**Sim No**	**Simulation Parameter**	**Initial RMSD (Å)**	**Final RMSD (Å)**
2RH1	3SN6	37	DF=0.40 Modemax=30 Rcut=8	2.8	1.5
		38	DF=0.40 Modemax=100 Rcut=8		1.3
		39	DF=0.50 Modemax=30 Rcut=8		1.5
		40	**DF=0.50 Modemax=100 Rcut=8**		1.3
		41	DF=0.60 Modemax=30 Rcut=8		1.6
		42	DF=0.60 Modemax=100 Rcut=8		1.3

Table 4.5. ANM-LD simulation summary of DRD3 receptor.

Initial Structure	**Final Structure**	**Sim No**	**Simulation Parameter**	**Initial RMSD (Å)**	**Final RMSD (Å)**
3PBL	8IRT	43	DF=0.40 Modemax=30 Rcut=8	2.3	1.4
		44	**DF=0.40 Modemax=100 Rcut=8**		1.0
		45	DF=0.50 Modemax=30 Rcut=8		1.7
		46	DF=0.50 Modemax=100 Rcut=8		1.0
		47	DF=0.60 Modemax=30 Rcut=8		1.6
		48	DF=0.60 Modemax=100 Rcut=8		1.8

Table 4.6. ANM-LD simulation summary of NTR1 receptor.

Initial Structure	**Final Structure**	**Sim No**	**Simulation Parameter**	**Initial RMSD (Å)**	**Final RMSD (Å)**
7UL2	6OSA	49	DF=0.40 Modemax=30 Rcut=8	2.6	1.6
		50	DF=0.40 Modemax=100 Rcut=8		1.3
		51	DF=0.50 Modemax=30 Rcut=8		1.6
		52	**DF=0.50 Modemax=100 Rcut=8**		1.3
		53	DF=0.60 Modemax=30 Rcut=8		2.5
		54	DF=0.60 Modemax=100 Rcut=8		2.4
7UL2	6PWC	55	DF=0.40 Modemax=30 Rcut=8	3.1	1.8
		56	DF=0.40 Modemax=100 Rcut=8		1.5
		57	**DF=0.50 Modemax=30 Rcut=8**		1.7
		58	DF=0.50 Modemax=100 Rcut=8		2.9
		59	DF=0.60 Modemax=30 Rcut=8		1.9
		60	DF=0.60 Modemax=100 Rcut=8		1.5

Table 4.7. ANM-LD simulation summary of V2R receptor.

Initial Structure	**Final Structure**	**Sim No**	**Simulation Parameter**	**Initial RMSD (Å)**	**Final RMSD (Å)**
AF2 Model	7DW9	61	DF=0.40 Modemax=30 Rcut=8	2.3	1.5
		62	DF=0.40 Modemax=100 Rcut=8		1.4
		63	DF=0.50 Modemax=30 Rcut=8		1.5
		64	DF=0.50 Modemax=100 Rcut=8		1.2
		65	DF=0.60 Modemax=30 Rcut=8		1.5
		66	**DF=0.60 Modemax=100 Rcut=8**		1.3
AF2 Model	7R0C	67	**DF=0.40 Modemax=30 Rcut=8**	2.8	1.8
		68	DF=0.40 Modemax=100 Rcut=8		1.8
		69	DF=0.50 Modemax=30 Rcut=8		2.0
		70	DF=0.50 Modemax=100 Rcut=8		2.2
		71	DF=0.60 Modemax=30 Rcut=8		1.9
		72	DF=0.60 Modemax=100 Rcut=8		2.0

Table 4.8. ANM-LD simulation summary of AGTR1 receptor.

Initial Structure	**Final Structure**	**Sim No**	**Simulation Parameter**	**Initial RMSD (Å)**	**Final RMSD (Å)**
4YAY	6DO1	73	DF=0.40 Modemax=30 Rcut=8	3.8	1.9
		74	**DF=0.40 Modemax=100 Rcut=8**		1.3
		75	DF=0.50 Modemax=30 Rcut=8		1.6
		76	DF=0.50 Modemax=100 Rcut=8		3.2
		77	DF=0.60 Modemax=30 Rcut=8		2.0
		78	DF=0.60 Modemax=100 Rcut=8		3.0

Table 4.9. ANM-LD simulation summary of OPRK receptor.

Initial Structure	**Final Structure**	**Sim No**	**Simulation Parameter**	**Initial RMSD (Å)**	**Final RMSD (Å)**
4DJH	6B73	79	DF=0.40 Modemax=30 Rcut=8	3.3	1.8
		80	DF=0.40 Modemax=100 Rcut=8		1.7
		81	DF=0.50 Modemax=30 Rcut=8		1.8
		82	**DF=0.50 Modemax=100 Rcut=8**		1.5
		83	DF=0.60 Modemax=30 Rcut=8		1.9
		84	DF=0.60 Modemax=100 Rcut=8		1.9

Table 4.10. ANM-LD simulation summary of OPRM receptor.

Initial Structure	**Final Structure**	**Sim No**	**Simulation Parameter**	**Initial RMSD (Å)**	**Final RMSD (Å)**
4DKL	5C1M	85	DF=0.40 Modemax=30 Rcut=8	3.1	3.1
		86	DF=0.40 Modemax=100 Rcut=8		3.1
		87	DF=0.50 Modemax=30 Rcut=8		1.7
		88	**DF=0.50 Modemax=100 Rcut=8**		1.3
		89	DF=0.60 Modemax=30 Rcut=8		2.1
		90	DF=0.60 Modemax=100 Rcut=8		1.8

Table 4.11. ANM-LD simulation summary of AA1R receptor.

Initial Structure	**Final Structure**	**Sim No**	**Simulation Parameter**	**Initial RMSD (Å)**	**Final RMSD (Å)**
5UEN	6D9H	91	DF=0.40 Modemax=30 Rcut=8	2.8	1.3
		92	**DF=0.40 Modemax=100 Rcut=8**		0.8
		93	DF=0.50 Modemax=30 Rcut=8		1.4
		94	DF=0.50 Modemax=100 Rcut=8		1.2
		95	DF=0.60 Modemax=30 Rcut=8		1.3
		96	DF=0.60 Modemax=100 Rcut=8		1.6

Table 4.12. ANM-LD simulation summary of AA2AR receptor.

Initial Structure	**Final Structure**	**Sim No**	**Simulation Parameter**	**Initial RMSD (Å)**	**Final RMSD (Å)**
5MZP	5G53	97	DF=0.40 Modemax=30 Rcut=8	3.7	1.7
		98	DF=0.40 Modemax=100 Rcut=8		2.1
		99	DF=0.50 Modemax=30 Rcut=8		1.7
		100	**DF=0.50 Modemax=100 Rcut=8**		1.4
		101	DF=0.60 Modemax=30 Rcut=8		2.4
		102	DF=0.60 Modemax=100 Rcut=8		1.7

Table 4.13. ANM-LD simulation summary of AA2BR receptor.

Initial Structure	**Final Structure**	**Sim No**	**Simulation Parameter**	**Initial RMSD (Å)**	**Final RMSD (Å)**
AF2 Model	8HDP	103	DF=0.40 Modemax=30 Rcut=8	3.8	1.6
		104	DF=0.40 Modemax=100 Rcut=8		1.7
		105	DF=0.50 Modemax=30 Rcut=8		1.5
		106	DF=0.50 Modemax=100 Rcut=8		1.8
		107	DF=0.60 Modemax=30 Rcut=8		1.7
		108	**DF=0.60 Modemax=100 Rcut=8**		1.2

Table 4.14. ANM-LD simulation summary of P2RY1 receptor.

Initial Structure	**Final Structure**	**Sim No**	**Simulation Parameter**	**Initial RMSD (Å)**	**Final RMSD (Å)**
AFMS Model	7XXH	109	DF=0.40 Modemax=30 Rcut=8	2.5	1.8
		110	**DF=0.40 Modemax=100 Rcut=8**		1.6
		111	DF=0.50 Modemax=30 Rcut=8		1.9
		112	DF=0.50 Modemax=100 Rcut=8		1.5
		113	DF=0.60 Modemax=30 Rcut=8		1.9
		114	DF=0.60 Modemax=100 Rcut=8		2.0

Table 4.15. ANM-LD simulation summary of P2Y12 receptor.

Initial Structure	**Final Structure**	**Sim No**	**Simulation Parameter**	**Initial RMSD (Å)**	**Final RMSD (Å)**
AFMS Model	7XXI	115	DF=0.40 Modemax=30 Rcut=8	2.6	2.2
		116	**DF=0.40 Modemax=100 Rcut=8**		1.7
		117	DF=0.50 Modemax=30 Rcut=8		2.1
		118	DF=0.50 Modemax=100 Rcut=8		1.7
		119	DF=0.60 Modemax=30 Rcut=8		2.1
		120	DF=0.60 Modemax=100 Rcut=8		2.2

Table 4.16. ANM-LD simulation summary of CNR1 receptor.

Initial Structure	**Final Structure**	**Sim No**	**Simulation Parameter**	**Initial RMSD (Å)**	**Final RMSD (Å)**
5TGZ	5XRA	121	DF=0.40 Modemax=30 Rcut=8	3.8	1.7
		122	**DF=0.40 Modemax=100 Rcut=8**		1.4
		123	DF=0.50 Modemax=30 Rcut=8		1.7
		124	DF=0.50 Modemax=100 Rcut=8		1.4
		125	DF=0.60 Modemax=30 Rcut=8		1.6
		126	DF=0.60 Modemax=100 Rcut=8		1.5

Table 4.17. ANM-LD simulation summary of DP2 receptor.

Initial Structure	**Final Structure**	**Sim No**	**Simulation Parameter**	**Initial RMSD (Å)**	**Final RMSD (Å)**
7M8W	AFMS Model	127	**DF=0.40 Modemax=30 Rcut=8**	2.7	1.2
		128	DF=0.40 Modemax=100 Rcut=8		1.2
		129	DF=0.50 Modemax=30 Rcut=8		1.3
		130	DF=0.50 Modemax=100 Rcut=8		1.0
		131	DF=0.60 Modemax=30 Rcut=8		1.4
		132	DF=0.60 Modemax=100 Rcut=8		2.0

Table 4.18. ANM-LD simulation summary of TA2R receptor.

Initial Structure	**Final Structure**	**Sim No**	**Simulation Parameter**	**Initial RMSD (Å)**	**Final RMSD (Å)**
6IIU	8XJO	133	**DF=0.40 Modemax=30 Rcut=8**	2.9	1.5
		134	DF=0.40 Modemax=100 Rcut=8		1.5
		135	DF=0.50 Modemax=30 Rcut=8		1.8
		136	DF=0.50 Modemax=100 Rcut=8		1.7
		137	DF=0.60 Modemax=30 Rcut=8		1.7
		138	DF=0.60 Modemax=100 Rcut=8		1.8

Table 4.19. ANM-LD simulation summary of LPAR1 receptor.

Initial Structure	**Final Structure**	**Sim No**	**Simulation Parameter**	**Initial RMSD (Å)**	**Final RMSD (Å)**
4Z34	7YU3	139	DF=0.40 Modemax=30 Rcut=8	2.8	1.7
		140	DF=0.40 Modemax=100 Rcut=8		1.9
		141	DF=0.50 Modemax=30 Rcut=8		2.0
		142	**DF=0.50 Modemax=100 Rcut=8**		1.5
		143	DF=0.60 Modemax=30 Rcut=8		2.1
		144	DF=0.60 Modemax=100 Rcut=8		1.6

Table 4.20. ANM-LD simulation summary of S1PR1 receptor.

Initial Structure	**Final Structure**	**Sim No**	**Simulation Parameter**	**Initial RMSD (Å)**	**Final RMSD (Å)**
AF2 Model	8G94	145	DF=0.40 Modemax=30 Rcut=8	2.9	1.6
		146	**DF=0.40 Modemax=100 Rcut=8**		1.3
		147	DF=0.50 Modemax=30 Rcut=8		2.3
		148	DF=0.50 Modemax=100 Rcut=8		1.5
		149	DF=0.60 Modemax=30 Rcut=8		1.5
		150	DF=0.60 Modemax=100 Rcut=8		1.5

Table 4.21. ANM-LD simulation summary of CCR1 receptor.

Initial Structure	**Final Structure**	**Sim No**	**Simulation Parameter**	**Initial RMSD (Å)**	**Final RMSD (Å)**
AF2 Model	7VLA	151	DF=0.40 Modemax=30 Rcut=8	2.0	1.3
		152	**DF=0.40 Modemax=100 Rcut=8**		1.0
		153	DF=0.50 Modemax=30 Rcut=8		1.5
		154	DF=0.50 Modemax=100 Rcut=8		1.4
		155	DF=0.60 Modemax=30 Rcut=8		1.4
		156	DF=0.60 Modemax=100 Rcut=8		1.3

Table 4.22. ANM-LD simulation summary of CCR5 receptor.

Initial Structure	**Final Structure**	**Sim No**	**Simulation Parameter**	**Initial RMSD (Å)**	**Final RMSD (Å)**
6AKY	7O7F	157	DF=0.40 Modemax=30 Rcut=8	2.9	1.4
		158	DF=0.40 Modemax=100 Rcut=8		1.1
		159	DF=0.50 Modemax=30 Rcut=8		1.4
		160	**DF=0.50 Modemax=100 Rcut=8**		1.1
		161	DF=0.60 Modemax=30 Rcut=8		1.6
		162	DF=0.60 Modemax=100 Rcut=8		1.4

Table 4.23. ANM-LD simulation summary of CCR8 receptor.

Initial Structure	**Final Structure**	**Sim No**	**Simulation Parameter**	**Initial RMSD (Å)**	**Final RMSD (Å)**
AF2 Model	8KFX	163	DF=0.40 Modemax=30 Rcut=8	1.9	1.1
		164	DF=0.40 Modemax=100 Rcut=8		0.8
		165	DF=0.50 Modemax=30 Rcut=8		1.2
		166	**DF=0.50 Modemax=100 Rcut=8**		0.9
		167	DF=0.60 Modemax=30 Rcut=8		1.3
		168	DF=0.60 Modemax=100 Rcut=8		1.0

Table 4.24. ANM-LD simulation summary of CXCR2 receptor.

Initial Structure	**Final Structure**	**Sim No**	**Simulation Parameter**	**Initial RMSD (Å)**	**Final RMSD (Å)**
6LFL	6LFM	169	DF=0.40 Modemax=30 Rcut=8	2.6	2.4
		170	DF=0.40 Modemax=100 Rcut=8		1.7
		171	DF=0.50 Modemax=30 Rcut=8		1.9
		172	DF=0.50 Modemax=100 Rcut=8		2.0
		173	DF=0.60 Modemax=100 Rcut=8		2.0
		174	**DF=0.70 Modemax=100 Rcut=8**		1.8

Table 4.25. ANM-LD simulation summary of CXCR4 receptor.

Initial Structure	**Final Structure**	**Sim No**	**Simulation Parameter**	**Initial RMSD (Å)**	**Final RMSD (Å)**
AF2 Model	8U4N	175	DF=0.40 Modemax=30 Rcut=8	2.3	1.2
		176	DF=0.40 Modemax=100 Rcut=8		1.5
		177	DF=0.50 Modemax=30 Rcut=8		1.1
		178	DF=0.50 Modemax=100 Rcut=8		1.0
		179	DF=0.60 Modemax=30 Rcut=8		1.2
		180	**DF=0.60 Modemax=100 Rcut=8**		1.0

4.1.1. M2 Muscarinic Acetylcholine Receptor (ACM2)

In this study, we performed ANM-LD simulations for M2R to investigate its conformational transition toward two active states: the G protein-bound conformation (PDB ID: 6OIK) and the β-arrestin-bound conformation (PDB ID: 6U1N), both starting from the inactive structure (PDB ID: 5ZK3). The simulation results targeting the G protein-bound state are presented in Figure 4.1, while those targeting the β-arrestin-bound state are shown in Figure 4.2. In the G protein-bound pathway (Figure 4.1), Panel (A) shows a reduction in RMSD to 1.0 Å, indicating excellent structural convergence toward the active conformation. Panel (B) illustrates the mode overlaps and collectivities, confirming that the selected ANM modes accurately guide the transition along a biologically meaningful pathway with high collectivity. Panel (C) visualizes the structural progression from inactive (blue) to active (red) conformations along the simulated trajectory. Panel (D) displays the TM3–TM6 and TM3–TM7 distance changes, which reflect hallmark features of GPCR activation: the TM3–TM6 distance increases due to the outward motion of TM6 (linked to the breaking of the ionic lock), while the TM3–TM7 distance decreases, consistent with the inward shift of TM7 and rearrangement of the NPxxY motif.

In the β-arrestin-bound pathway (Figure 4.2), a similar analysis reveals an RMSD decrease to 1.4 Å (Panel A), again indicating strong convergence. Panels (B-D) display analogous results, confirming that both transition pathways exhibit physically plausible and biologically consistent dynamic features. These findings support the reliability of ANM-LD in modeling distinct activation routes and lay the foundation for downstream analysis of signaling bias in M2R.

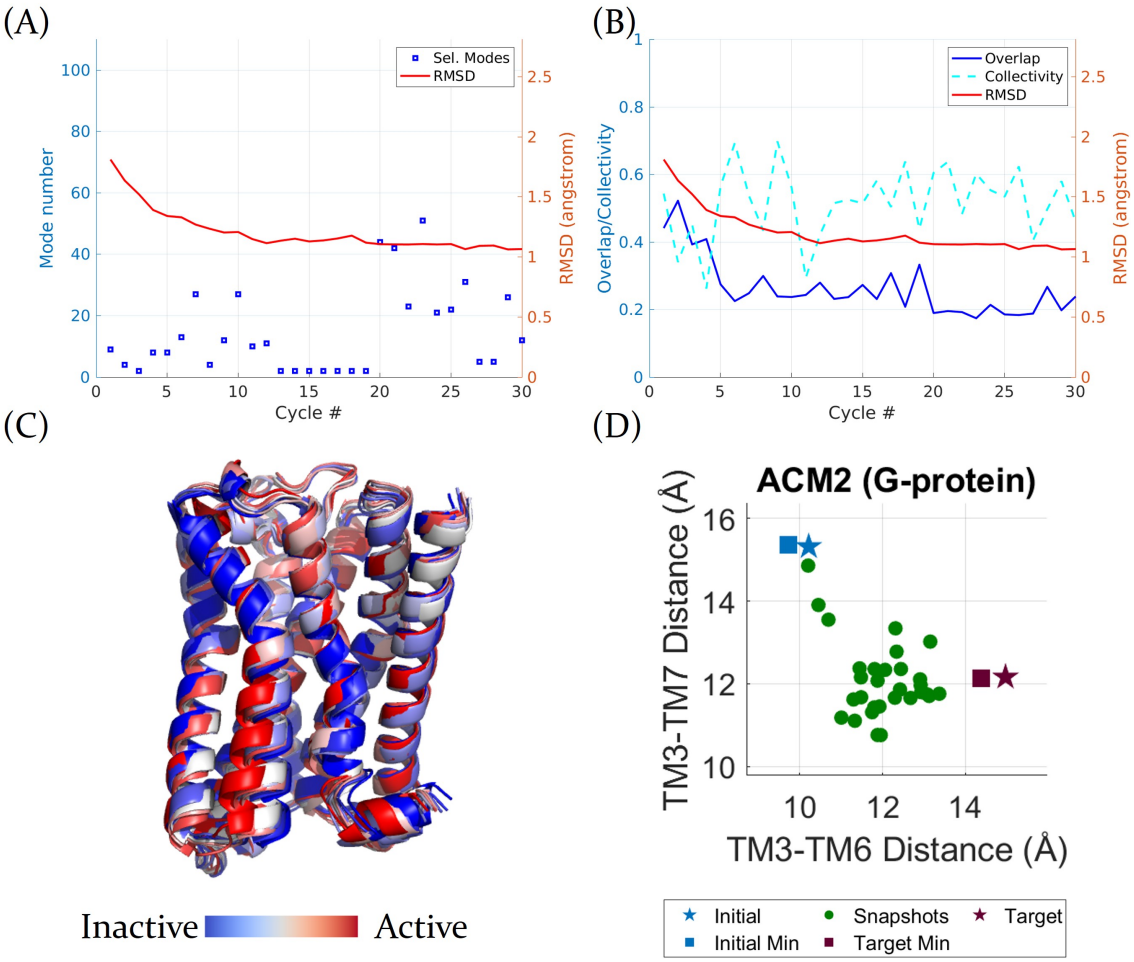

Figure 4.1. ANM-LD simulation of ACM2 conformational transition from inactive to the G protein-bound active state. (A) RMSD progression. (B) Mode overlap and collectivity of selected ANM modes. (C) Transition snapshots colored from blue (inactive) to red (active). (D) TM3–TM6 and TM3–TM7 distance changes over the simulation.

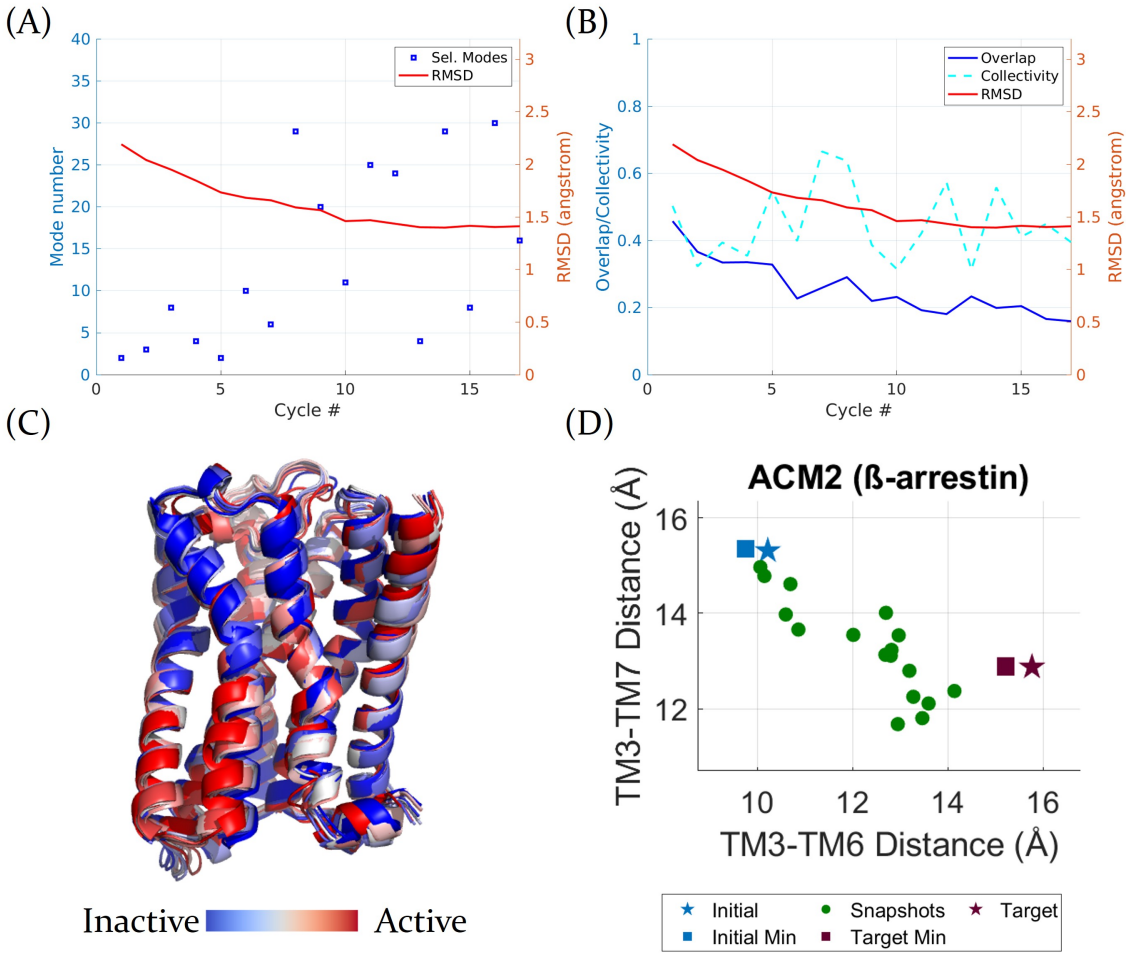

Figure 4.2. ANM-LD simulation of ACM2 conformational transition from inactive to the β-arrestin-bound active state. (A) RMSD progression. (B) Mode overlap and collectivity of selected ANM modes. (C) Transition snapshots colored from blue (inactive) to red (active). (D) TM3–TM6 and TM3–TM7 distance changes over the simulation.

4.1.2. Serotonin Receptor 2B (5HT2B)

In the absence of an experimentally resolved inactive structure, we used an AlphaFold2-predicted model from GPCRdb [42] as the starting conformation for ANM-LD simulations. Two distinct activation pathways were modeled, targeting the G protein-bound structure (PDB ID: 7SRR) and the β-arrestin-bound structure (PDB

ID: 7SRS). In the G protein-bound targeting simulation (Figure 4.3), (A) the RMSD decreases to 1.0 Å, indicating effective convergence toward the active conformation. (B) Mode overlap and collectivity analyses support the biological plausibility of the transition, with high overlap scores and cooperative motion. (C) Structural snapshots illustrate a gradual conformational shift from the AlphaFold-predicted inactive model (blue) to the active structure (red). (D) The TM3–TM6 and TM3–TM7 distance profiles reveal a widening of the intracellular cavity and rearrangement of the NPxxY motif, in line with canonical GPCR activation. In the β-arrestin-bound pathway (Figure 4.4), (A) RMSD improves from 2.5 Å to 1.0 Å, also reflecting strong structural convergence. (B–D) The selected modes and structural changes similarly capture hallmark features of β-arrestin-biased activation, suggesting that ANM-LD can effectively model distinct signaling routes even when starting from predicted structures.

4.1.3. β_1-adrenergic receptor (ADRB1)

To investigate its activation dynamics, ANM-LD simulations were performed using the inactive conformation of ADRB1 (PDB ID: 4GPO) as the starting structure. Two separate transition pathways were modeled toward the G protein-bound structure (PDB ID: 7JJO) and the β-arrestin-bound structure (PDB ID: 6TKO). In the G protein-bound simulation (4.5), (A) RMSD decreased to 1.1 Å, indicating a reliable transition toward the target conformation. (B) The selected ANM modes showed high overlap with the target and maintained collective dynamics throughout the simulation. (C) Structural morphs demonstrate the progressive change from inactive (blue) to active (red). (D) Changes in TM3–TM6 and TM3–TM7 distances reflect classical activation signatures, including the outward movement of TM6 and inward rearrangement of TM7. In the β-arrestin-bound pathway (4.6), (A) RMSD decreased to 1.0 Å, indicating high-quality convergence. (B–D) The dynamic properties of the selected modes and the resulting conformational changes highlight distinct but equally plausible features of β-arrestin-biased activation. These results demonstrate that ANM-LD can reliably reconstruct alternative activation routes for ADRB1, consistent with its bifunctional signaling role.

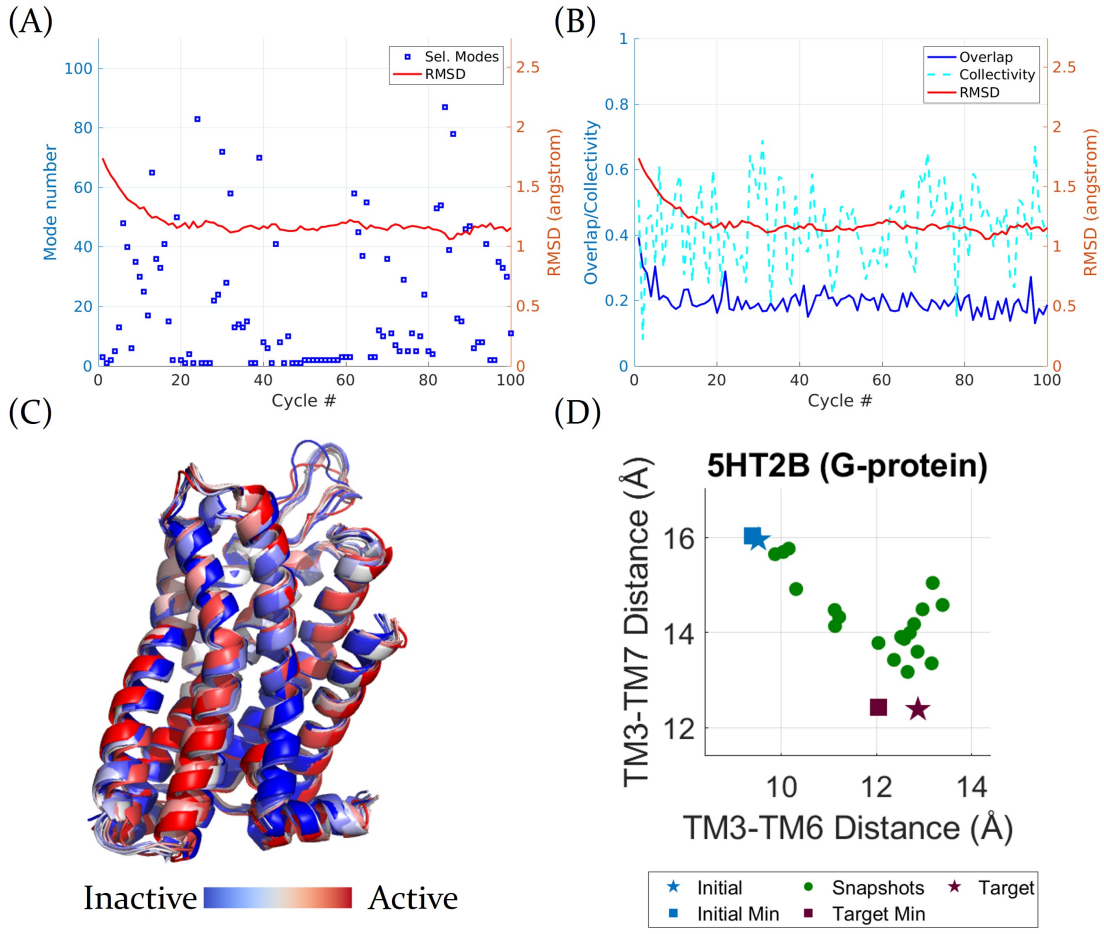

Figure 4.3. ANM-LD simulation of 5HT2B conformational transition from inactive to the G protein-bound active state. (A) RMSD progression. (B) Mode overlap and collectivity of selected ANM modes. (C) Transition snapshots colored from blue (inactive) to red (active). (D) TM3–TM6 and TM3–TM7 distance changes over the simulation.

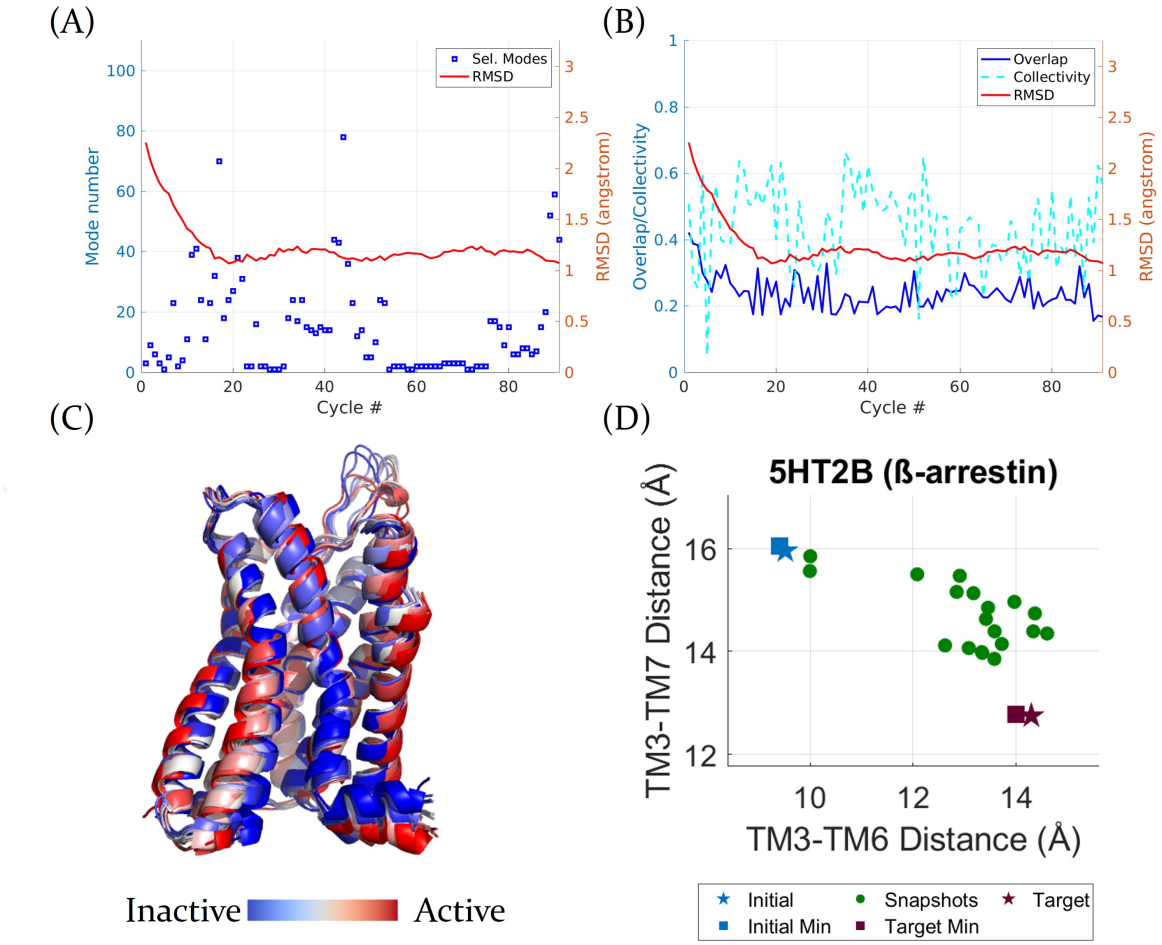

Figure 4.4. ANM-LD simulation of 5HT2B conformational transition from inactive to the β-arrestin-bound active state. (A) RMSD progression. (B) Mode overlap and collectivity of selected ANM modes. (C) Transition snapshots colored from blue (inactive) to red (active). (D) TM3–TM6 and TM3–TM7 distance changes over the simulation.

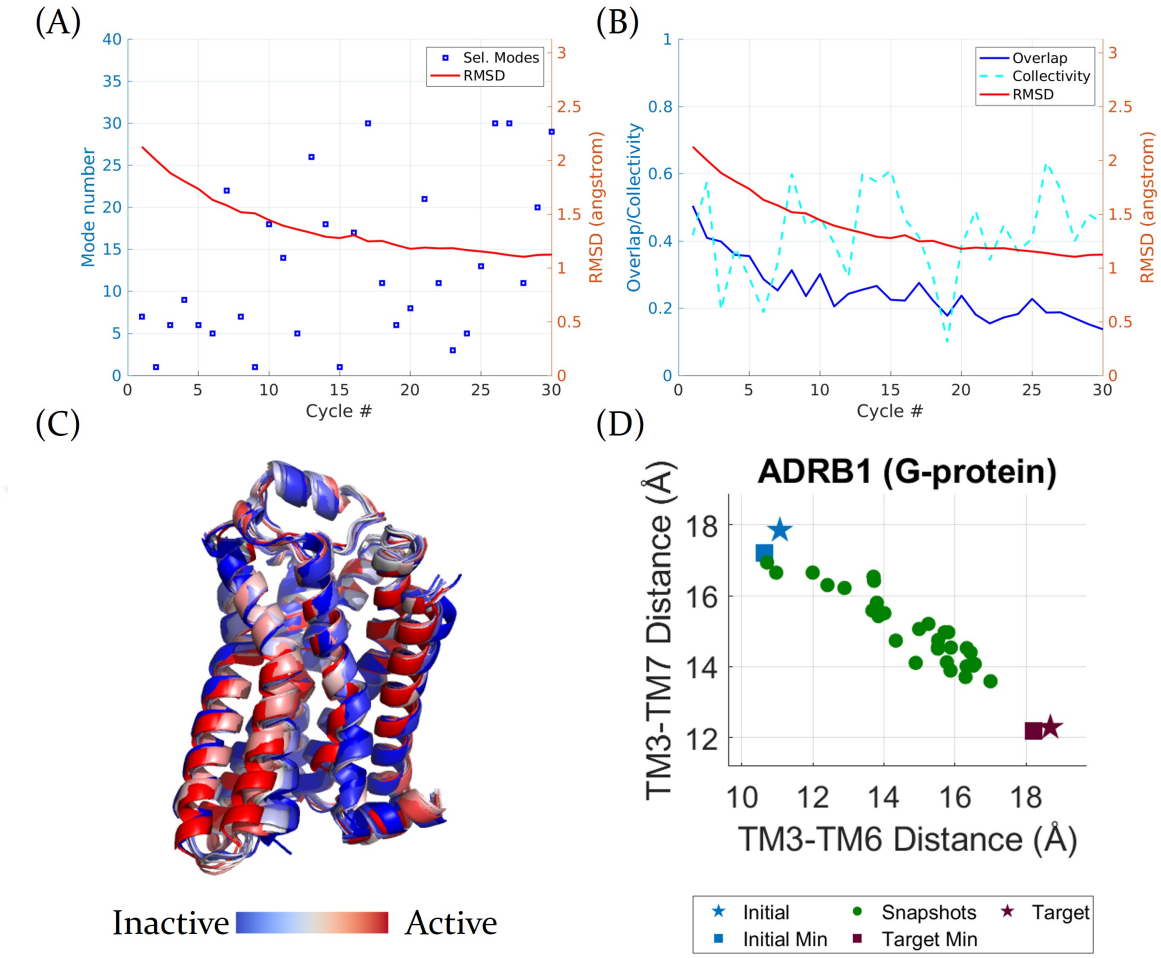

Figure 4.5. ANM-LD simulation of ADRB1 conformational transition from inactive to the G protein-bound active state. (A) RMSD progression. (B) Mode overlap and collectivity of selected ANM modes. (C) Transition snapshots colored from blue (inactive) to red (active). (D) TM3–TM6 and TM3–TM7 distance changes over the simulation.

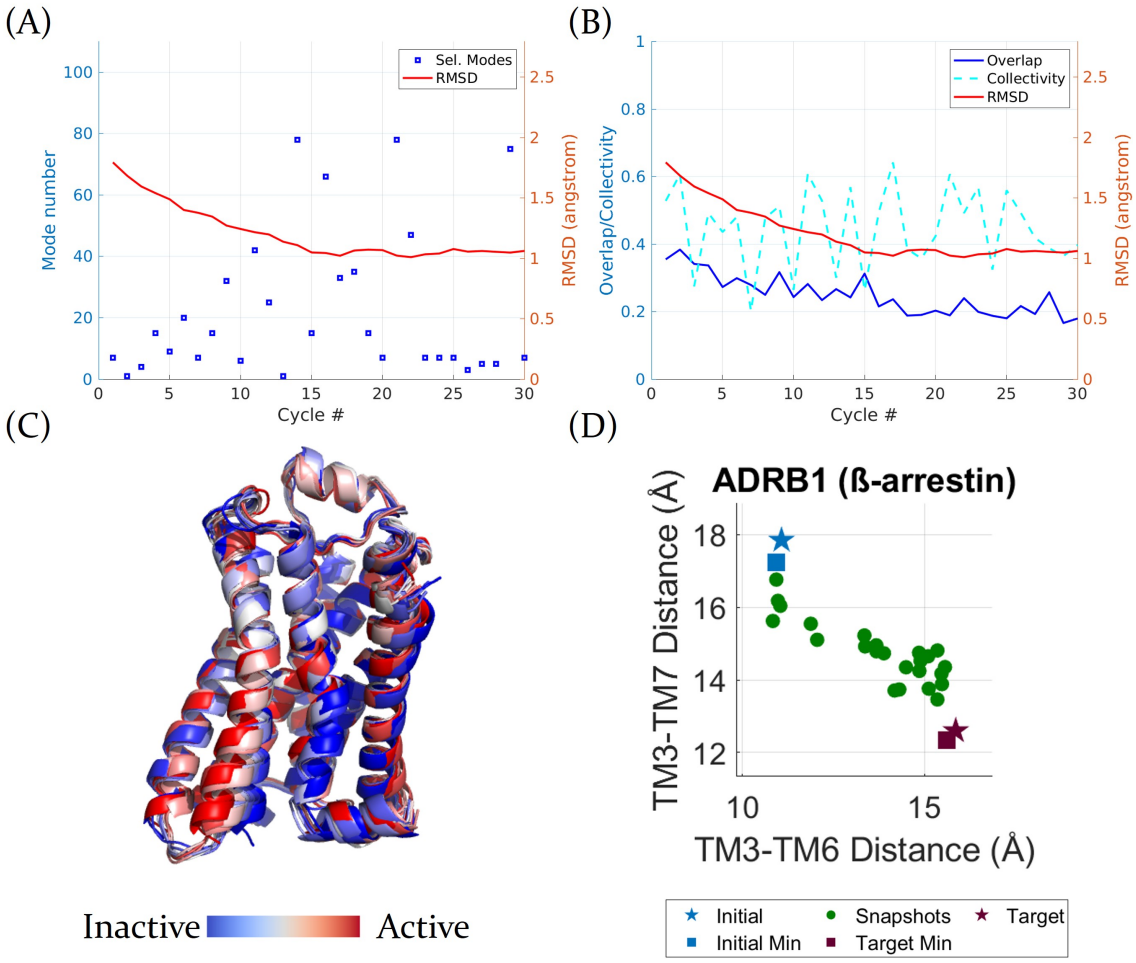

Figure 4.6. ANM-LD simulation of ADRB2 conformational transition from inactive to active state. (A) RMSD progression. (B) Mode overlap and collectivity of selected ANM modes. (C) Transition snapshots colored from blue (inactive) to red (active). (D) TM3–TM6 and TM3–TM7 distance changes over the simulation.

4.1.4. β_2-adrenergic receptor (ADRB2)

To model the conformational transition of ADRB2, we performed ANM-LD simulations starting from the inactive crystal structure (PDB ID: 2RH1) and targeting the G protein-bound active state (PDB ID: 3SN6). As shown in Figure 4.7, (A) the RMSD decreased to 1.3 Å over the course of the simulation, demonstrating substantial convergence toward the target active conformation. (B) Mode overlap and collectivity

metrics confirmed that the selected modes captured coherent and functionally relevant dynamics. (C) Structural snapshots along the ANM-LD trajectory illustrate the gradual transition from the inactive (blue) to active (red) state. (D) The TM3–TM6 and TM3–TM7 distance plots reveal activation-associated structural changes, including outward movement of TM6 and rearrangement of the TM7 helix, consistent with established ADRB2 activation mechanisms.

To further validate the ANM-LD–derived intermediate structures, we conducted a comparative analysis with 20 cryo-EM structures of β2-adrenergic receptor–Gs protein complexes presented in a recent time-resolved study of G protein activation. This study employed pre-steady-state cryo-EM to capture structural snapshots following GTP addition, providing a detailed conformational trajectory of Gα activation and dissociation from the receptor [150]. These structures were analyzed using two key collective variables: the TM3–TM6 and TM3–TM7 distances, which reflect critical rearrangements during GPCR activation. As shown in Figure 4.8, most cryo-EM structures exhibit distances corresponding to fully active-like conformations and fail to sample intermediate TM3–TM6 distances that are essential for capturing early transition states. In contrast, our ANM-LD simulations successfully populate a broader conformational space, including key intermediates. Notably, three cryo-EM structures—8GEJ, 8GG9, and 8GGE—align well with specific ANM-LD–generated intermediates, supporting the physiological relevance of our computational trajectories. Cryo-EM–derived structures are indicated as diamonds in Figure 4.8, highlighting their relative distribution compared to the ANM-LD ensemble.

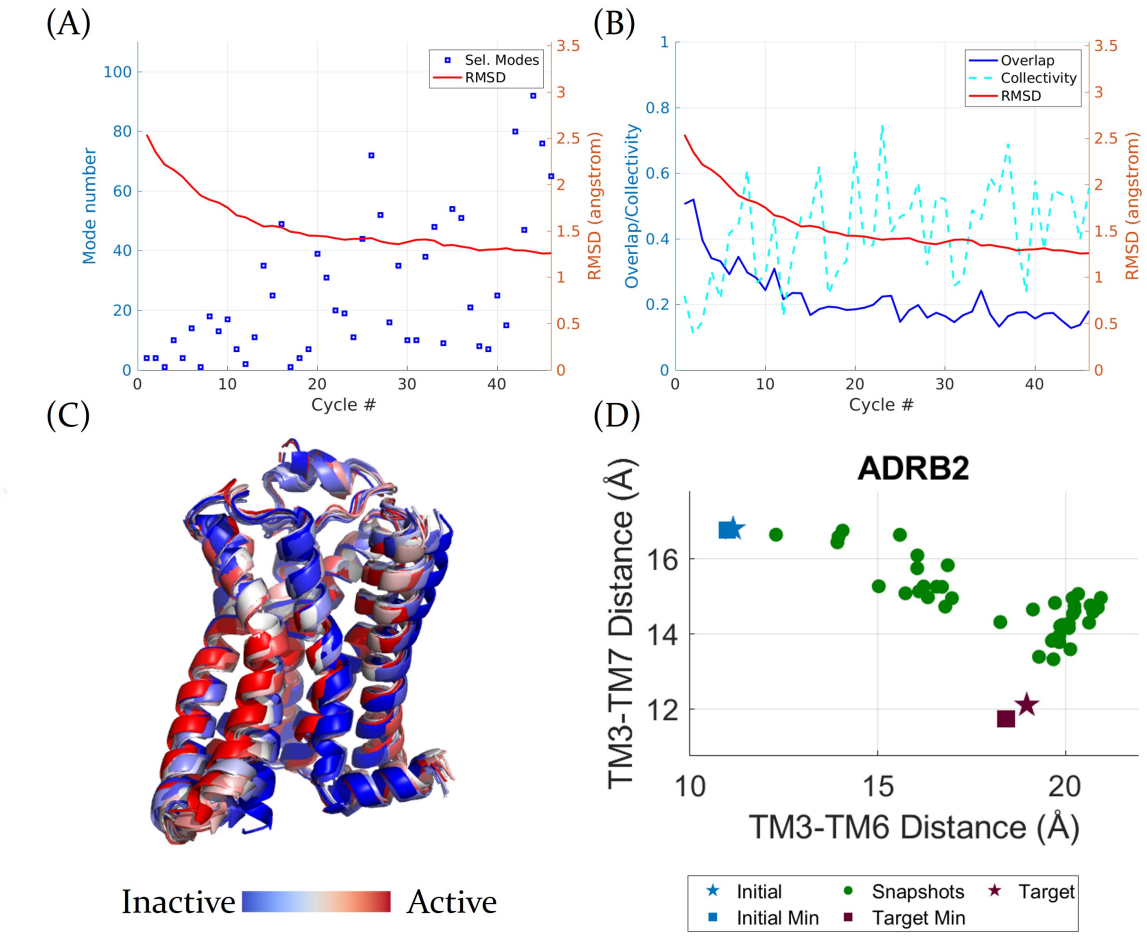

Figure 4.7. ANM-LD simulation of ADRB2 conformational transition from inactive to active state. (A) RMSD progression. (B) Mode overlap and collectivity of selected ANM modes. (C) Transition snapshots colored from blue (inactive) to red (active). (D) TM3–TM6 and TM3–TM7 distance changes over the simulation.

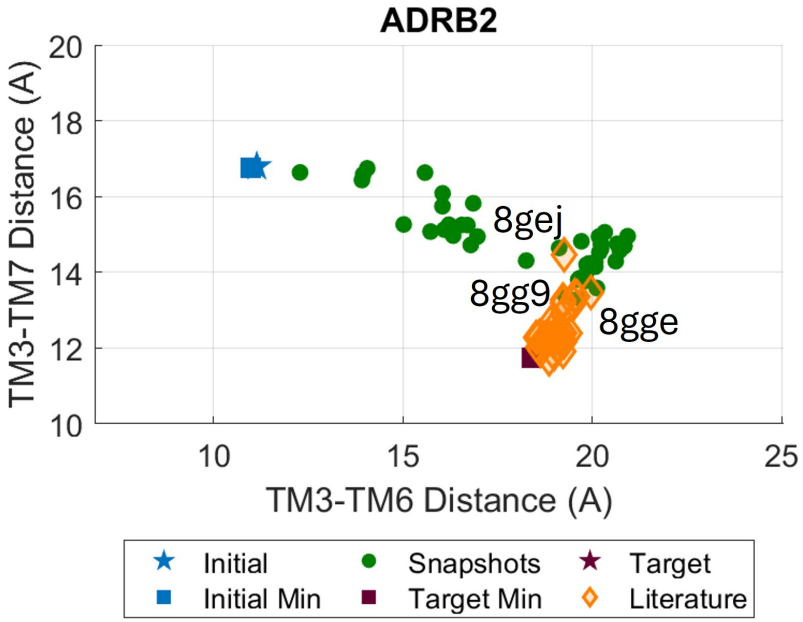

Figure 4.8. Comparison of ANM-LD intermediates with time-resolved cryo-EM structures of the β2AR–Gs complex. The conformational landscape is mapped using TM3–TM6 and TM3–TM7 distances. Symbols indicate inactive (blue), active (red), and ANM-LD (green) states; cryo-EM structures appear as orange diamonds.

4.1.5. Dopamine D3 receptor (DRD3)

To investigate the activation mechanism of DRD3, we performed ANM-LD simulations starting from the inactive structure (PDB ID: 3PBL) and targeting the G protein-bound active conformation (PDB ID: 8IRT). As illustrated in Figure 4.9, (A) the RMSD decreased to 1.0 Å, indicating high-quality convergence toward the active state. (B) Mode overlap and collectivity values confirmed the selection of biologically relevant transition modes. (C) Structural morphing from inactive (blue) to active (red) states demonstrates a smooth progression along the simulated pathway. (D) The TM3–TM6 and TM3–TM7 distance plots reflect canonical activation changes, supporting the functional accuracy of the modeled transition.

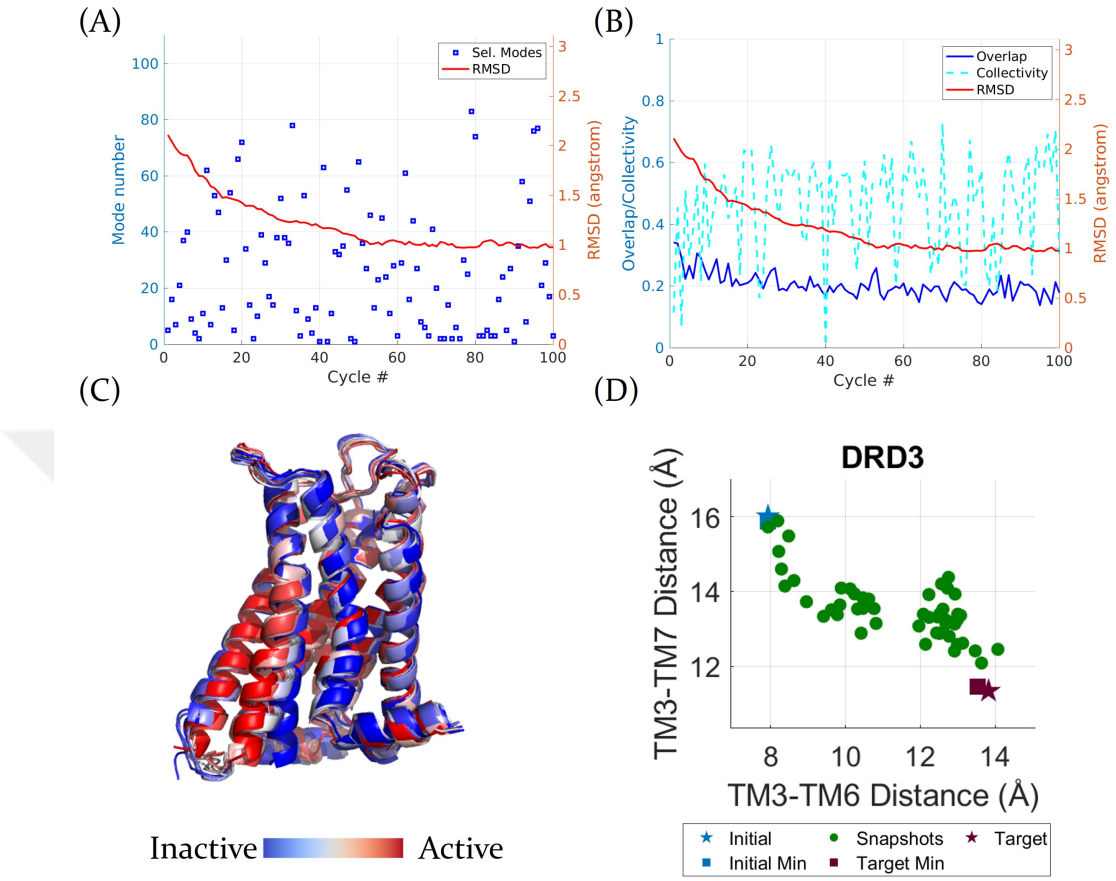

Figure 4.9. ANM-LD simulation of DRD3 conformational transition from inactive to active state. (A) RMSD progression. (B) Mode overlap and collectivity of selected ANM modes. (C) Transition snapshots colored from blue (inactive) to red (active). (D) TM3–TM6 and TM3–TM7 distance changes.

4.1.6. Neurotensin receptor 1 (NTR1)

To model its activation pathways, ANM-LD simulations were performed using the inactive structure of NTR1 (PDB ID: 7UL2) as the starting point. Two transition pathways were generated: one toward the G protein-bound active state (PDB ID: 6OSA) and one toward the β-arrestin-bound active state (PDB ID: 6PWC). In the G protein-bound simulation (Figure 4.10), (A) the RMSD decreased to 1.3 Å, demonstrating significant structural convergence. (B) Mode overlap and collectivity analyses

confirmed the biological plausibility of the selected transition pathway. (C) Structural snapshots from the simulation visualize the stepwise transition from the inactive (blue) to the active (red) conformation. (D) Distance plots for TM3–TM6 and TM3–TM7 reflect activation-associated changes, consistent with canonical GPCR behavior. In the β-arrestin-bound pathway (Figure 4.11), (A) the RMSD decreased to 1.7 Å, indicating moderate but reliable convergence. (B–D) Dynamic features of the transition pathway show a coherent structural rearrangement, capturing β-arrestin-biased activation features. These results further support the capacity of ANM-LD to model distinct activation routes of NTR1.

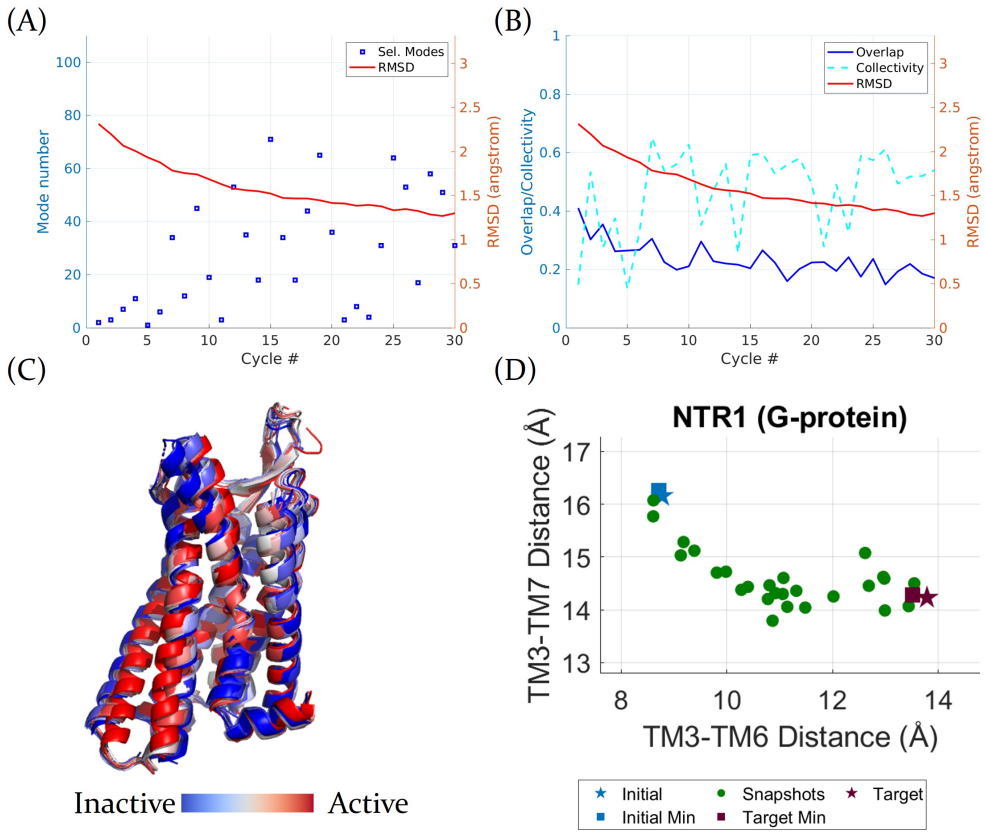

Figure 4.10. ANM-LD simulation of NTR1 conformational transition from inactive to the G protein-bound active state. (A) RMSD progression. (B) Mode overlap and collectivity of selected ANM modes. (C) Transition snapshots colored from blue (inactive) to red (active). (D) TM3–TM6 and TM3–TM7 distance changes.

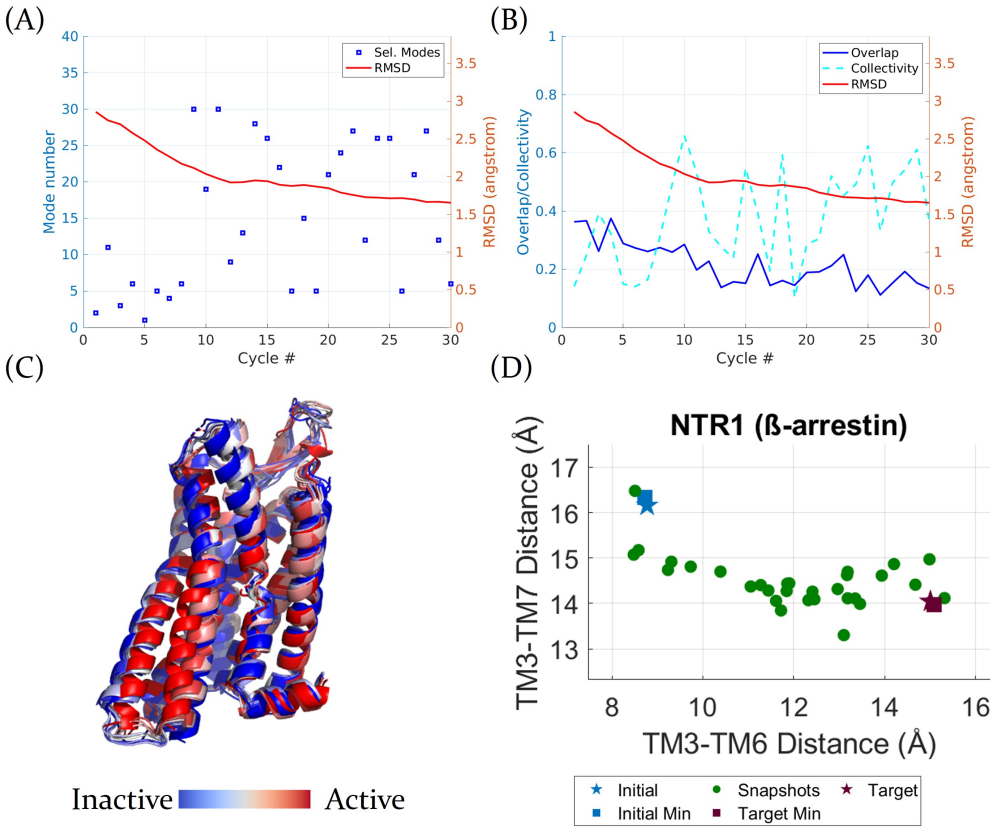

Figure 4.11. ANM-LD simulation of NTR1 conformational transition from inactive to the β-arrestin-bound active state. (A) RMSD progression. (B) Mode overlap and collectivity of selected ANM modes. (C) Transition snapshots colored from blue (inactive) to red (active). (D) TM3–TM6 and TM3–TM7 distance changes.

4.1.7. Vasopressin V2 receptor (V2R)

Due to the lack of an experimentally resolved inactive structure for V2R, we used an AlphaFold2-predicted model from GPCRdb [32] as the starting conformation for our ANM-LD simulations. We modeled two distinct activation pathways: one targeting the G protein-bound active state (PDB ID: 7DW9) and the other targeting the β-arrestin-bound active state (PDB ID: 7R0C). In the G protein-bound simulation (Figure 4.12), (A) the RMSD decreased to 1.3 Å, indicating strong structural convergence toward the experimentally determined active conformation. (B) Mode overlap and collectivity

metrics further validated the selected transition pathway, with cooperative dynamics aligned with functional motion. (C) Structural morphs visualize the transition from the predicted inactive model (blue) to the G protein-bound state (red). (D) TM3–TM6 and TM3–TM7 distance changes reflect expected features of receptor activation, including the outward displacement of TM6 and NPxxY motif rearrangement. In the β-arrestin-bound simulation (Figure 4.13), (A) RMSD reduced to 1.8 Å, suggesting a moderate but reliable transition. (B–D) The selected modes captured a distinct conformational trajectory that reflects the structural features of arrestin-biased activation. These results confirm the utility of ANM-LD in modeling alternative signaling pathways.

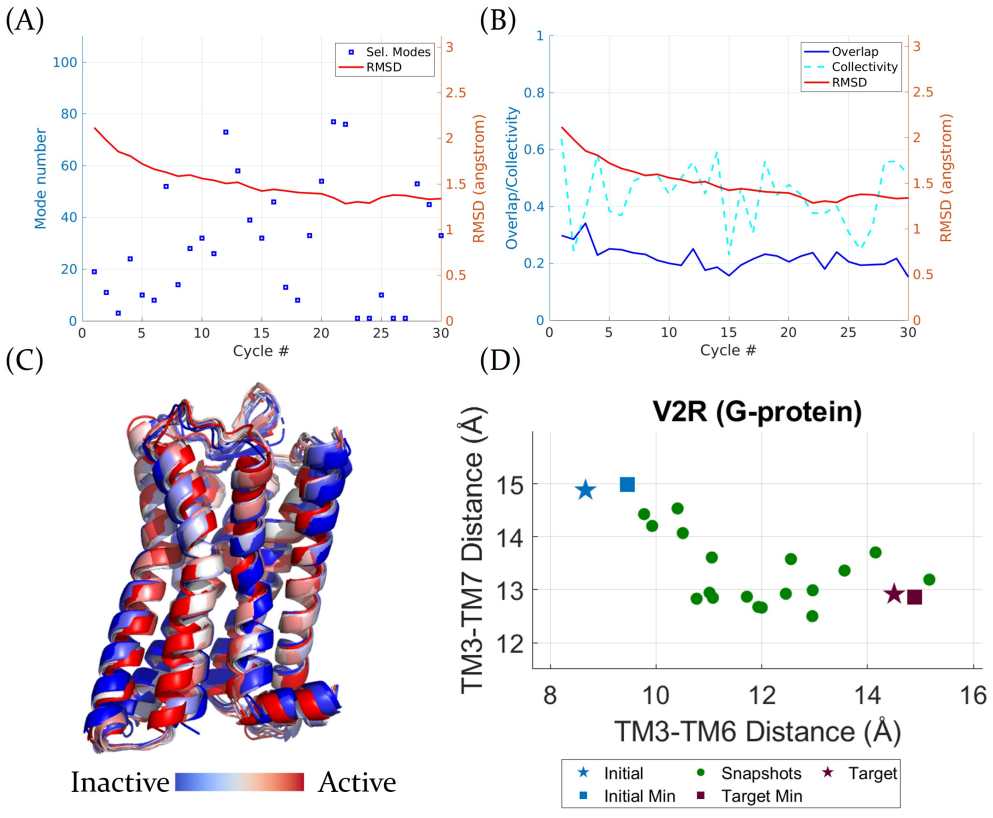

Figure 4.12. ANM-LD simulation of V2R conformational transition from inactive to the G protein-bound active state. (A) RMSD progression. (B) Mode overlap and collectivity of selected ANM modes. (C) Transition snapshots colored from blue (inactive) to red (active). (D) TM3–TM6 and TM3–TM7 distance changes.

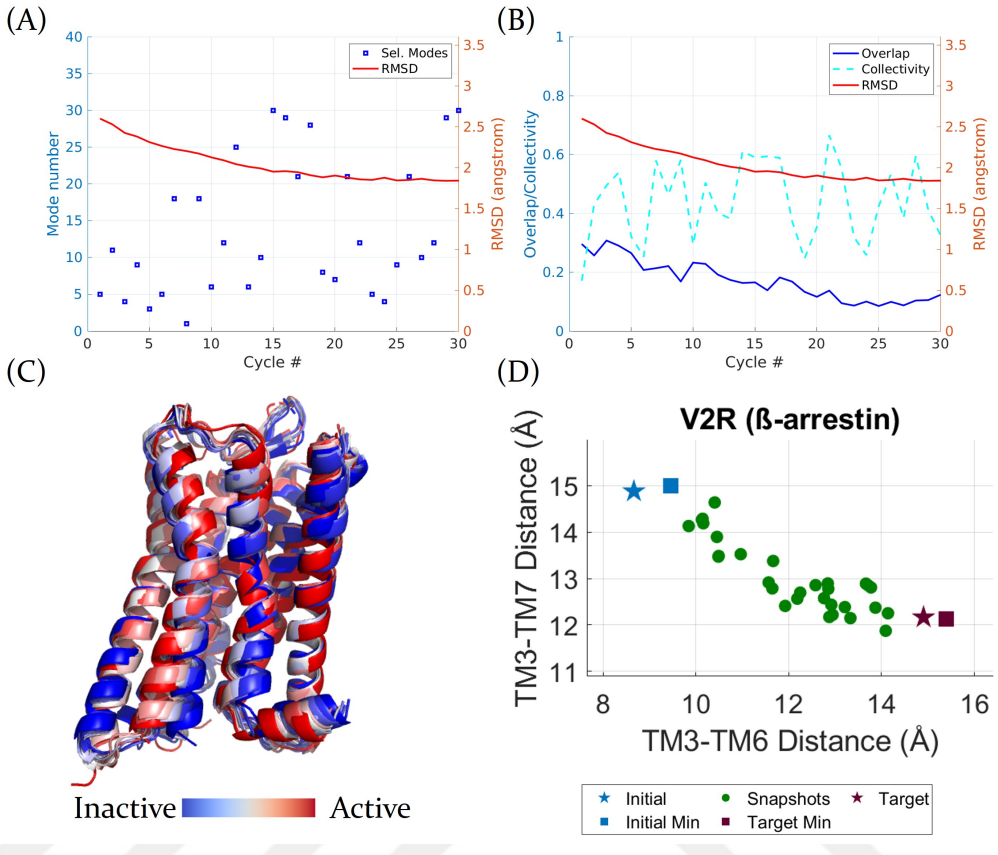

Figure 4.13. ANM-LD simulation of V2R conformational transition from inactive to the β-arrestin-bound active state. (A) RMSD progression. (B) Mode overlap and collectivity of selected ANM modes. (C) Transition snapshots colored from blue (inactive) to red (active). (D) TM3–TM6 and TM3–TM7 distance changes.

4.1.8. Angiotensin II Type 1 Receptor (AGTR1)

To investigate the activation dynamics of AT1R, ANM-LD simulations were performed using the inactive structure (PDB ID: 4YAY) as the starting point and targeting the nanobody-stabilized active state (PDB ID: 6DO1). As shown in Figure 4.14, (A) RMSD decreased to 1.3 Å over the course of the simulation, indicating a substantial structural transition. (B) Mode overlap and collectivity values demonstrated the effectiveness of the selected modes in driving biologically relevant motions. (C) Structural snapshots depict the conformational transition from the inactive (blue) to the active

(red) state. (D) TM3–TM6 and TM3–TM7 distance profiles show expected activation-related trends, with outward displacement of TM6 and inward rearrangement of TM7, consistent with canonical GPCR activation.

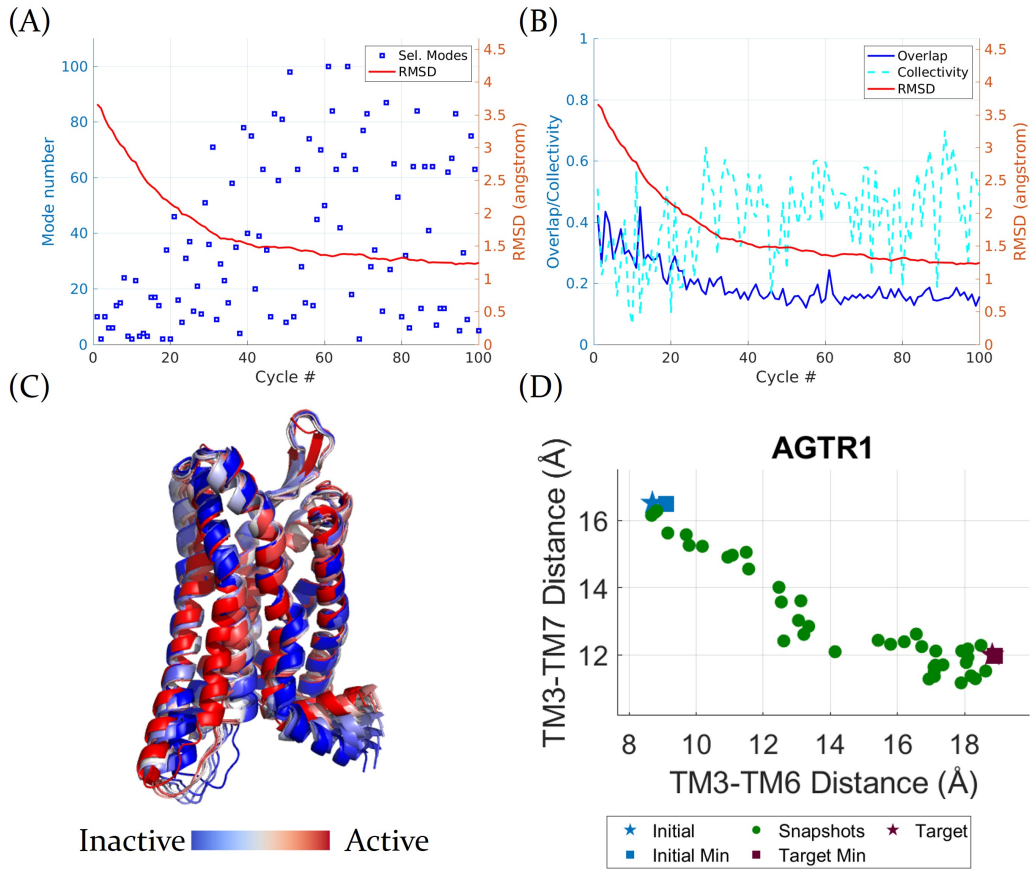

Figure 4.14. ANM-LD simulation of AT1R conformational transition from inactive to active state. (A) RMSD progression. (B) Mode overlap and collectivity of selected ANM modes. (C) Transition snapshots colored from blue (inactive) to red (active). (D) TM3–TM6 and TM3–TM7 distance changes over the simulation.

4.1.9. K-Opioid Receptor (OPRK)

To explore its activation mechanism, we performed ANM-LD simulations starting from the inactive conformation (PDB ID: 4DJH) and targeting the nanobody-stabilized active state (PDB ID: 6B73). As shown in Figure 4.15, (A) RMSD decreased to 1.5 Å,

demonstrating reliable structural convergence. (B) The selected modes showed high overlap and collectivity, indicating functionally coherent dynamics. (C) Structural morphing illustrates a gradual transition from inactive (blue) to active (red) state. (D) TM3–TM6 and TM3–TM7 distance profiles reveal activation-consistent changes.

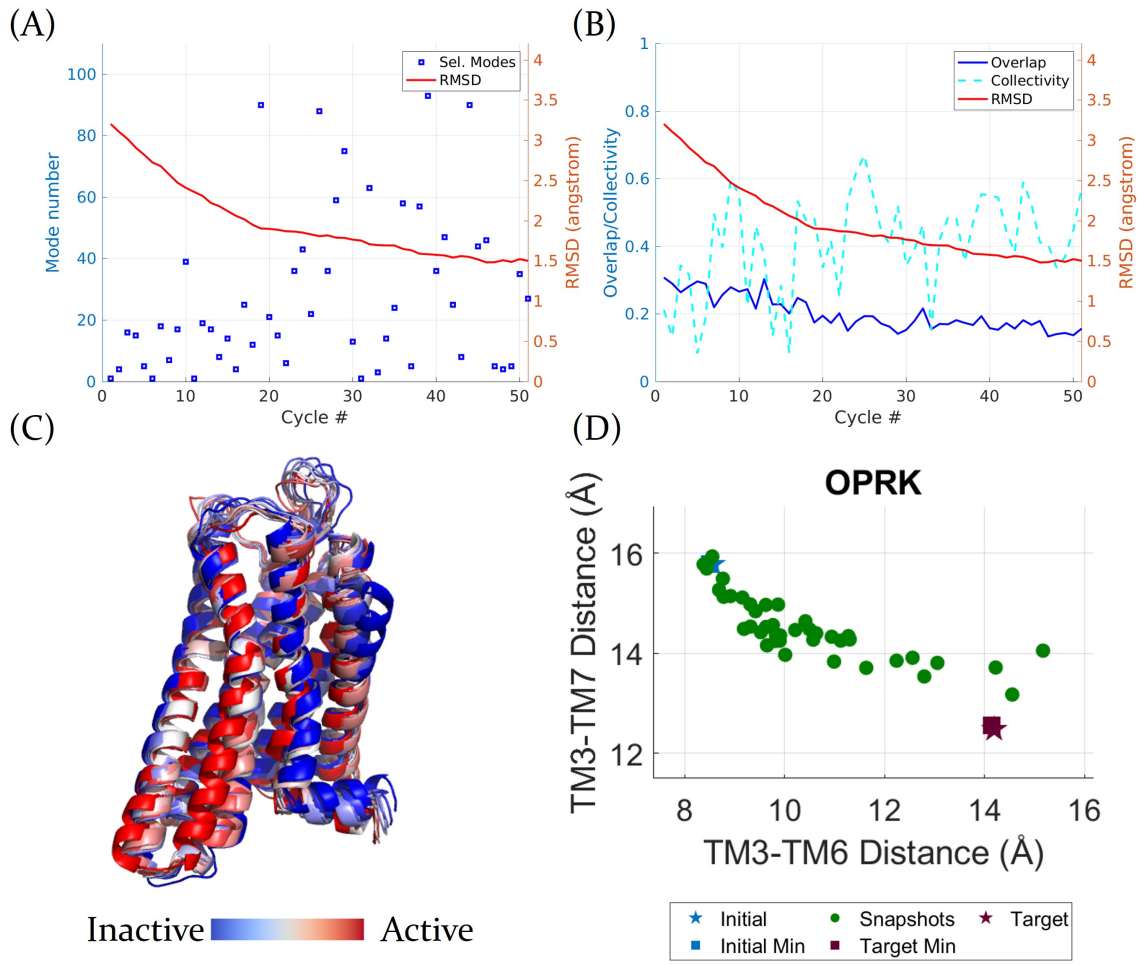

Figure 4.15. ANM-LD simulation of OPRK conformational transition from inactive to active state. (A) RMSD progression. (B) Mode overlap and collectivity of selected ANM modes. (C) Transition snapshots colored from blue (inactive) to red (active). (D) TM3–TM6 and TM3–TM7 distance changes over the simulation.

4.1.10. μ-opioid receptor (OPRM)

To model the conformational transition of OPRM, we performed ANM-LD simulations starting from the inactive crystal structure (PDB ID: 4DKL) and targeting active state (PDB ID: 5C1M). As illustrated in Figure 4.16, (A) RMSD decreased to 1.3 Å, indicating convergence toward the target. (B) Mode overlap and collectivity validated the relevance of selected modes. (C) Snapshots depict a smooth transition from inactive (blue) to active (red). (D) TM3–TM6 and TM3–TM7 distance changes highlight TM6 outward and TM7 inward shifts during activation.

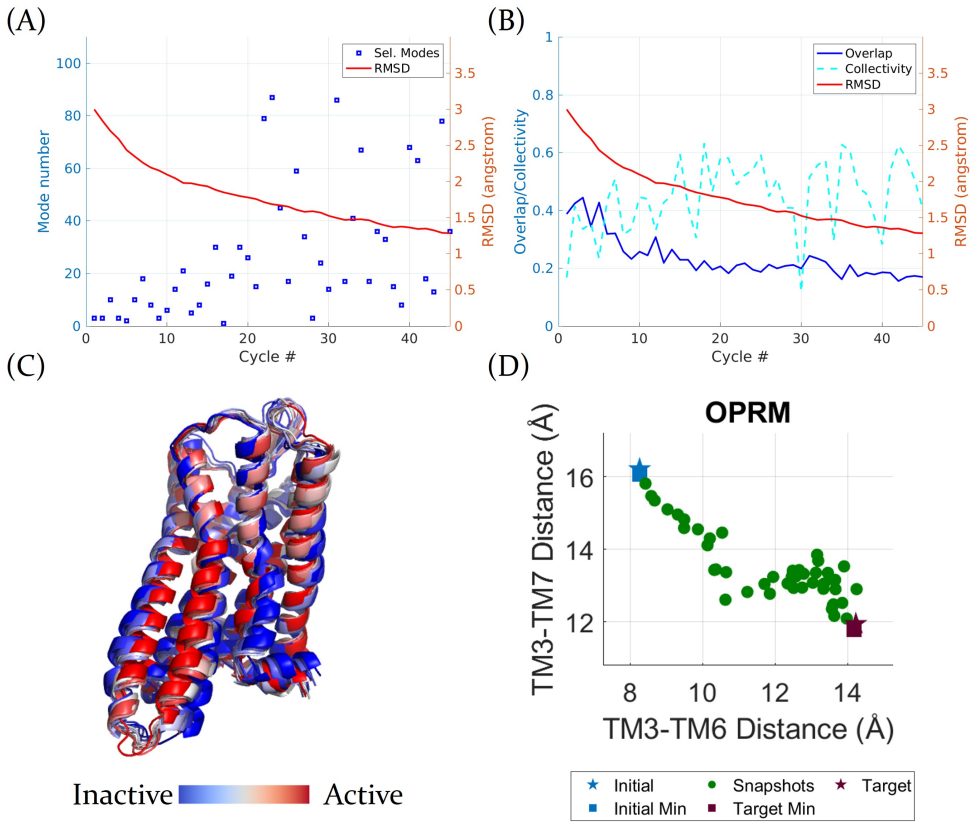

Figure 4.16. ANM-LD simulation of OPRM conformational transition from inactive to active state. (A) RMSD progression. (B) Mode overlap and collectivity of selected ANM modes. (C) Transition snapshots colored from blue (inactive) to red (active). (D) TM3–TM6 and TM3–TM7 distance changes over the simulation.

4.1.11. Adenosine A1 Receptor (AA1R)

To investigate A1R's activation mechanism, ANM-LD simulations were performed starting from the inactive structure (PDB ID: 5UEN) and targeting the G protein-bound active state (PDB ID: 6D9H) As shown in Figure 4.17, (A) the RMSD decreased to 0.8 Å, indicating high-fidelity convergence toward the active conformation. (B) Mode overlap and collectivity analysis confirmed that the selected modes effectively captured functionally relevant motion. (C) Structural snapshots illustrate the progressive transition from the inactive (blue) to active (red) conformation. (D) TM3–TM6 and TM3–TM7 distance profiles reflect hallmark features of GPCR activation, including the outward movement of TM6 and the inward displacement of TM7.

To further evaluate the performance of our ANM-LD simulations, we compared their sampling behavior against a state-of-the-art AI-based generative approach, AlphaFlow, recently developed by Jing et al. (2024) [151]. AlphaFlow fine-tunes AlphaFold models using flow-matching and is trained on molecular dynamics (MD)-derived ensembles to generate diverse conformational states from static structures. For this comparison, we selected the A1R and tracked two key activation markers, TM3–TM6 and TM3–TM7 distances, across the transition ensembles generated by ANM-LD and AlphaFlow.

As shown in Figure 4.18, AlphaFlow (cyan) samples a broader conformational space and reaches equilibrium-like diversity faster than physics-based simulations. However, while AlphaFlow provides enhanced diversity, ANM-LD (red) more accurately captures activation-relevant collective motions—particularly the pronounced outward movement of TM6, a hallmark of GPCR activation. This distinction is evidenced by the separation of ANM-LD samples toward larger TM3–TM6 distances, closely aligning with the known active conformation of A1R. These results suggest that while AlphaFlow may serve as a rapid tool for ensemble generation, physics-based approaches like ANM-LD remain indispensable for mechanistically interpretable sampling of functional transitions.

To evaluate the relevance of our ANM-LD–generated intermediate structures for the adenosine A1 receptor (A1R), we projected them onto the free energy landscape (FEL) derived from metadynamics simulations reported in a recent study of A1R activation [78]. This FEL characterizes the TM6 inward-to-outward transition using two collective variables: the TM6 torsion angle and the intracellular TM3–TM6 distance (Figure 4.19). The TM6 torsion corresponds to the dihedral angle formed by the alpha carbon atoms of L236$^{6.37}$, W247$^{6.48}$, T277$^{7.42}$, and T270$^{7.35}$. For the TM3-TM6 intracellular ends distance, we computed the center of mass (COM) distances between the backbone atoms of TM3(Y226$^{6.27}$, G227$^{6.28}$, K228$^{6.29}$, L230$^{6.30}$, and E230$^{6.31}$) and TM6(R105$^{3.50}$, Y106$^{3.51}$, L107$^{3.52}$, R108$^{3.53}$, and V109$^{3.54}$) [78]. The landscape includes five distinct conformational states, along with experimentally resolved inactive (PDB 5N2S) and active (PDB 6D9H) structures. In our projection, green spheres represent the ANM-LD–generated intermediates, which broadly cover the conformational space between inactive and active states. Our analysis employs a different inactive structure than the original study (shown as a blue square), and its minimized form is shown as a blue diamond. The active structure, however, is identical to the one used in the metadynamics study (PDB 6D9H) and is marked as a pink star, while its minimized version is displayed as a red square. This comparison illustrates that despite differences in the starting point, our ANM-LD intermediates effectively sample a wide range of activation-relevant conformations and align with key low-energy regions of the FEL, supporting their utility in mapping functionally important transitions in A1R.

Our results show that the ANM-LD–generated intermediates approach the region corresponding to State 2 of the metadynamics-derived free energy landscape. However, despite this proximity, the additional outward displacement of TM6 observed in the pre-active state could not be fully captured in our simulations. Nevertheless, we observed that several of our intermediate structures exhibit TM6 torsional changes consistent with those reported for the experimentally derived intermediate conformation in the study. This suggests that while the large-scale outward movement of TM6 may be underrepresented, ANM-LD effectively captures key torsional features associated with functionally relevant transitions.

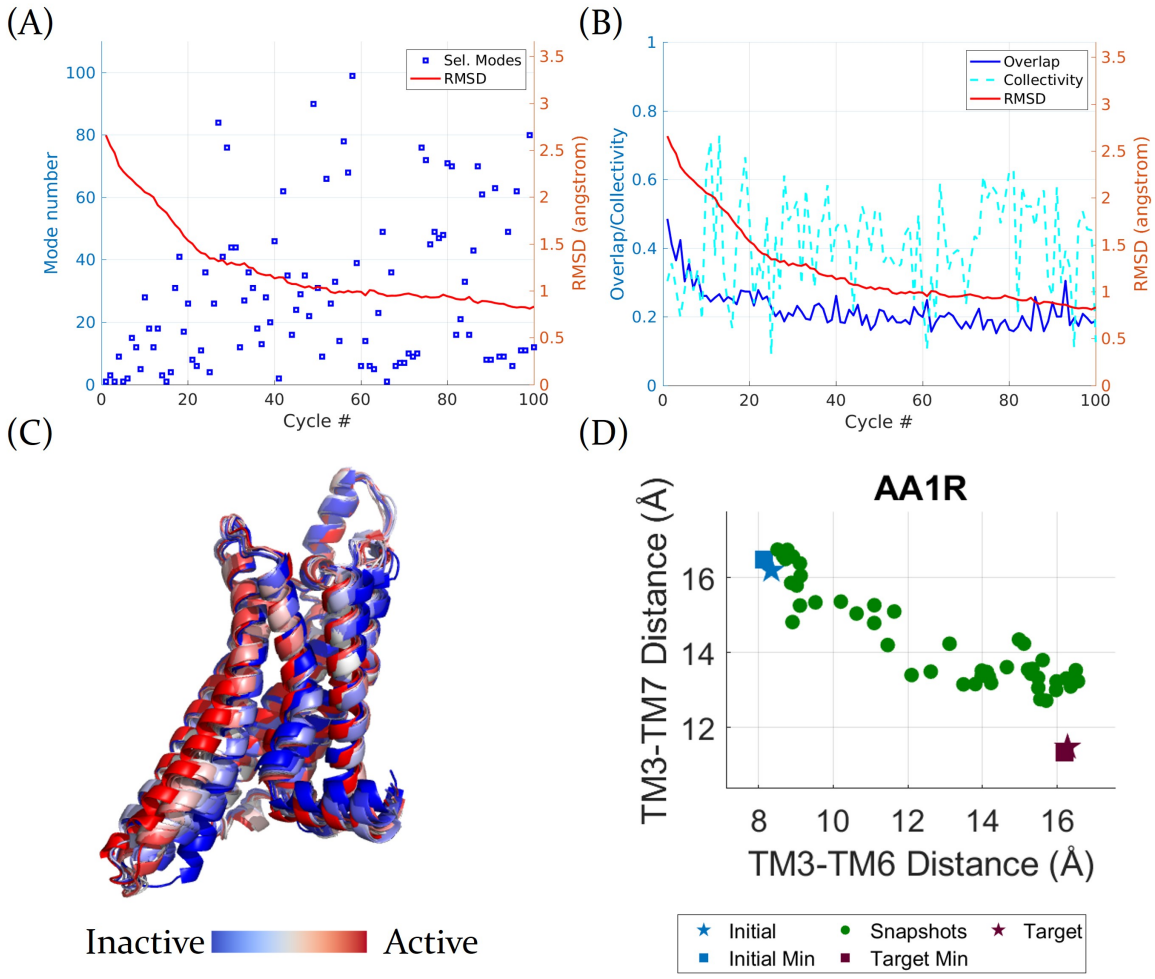

Figure 4.17. ANM-LD simulation of AA1R conformational transition from inactive to active state. (A) RMSD progression. (B) Mode overlap and collectivity of selected ANM modes. (C) Transition snapshots colored from blue (inactive) to red (active). (D) TM3–TM6 and TM3–TM7 distance changes over the simulation.

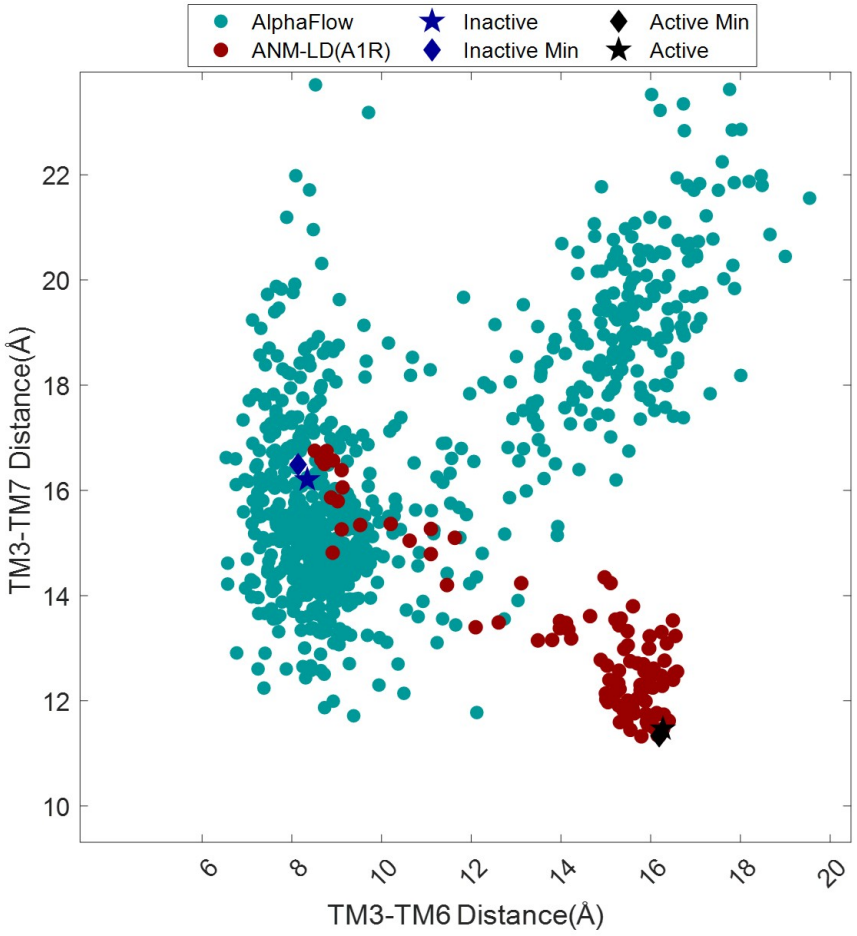

Figure 4.18. Comparison of the conformational sampling capabilities of the physics-based ANM-LD method and the AI-driven AlphaFlow algorithm on the A1R activation.Red dots represent ANM-LD intermediate structures, while cyan dots correspond to AlphaFlow-generated conformers. Static experimental structures (stars) and minimized endpoints (squares) are included for reference.

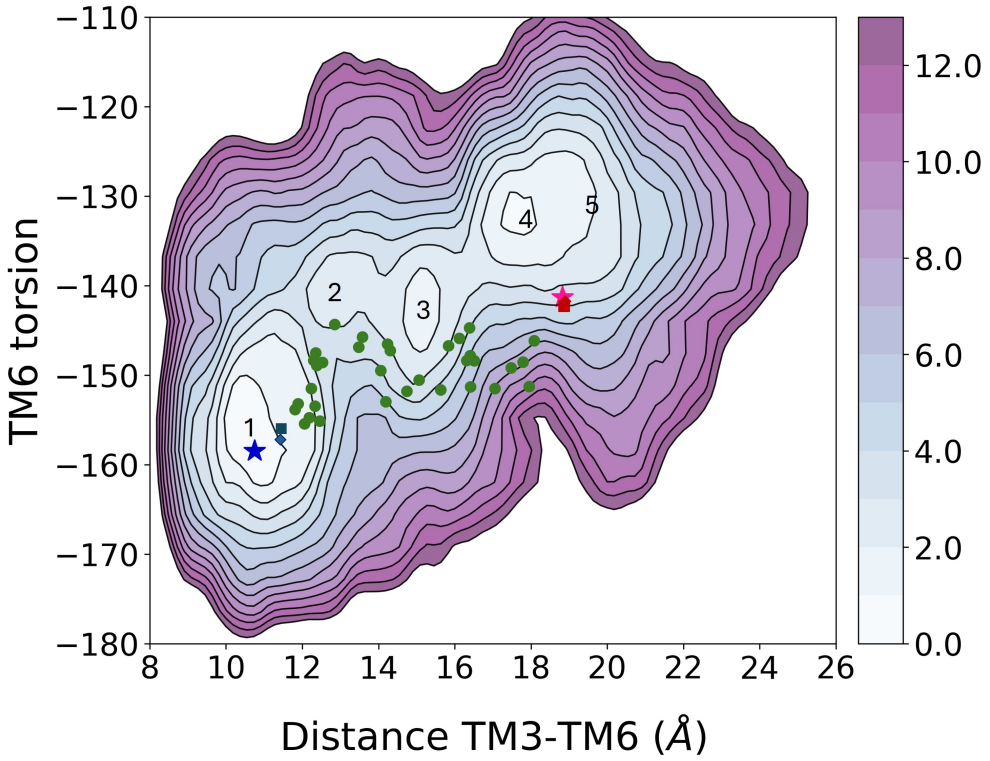

Figure 4.19. Projection of ANM-LD–generated intermediate structures onto the free energy landscape (FEL) of adenosine A1 receptor (A1R) activation, adapted from metadynamics simulations.The FEL was constructed using TM6 torsion angles and TM3–TM6 intracellular distances, capturing key conformational states along the A1R activation pathway.

4.1.12. Adenosine A2A receptor (AA2AR)

To model its conformational transition, ANM-LD simulations were performed starting from the inactive state (PDB ID: 5MZP) and targeting the G protein-bound active conformation (PDB ID: 5G53). As illustrated in Figure 4.20, (A) the RMSD decreased to 1.4 Å over the course of the simulation, demonstrating reliable convergence toward the active state. (B) Mode overlap and collectivity analysis validated the selection of effective transition modes. (C) Structural morphs show a clear transition from the inactive (blue) to active (red) state. (D) TM3–TM6 and TM3–TM7 distance profiles exhibit expected changes, consistent with A2AR activation dynamics.

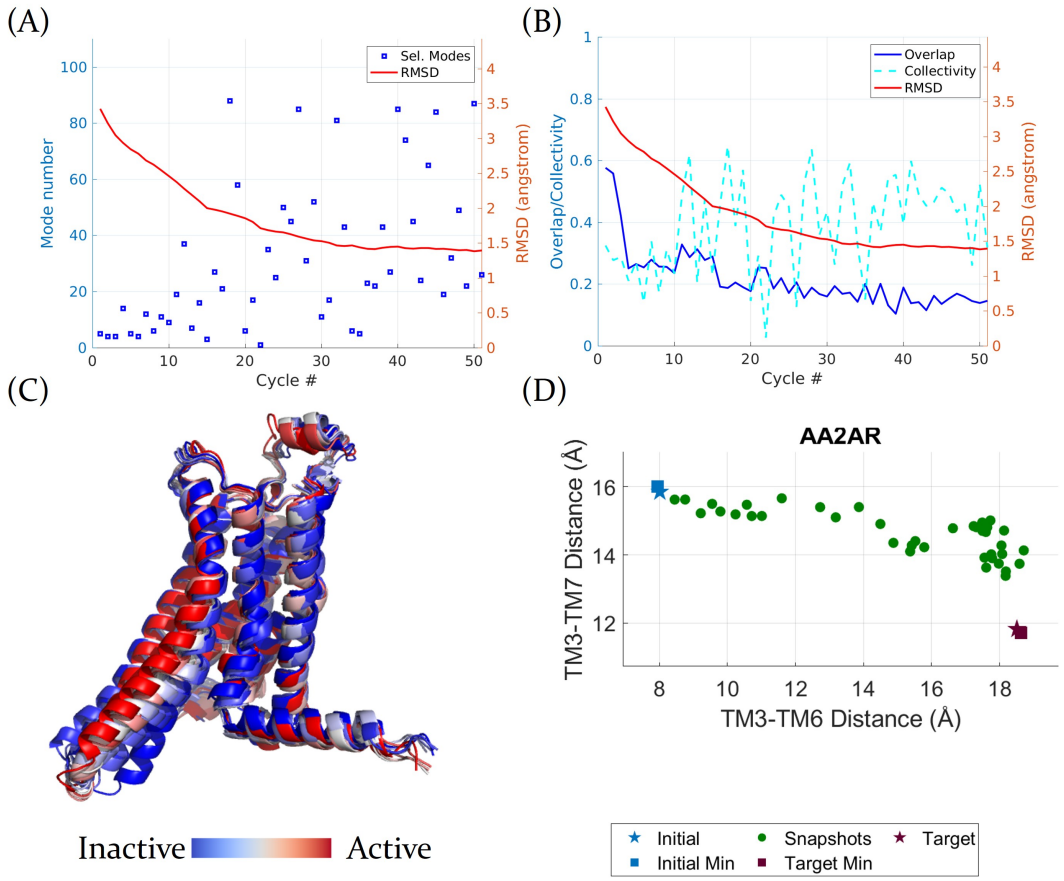

Figure 4.20. ANM-LD simulation of AA2AR conformational transition from inactive to active state. (A) RMSD progression. (B) Mode overlap and collectivity of selected ANM modes. (C) Transition snapshots colored from blue (inactive) to red (active). (D) TM3–TM6 and TM3–TM7 distance changes over the simulation.

4.1.13. Adenosine A2B receptor (AA2BR)

As no experimentally resolved inactive structure currently exists for AA2BR, we utilized an AlphaFold2-predicted model from GPCRdb [42] as the starting conformation for ANM-LD simulations. The transition was modeled toward the G protein-bound active state (PDB ID: 8HDP). As presented in Figure 4.21, (A) RMSD decreased to 1.2 Å, indicating a successful transition toward the active conformation. (B) Mode overlap and collectivity analyses confirmed the effectiveness of the selected modes in producing

biologically meaningful motion. (C) Structural morphs depict a smooth progression from the predicted inactive state (blue) to the active structure (red). (D) TM3–TM6 and TM3–TM7 distance profiles show activation-consistent changes, supporting the validity of the modeled transition.

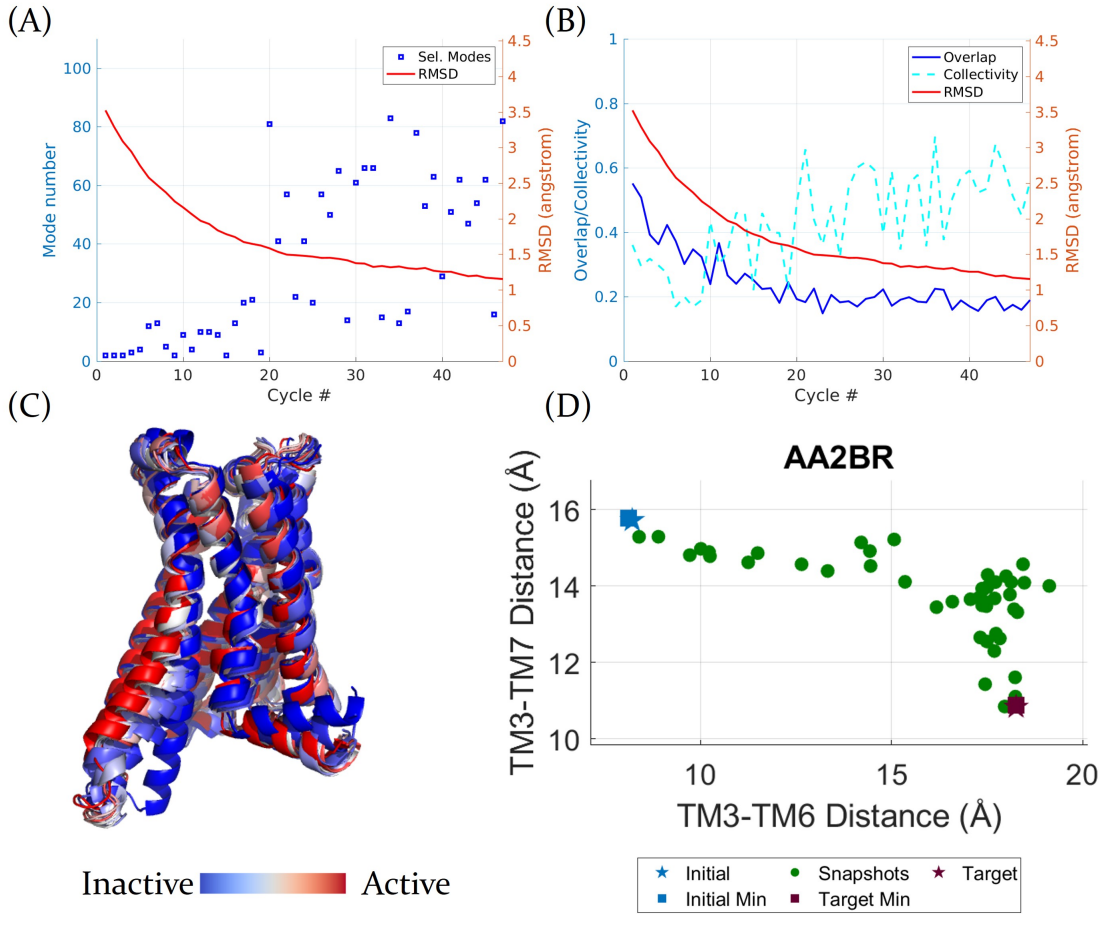

Figure 4.21. ANM-LD simulation of AA2BR conformational transition from inactive to active state. (A) RMSD progression. (B) Mode overlap and collectivity of selected ANM modes. (C) Transition snapshots colored from blue (inactive) to red (active). (D) TM3–TM6 and TM3–TM7 distance changes over the simulation.

4.1.14. Purinergic Receptor 1 (P2RY1)

Due to the lack of an experimentally resolved inactive structure for P2RY1, we used the AlphaFold Multistate model from GPCRdb [42] as the starting conformation, with the G protein-bound structure (PDB ID: 7XXH) serving as the active target in ANM-LD simulations.target structure was the G protein-bound state (PDB ID: 7XXH).

As shown in Figure 4.22, (A) RMSD decreased to 1.6 Å during the simulation. (B) Mode overlap and collectivity confirmed biologically relevant modes. (C) Structural morphs illustrate the conformational transition from the predicted inactive state (blue) to the G protein-bound active state (red). (D) TM3–TM6 and TM3–TM7 distances reflect activation-associated changes.

4.1.15. Purinergic Receptor 12 (P2Y12)

Due to the lack of an inactive structure for P2Y12, the AlphaFold Multistate model from GPCRdb [42] was used as the initial state and 7XXI as the active target in ANM-LD simulations.

As shown in Figure 4.23, (A) RMSD decreased to 1.7 Å, indicating a well-resolved conformational transition. (B) Mode overlap and collectivity analysis confirmed that the selected ANM modes captured coherent and biologically relevant dynamics. (C) Structural morphs show the progression from the AlphaFold2-predicted inactive state (blue) to the active conformation (red). (D) TM3–TM6 and TM3–TM7 distance profiles reveal conformational changes associated with P2Y12 activation.

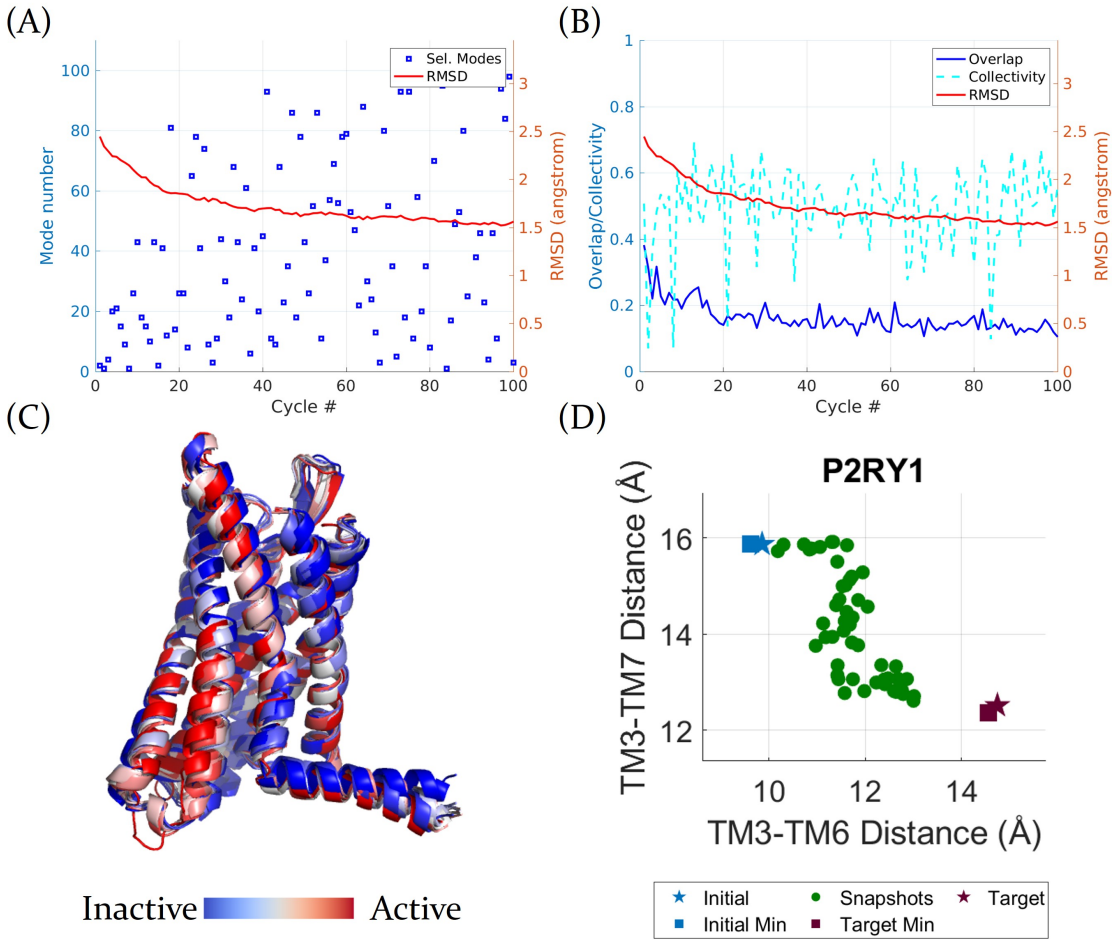

Figure 4.22. ANM-LD simulation of P2RY1 conformational transition from inactive to active state. (A) RMSD progression. (B) Mode overlap and collectivity of selected ANM modes. (C) Transition snapshots colored from blue (inactive) to red (active). (D) TM3–TM6 and TM3–TM7 distance changes over the simulation.

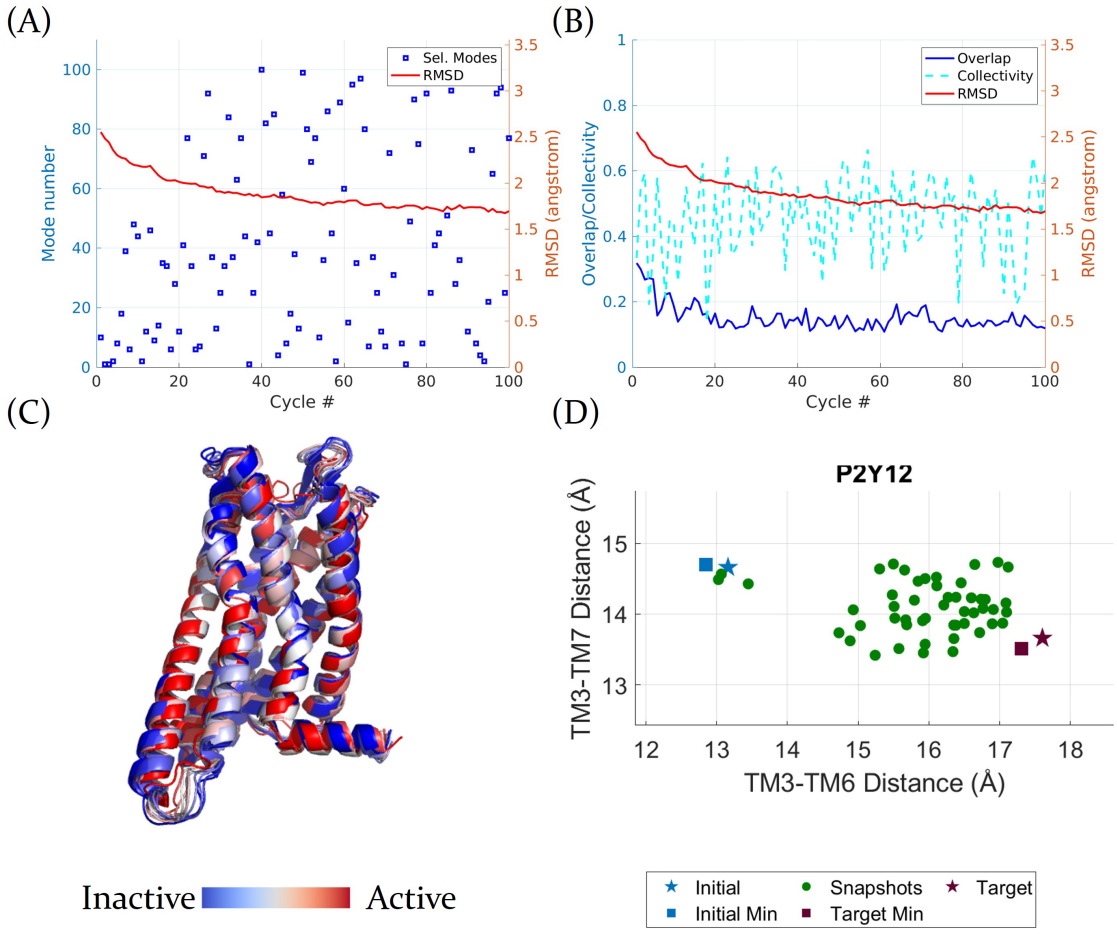

Figure 4.23. ANM-LD simulation of P2Y12 conformational transition from inactive to active state. (A) RMSD progression. (B) Mode overlap and collectivity of selected ANM modes. (C) Transition snapshots colored from blue (inactive) to red (active). (D) TM3–TM6 and TM3–TM7 distance changes over the simulation.

4.1.16. Cannabinoid Receptor 1 (CNR1)

To explore the conformational activation of CNR1, ANM-LD simulations were performed starting from the inactive state (PDB ID: 5TGZ) and targeting the active conformation (PDB ID: 5XRA). As shown in Figure 4.24, (A) the RMSD decreased to 1.4 Å, demonstrating successful structural convergence. (B) Mode overlap and collectivity values confirmed that the selected modes captured biologically relevant transition dynamics. (C) Structural morphs illustrate the conformational change from

the inactive (blue) to the active (red) state. (D) TM3–TM6 and TM3–TM7 distance profiles reflect hallmark activation features, including TM6 outward movement and TM7 rearrangement.

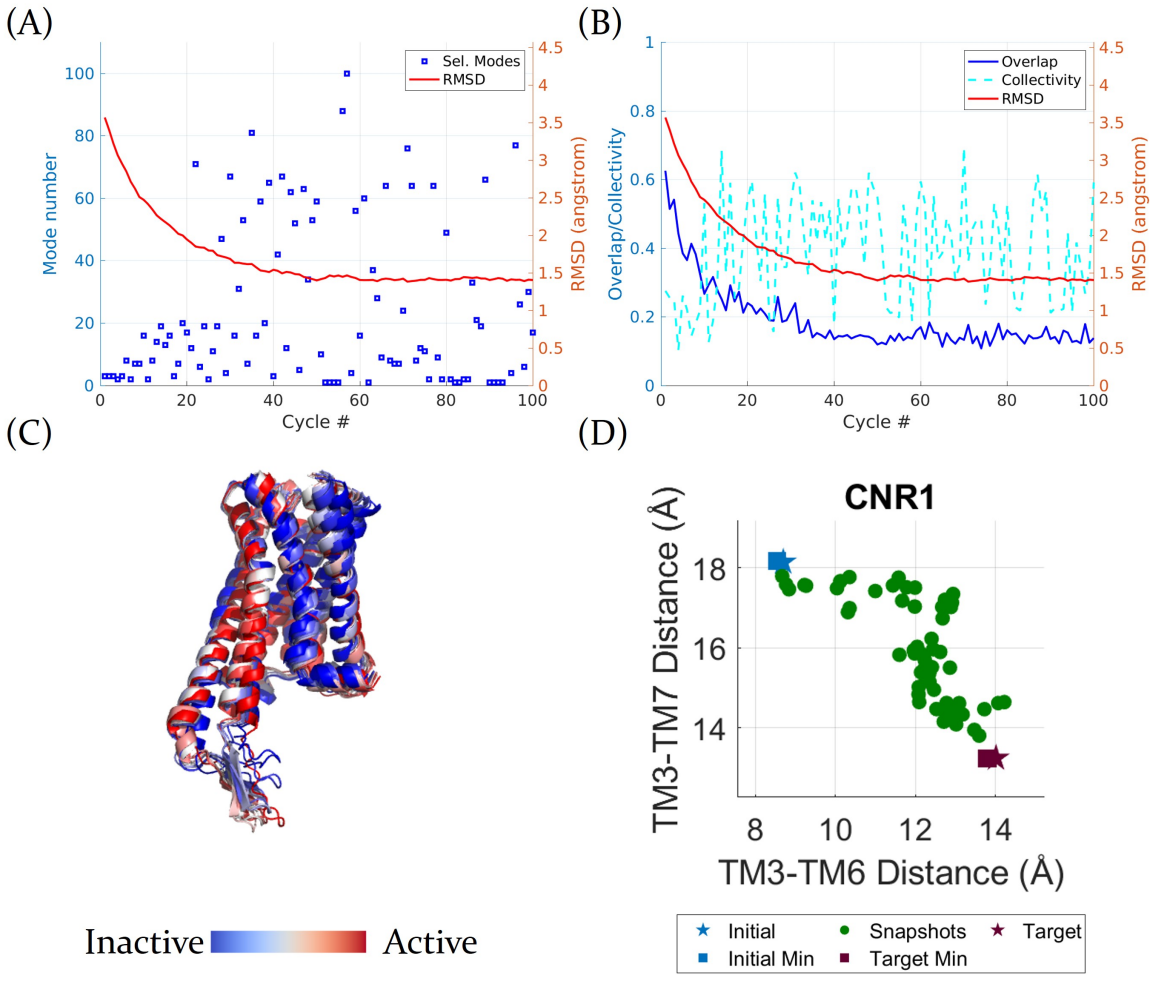

Figure 4.24. ANM-LD simulation of CNR1 conformational transition from inactive to active state. (A) RMSD progression. (B) Mode overlap and collectivity of selected ANM modes. (C) Transition snapshots colored from blue (inactive) to red (active). (D) TM3–TM6 and TM3–TM7 distance changes over the simulation.

4.1.17. Prostaglandin D_2 Receptor 2 (PD2R2)

Because no experimentally resolved active-state structure of PD2R2 is available, we performed ANM-LD simulations using the inactive crystal structure (PDB ID: 7M8W) as the starting point and the AlphaFold Multistate model from GPCRdb [42] as the predicted active conformation. As shown in 4.25, (A) RMSD decreased to 1.2 Å, indicating successful structural convergence. (B) Mode overlap and collectivity values confirmed that the selected ANM modes captured coherent and functionally relevant dynamics. (C) Structural snapshots illustrate the progression from inactive (blue) to active (red) conformation. (D) TM3–TM6 and TM3–TM7 distance changes reflect structural rearrangements consistent with canonical GPCR activation.

4.1.18. Thromboxane A_2 Receptor TA2R

To investigate the conformational transition of TA2R, ANM-LD simulations were performed from the inactive structure (PDB ID: 6IIU) to the active, G protein-bound conformation (PDB ID: 8XJO). As shown in Figure 4.26, (A) the RMSD decreased to 1.5 Å, indicating robust structural convergence. (B) Mode overlap and collectivity values confirm that the selected ANM modes effectively represent functional transition dynamics. (C) Structural morphs display the transition from inactive (blue) to active (red) conformations. (D) TM3–TM6 and TM3–TM7 distance changes illustrate canonical activation-associated rearrangements, including intracellular opening and TM7 repositioning.

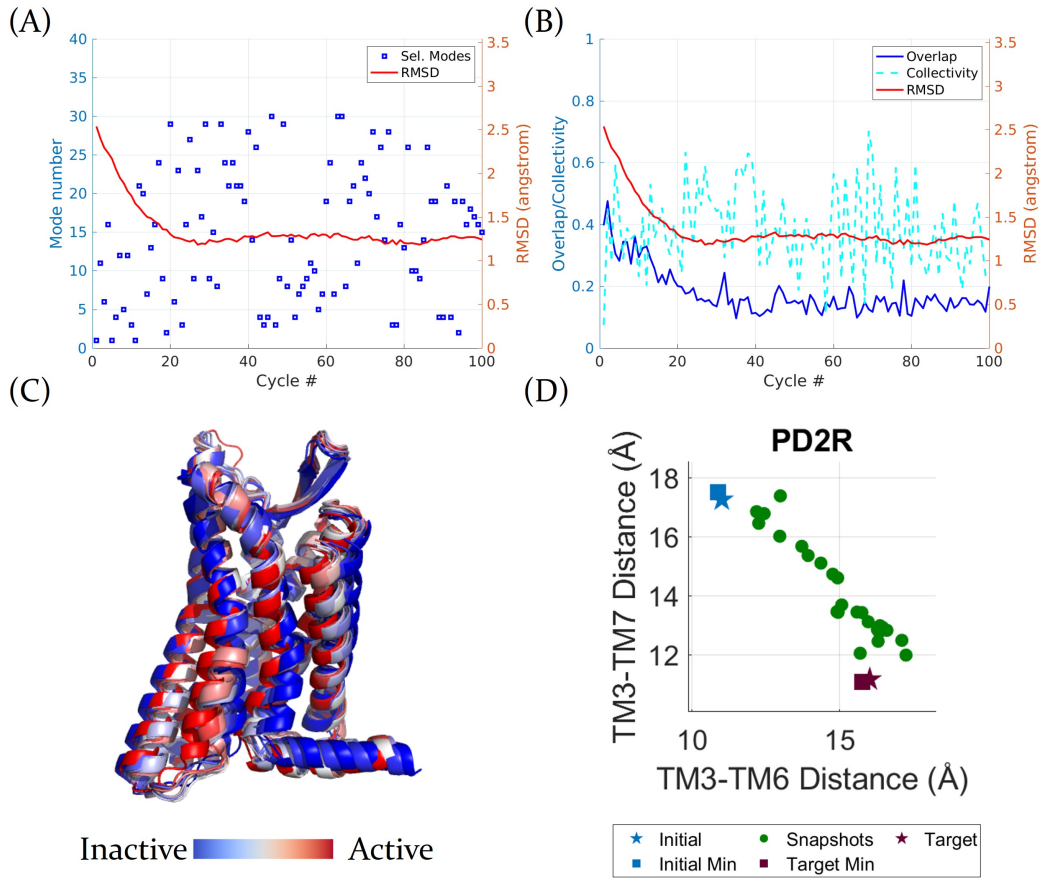

Figure 4.25. ANM-LD simulation of PD2R2 conformational transition from inactive to active state. (A) RMSD progression. (B) Mode overlap and collectivity of selected ANM modes. (C) Transition snapshots colored from blue (inactive) to red (active). (D) TM3–TM6 and TM3–TM7 distance changes over the simulation.

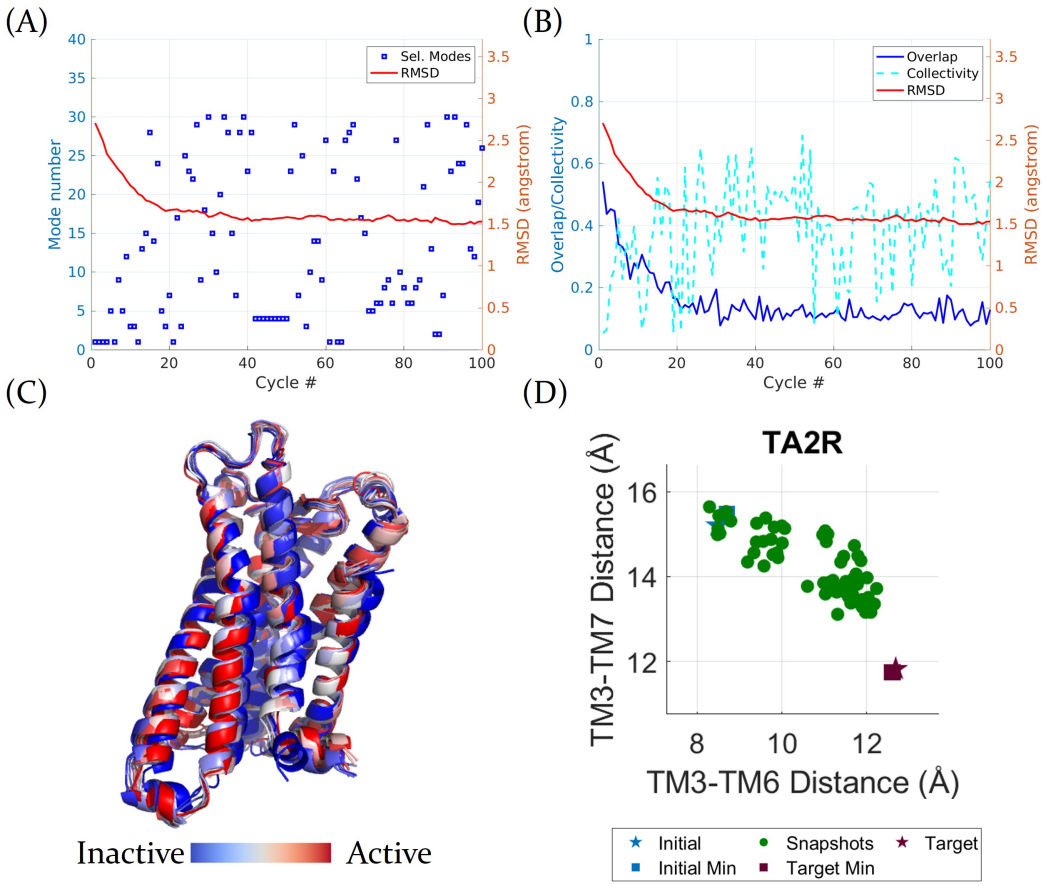

Figure 4.26. ANM-LD simulation of TA2R conformational transition from inactive to active state. (A) RMSD progression. (B) Mode overlap and collectivity of selected ANM modes. (C) Transition snapshots colored from blue (inactive) to red (active). (D) TM3–TM6 and TM3–TM7 distance changes over the simulation.

4.1.19. Lysophosphatidic Acid Receptor 1 (LPAR1)

To investigate the activation mechanism of LPAR1, ANM-LD simulations were performed using the inactive structure (PDB ID: 4Z34) as the starting conformation and targeting the G protein-bound active structure (PDB ID: 7YU3). As shown in Figure 4.27, (A) the RMSD decreased to 1.5 Å, indicating strong structural convergence. (B) Mode overlap and collectivity metrics validated the selection of functionally relevant ANM modes. (C) Structural morphs display a gradual transition from inactive

(blue) to active (red) conformations. (D) TM3–TM6 and TM3–TM7 distance profiles reflect characteristic GPCR activation features, including the outward movement of TM6 and rearrangement of TM7.

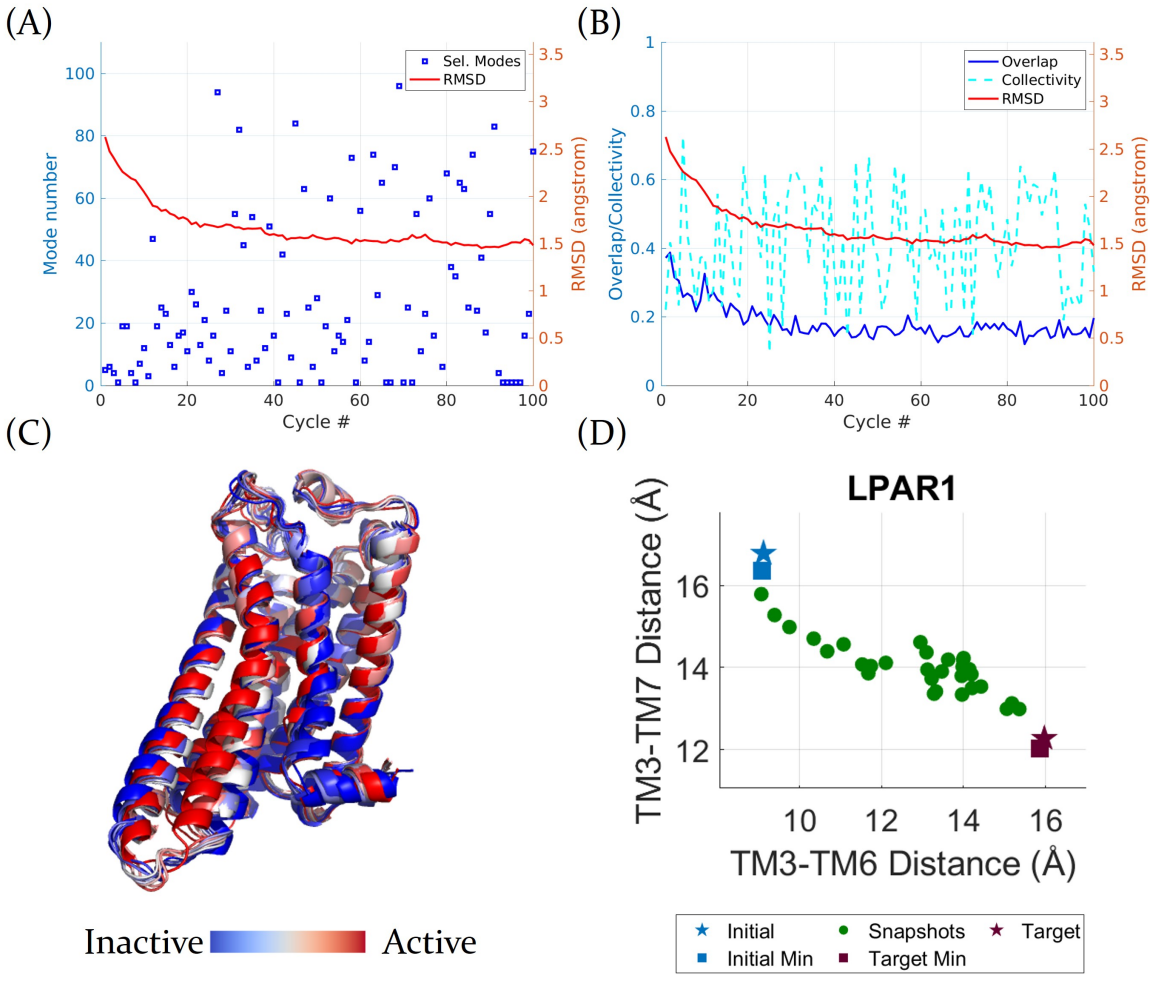

Figure 4.27. ANM-LD simulation of LPAR1 conformational transition from inactive to active state. (A) RMSD progression. (B) Mode overlap and collectivity of selected ANM modes. (C) Transition snapshots colored from blue (inactive) to red (active). (D) TM3–TM6 and TM3–TM7 distance changes over the simulation.

4.1.20. Sphingosine-1-phosphate receptor 1 (S1PR1)

In the absence of an experimentally resolved inactive structure, we used the AlphaFold2-predicted model from GPCRdb [42] as the starting conformation in ANM-LD simulations. The active target was defined as the G protein-bound structure (PDB ID: 8G94). As shown in Figure 4.28, (A) RMSD decreased to 1.3 Å, indicating a successful and stable transition toward the active conformation. (B) Mode overlap and collectivity analyses support the biological relevance of the selected ANM modes. (C) Structural morphs display the transition from the predicted inactive (blue) to the experimentally resolved active (red) conformation. (D) TM3–TM6 and TM3–TM7 distance profiles highlight structural changes consistent with canonical GPCR activation.

4.1.21. C-C chemokine receptor 1 (CCR1)

In the absence of an experimentally resolved inactive-state structure, we employed the AlphaFold2 model from GPCRdb as the starting conformation in ANM-LD simulations. The active-state target was defined using the G protein-bound structure (PDB ID: 7VLA). As shown in Figure 4.29, (A) RMSD decreased to 1.0 Å, indicating excellent convergence toward the active conformation. (B) Mode overlap and collectivity values support the use of selected modes to capture the biologically relevant transition. (C) Structural morphs illustrate the progressive transformation from the predicted inactive state (blue) to the active state (red). (D) TM3–TM6 and TM3–TM7 distance profiles reveal hallmark structural changes consistent with CCR1 activation.

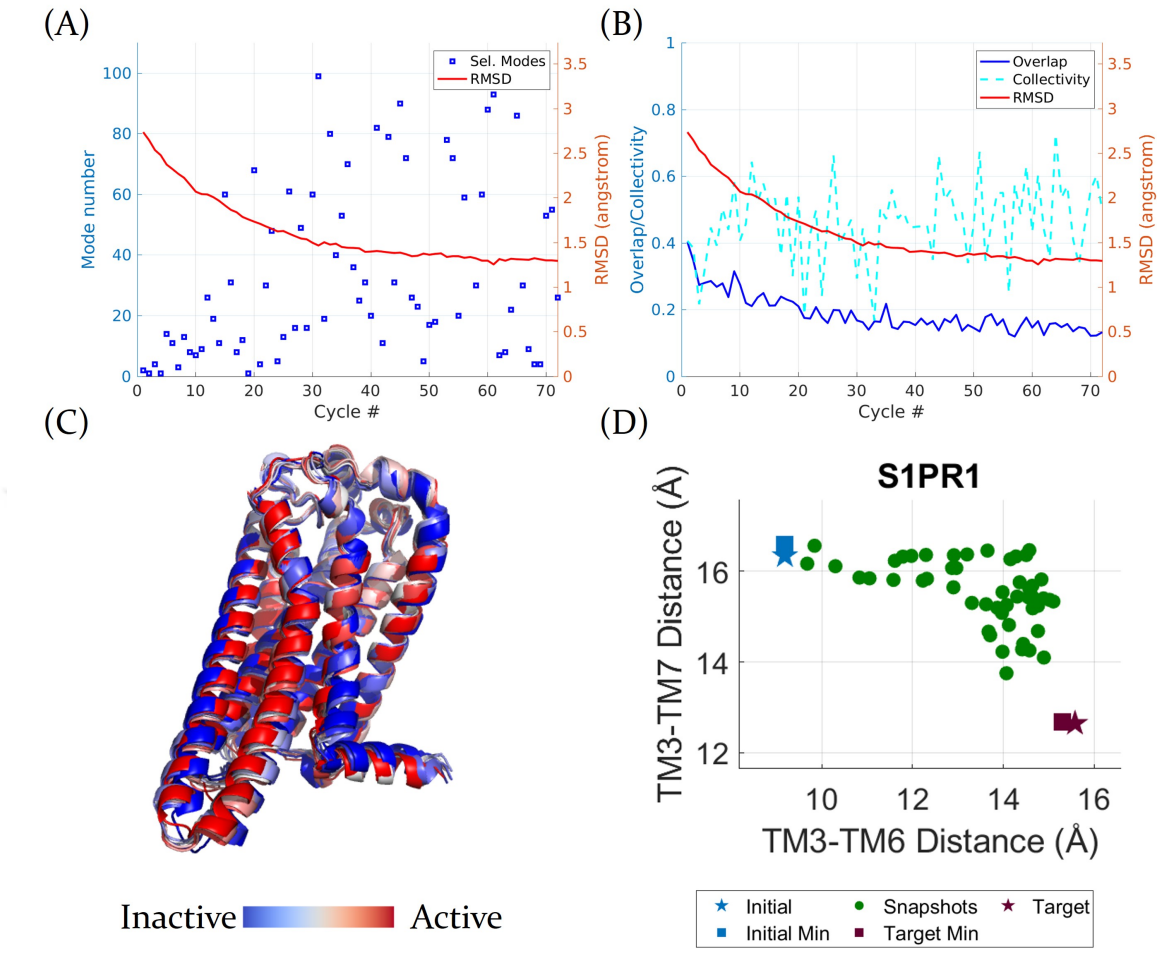

Figure 4.28. ANM-LD simulation of S1PR1 conformational transition from inactive to active state. (A) RMSD progression. (B) Mode overlap and collectivity of selected ANM modes. (C) Transition snapshots colored from blue (inactive) to red (active). (D) TM3–TM6 and TM3–TM7 distance changes over the simulation.

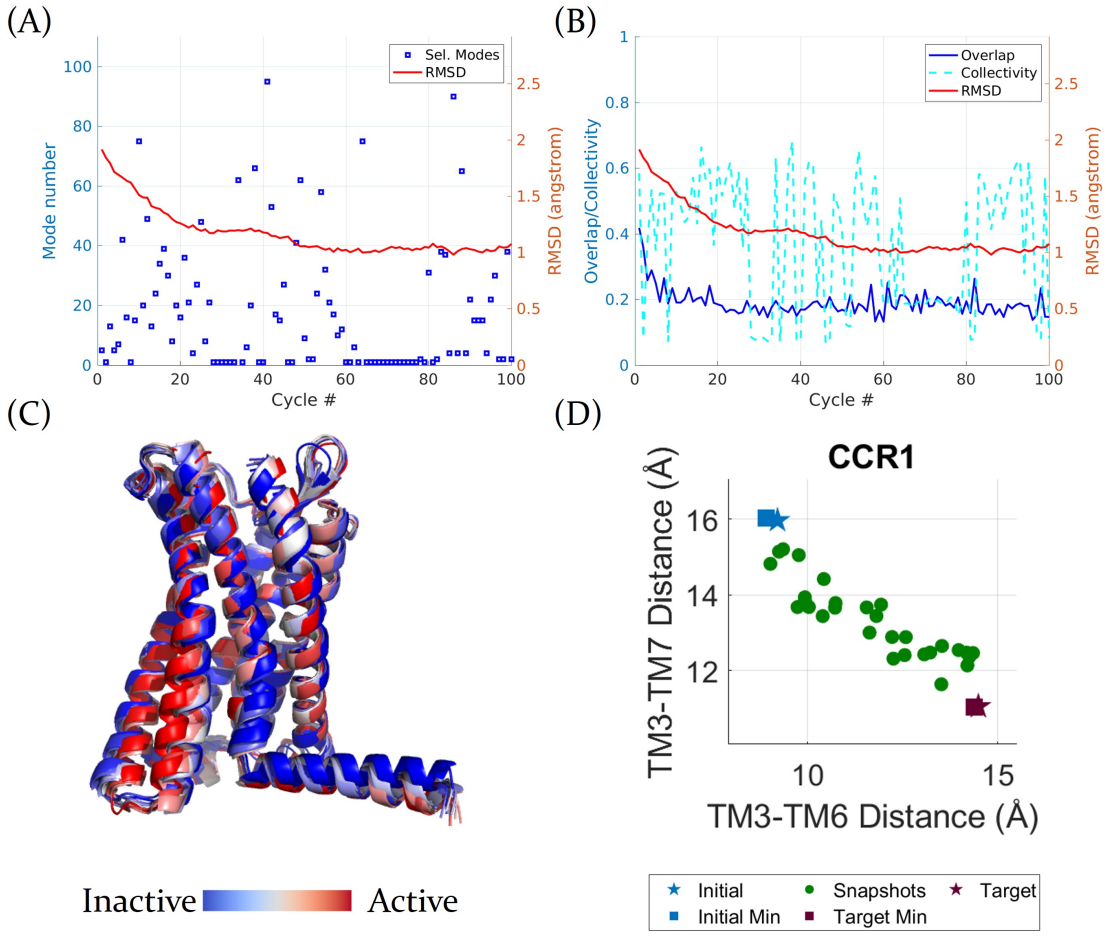

Figure 4.29. ANM-LD simulation of CCR1 conformational transition from inactive to active state. (A) RMSD progression. (B) Mode overlap and collectivity of selected ANM modes. (C) Transition snapshots colored from blue (inactive) to red (active). (D) TM3–TM6 and TM3–TM7 distance changes over the simulation.

4.1.22. C-C chemokine receptor 5 (CCR5)

To investigate the conformational activation of CCR5, ANM-LD simulations were performed starting from the inactive crystal structure (PDB ID: 6AKY) and targeting the G protein-bound active conformation (PDB ID: 7O7F). As presented in Figure 4.30, (A) RMSD decreased to 1.1 Å, indicating effective convergence toward the target active structure. (B) Mode overlap and collectivity analysis confirmed that the selected ANM modes captured coherent and biologically relevant transition dynamics. (C)

Structural morphs illustrate the transition from the inactive (blue) to the active (red) conformation. (D) TM3–TM6 and TM3–TM7 distance profiles highlight hallmark rearrangements associated with GPCR activation, supporting the functional validity of the modeled transition.

To further validate the biological relevance of ANM-LD–derived conformational transitions, we compared the ANM-LD trajectory with a long (1.5 μs) MD simulation of the CCR5 receptor [32], initiated from the inactive state (PDB ID: 6AKY) 4.31. TM3–TM6 and TM3–TM7 distances were selected as functional activation metrics to visualize the conformational space. While MD extensively sampled a dense, localized cloud around the initial structure, ANM-LD produced a directed transition pathway leading toward the active conformation (PDB ID: 7O7F), effectively capturing large-scale structural rearrangements such as TM6 displacement. This example highlights the ability of ANM-LD to explore functionally important transitions that remain inaccessible to conventional MD within feasible timescales.

4.1.23. C-C Chemokine Receptor 8 (CCR8)

In the absence of an experimentally resolved inactive structure, we used an AlphaFold2-predicted model from GPCRdb (Pándy-Szekeres et al., 2023) as the starting conformation for ANM-LD simulations. The transition was modeled toward the active, G protein-bound state (PDB ID: 8KFX). As shown in Figure 4.32, (A) RMSD decreased to 0.9 Å, demonstrating excellent convergence toward the target active conformation. (B) Mode overlap and collectivity metrics confirmed the biological plausibility of the selected transition modes. (C) Structural morphs depict the transition from the predicted inactive (blue) to the active (red) state. (D) TM3–TM6 and TM3–TM7 distance changes reflect key structural rearrangements associated with GPCR activation, including intracellular cavity expansion and TM7 repositioning.

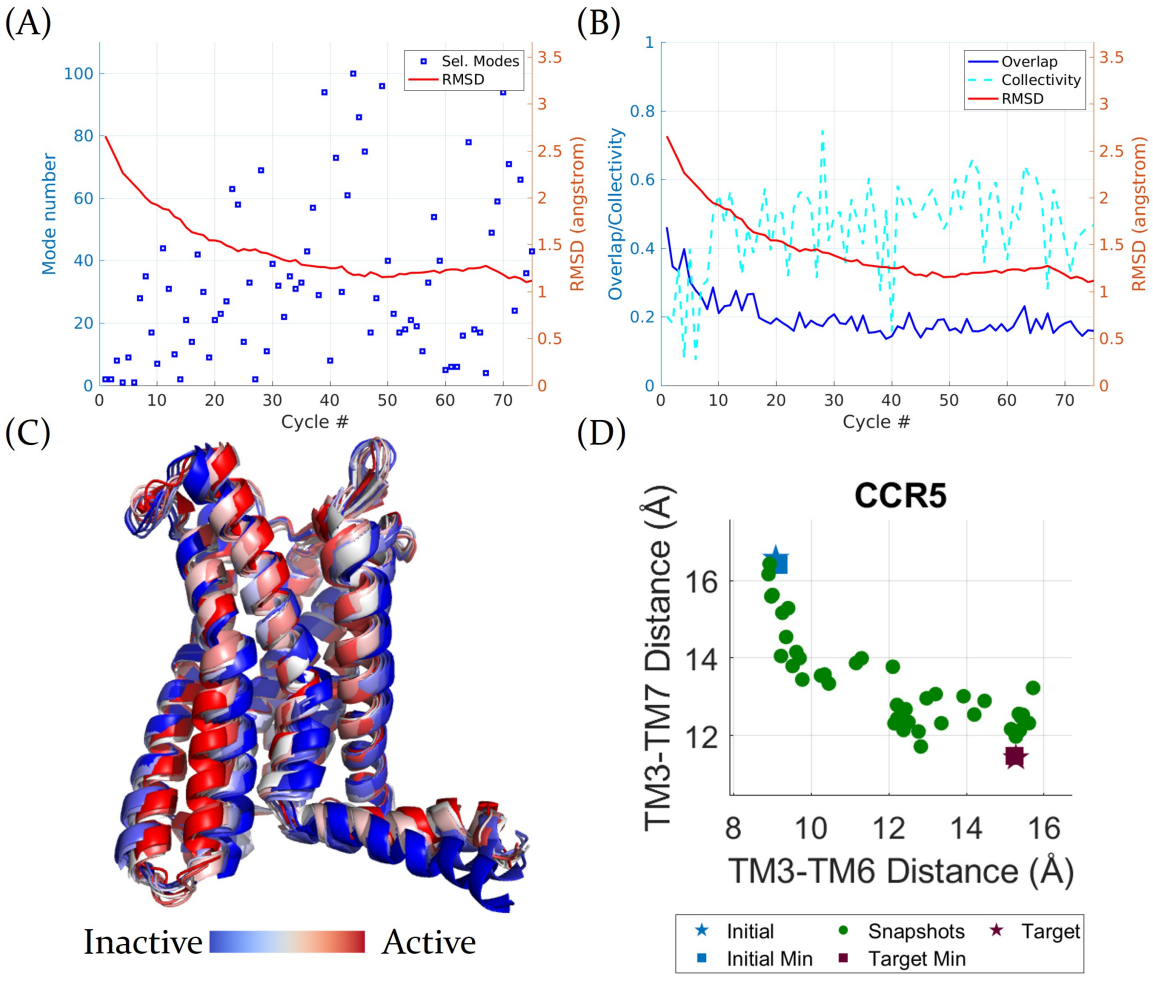

Figure 4.30. ANM-LD simulation of CCR5 conformational transition from inactive to active state. (A) RMSD progression. (B) Mode overlap and collectivity of selected ANM modes. (C) Transition snapshots colored from blue (inactive) to red (active). (D) TM3–TM6 and TM3–TM7 distance changes over the simulation.

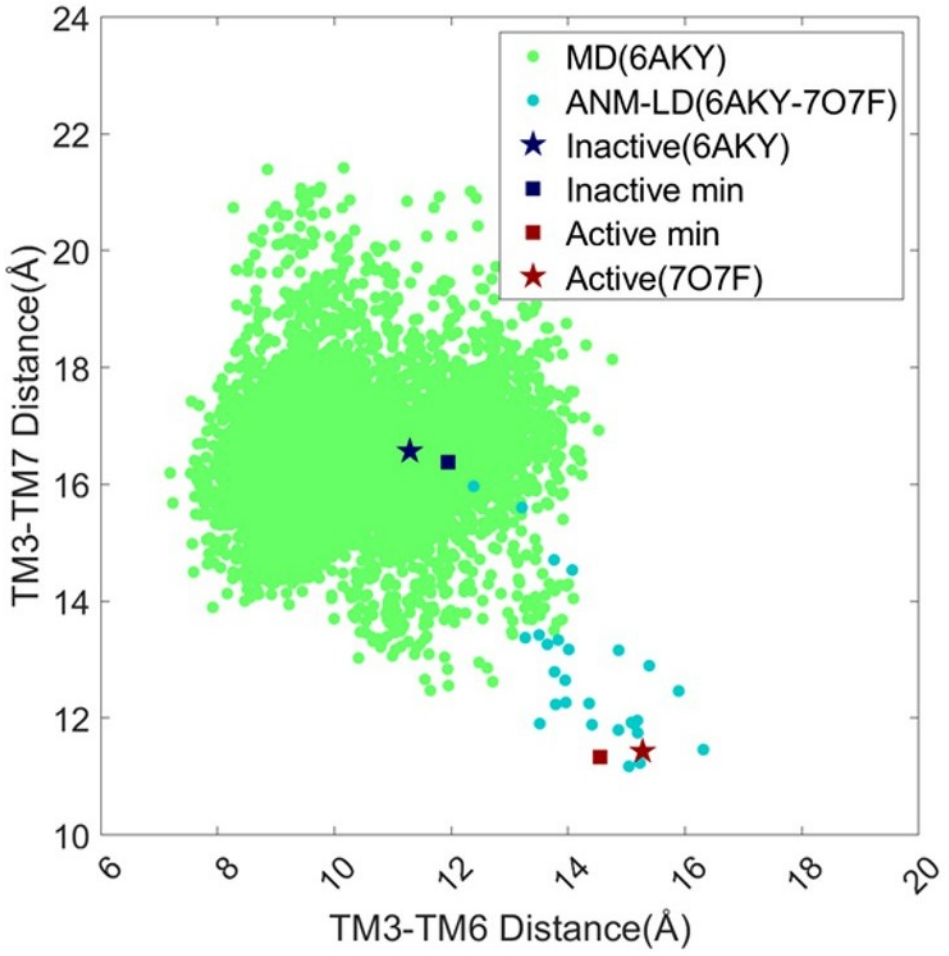

Figure 4.31. Comparison of ANM-LD and MD sampling for the CCR5 receptor. Functionally relevant TM3–TM6 and TM3–TM7 distances are plotted for structures generated from a 1.5 μs MD simulation (green points, starting from 6AKY) and ANM-LD trajectory (cyan points, interpolating from 6AKY to 7O7F).

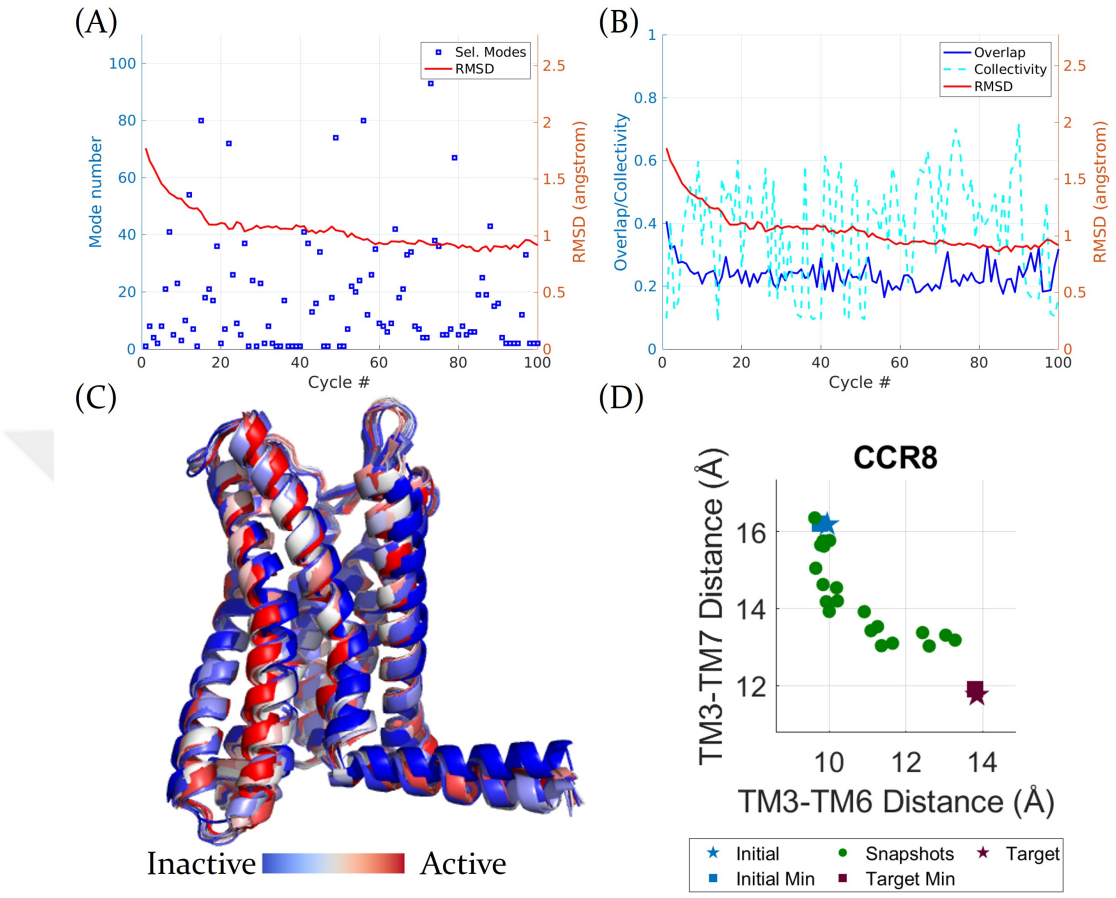

Figure 4.32. ANM-LD simulation of CCR8 conformational transition from inactive to active state. (A) RMSD progression. (B) Mode overlap and collectivity of selected ANM modes. (C) Transition snapshots colored from blue (inactive) to red (active). (D) TM3–TM6 and TM3–TM7 distance changes over the simulation.

4.1.24. C-X-C Chemokine Receptor 2 (CXCR2)

To explore the conformational activation of CXCR2, ANM-LD simulations were performed starting from the inactive structure (PDB ID: 6LFL) and targeting the G protein-bound active conformation (PDB ID: 6LFM). As shown in Figure 4.33, (A) RMSD decreased to 1.8 Å, indicating moderate but consistent structural convergence. (B) Mode overlap and collectivity metrics support the functional plausibility of the

simulated transition. (C) Structural morphs illustrate the conformational change from the inactive (blue) to active (red) state. (D) TM3–TM6 and TM3–TM7 distance profiles demonstrate characteristic GPCR activation movements, including intracellular opening and TM7 rearrangement.

4.1.25. C-X-C Chemokine Receptor 4 (CXCR4)

Due to the lack of an experimentally determined inactive-state structure, ANM-LD simulations were performed using the AlphaFold2 model from GPCRdb [42] as the starting conformation and targeting the G protein-bound active state (PDB ID: 8U4N). As illustrated in Figure 4.34, (A) the RMSD decreased to 1.0 Å, demonstrating highly accurate structural convergence. (B) Mode overlap and collectivity values supported the selection of biologically meaningful modes. (C) Structural morphs show the progression from the AlphaFold2-predicted inactive conformation (blue) to the active conformation (red). (D) TM3–TM6 and TM3–TM7 distance profiles reflect hallmark activation features, including intracellular opening and TM7 repositioning.

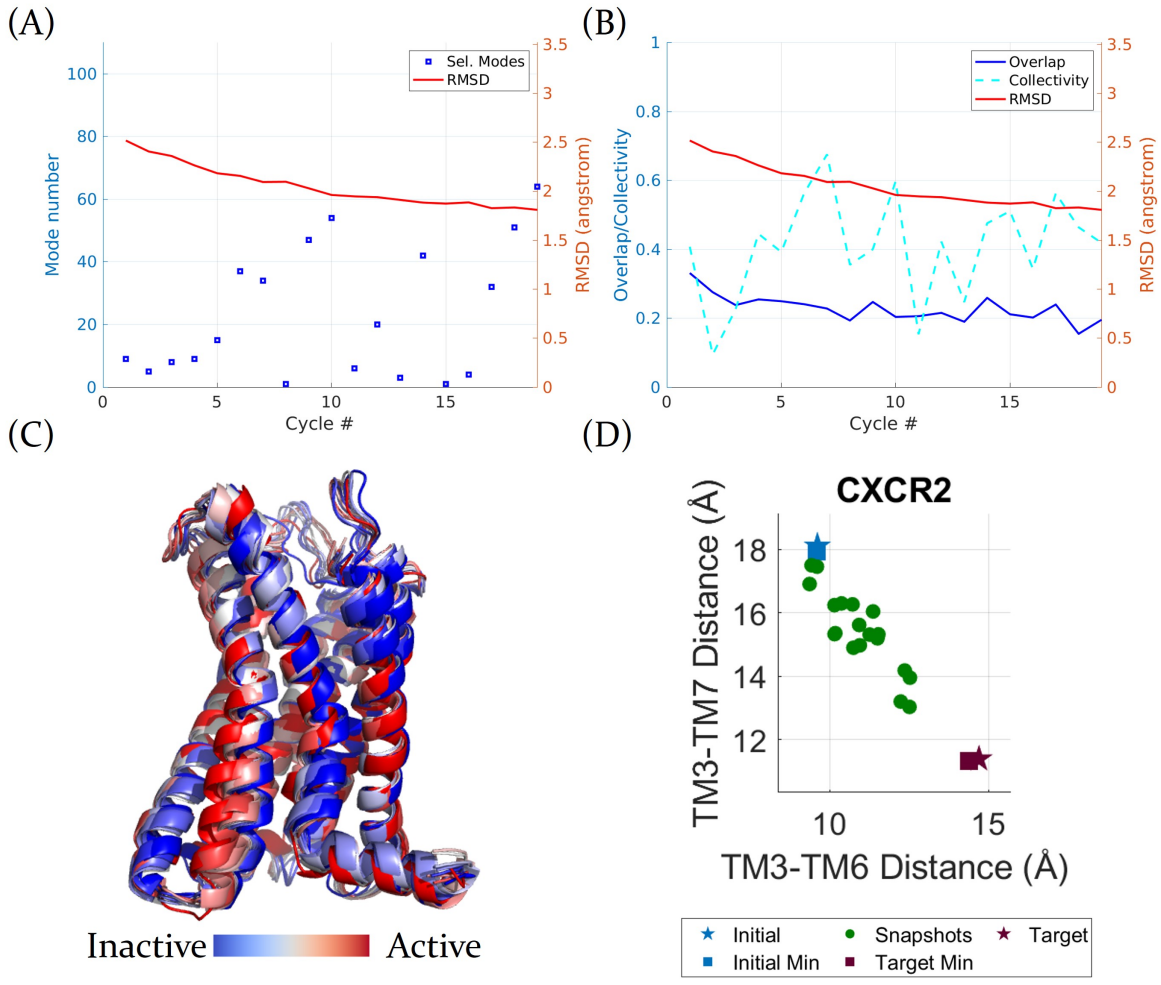

Figure 4.33. ANM-LD simulation of CXCR2 conformational transition from inactive to active state. (A) RMSD progression. (B) Mode overlap and collectivity of selected ANM modes. (C) Transition snapshots colored from blue (inactive) to red (active). (D) TM3–TM6 and TM3–TM7 distance changes over the simulation.

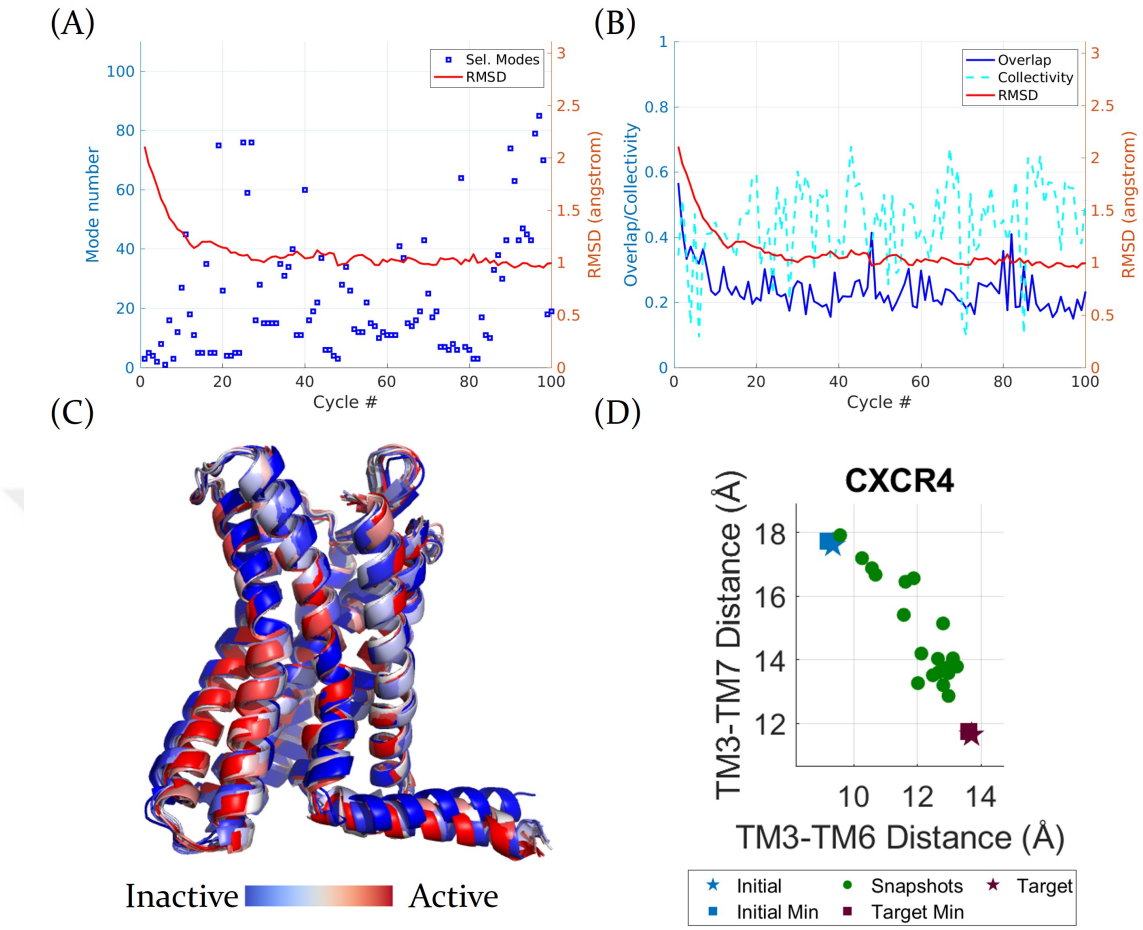

Figure 4.34. ANM-LD simulation of CXCR4 conformational transition from inactive to active state. (A) RMSD progression. (B) Mode overlap and collectivity of selected ANM modes. (C) Transition snapshots colored from blue (inactive) to red (active). (D) TM3–TM6 and TM3–TM7 distance changes over the simulation.

4.1.26. Evaluating Transition Pathways via Allosteric Co-Vibrational ANM Modes

In this study, we adopt the allosteric co-vibrational mode framework recently proposed by Kolossváry (2024) [38], which introduces a new way to analyze protein conformational transitions by constructing a weighted combination of low-frequency vibrational modes. Instead of analyzing modes individually, this approach generates a mixed mode that better represents the collective motions underlying the transition.

While Kolossváry originally formulated this method using general vibrational modes, we extend its application to ANM, enabling us to capture functionally relevant dynamics in a coarse-grained, computationally efficient manner.

To evaluate whether ANM modes can accurately model conformational transitions, we applied the co-vibrational mode framework to the inactive structures of 25 GPCR family members. For each receptor, the co-vibrational ANM modes—computed as weighted combinations of the first 200 low-frequency modes—were compared to the structural difference vector between the inactive and active states. The resulting overlap values, presented in Figures 4.35-4.39, reveal a strong agreement between the co-vibrational modes and the actual transition direction, indicating that this approach captures the essential dynamics of activation.

To investigate the conformational basis of biased signaling, we analyzed five GPCRs —ACM2, 5HT2B, ADRB1, NTR1, and V2R— for which dual activation pathways were generated from a common inactive structure to two distinct active conformations (G protein- and β-arrestin-bound). For each receptor, we computed the structural difference vectors between the inactive state and each of the two active states and compared them with the co-vibrational ANM modes. Notably, for four out of five receptors (excluding NTR1), clear differences emerged between the two pathways. In all four cases, the overlap between the co-vibrational mode and the difference vector was consistently higher for the G protein-targeted pathway, suggesting that the dominant collective dynamics align more closely with G protein-mediated activation.

In the M2 receptor (ACM2), the first ANM mode showed minimal overlap with the G protein-targeted pathway but a moderate overlap of 0.2 with the β-arrestin-targeted one. From mode 15 onward, the distinction became more evident, with overlaps reaching 0.88 for the G protein pathway versus 0.75 for the β-arrestin pathway. In 5HT2B, the separation between pathways became more pronounced starting at slowest 37th ANM mode, where the overlap rose to 0.87 for the G protein target compared to 0.78 for the β-arrestin target.

For the ADRB1 receptor, early mode overlaps were initially similar, but a divergence began at slowest 4th ANM mode, with the G protein-bound pathway reaching 0.92, while the β-arrestin-bound pathway plateaued around 0.80.

Interestingly, in V2R, the trend is initially reversed: at mode 4, the β-arrestin-targeted pathway shows higher overlap (0.52) than the G protein pathway (0.29). However, from slowest 11th ANM mode onward, the G protein overlap increases sharply, reaching 0.93, while the β-arrestin overlap remains lower, peaking at 0.67. This indicates that although β-arrestin dynamics may dominate early low-frequency modes, the G protein transition aligns more strongly with the global collective dynamics as captured by higher co-vibrational modes.

The unique trend observed in V2R, where β-arrestin-targeted overlaps are initially higher but later surpassed by G protein-targeted overlaps, highlights that biased signaling may arise not only from differences in motion amplitude but also from distinct temporal and modal hierarchies in collective dynamics. This further supports the idea that G protein-mediated transitions are more deeply encoded in the receptor's global motion landscape, whereas β-arrestin-biased transitions may rely on early, more localized modes or alternative dynamic pathways.

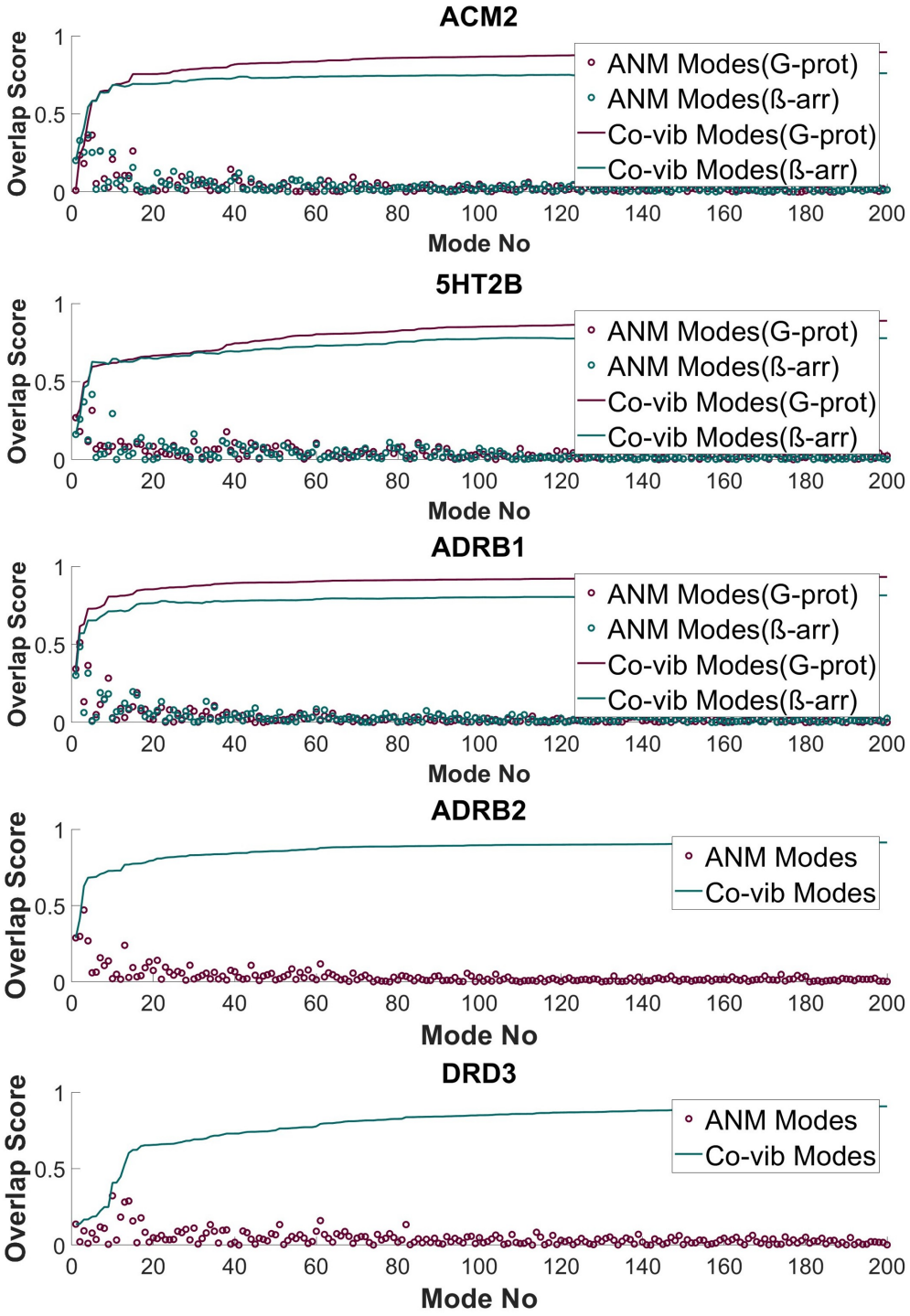

Figure 4.35. Overlap analysis between co-vibrational ANM modes and structural difference vectors for aminergic-bound receptors. For each receptor, a weighted combination of the first 200 low-frequency ANM modes—termed the co-vibrational mode.

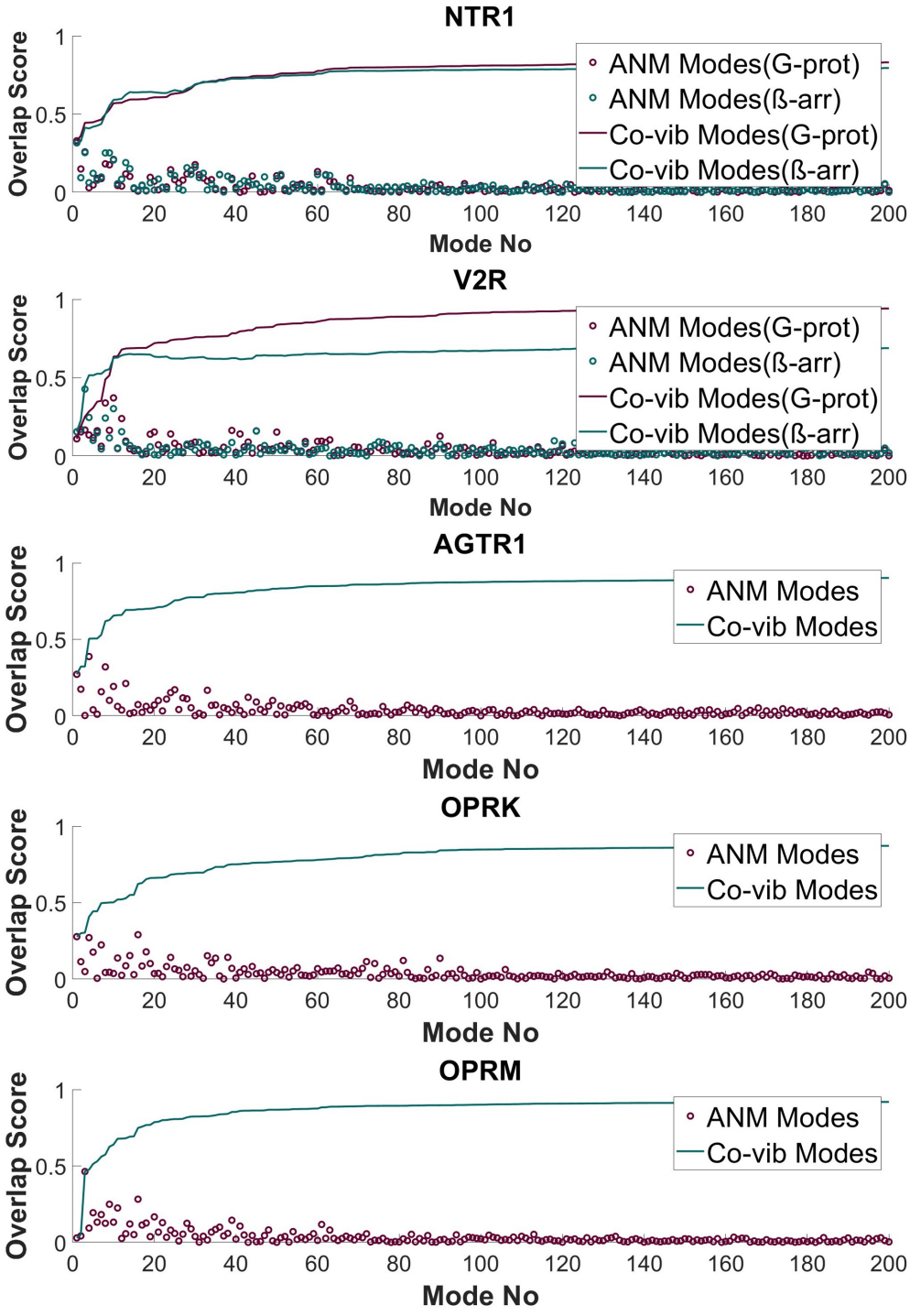

Figure 4.36. Overlap analysis between co-vibrational ANM modes and structural difference vectors for peptide-bound receptors. For each receptor, a weighted combination of the first 200 low-frequency ANM modes—termed the co-vibrational mode.

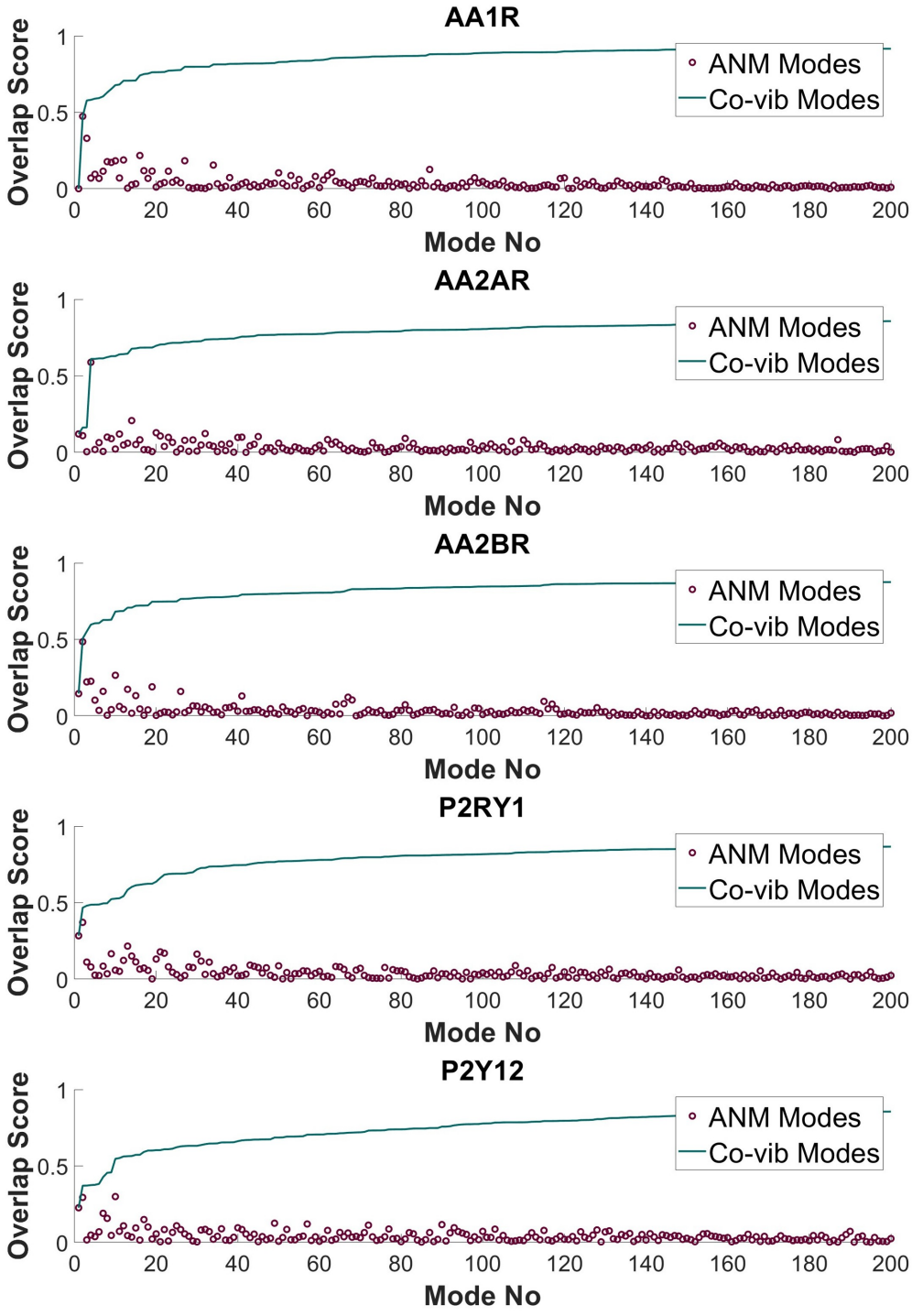

Figure 4.37. Overlap analysis between co-vibrational ANM modes and structural difference vectors for nucleotide-bound receptors. For each receptor, a weighted combination of the first 200 low-frequency ANM modes—termed the co-vibrational mode.

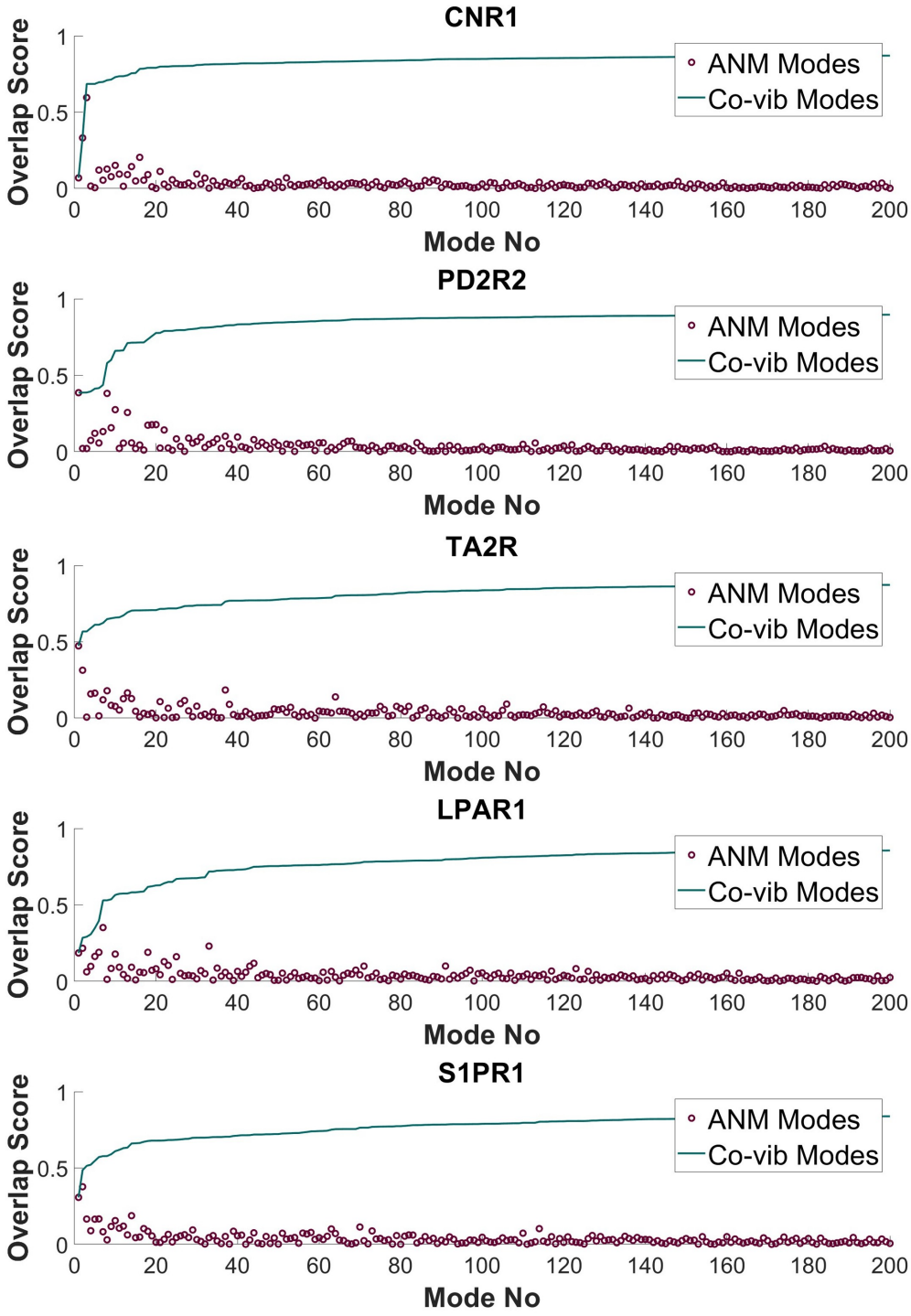

Figure 4.38. Overlap analysis between co-vibrational ANM modes and structural difference vectors for lipid-bound receptors. For each receptor, a weighted combination of the first 200 low-frequency ANM modes—termed the co-vibrational mode.

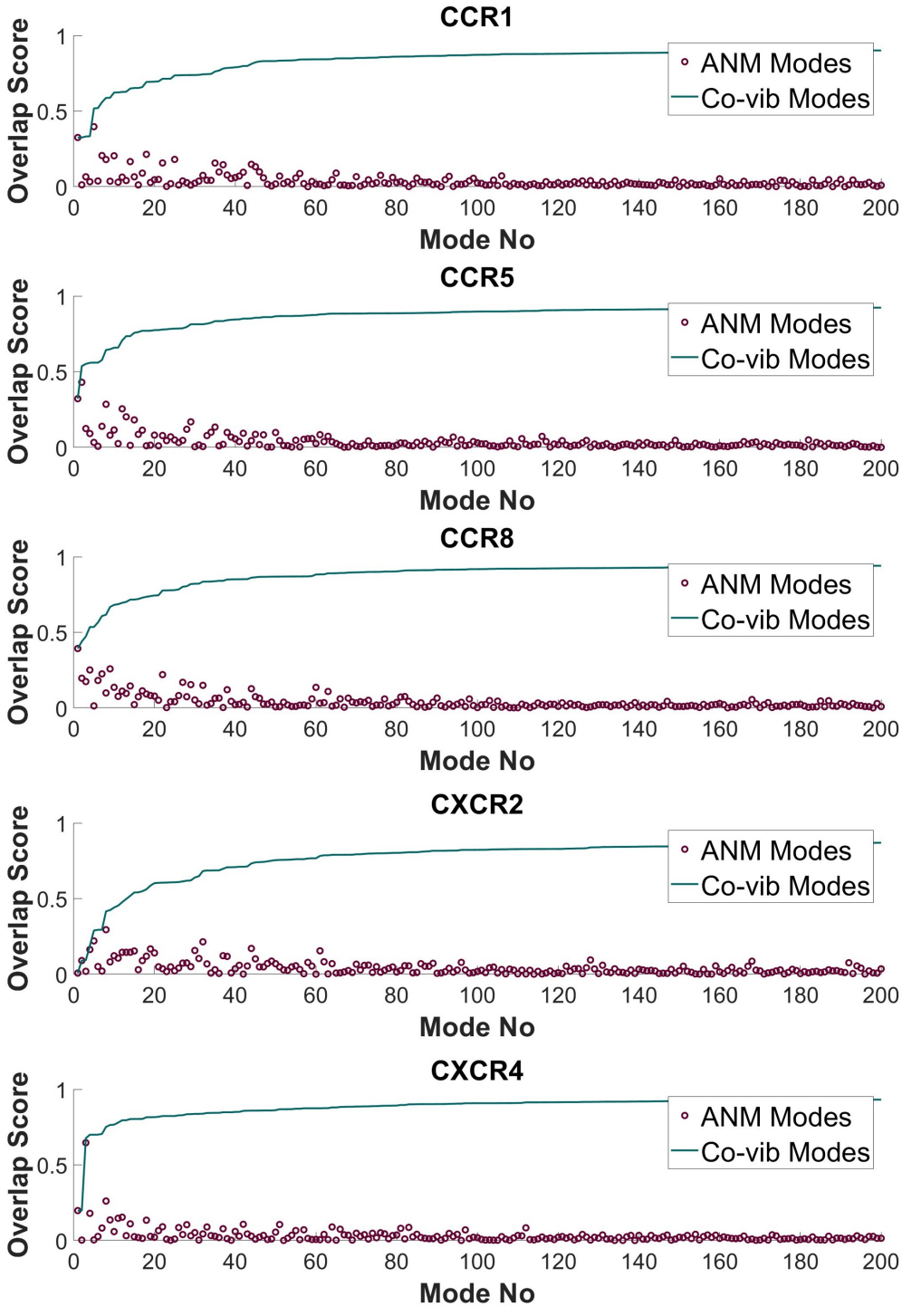

Figure 4.39. Overlap analysis between co-vibrational ANM modes and structural difference vectors for protein-bound receptors. For each receptor, a weighted combination of the first 200 low-frequency ANM modes—termed the co-vibrational mode.

4.2. Switching Signals: Conformational transitions pathway underly dynamic communication bias in GPCRs

Here, we investigate five G protein–coupled receptors (GPCRs) that have experimentally resolved structures in both G protein-bound and β-arrestin-bound active states. These include the 5-hydroxytryptamine receptor 2B (5HT2B), adrenergic β1 receptor (ADRB1), muscarinic acetylcholine M2 receptor (ACM2), vasopressin V2 receptor (V2R), and neurotensin receptor 1 (NTR1). These receptors serve as ideal systems to study biased signaling, where the same receptor can activate distinct intracellular pathways depending on the bound signaling protein. Among them, we selected 5HT2B as a model system to explore the dynamic and allosteric mechanisms underlying signaling bias. The 5-HT2 family of serotonin receptors couples to both Gq proteins and β-arrestins [27, 152] and is particularly important in the treatment of neuropsychiatric disorders, making it a therapeutically relevant focus for in-depth dynamic analysis.

In the following subsections, we present a comprehensive analysis through four complementary lenses, each aimed at uncovering different aspects of its dynamic behavior underlying biased signaling. First, we examine the key modes of motion derived from ANM-LD simulations to identify global structural changes along activation pathways. Next, we investigate allosteric interactions by applying both conventional and time-delayed cross-correlation analyses to map functionally relevant residue-residue couplings. We then explore information flow across the receptor using Gaussian Network Model–based transfer entropy (GNM-TE), which provides insight into the directionality and distribution of allosteric communication. Finally, we introduce the Differential Coupling Score, a novel metric developed in this study, which integrates changes in cross-correlation and transfer entropy to detect residues whose dynamic roles diverge depending on the signaling pathway—thereby highlighting potential differential coupling elements that contribute to biased signaling.

4.2.1. Key Modes of Motion

The selected ANM modes that drive the transition pathway from the inactive to active structures provide insight into the intrinsic dynamics underlying receptor activation. To identify the dominant motions involved, the ANM modes selected at each cycle of the simulation were cumulatively summed allowing us to capture the average collective motion responsible for the transition. The resulting cumulative ANM mode shapes for both the G protein-targeted and β-arrestin-targeted pathways, along with the difference vectors between the inactive and active states, are shown in Figure 4.40.

As shown in Figure 4.40A, comparison of the G protein-bound and inactive states of the 5HT2B receptor reveals that the largest conformational displacements occur in ECL2, the cytoplasmic ends of TM5–TM6, and the C-terminal region of TM7. When comparing the β-arrestin-bound state to the inactive state, an additional displacement is observed in helix 8, highlighting pathway-specific conformational features. A direct comparison of the difference vectors between the G protein- and β-arrestin-bound transitions reveals notable divergences in ICL1, the intracellular ends of TM6 and TM7, and helix 8. Specifically, fluctuations in ICL1 and helix 8 are more pronounced in the β-arrestin-bound pathway, whereas greater displacement is observed in ECL2 and TM7 in the G protein-bound transition. These findings are consistent with structural data reported by Cao et al. (2022) [27], which described an outward displacement of ICL1 and a downward tilt of helix 8 in the β-arrestin-1–bound conformation. Furthermore, the same study showed that TM5 and TM6 undergo an enhanced outward movement in the β-arrestin-bound state compared to the G protein-bound conformation, likely to accommodate the arrestin finger loop.

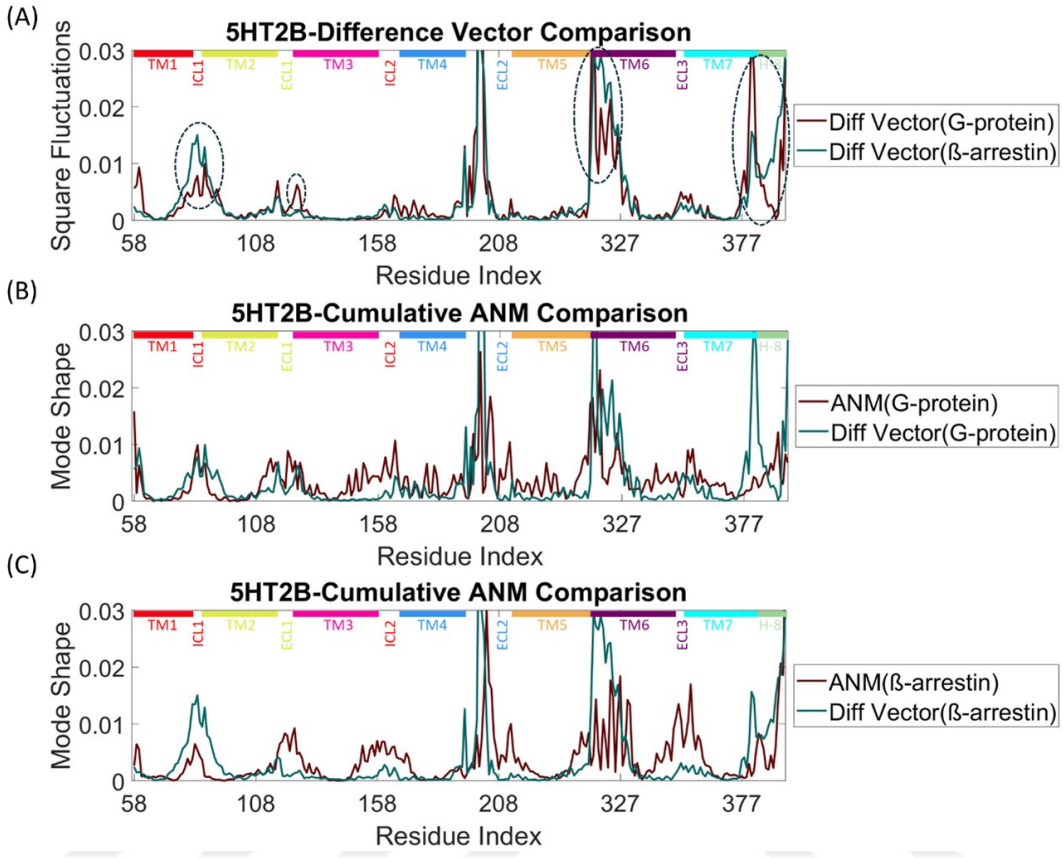

Figure 4.40. Comparison of difference vectors and cumulative ANM mode shapes for 5HT2B activation. (A) Difference vectors between the inactive AF2 model and active states: G protein-bound (7SRR) and β-arrestin-bound (7SRS); key changes circled. (B) Cumulative ANM mode shape for G protein-bound transition. (C) Cumulative ANM mode shape for β-arrestin-bound transition.

To explore the intrinsic dynamics underlying transducer-specific activation, we analyzed the cumulative ANM mode shapes for the G protein- and β-arrestin-targeted transition pathways. The cumulative mode shapes, shown in Figure 4.41A-B, along with the difference profile between the two cumulative shapes is presented in Figure 4.41C. The corresponding structures are mapped on the left side of each panel using a blue-to-red color gradient to reflect residue-level motion amplitudes, with blue indicating low mobility and red indicating high mobility. Functionally important hinge residues were identified as local peaks below the mean cumulative value but with above-

mean prominence using the "findpeaks" function in MATLAB. These residues, marked as red circles in the plots, are positioned in dynamically constrained regions likely to serve as mechanical pivots during activation. To investigate the functional relevance of these hinges, we examined their spatial proximity to experimentally or structurally annotated functional sites. Residues within 7 Å of a hinge site are visualized for the G protein-bound (Table 4.26) and β-arrestin-bound (Table 4.27) simulations. These proximity maps reveal potential allosteric communication hubs that may facilitate differential coupling of G proteins and β-arrestins.

The comparison of hinge-functional residue pairs between the G protein- and β-arrestin-targeted ANM-LD simulations (Tables 4.26–4.27) reveals both shared and distinct dynamic features. Several residues—such as R321$^{6.32}$ and A322$^{6.33}$—are located near hinge points in both pathways, suggesting their conserved role in general transducer engagement. The PIF motif, sodium binding site, rotamer toggle switch, and ionic lock (E319$^{6.30}$) are also identified as hinge-associated in both conditions, indicating that these structural elements participate in a shared core activation mechanism of 5HT2B. In contrast, the DRY motif (D152$^{3.49}$, R153$^{3.50}$, Y154$^{3.51}$) and the NPxxY motif (N376$^{7.49}$–P377$^{7.50}$) are only observed near hinge residues in the G protein-bound pathway, implying a more prominent role in G protein-selective transitions. The β-arrestin-targeted pathway, on the other hand, shows hinge proximity to residues such as F387$^{7.50}$, suggesting involvement of alternative regions during β-arrestin engagement. These findings support a model in which both shared and distinct hinge dynamics facilitate differential transducer coupling and biased signaling in 5HT2B.

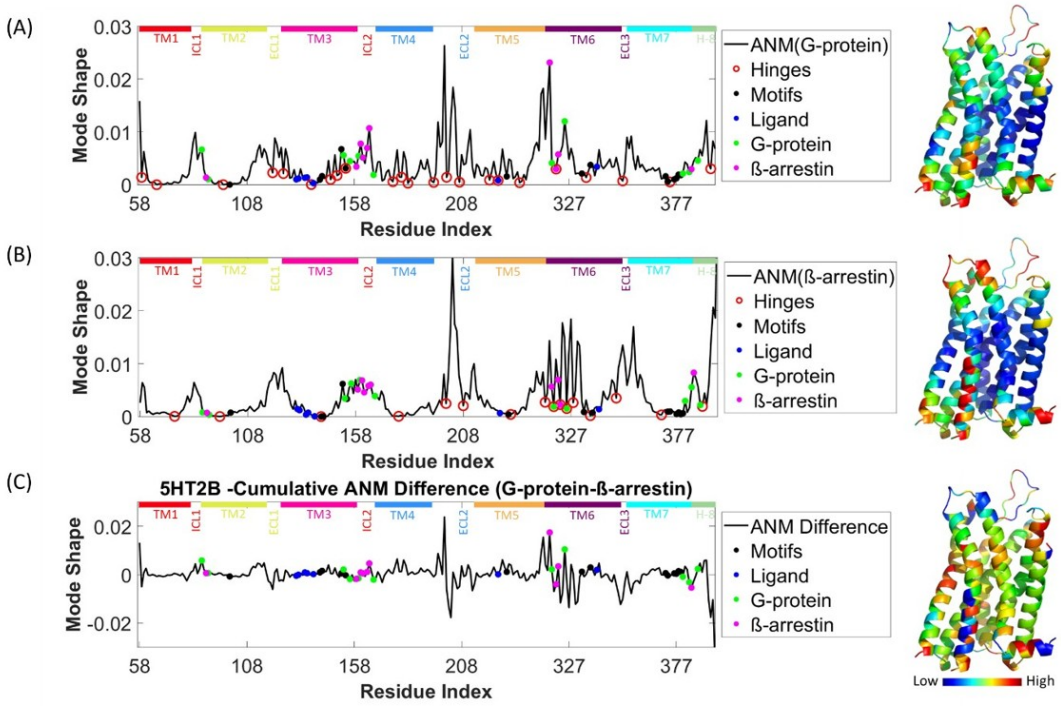

Figure 4.41. Cumulative ANM mode shapes and identification of hinge regions in 5HT2B activation pathways. (A) Cumulative ANM mode shape targeting the G protein-bound state. (B) Cumulative ANM mode shape targeting the β-arrestin-bound state. (C) Difference between the two cumulative mode shapes, with structural mappings shown on the left side of each panel.

Table 4.26. Proximity analysis between functionally annotated residues and hinge residues, where residues within 7 $\AA$ are plotted for the G protein-bound case.

Functionally Important Residue	**Residue ID**	**Distance (Å)**	**Hinge Residue**
Sodium Binding Site	$D100^{2.50}$	5.02	$A97^{2.47}$
Ligand Binding Site	$D135^{3.32}$	5.46	$F138^{3.35}$
Ligand Binding Site	$V136^{3.33}$	5.72	$F138^{3.35}$
Ligand Binding Site	$S139^{3.36}$	3.85	$F138^{3.35}$

Table 4.26 Proximity analysis between functionally annotated residues and hinge residues, where residues within 7 $\AA$ are plotted for the G protein-bound case. (cont.)

Functionally Important Residue	**Residue ID**	**Distance (Å)**	**Hinge Residue**
Sodium Binding Site	S142$^{3.39}$	6.19	F138$^{3.35}$
PIF Motif	I143$^{3.40}$	6.32	C147$^{3.44}$
DRY Motif	D152$^{3.49}$	5.52	Y154$^{3.51}$
DRY Motif	R153$^{3.50}$	3.82	Y154$^{3.51}$
DRY Motif	Y154$^{3.51}$	0.00	Y154$^{3.51}$
G-protein Binding Site	A156$^{3.53}$	5.53	Y154$^{3.51}$
Ligand Binding Site	A225$^{5.46}$	0.00	A225$^{5.46}$
PIF Motif	P229$^{5.50}$	5.75	C147$^{3.44}$
G-protein & β-arrestin Binding Site	N318$^{6.29}$	5.04	R321$^{6.32}$
Ionic Lock	E319$^{6.30}$	5.50	R321$^{6.32}$
β-arrestin Binding Site	R321$^{3.32}$	0.00	R321$^{6.32}$
β-arrestin Binding Site	A322$^{3.33}$	3.84	R321$^{6.32}$
G-protein Binding Site	V325$^{6.36}$	6.32	R321$^{6.32}$
PIF Motif	F333$^{6.44}$	5.61	L335$^{6.46}$
Rotamer Toggle Switch	W337$^{6.48}$	5.92	L335$^{6.46}$
Sodium Binding Site	S372$^{7.45}$	5.39	G374$^{7.47}$
Sodium Binding Site	S373$^{7.46}$	3.86	G374$^{7.47}$
NPxxY Motif	N376$^{7.49}$	5.73	G374$^{7.47}$
NPxxY Motif	P377$^{7.50}$	6.52	G374$^{7.47}$

Table 4.27. Proximity analysis between functionally annotated residues and hinge residues, where residues within 7 $\AA$ are plotted for the β-arrestin-bound case.

Functionally Important Residue	**Residue ID**	**Distance (Å)**	**Hinge Residue**
Sodium Binding Site	$D100^{2.50}$	6.66	$S142^{3.39}$
Ligand Binding Site	$S139^{3.36}$	5.26	$S142^{3.39}$
Sodium Binding Site	$S142^{3.39}$	0.00	$S142^{3.39}$
PIF Motif	$I143^{3.40}$	3.88	$S142^{3.39}$
PIF Motif	$P229^{5.50}$	3.82	$L230^{5.51}$
G-protein & β-arrestin Binding Site	$N318^{6.29}$	3.86	$E319^{6.30}$
Ionic Lock	$E319^{6.30}$	0.00	$E319^{6.30}$
β-arrestin Binding Site	$R321^{3.32}$	3.84	$A322^{6.33}$
β-arrestin Binding Site	$A322^{3.33}$	0.00	$A322^{6.33}$
G-protein Binding Site	$V325^{6.36}$	0.00	$V325^{6.36}$
PIF Motif	$F333^{6.44}$	5.33	$M336^{6.47}$
Rotamer Toggle Switch	$W337^{6.48}$	3.86	$M336^{6.47}$
Sodium Binding Site	$S372^{7.45}$	5.50	$G369^{7.42}$
G-protein Binding Site	$F383^{7.56}$	6.17	$V325^{6.36}$
G-protein & β-arrestin Binding Site	$N384^{8.47}$	6.36	$R388^{8.51}$
G-protein Binding Site	$F387^{8.50}$	3.84	$R388^{8.51}$

We applied cumulative ANM mode shape analysis to all four receptors—ADRB1, ACM2, V2R, and NTR1—to examine collective motions along their G protein– and β-arrestin–targeted activation pathways (Figures 4.42–4.45). In ADRB1, cumulative

mode shapes revealed dominant flexibility in ICL1, ICL2, TM6, and TM7 along the G protein–bound pathway, whereas ECL1, TM5-IC, and TM6-IC were more pronounced in the β-arrestin–bound case. For ACM2, enhanced motions in TM5-IC, TM6-IC, ECL1, and ECL3 were observed along the G protein pathway, while helix 8 exhibited higher flexibility in the β-arrestin–targeted ensemble. In V2R, TM6-IC, ECL2, and ECL3 displayed stronger fluctuations in the G protein–bound simulation, while TM1-EC became more mobile in the β-arrestin–bound case. Lastly, in NTR1, the G protein–bound ensemble showed greater mobility in ICL2, ECL2, ECL3, and helix 8, while TM3-IC, TM5-IC, and TM6-IC were more flexible in the β-arrestin–bound pathway.

Cumulative ANM mode shape analysis across the five receptors reveals that distinct regions undergo dominant fluctuations depending on the signaling pathway, indicating that the collective dynamics differ between G protein– and β-arrestin–targeted transitions. Rather than a uniform shift across all receptors, each case demonstrates receptor- and pathway-specific redistribution of flexibility. For example, in ADRB1 and ACM2, the intracellular domains of TM5 and TM6 display higher mobility in the β-arrestin–bound transitions, whereas in V2R and 5HT2B, these regions are more dynamic in the G protein–bound transitions. Notably, helix 8 exhibits enhanced fluctuations specifically in the β-arrestin–targeted transitions of ACM2 and NTR1, while extracellular loops such as ECL2 and ECL3 are prominently mobile in the G protein–bound transitions of V2R and NTR1. These findings suggest that the regions contributing most to pathway-specific transitions vary across receptors, reflecting diverse mechanisms of biased activation rather than a single conserved dynamic feature. Thus, cumulative ANM mode shapes provide a powerful lens to detect how functional dynamics reorganize along different signaling trajectories, and support the idea that biased signaling is not only structurally encoded at the binding interface but dynamically shaped throughout the receptor's collective motion landscape.

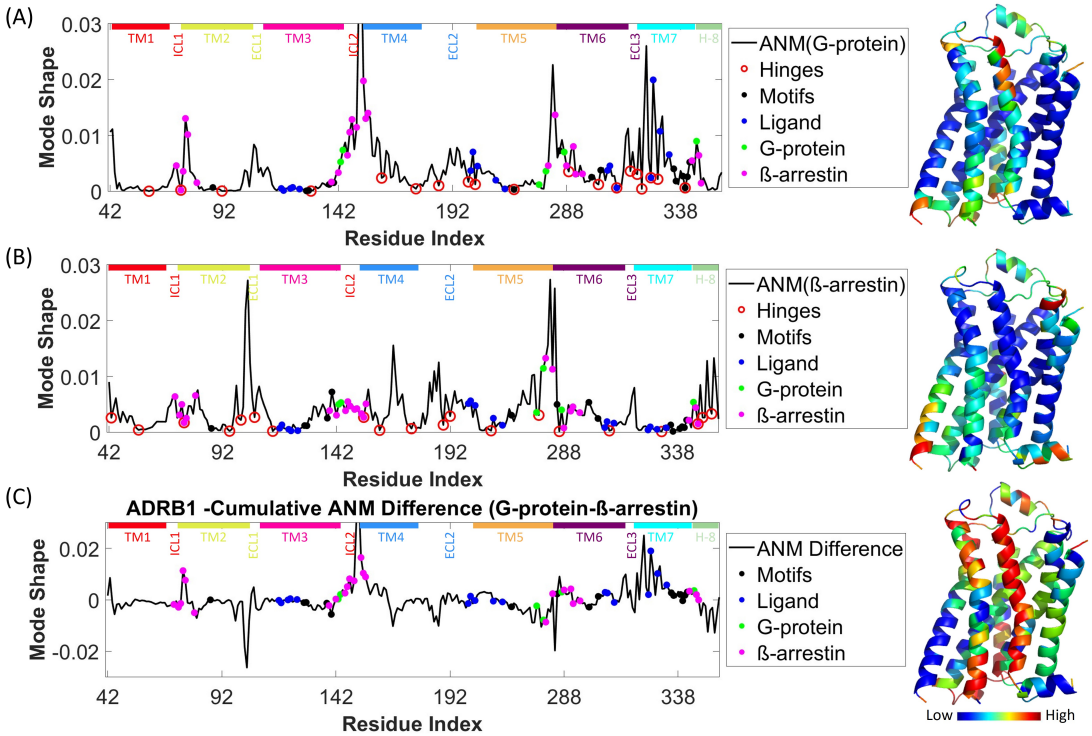

Figure 4.42. Cumulative ANM mode shapes and identification of hinge regions in ADRB1 activation pathways. (A) Cumulative ANM mode shape targeting the G protein-bound state. (B) Cumulative ANM mode shape targeting the β-arrestin-bound state. (C) Difference between the two cumulative mode shapes, with structural mappings shown on the left side of each panel.

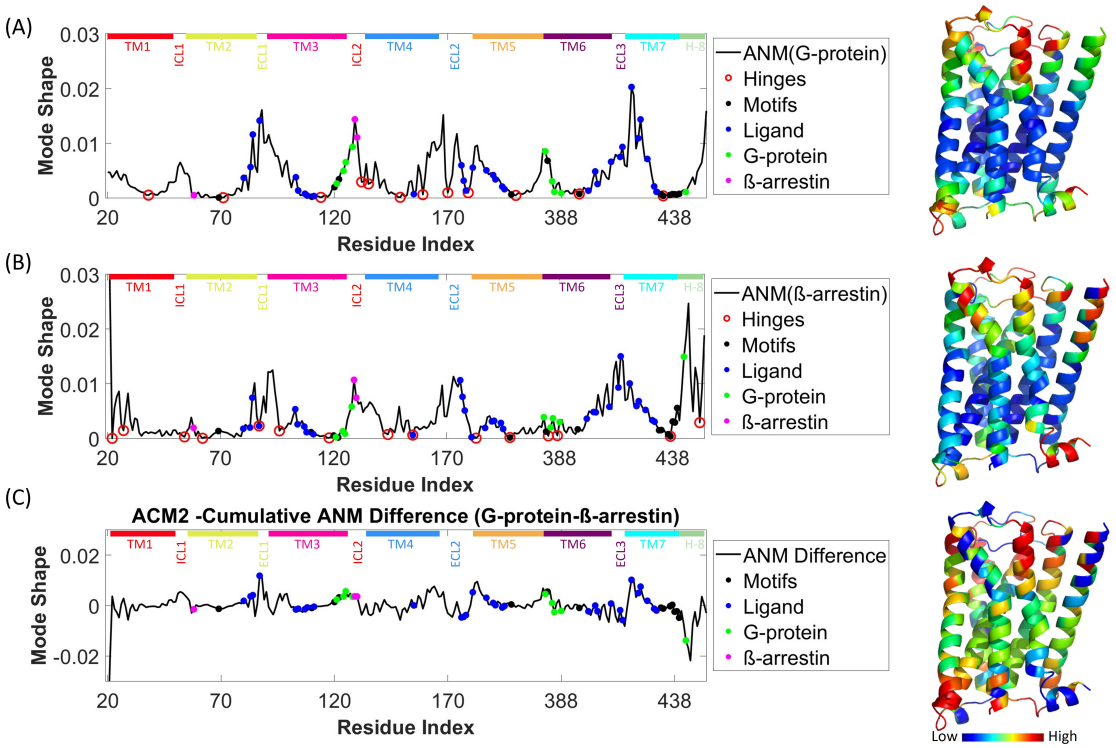

Figure 4.43. Cumulative ANM mode shapes and identification of hinge regions in ACM2 activation pathways. (A) Cumulative ANM mode shape targeting the G protein-bound state. (B) Cumulative ANM mode shape targeting the β-arrestin-bound state. (C) Difference between the two cumulative mode shapes, with structural mappings shown on the left side of each panel.

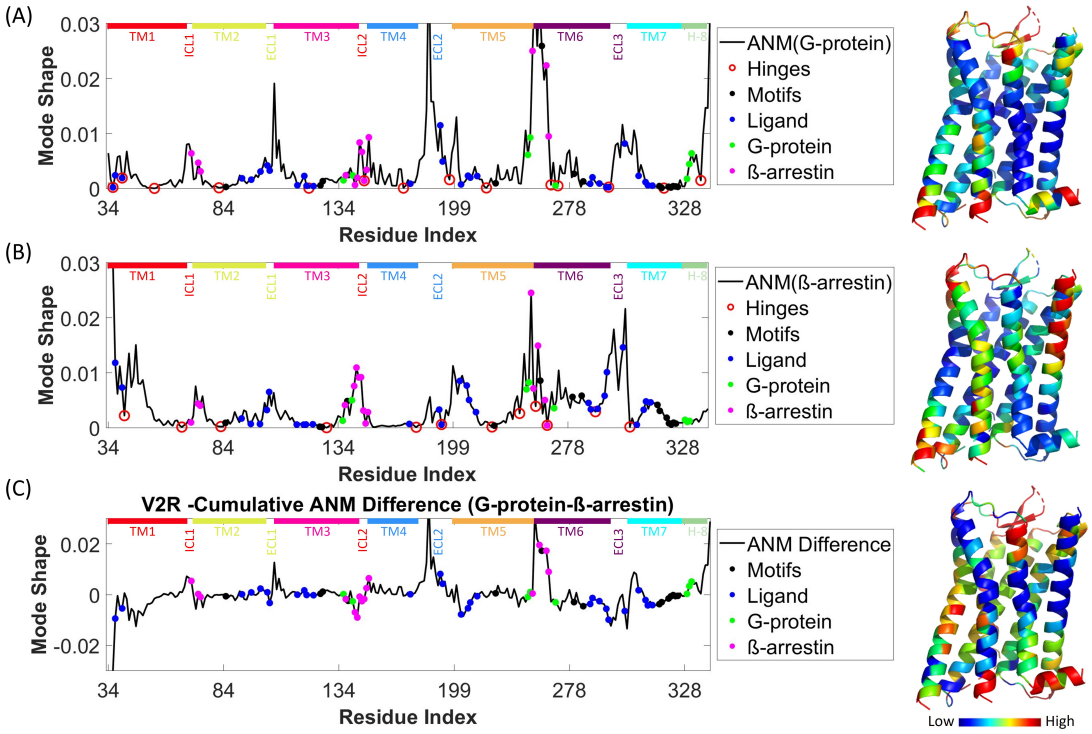

Figure 4.44. Cumulative ANM mode shapes and identification of hinge regions in V2R activation pathways. (A) Cumulative ANM mode shape targeting the G protein-bound state. (B) Cumulative ANM mode shape targeting the β-arrestin-bound state. (C) Difference between the two cumulative mode shapes, with structural mappings shown on the left side of each panel.

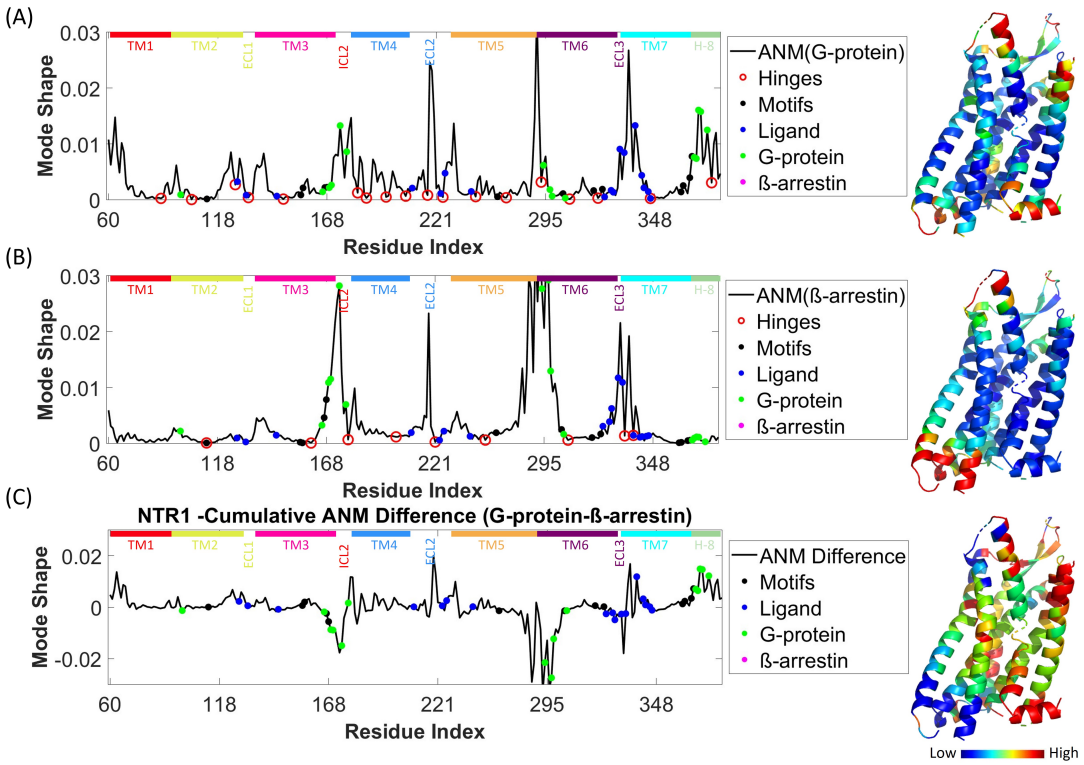

Figure 4.45. Cumulative ANM mode shapes and identification of hinge regions in NTR1 activation pathways. (A) Cumulative ANM mode shape targeting the G protein-bound state. (B) Cumulative ANM mode shape targeting the β-arrestin-bound state. (C) Difference between the two cumulative mode shapes, with structural mappings shown on the left side of each panel.

4.2.2. The Allosteric Interactions of 5HT2B

Normalized cross-correlation analysis was employed to identify residue pairs that exhibit coordinated fluctuations during receptor activation. The normalized correlation values range between -1 and 1, where positive values indicate that residues move in the same direction (i.e., parallel fluctuations), while negative values indicate anti-correlated motion. Residues with strong positive correlations are often interpreted as functionally coupled and potentially significant in driving collective motions. The analysis was performed using intermediate conformations sampled along the activation pathway from the inactive to the active state of the 5HT2B receptor for both G protein and β-arrestin

signaling pathways. To better quantify and visualize inter-structural segment communication within the 5HT2B receptor, we divided the structure into 21 structural segments. These included the three extracellular loops (ECL1–ECL3), three intracellular loops (ICL1–ICL3), the extracellular and intracellular segments of each transmembrane helix (TMx-EC and TMx-IC), and Helix 8. Segment-averaged cross-correlation values were computed to evaluate the collective motions and dynamic couplings between these structural segments. The resulting structural segment-wise correlation matrices are shown in Figure 4.46A for the G protein-targeting simulation and in Figure 4.47A for the β-arrestin-targeting simulation. The difference map between the two is presented in Figure 4.48A. To further highlight functional couplings, segment-level correlation networks are shown in Figures 4.46B, 4.47B, and 4.48B, where edges represent significant dynamic correlations. Red edges indicate strong positive correlations ($C \geq 0.30$), and blue edges indicate strong anti-correlations ($C \leq -0.30$), illustrating the distinct communication patterns associated with different signaling pathways.

In both the G protein- and β-arrestin-targeting activation pathways, we observe several conserved inter-structural segment correlation patterns that appear to play a key role in receptor activation. (Figures 4.46-4.48). Notably, TM6-IC exhibits strong negative correlations with TM2-IC, ICL1, and TM1-IC, a dynamic relationship that likely facilitates the characteristic outward displacement of TM6 during activation. This anti-correlation suggests that as TM6 moves away from the receptor core, the intracellular ends of TM1 and TM2—as well as ICL1—move in the opposite direction, contributing to the expansion of the intracellular binding cavity. In addition, TM1-IC, ICL1, and TM2-IC are positively correlated with one another, forming a tightly coupled dynamic unit. A strong positive correlation between Helix 8 and ICL1 is also observed in both pathways, suggesting a conserved role for this interaction in maintaining the structural integrity of the intracellular signaling interface. The preservation of these correlation patterns across both pathways points to a shared structural mechanism underlying the initial stages of activation, regardless of the specific signaling outcome.

In the G protein-targeting activation pathway, we observe strong negative correlations between ECL3 and intracellular regions such as TM5-IC and TM7-IC. This anti-correlation suggests a dynamic decoupling between extracellular and intracellular domains, implying that movements in ECL3 are inversely related to those in key intracellular segments involved in G protein binding. While the exact nature of ECL3's motion remains unclear, its opposing correlation with intracellular domains may reflect a broader allosteric network that links ligand-binding events at the extracellular surface to conformational changes at the cytoplasmic interface. In contrast, Helix 8 and TM1-IC display strong positive correlations, indicating cohesive motion among these intracellular regions. This correlated dynamic behavior is consistent with their known functional roles in stabilizing G protein coupling. The alignment and concerted motion of these regions may facilitate the formation of a favorable interface for G protein engagement and help maintain the active-state conformation of the receptor. In the β-arrestin-targeting activation pathway, unique long-range correlations emerge that distinguish it from the G protein pathway. Positive correlations between TM4-IC and TM7-EC, as well as between TM6-IC and TM2-EC, point to the presence of allosteric coupling between intracellular and extracellular regions. These long-range interactions may reflect an alternative route of signal propagation, potentially involving more distributed conformational shifts across the receptor. Within the extracellular region, TM7-EC exhibits strong positive correlations with ECL3 and TM6-EC, while ECL1 shows coordinated motion with TM2-EC. These patterns suggest a well-connected dynamic network across the extracellular surface that may contribute to ligand recognition and biased signaling.

In the β-arrestin-targeting activation pathway, several key intracellular correlations appear weakened compared to the G protein pathway. Specifically, the correlations between ICL2 and TM7-IC, Helix 8, as well as between TM3-IC and TM7-IC, are markedly reduced. Additionally, the correlation between TM1-IC and Helix 8 is also diminished. These observations suggest a less cohesive dynamic coupling across the intracellular regions that are typically involved in transducer engagement. Notably, while LSD-induced β-arrestin coupling has been shown to require conformational

changes in ICL2, the reduced correlations involving ICL2 in our data indicate that it may participate in a distinct allosteric network in the arrestin-biased pathway. This suggests that, although similar structural elements are involved, the dynamic coordination among them differs depending on the signaling context, potentially reflecting different requirements for arrestin versus G protein engagement.

Across all four receptors analyzed—ADRB1, ACM2, V2R, and NTR1—a consistent dynamic feature was observed (Figures 4.49 - 4.52): the coupling between ICL1 and the ECL3 region (or their immediate structural neighbors, such as TM1-IC and TM2-IC in the case of truncated ICL1 in NTR1) was stronger in the β-arrestin–targeted transition pathways. This is reflected by the prevalence of blue edges connecting these regions in the segment-level difference networks. The repeated appearance of this pattern suggests that β-arrestin–biased transitions promote long-range dynamic coordination between the extracellular and intracellular ends of the receptor, specifically linking ECL3 to the TM1–ICL1 axis. A plausible explanation for this behavior is that β-arrestin engagement may involve a different mode of allosteric propagation that stabilizes the intracellular region via interactions extending from the extracellular surface. Rather than relying solely on central transmembrane helical rearrangements (such as TM6), β-arrestin–biased signaling may mobilize more peripheral or surface-accessible elements, leading to enhanced fluctuation coherence between ICL1 and ECL3. This could represent a receptor-spanning allosteric bridge, functionally relevant for maintaining structural alignment during arrestin recruitment, or facilitating specific phosphorylation and recognition events.

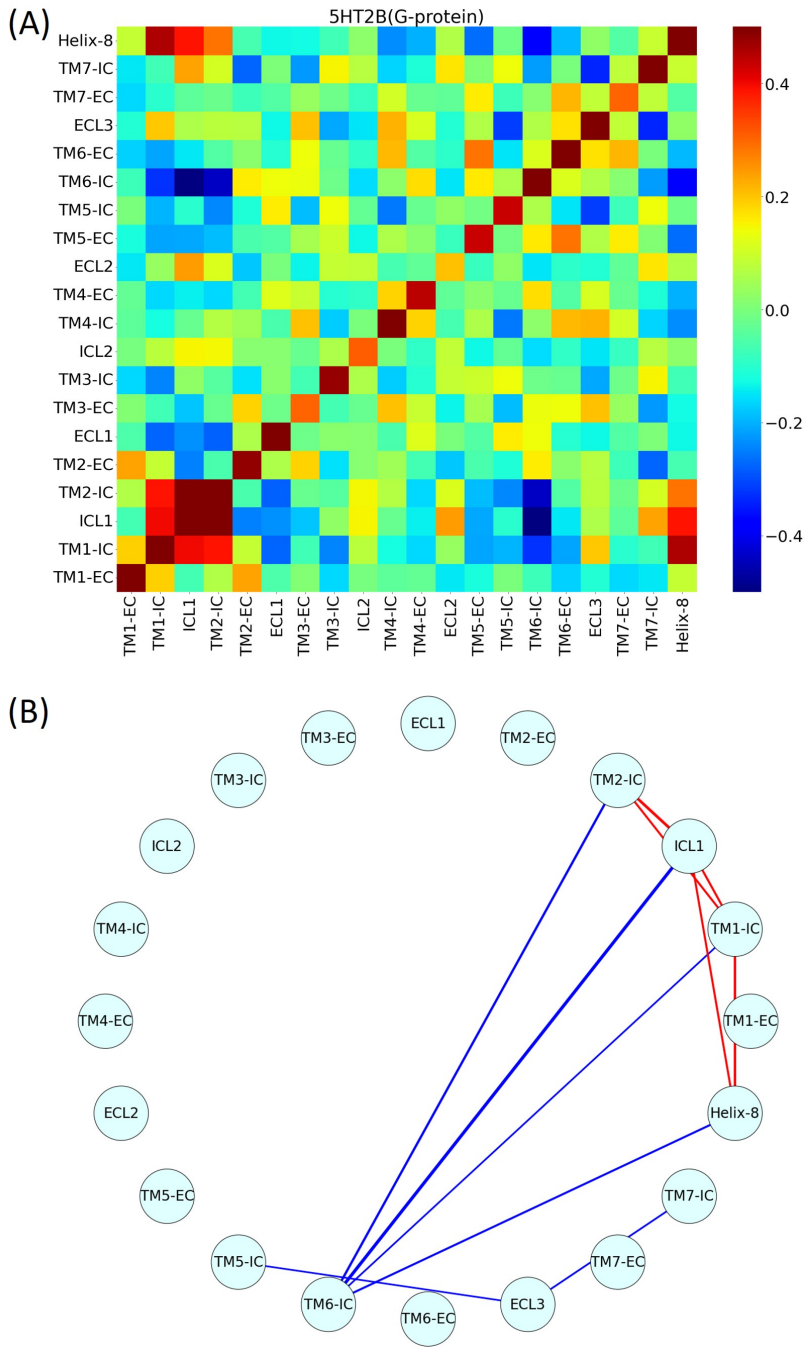

Figure 4.46. Segment-level cross-correlation analysis for the G protein–targeted activation pathway of 5HT2B receptor. (A) Segment-averaged cross-correlation matrix. (B) Corresponding structural segment correlation network, where red edges represent strong positive correlations (C≥0.30), and blue edges represent strong negative correlations (C≤–0.30).

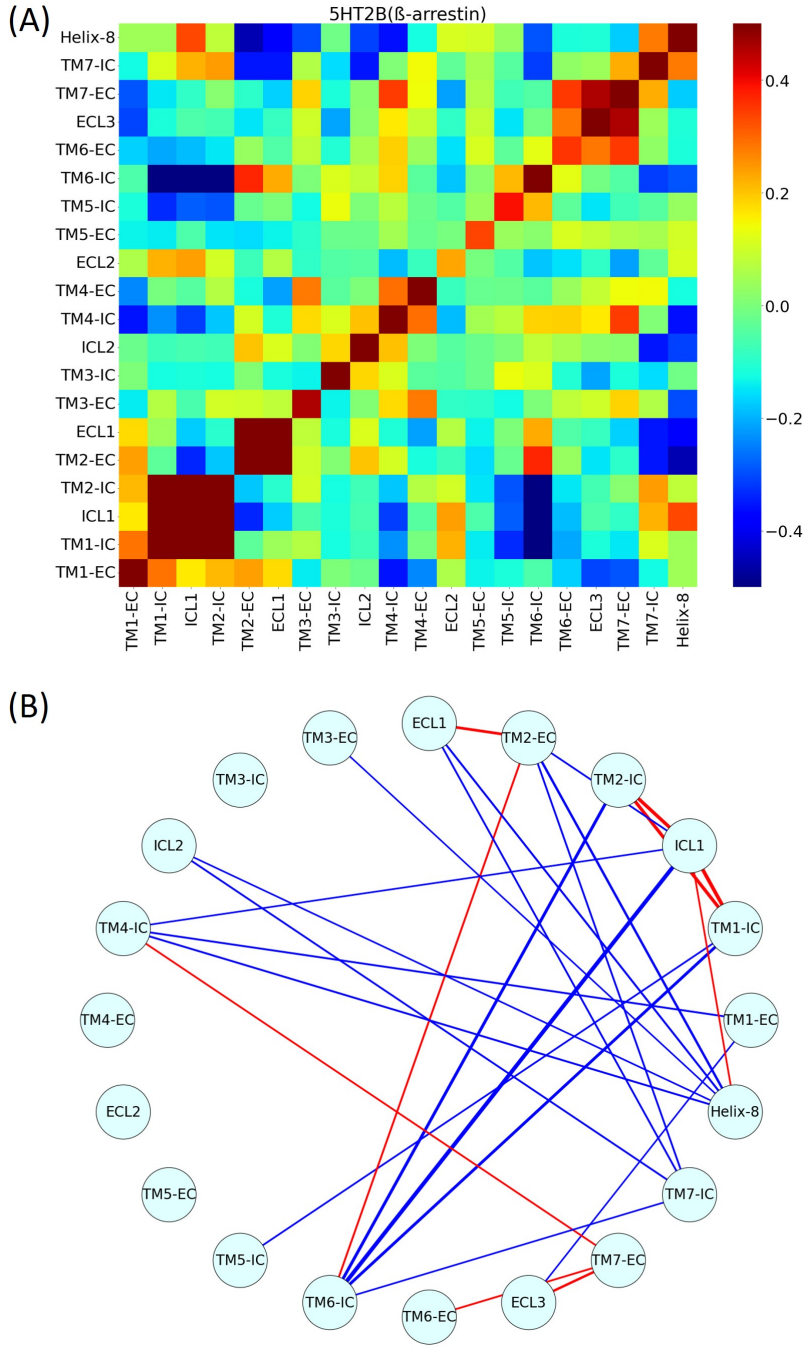

Figure 4.47. Segment-level cross-correlation analysis for the β-arrestin–targeted activation pathway of 5HT2B receptor. (A) Segment-averaged cross-correlation matrix. (B) Corresponding structural segment correlation network, where red edges represent strong positive correlations (C$\geq$0.30), and blue edges represent strong negative correlations (C$\leq$–0.30).

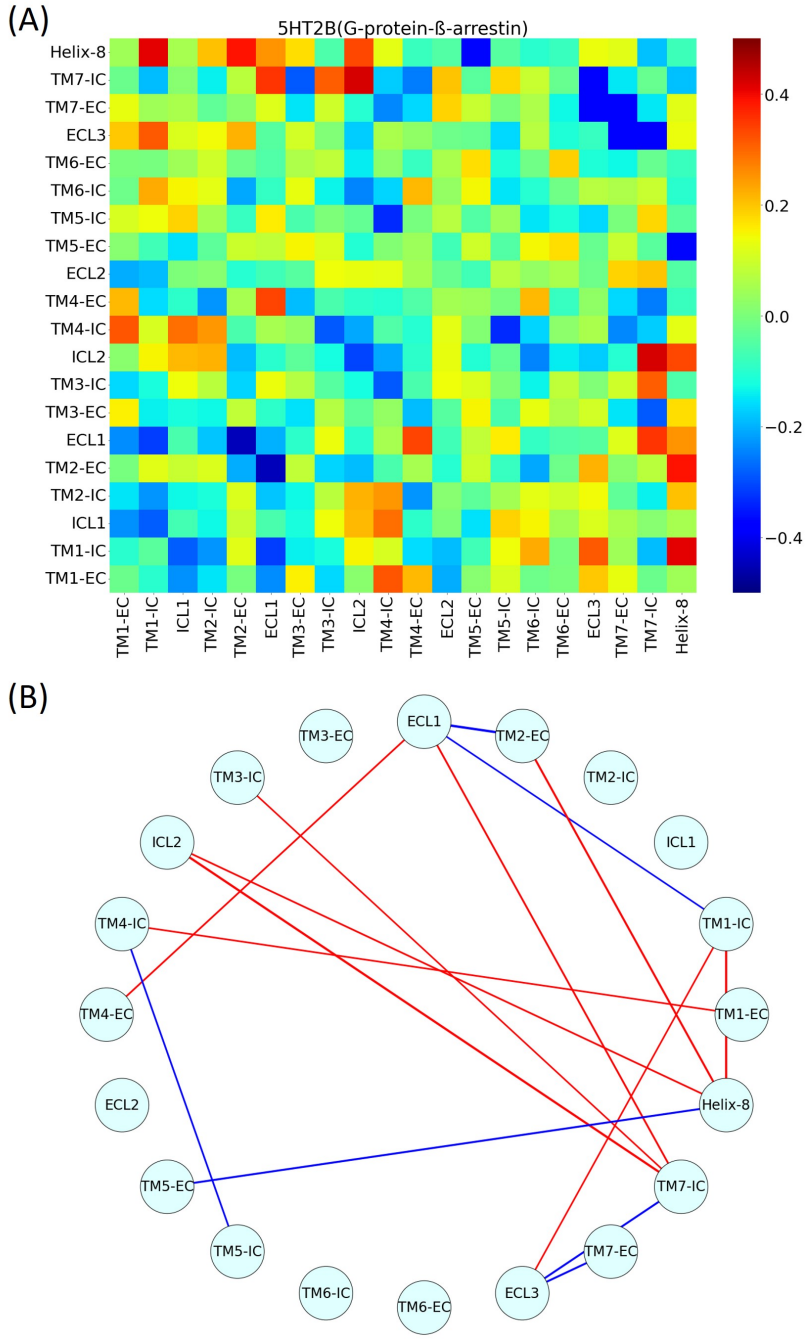

Figure 4.48. Segment-level cross-correlation difference analysis for the G portein- and β-arrestin–targeted activation pathway of 5HT2B receptor. (A) Segment-averaged cross-correlation difference matrix. (B) Corresponding structural segment correlation network, where red edges represent strong positive correlations (C≥0.30), and blue edges represent strong negative correlations (C≤–0.30).

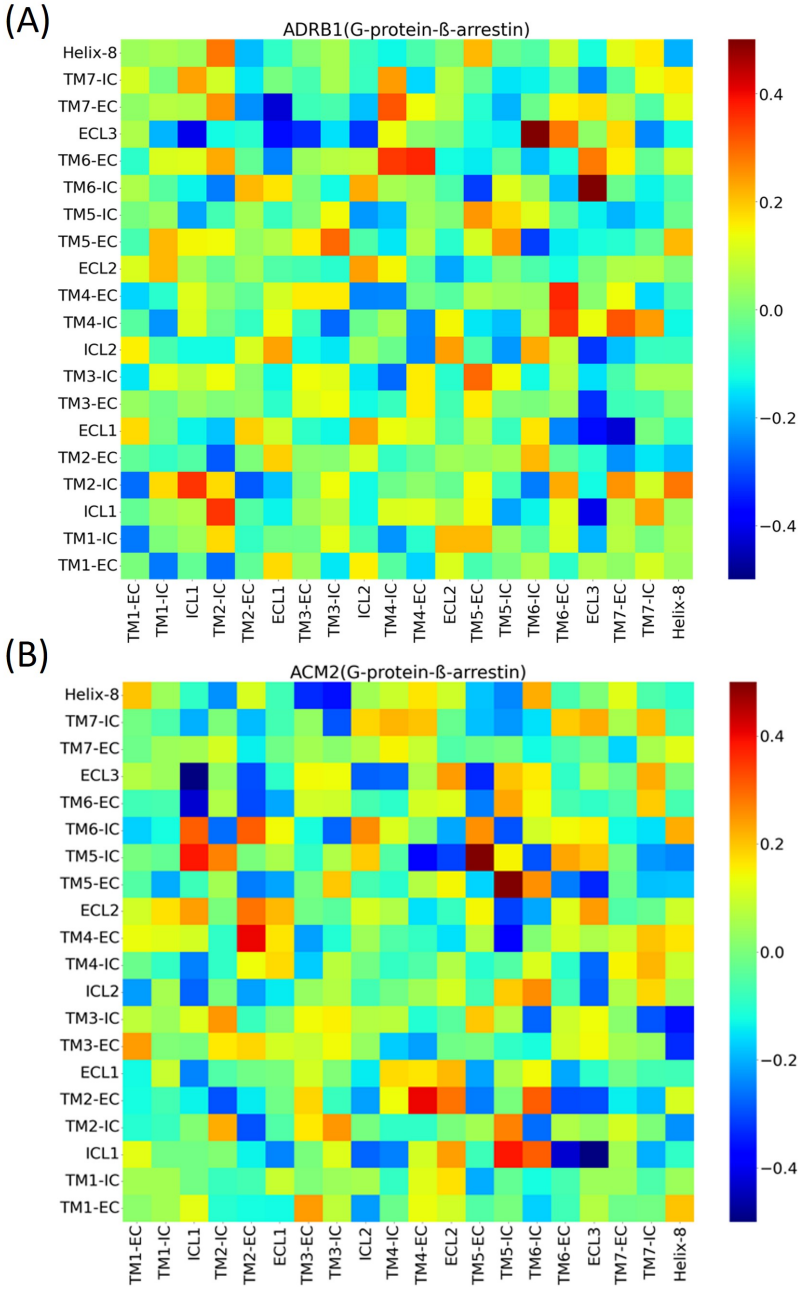

Figure 4.49. Segment-level cross-correlation difference networks for distinct receptor activation pathways for (A) ADRB1 and (B) ACM2.

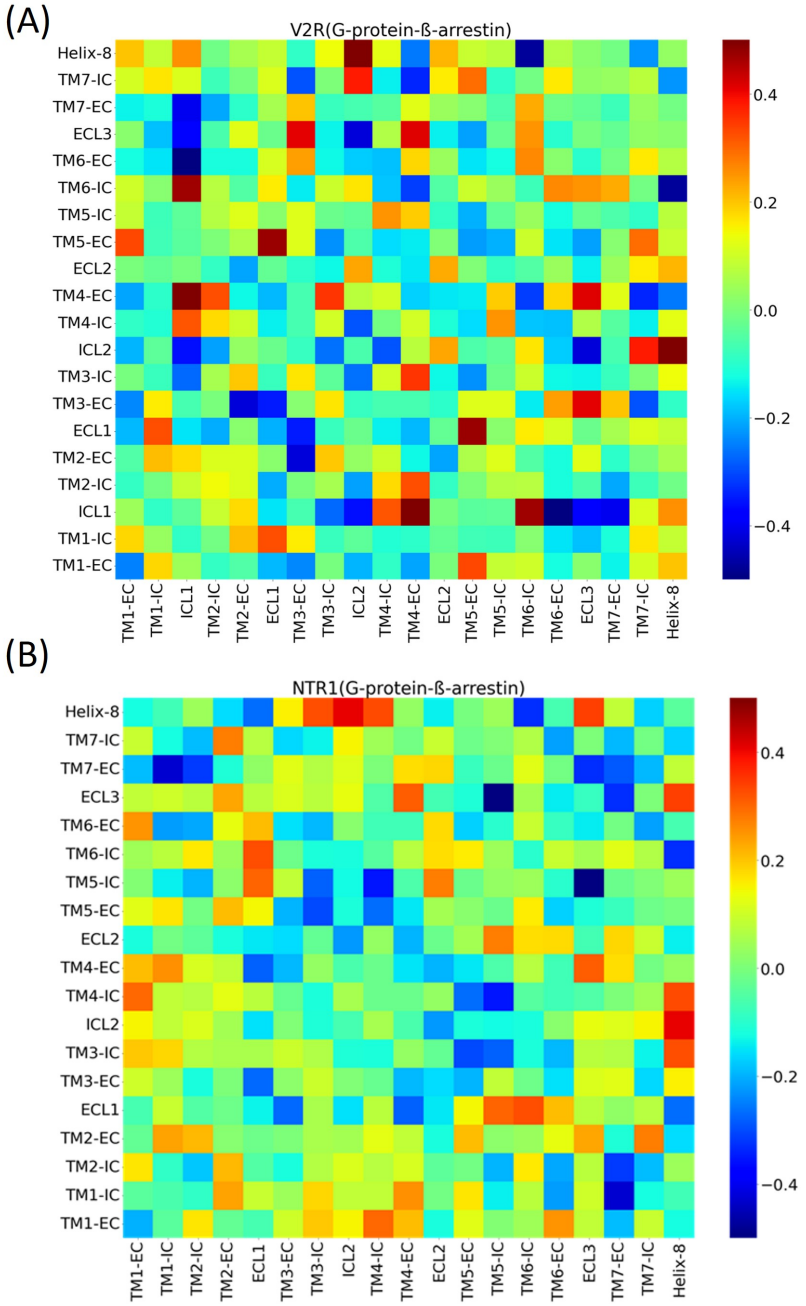

Figure 4.50. Segment-level cross-correlation difference networks for distinct receptor activation pathways for (A) V2R and (B) NTR1.

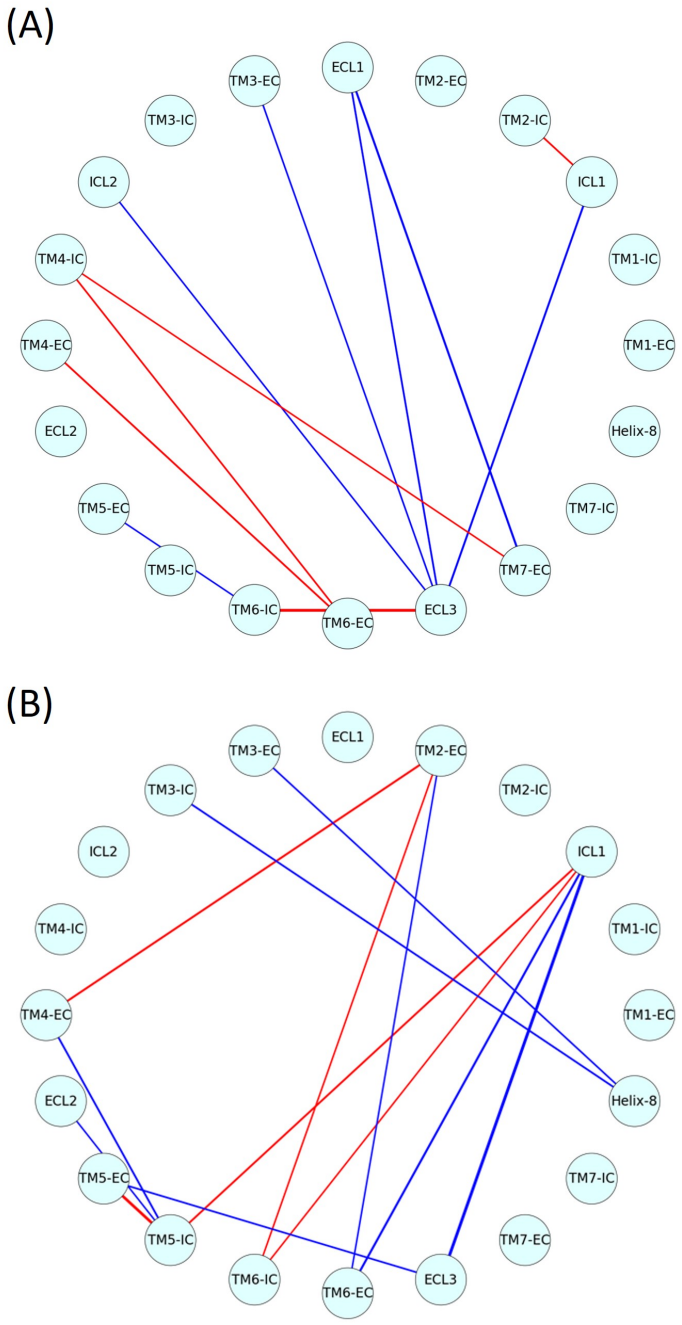

Figure 4.51. Segment-level correlation difference networks for different receptor activation pathways. Structural segment correlation networks are shown for (A) ADRB1 and (B) ACM2. Red edges indicate segment pairs with stronger cross-correlations in the G protein–targeted pathway, while blue edges indicate stronger correlations in the β-arrestin–targeted pathway.

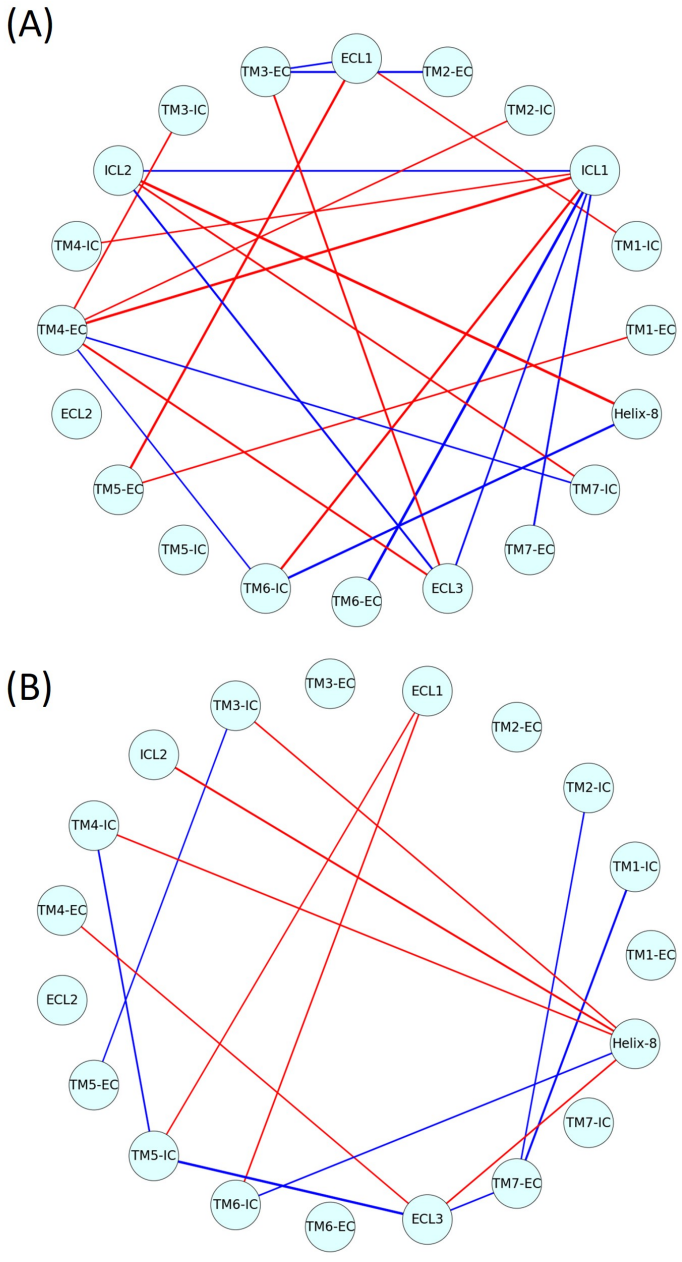

Figure 4.52. Segment-level correlation difference networks for different receptor activation pathways. Structural segment correlation networks are shown for (A) V2R and (B) NTR1. Red edges indicate segment pairs with stronger cross-correlations in the G protein–targeted pathway, while blue edges indicate stronger correlations in the β-arrestin–targeted pathway.

4.2.3. Temporal order of allosteric communication

In addition to capturing large-scale transitions, ANM-LD simulations offer valuable insights into the temporal organization of conformational changes—details that are often inaccessible through experimental techniques. To investigate whether specific regions of the 5HT2B receptor exhibit ordered dynamics during activation, we extended our analysis to include a time delay between the motions of structural segments. By introducing a fixed delay (expressed in simulation cycles) into cross-correlation calculations, we were able to assess whether the motion of one region precedes and is consistently followed by that of another. When a delayed correlation between two regions remains positive, it suggests that the preceding region may play a driving role in the conformational sequence, while the latter follows its motion. While this approach does not establish strict causality, it allows for the identification of driver–responder relationships that reflect the likely order of conformational events. Using this framework, we characterized precedence relationships between key structural segments to better understand the directional flow of allosteric communication along the activation pathway.

The results of the time-delayed cross-correlation analysis are presented at two levels of granularity: Figure 4.53 shows the residue-level directional cross-correlation maps for the G protein-bound (A) and β-arrestin-bound (B) activation pathways, along with their difference (C), using a time lag of 5 simulation cycles. Figures 4.54-4.55 present the corresponding Segment-level analysis with cross-correlation maps in panels A and C, and directional influence networks in panels B and D. These maps reveal asymmetric interaction patterns that reflect directional allosteric communication across the receptor. To further interpret these relationships at a higher level, we computed segment-averaged delayed correlations and visualized the results as directional influence networks (Figure 4.54B and 4.55B). In these networks, arrows point from the driving segment to the driven segment, with the arrow color indicating the nature of the delayed correlation—red for positive, suggesting coordinated movement, and blue for negative, indicating opposing motions. This segment-level view provides a mechanistic

framework for understanding how information propagates through distinct regions of the receptor during activation along different signaling pathways.

In the G protein-targeting simulations (Figure 4.54), several extracellular and intracellular domains emerged as prominent drivers. ECL1 exhibited a central role, positively driving multiple regions including TM4-EC, ECL3, and TM6-IC, indicating that it serves as an important modulator linking extracellular ligand binding to intracellular signaling responses. Interestingly, Helix 8 acted both as a target and a driver: it was positively driven by ICL1 and TM2-IC, while also positively influencing ECL1 and TM1-EC. This bidirectional involvement of Helix 8 underscores its crucial role as a signaling relay hub connecting the intracellular interface to upper transmembrane segments. On the negative side, TM6-IC was repeatedly targeted by TM1-IC, ICL1, and TM2-IC, suggesting that its outward displacement—a hallmark of G protein engagement—is tightly modulated by anticorrelated movements in adjacent intracellular loops. ECL1, despite being a strong driver, was also the recipient of negative signals from TM6-IC, TM4-EC, and ECL3, hinting at a potential feedback mechanism regulating its influence over downstream structural segments.

In contrast, the β-arrestin-targeting simulations (Figure 4.55) revealed a more distributed and loop- and helix-end–dominated network of drivers. TM1-IC and ICL1 emerged as prominent initiators of positive influence toward other intracellular domains, such as TM2-IC and TM7-EC, indicating that early intracellular rearrangements propagate outward toward the extracellular surface. Several loop regions, including ECL1, ICL2, and ECL2, also acted as sources of positive delayed influence. Notably, TM3-EC and TM7-EC—both located on the extracellular side—helped shape the dynamics of ICL2 and TM4-IC, pointing to a more complex interconnection between extracellular loops and intracellular transducers in this pathway. Negative influences were notably concentrated around TM3-IC, which exerted anticorrelated control over multiple regions including ICL2, ECL3, and TM7-EC. This suggests that TM3 may act as a regulatory gate, dampening motions in adjacent structural segment to stabilize a β-arrestin-competent conformation. Additionally, Helix 8—a critical player in G pro-

tein signaling [44] —was primarily a target of negative influence in the β-arrestin case, particularly from TM3-EC, ECL3, and TM3-IC, indicating a reduced role or different conformational behavior during β-arrestin engagement.

Overall, these findings reveal distinct directional control architectures for each pathway: the G protein route is characterized by strong ECL1-driven and Helix 8-integrated signaling, while the β-arrestin route exhibits loop-centric, multi-source regulation with reduced Helix 8 engagement. The directional network view offers a mechanistic interpretation of how the same receptor structure may selectively channel conformational energy along divergent functional routes, consistent with the concept of biased signaling.

We investigate time-delayed cross-correlation patterns for ADRB1 and ACM2 in Figures 4.56-4.57, highlighting pathway-specific differences in the temporal ordering of dynamic interactions between structural segments. Time-delayed cross-correlation analysis of the β1-adrenergic receptor (ADRB1) reveals distinct driver–responder relationships that vary depending on the signaling pathway. In the G protein–targeted transition, ECL3 emerges as a central dynamic driver, exerting a positive influence on ICL1, TM2-IC, and helix 8. This suggests that extracellular signals propagate inwardly through coordinated motions, potentially facilitating intracellular rearrangements needed for G protein coupling. Notably, this is consistent with structural evidence that ECL3 plays a role in ligand-induced stabilization of transmembrane helices, particularly in active G protein–bound states [22]. In contrast, the β-arrestin–targeted transition features ECL3 and ECL1 driving motion in helix 8 and TM7-IC, elements implicated in arrestin binding and receptor desensitization. These observations align with the conformational rearrangements described in [27], where helix 8 tilts downward and repositions to accommodate arrestin binding, often without the extensive outward movement of TM6 seen in G protein coupling. The emergence of helix 8 as a convergence point for both positive and negative delayed influences (e.g., ECL1 $\rightarrow$ helix 8; TM1-EC $\rightarrow$ helix 8 in opposing fashion) suggests that its dynamic regulation is finely tuned based on the target signaling partner.

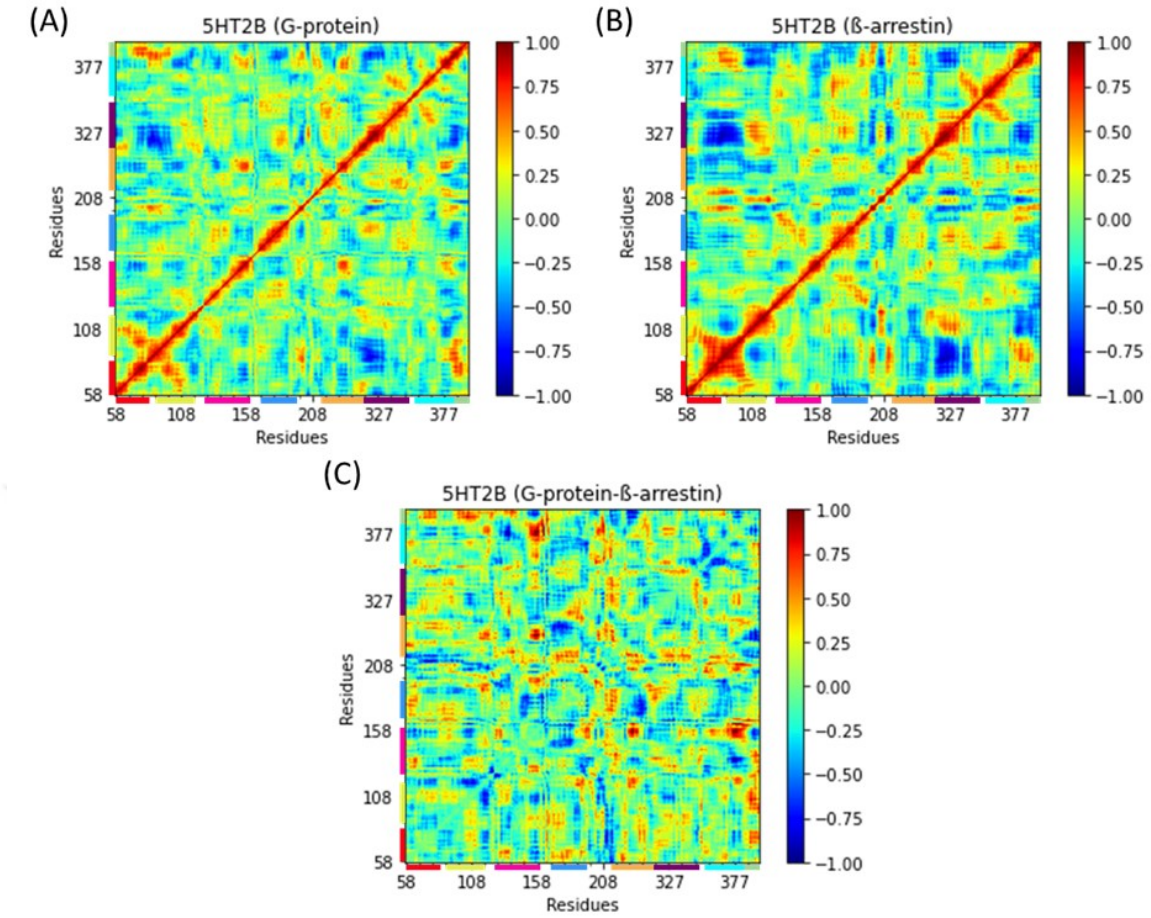

Figure 4.53. Time-delayed dynamic cross-correlation maps for 5HT2B activation. A delay of 5 steps was applied to capture directional influence from residue i to j. (A) G protein-bound pathway; (B) β-arrestin-bound pathway; (C) Difference map. Red/blue indicate positive/negative delayed correlations. TM regions colored as in Figure 4.41.

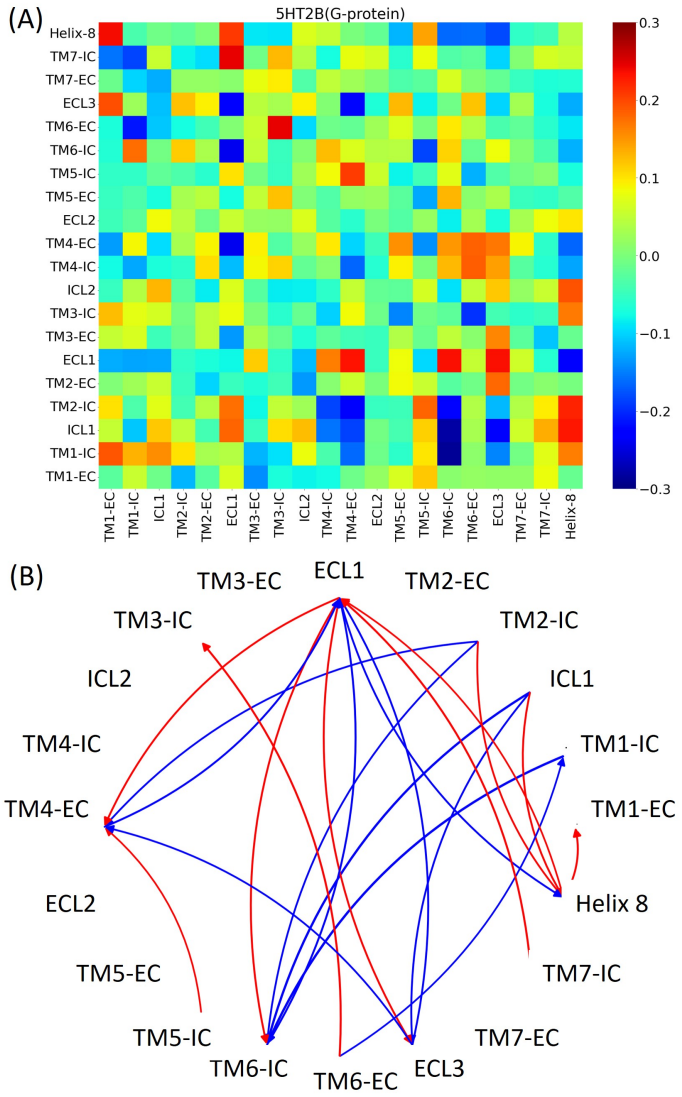

Figure 4.54. Segment-level time-delayed cross-correlation for 5HT2B G protein–targeted activation. A delay of 5 steps (out of 20) was used to assess motion ordering. (A) Segment-averaged delayed correlation map. (B) Directional influence network; arrows indicate precedence in motion.

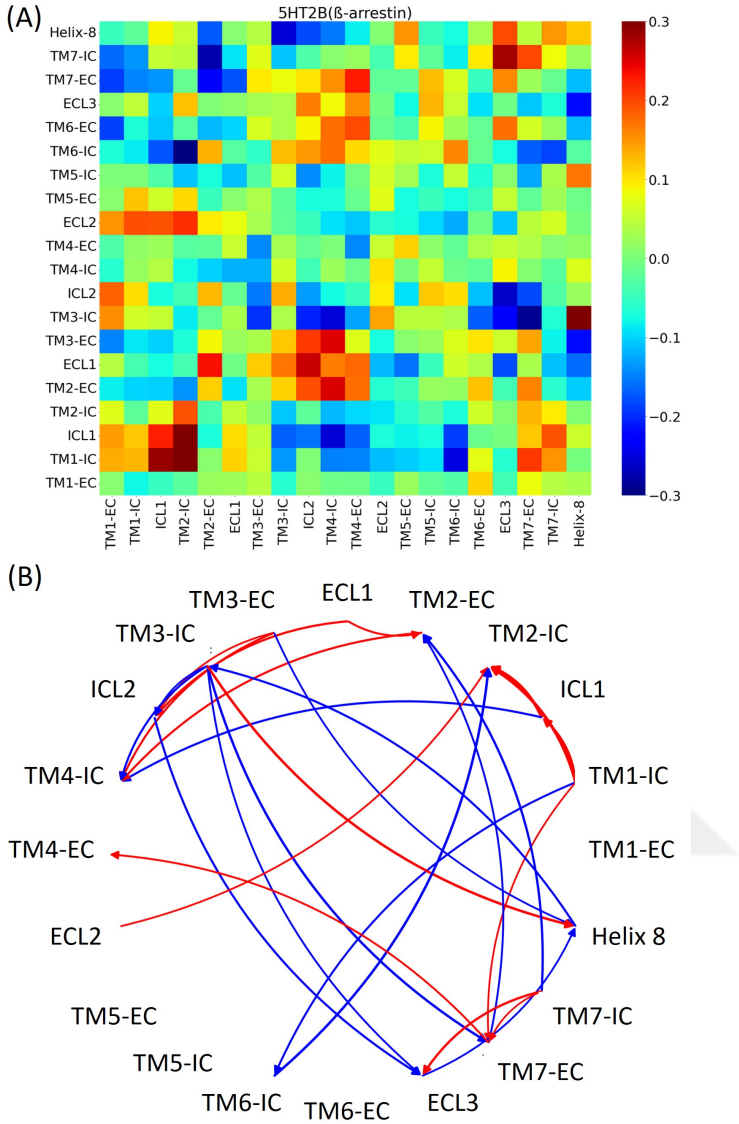

Figure 4.55. Segment-level time-delayed cross-correlation for 5HT2B β–arrestin-targeted activation. A delay of 5 steps (out of 20) was used to assess motion ordering. (A) Segment-averaged delayed correlation map. (B) Directional influence network; arrows indicate precedence in motion.

Interestingly, the negative influence from ECL3 to ECL1 and TM6-IC in the G protein pathway may reflect competitive or compensatory inter-loop interactions, possibly acting to restrict excess extracellular flexibility during productive coupling. These findings collectively highlight ECL3 as a dynamic initiator and helix 8 as a flexible

modulator, with their pathway-specific coupling patterns underscoring the mechanistic divergence between G protein and β-arrestin signaling in ADRB1.

Time-delayed dynamic cross-correlation analysis of the M2 muscarinic receptor (ACM2) reveals clear distinctions in the temporal ordering of inter-segment interactions between the G protein– and β-arrestin–targeted activation pathways. In the G protein–targeted transition, TM7-IC positively drives ICL2, suggesting that intracellular rearrangements near TM7 precede conformational changes in the G protein–coupling interface. This directional relationship supports findings from [19], where TM7 and the conserved NPxxY motif were implicated in early conformational priming for G protein engagement. Additionally, TM4-EC driving TM4-IC suggests a top-down mechanical relay along the same helix, potentially reinforcing intra-helical rigidity during receptor activation. In contrast, the β-arrestin–targeted pathway shows a strikingly different pattern centered on TM7-EC, which is the recipient of multiple negative delayed influences from TM5-EC, TM6-EC, TM4-EC, and ECL3. This configuration suggests that TM7-EC movement is temporally suppressed or constrained by upstream extracellular dynamics in the β-arrestin pathway. Given structural evidence that TM7 adopts a distinct orientation during β-arrestin engagement, and that helix 8 and TM7 together form a key arrestin-binding interface, these findings imply that extracellular regulation of TM7 may be a critical control point during biased signaling. Furthermore, the positive influence from TM6-IC to TM7-EC aligns with structural models where cytoplasmic TM6 rearrangement precedes changes at the extracellular TM7 end, possibly facilitating selective arrestin recruitment [23].

Taken together, these results highlight TM7 as a dynamic convergence hub, where G protein–targeted transitions are initiated intracellularly, while β-arrestin–targeted transitions involve extracellular modulation of the TM7 region. The distinct flow of conformational precedence along TM7 reinforces its dual role in mediating allosteric communication across the membrane and in guiding signaling specificity in ACM2.

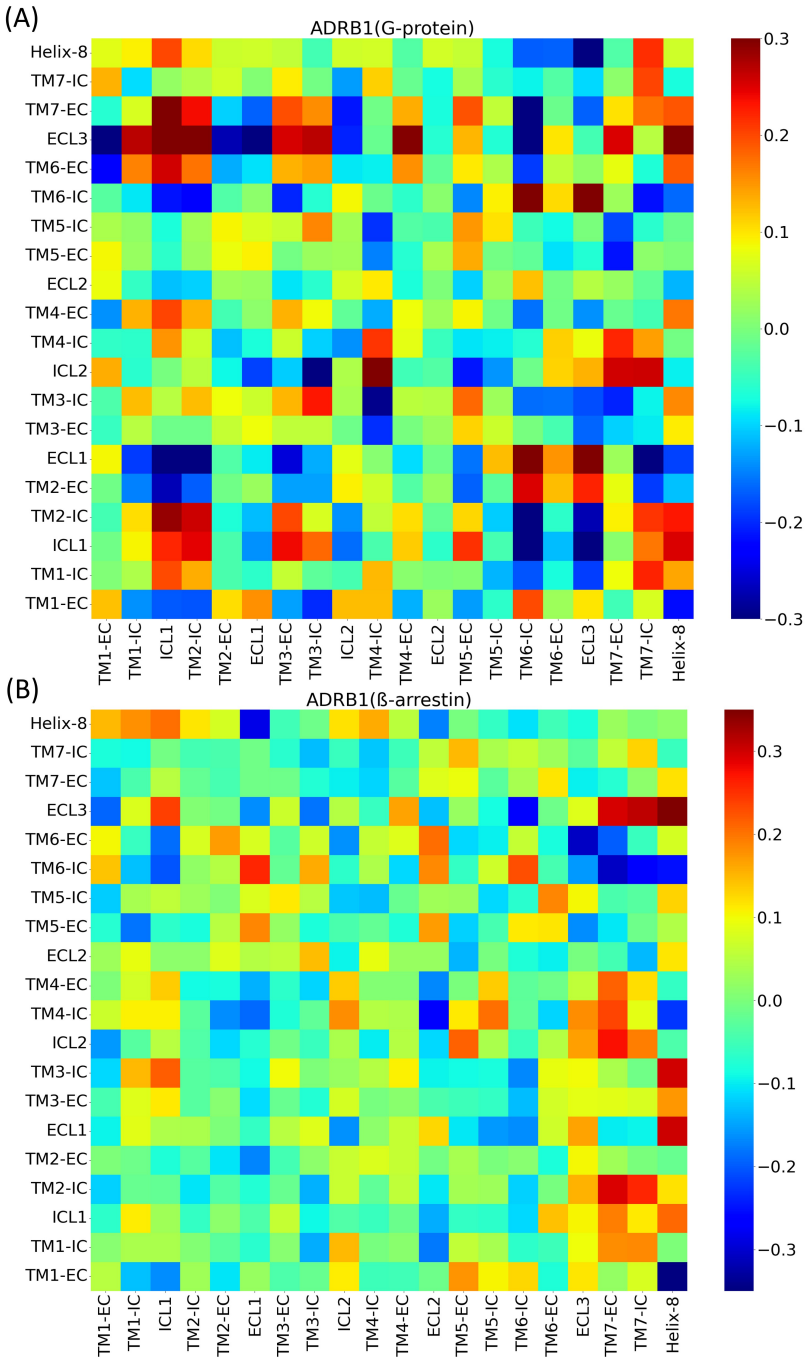

Figure 4.56. Segment-level time-delayed dynamic cross-correlation analysis of ADRB1. Panels (A) and (B) show the directional dynamic interactions for ADRB1 during the G protein–bound ($\tau = 6$) and β-arrestin–bound ($\tau = 6$) transitions, respectively.

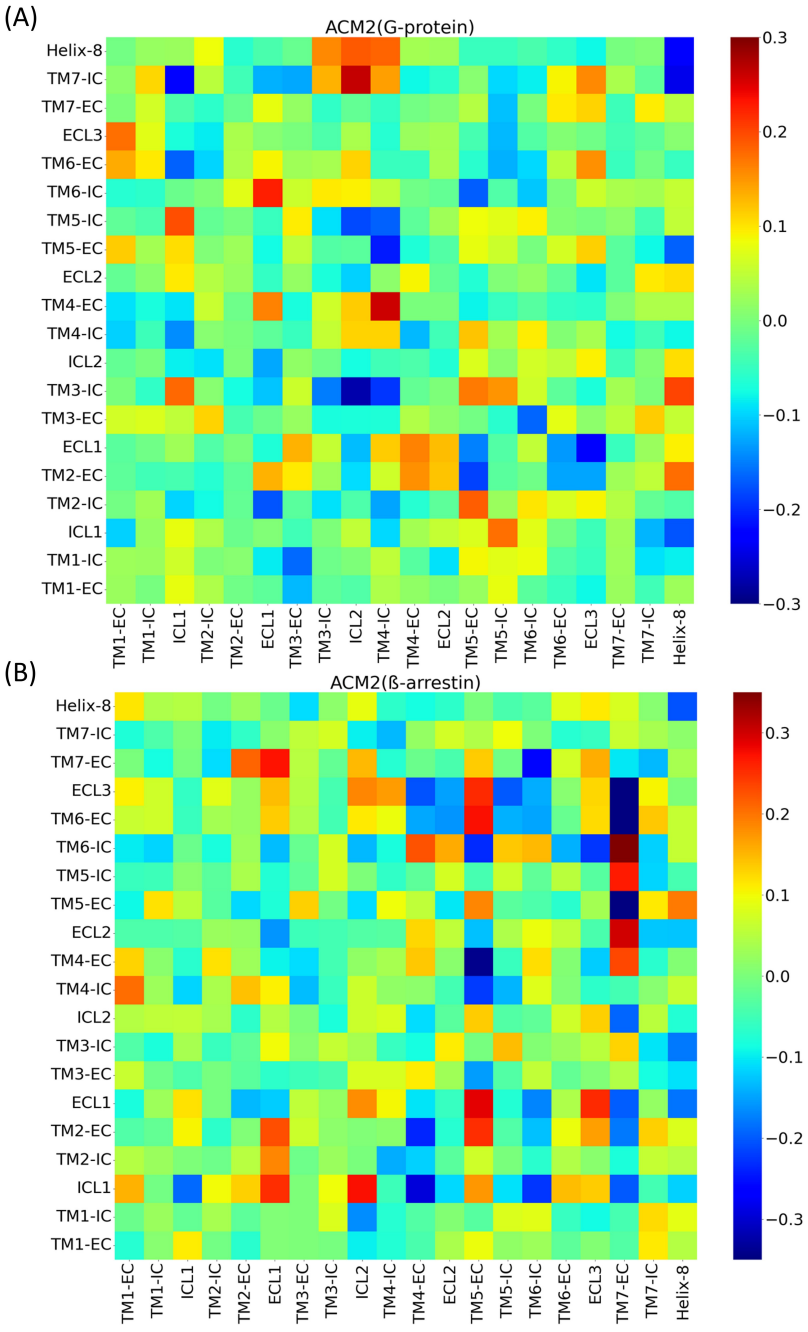

Figure 4.57. Segment-level time-delayed dynamic cross-correlation analysis of ACM2 activation pathways. Panels (A) and (B) present corresponding results for ACM2, with time delays of $\tau = 7$ for the G protein–bound transition and $\tau = 4$ for the β-arrestin–bound transition.

4.2.4. Information Flow and Allosteric Communication

Allosteric communication plays a fundamental role in regulating the function of GPCRs, enabling distant ligand-binding events to influence intracellular signaling. To capture the directionality and magnitude of this communication, we employed a GNM-Transfer Entropy (GNM-TE)-based approach that quantifies information flow between residue pairs [37, 144, 145]. Unlike static correlation metrics, TE allows for the detection of asymmetrical dependencies and causal influences, offering a dynamic perspective on allosteric signaling. Here, we applied TE analysis to the 5HT2B receptor in both its G protein-bound and β-arrestin-bound states to uncover key information-sending and -receiving residues, identify allosteric hotspots, and evaluate differences in communication networks driven by distinct signaling partners.

To investigate how information is transmitted through the 5HT2B receptor during activation, we computed Net Transfer Entropy (Net TE) matrices in 1-10 modes for both G protein-bound and β-arrestin-bound states (Figure 4.58A–B). To facilitate interpretation, we aggregated Net TE values at the chain level. (Figure 4.58C–D), summarizing how information is exchanged between major structural components. In these 2D maps, TE values from effector residues (Y-axis) to affected residues (X-axis) are color-coded. Red indicates high outgoing information flow, while blue denotes low flow. In the G protein-bound complex, these chains include the receptor (Chain R), Gαq (Chain B), Gβ (Chain C), and Gγ (Chain D), while in the β-arrestin-bound complex, information exchange is mapped between the receptor (Chain R) and β-arrestin1 (Chain C) [27]. In the G protein-bound state, the primary sources of information flow were identified as the receptor itself and the Gβ subunit. The receptor was found to transmit the highest amount of information to the Gγ subunit, but also sent information to other regions of the complex. In the β-arrestin-bound state, the receptor again emerged as the major information source. Although the β-arrestin region does transmit some information back to the receptor, it also receives substantial information, resulting in an overall net information outflow that averages out at the chain level. TEcol scores integrate both the Net TE values (i.e., the magnitude of net information

transmitted by a residue) and the degree of collectivity (i.e., the number of residues affected by the information, see Methods for details). These scores were calculated for both G protein- and β-arrestin-bound structures to identify key allosteric nodes. Residues with high TEcol scores appear as sharp peaks in Figures 4.59. These peaks were compared to a curated list of functionally conserved residues and ligand-binding sites. Red circles indicate TEcol peaks, with solid red circles denoting exact matches to known functional residues or binding sites, and teal circles highlighting residues within 4 Å of such sites. Structures on the right are color-coded according to the TEcol score per residue, with blue and red indicating low and high allosteric output, respectively.

3D representations further visualize TEcol scores mapped onto the receptor structures, revealing state-specific allosteric hotspots. Interestingly, in both activation states, the predicted allosteric hotspots tend to cluster around the ligand-binding site. This observation is both intriguing and expected: intriguing because the complexes engage different signaling proteins, yet predictable due to the shared involvement of conserved receptor regions and the ligand-binding pocket. Residues with TEcol values exceeding both the mean score and average peak prominence were classified as allosteric hotspots. To validate the accuracy of the GNM-TE predictions, we examined the overlap between predicted hotspots and experimentally or evolutionarily validated functional sites. Notably, 6 out of 10 predicted allosteric hotspots in the G protein-bound structure and 6 out of 11 in the β-arrestin-bound structure aligned with known conserved or ligand-interacting residues. Among these, residues such as A99$^{2.49}$ (near the conserved sodium-binding site D1002.50), T140$^{3.37}$ (near the S139$^{3.36}$ ligand-binding site), and A225$^{5.46}$ (ligand-binding site) were identified. An exact match was found at F333$^{6.44}$, a component of the PIF motif, in the G protein-bound structure, with its neighbor M336$^{6.47}$ appearing in the β-arrestin-bound case. Additionally, S372$^{7.45}$, located in the conserved sodium-binding site, was also marked as an allosteric peak. These findings demonstrate the robustness of GNM-TE analysis in capturing functionally relevant allosteric communication pathways across distinct receptor activation states.

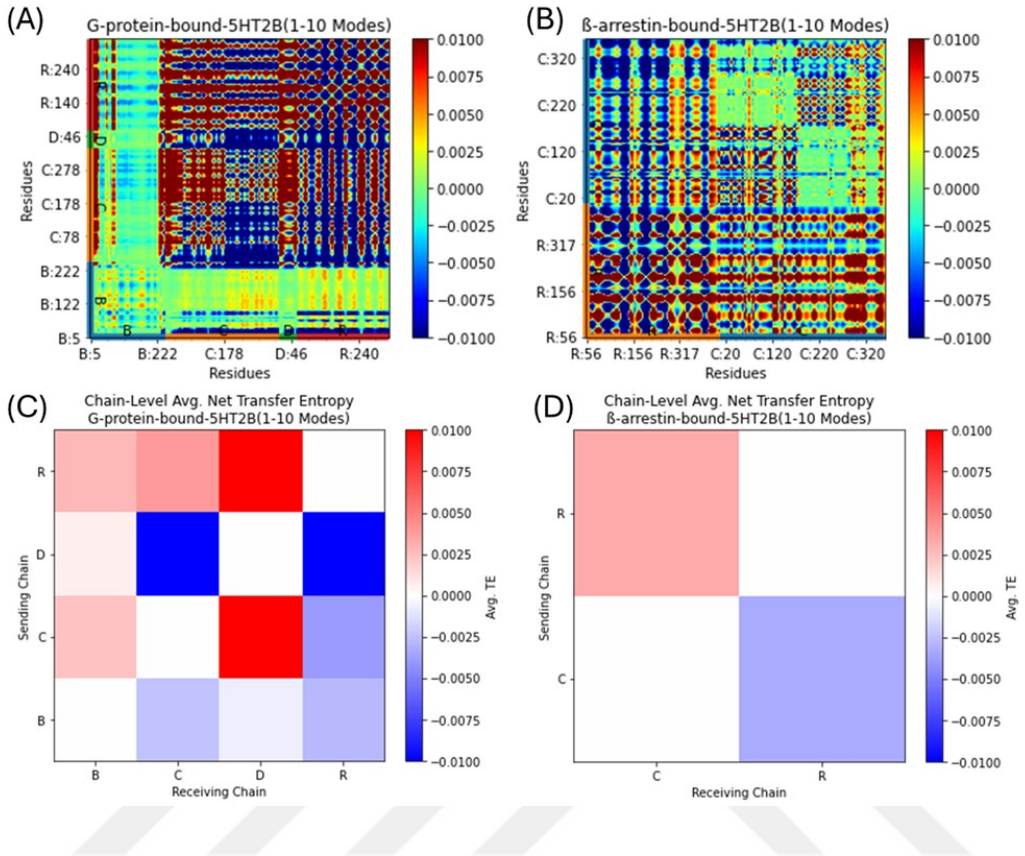

Figure 4.58. Transfer Entropy (TE) analysis of 5HT2B in modes 1–10. (A–B) Net TE matrices for G protein-bound (7SRR) and -arrestin-bound (7SRS) states. (C–D) Segment-level Net TE maps showing directional information flow between structural regions for G protein-bound (7SRR) and β-arrestin-bound (7SRS) states.

Importantly, two allosteric hotspots located in functionally uncharacterized regions were also identified through GNM-TE analysis. One of these, T68$^{1.46}$, was consistently detected in both the G protein-bound and β-arrestin-bound states, suggesting a potential state-independent role in the receptor's signaling dynamics. The other hotspots, I182$^{4.52}$ (in the G protein-bound structure) and I186$^{4.56}$ (in the β-arrestin-bound structure), were found in close spatial proximity to each other. These residues, although not previously recognized as functionally essential, may play critical roles in modulating the signaling mechanisms of the 5HT2B receptor. Their identification as allosteric peaks highlight the potential of GNM-TE to uncover novel functional sites that warrant future experimental investigation.

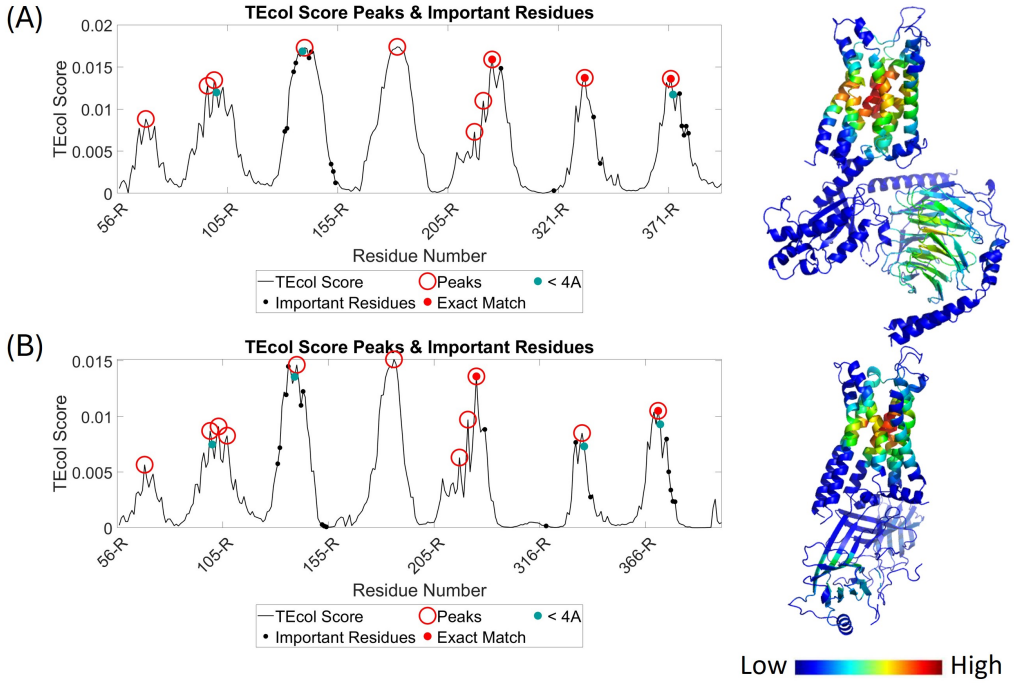

Figure 4.59. Demonstration of TEcol scores across residue indices for the G protein-bound (A) and β-arrestin-bound (B) states.

To assess the statistical significance of these predictions, we generated 100,000 sets of 10 and 11 randomly localized allosteric hotspots for the G protein-bound and β-arrestin-bound cases, respectively. For each set, we calculated how often these randomly assigned positions coincided with functionally important residues. As shown in Figure 4.60, the GNM-TE predictions significantly outperformed the random models. While GNM-TE correctly predicted 6 out of 10 and 6 out of 11 functional residues for the G protein- and β-arrestin-bound states, the corresponding distributions of random guesses had mean values of only 2.54 and 2.67, with p-values of 0.041 and 0.048, respectively. These results confirm that the observed agreement is unlikely to be due to chance and underscores the predictive power of GNM-TE in identifying true allosteric hotspots.

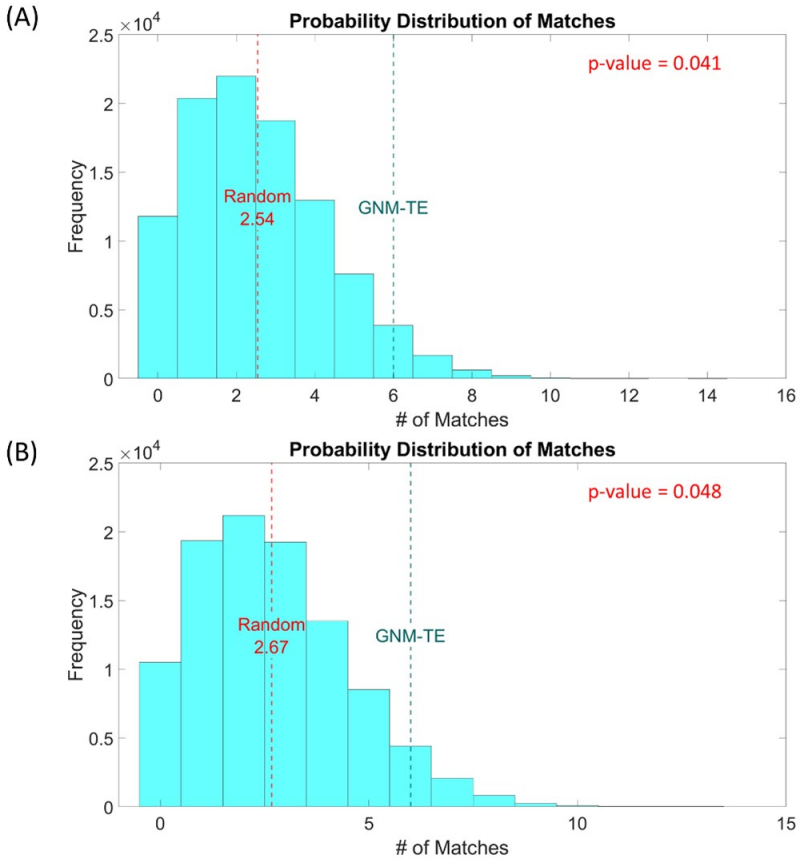

Figure 4.60. Statistical validation of GNM-TE predicted allosteric hotspots. Histograms show overlap between random residue sets (n=100,000) and functional residues for (A) G protein-bound and (B) β-arrestin-bound states. Dashed lines mark overlap from GNM-TE predictions (6 matches); means of random distributions are 2.54 and 2.67, respectively.

We also analyzed GNM-TE using different mode regimes to assess the consistency and resolution of information flow predictions (Figure 4.61). In the G protein-bound state, the 2–10 mode regime revealed information is broadly distributed, with both the Gαq subunit and the receptor's orthosteric site emerging as dominant sources of allosteric signaling (Figure 4.62). Notably, residues between TM3 and TM4 consistently function as high-output nodes across multiple mode regimes, indicating their critical role in coupling ligand binding to downstream signaling. The TEcol analysis further highlights the involvement of core transmembrane helices (TM1, TM2, TM3, TM4, and

TM7) and ICL2 as information-sending elements. Interestingly, under the 3–10 mode regime, Gγ also appears as a major source, suggesting mode-specific modulation of communication pathways and subunit contributions. Additionally, residues within the receptor core formed by TM1, TM2, TM3, TM4, and TM7, along with the intracellular loop 2 (ICL2), were identified as significant contributors to information transmission.

In contrast, the β-arrestin-bound state is characterized by a more focused and centralized flow of information, with β-arrestin itself acting as the principal sender in 2-10 and 3-10 mode regimes (Figure 4.63). This suggests a more directed or possibly feedback-oriented interaction between β-arrestin and the receptor. Nonetheless, the receptor still participates in information propagation—particularly through TM3–TM4 residues and ICL2—emphasizing that the same intracellular region (ICL2) plays a prominent role regardless of the bound transducer (Figure 4.63). This observation aligns with prior findings that LSD-induced biased signaling requires conformational changes in ICL2 to engage distinct transducers. Notably, we also observe strong information flow from the ICL2 region in the G protein-bound state, further supporting its dual functional role in coordinating both G protein and β-arrestin interactions. The consistent identification of ICL2 as an allosteric source across activation contexts suggests it may serve as a dynamic hub facilitating receptor-specific signaling bias.

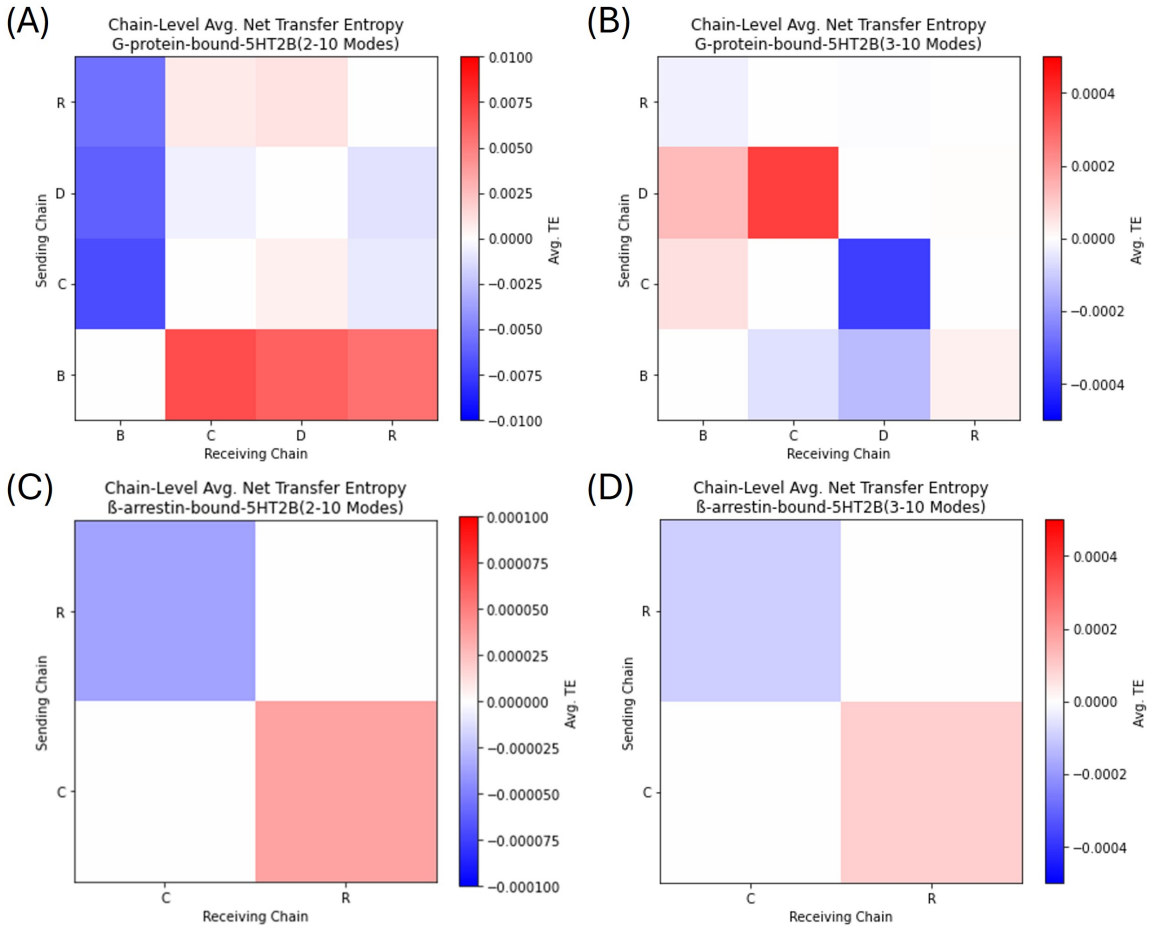

Figure 4.61. Chain-level net transfer entropy (Net TE) maps for G protein– and β-arrestin–bound states. Panels (A) and (B) show Net TE maps for the G protein–bound state, calculated using mode ranges 2–10 and 3–10, respectively. Panels (C) and (D) present the corresponding Net TE maps for the β-arrestin–bound state, using the same mode ranges.

From the ligand-binding region to the receptor binding: To further understand how identical ligand binding events can lead to distinct signaling outcomes, we analyzed the direction and localization of information transfer from the ligand-binding region to the receptor–signaling complex across different mode regimes (Figure 4.64). Although the same orthosteric ligand is bound in both activation states, the downstream allosteric communication patterns differ significantly.

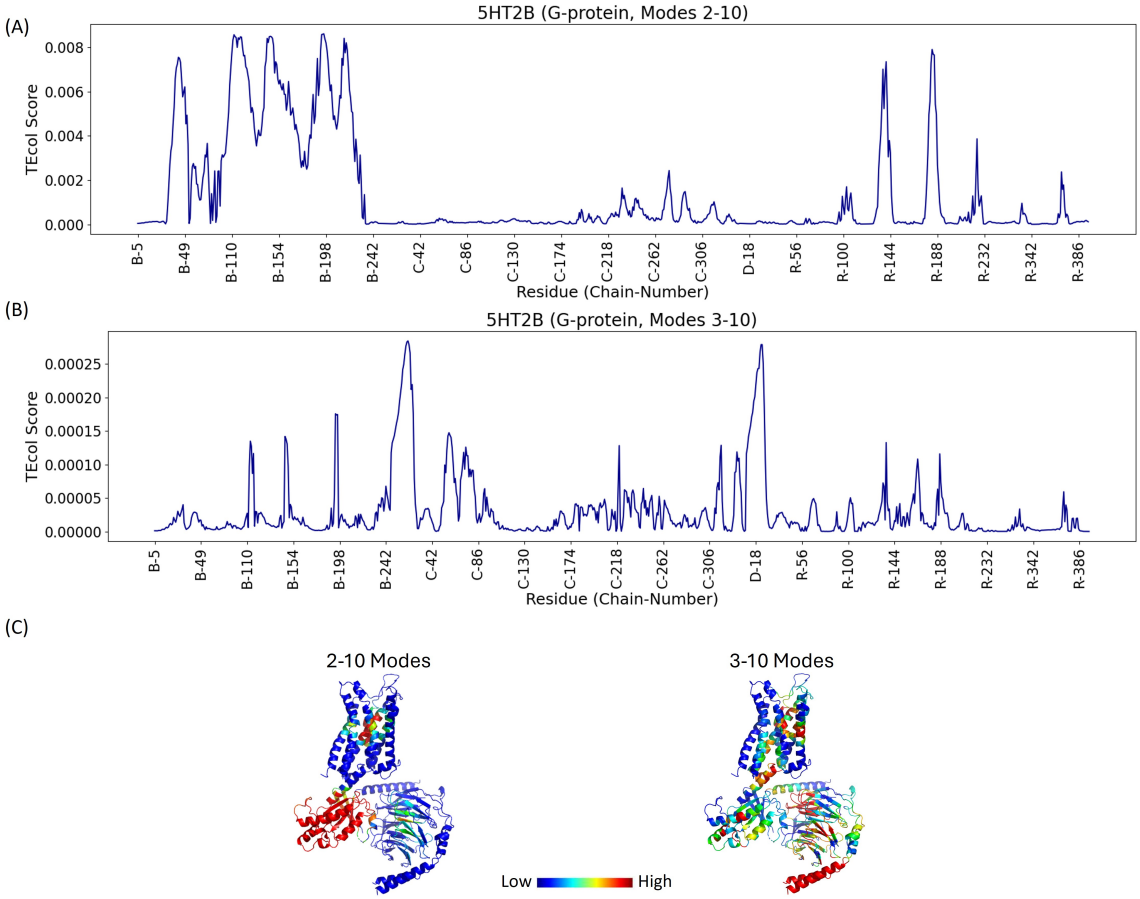

Figure 4.62. TEcol score profiles across residues for G protein– and β-arrestin–bound states. Panels (A) and (B) show the residue-wise TEcol scores, calculated using mode ranges 2–10 and 3–10, respectively. (C) Structures color-mapped by TEcol score with blue indicating residues with low and red indicating those with high allosteric output.

In the 1–10 mode regime, the G protein-bound structure exhibits intensified information flow from ligand binding site toward TM5-IC, TM6-IC, and helix 8—regions closely associated with G protein coupling. In contrast, the β-arrestin-bound receptor displays enhanced information reception from ligand binding site slightly below the core of TM1, TM2, TM3, TM5, TM6, and TM7. This shift may be attributed to the additional outward displacement of TM6 in the β-arrestin-bound state, which allows β-arrestin-1 not only to overlap with the Gq binding site but also to occupy a broader intracellular cavity.

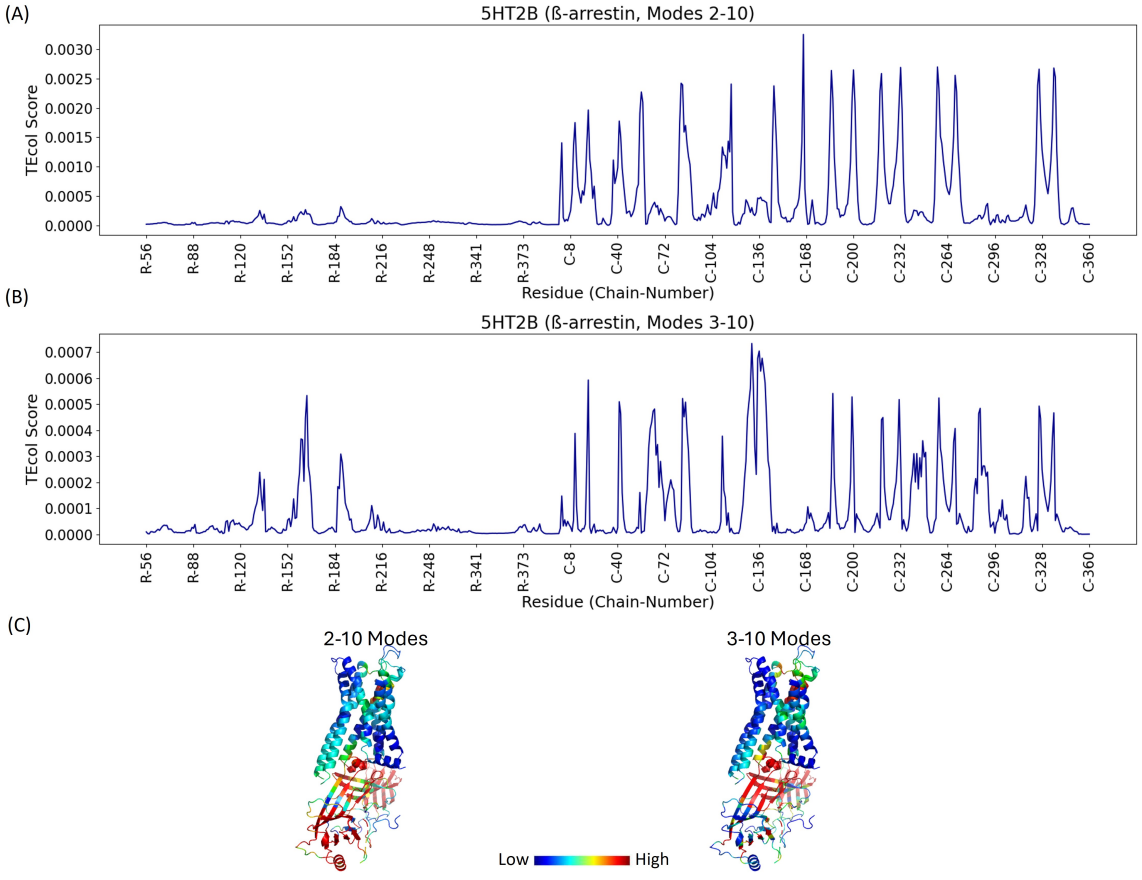

Figure 4.63. TEcol score profiles across residues for β-arrestin–bound states. Panels (A) and (B) show the residue-wise TEcol scores calculated using mode ranges 2–10 and 3–10, respectively. (C) Structures color-mapped by TEcol score with blue indicating residues with low allosteric output and red indicating those with high allosteric output.

This expanded binding footprint likely alters the topology of intracellular communication pathways. In the 2–10 mode regime, the G protein-bound structure transmits information from the ligand-binding site primarily to the extracellular halves of the transmembrane helices and to the Gβ and Gγ subunits. In contrast, the β-arrestin-bound structure exhibits increased information flow toward TM5-IC and TM6-IC, in addition to direct flow into the β-arrestin itself. In the 3–10 mode regime, the two signaling states show nearly identical information flow profiles, except for a localized difference beneath TM3—specifically below the orthosteric ligand-binding pocket. This

subtle divergence likely reflects transducer-specific fine-tuning and suggests that, despite binding at the same site, dynamic conformational changes dictate which intracellular signaling pathway is activated.

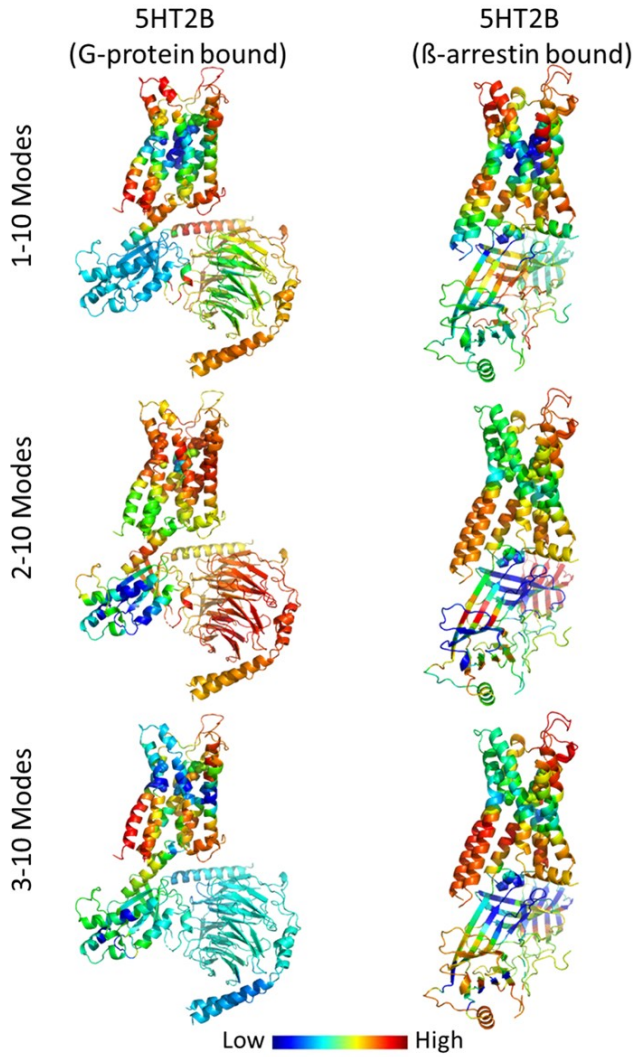

Figure 4.64. Information transfer from the ligand-binding region to the receptor–signaling complex across different mode regimes. Information flow was mapped onto structure using different mode regimes (1–10, 2–10, and 3–10 modes) for both the G protein-bound and β-arrestin-bound structures of the 5HT2B receptor. Ligand binding site is represented as spheres.

To evaluate whether the biased dynamic communication observed in the 5HT2B receptor generalizes to other GPCRs, we extended our GNM-TE analysis to two additional receptors: ADRB1 and ACM2 (Figures 4.65-4.74). For both receptors, Net TE maps at the residue and chain levels (Figures 4.65-4.72) revealed clear differences between the G protein– and β-arrestin–bound states, mirroring the pathway-specific information flow patterns previously identified in 5HT2B.

In the 1–10 mode range, which captures global and large-scale collective motions, distinct patterns of information flow emerged between the G protein– and β-arrestin–bound states. In the G protein–bound conformation, both the receptor and the Gβ subunit acted as major information sources. Notably, the receptor transmitted the highest amount of information to the Gγ subunit, reflecting strong outward communication from the receptor into the G protein heterotrimer. This broad distribution of net transfer entropy (Net TE) highlights the integrative role of the receptor as a central hub for activating downstream signaling partners.

In contrast, in the β-arrestin–bound complex, while the receptor remained the dominant information sender, β-arrestin itself exhibited moderate but detectable outgoing information flow, along with incoming communication from the receptor. This bidirectional interaction led to a more evenly distributed net TE profile at the chain level, reflecting a less hierarchical and more reciprocal dynamic relationship between the receptor and β-arrestin. These results suggest that, under low-frequency collective modes, G protein signaling is characterized by stronger unidirectional drive, whereas β-arrestin engagement establishes a more balanced dynamic coupling with the receptor.

Mode-specific trends revealed additional layers of communication dynamics. In the 2–10 mode range, information flow in the G protein–bound state was broadly distributed, with strong allosteric signaling from both the Gαq subunit and the receptor's orthosteric binding site, indicating a robust network of inter-subunit coordination. However, in the 3–10 mode range, the Gγ subunit emerged as a prominent information source, suggesting that low-frequency modes (2–10) favor central, large-scale

communication, while higher-frequency modes (3–10) may capture more peripheral or specialized signaling contributions. Notably, in the β-arrestin–bound state, β-arrestin itself consistently appeared as a major information source in both mode ranges, highlighting a receptor-to-arrestin signaling route that is more dominant than in the G protein pathway.

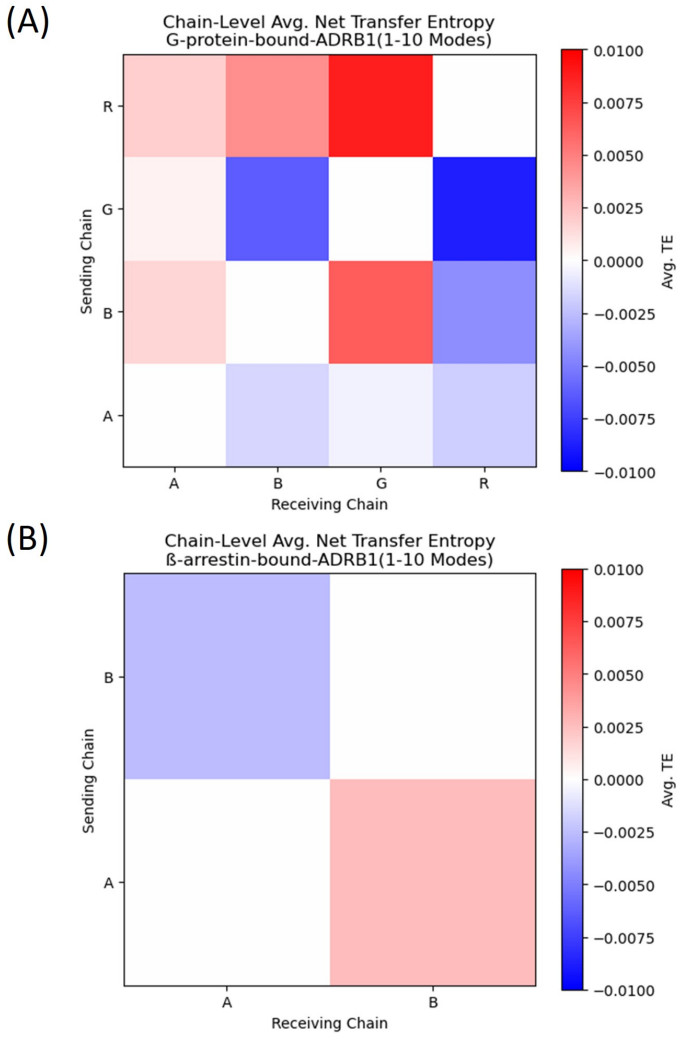

Figure 4.65. Chain-level Net transfer entropy (Net TE) analysis of ADRB1 for G protein– (A) and β-arrestin–bound (B) states in 1-10 mode subset.

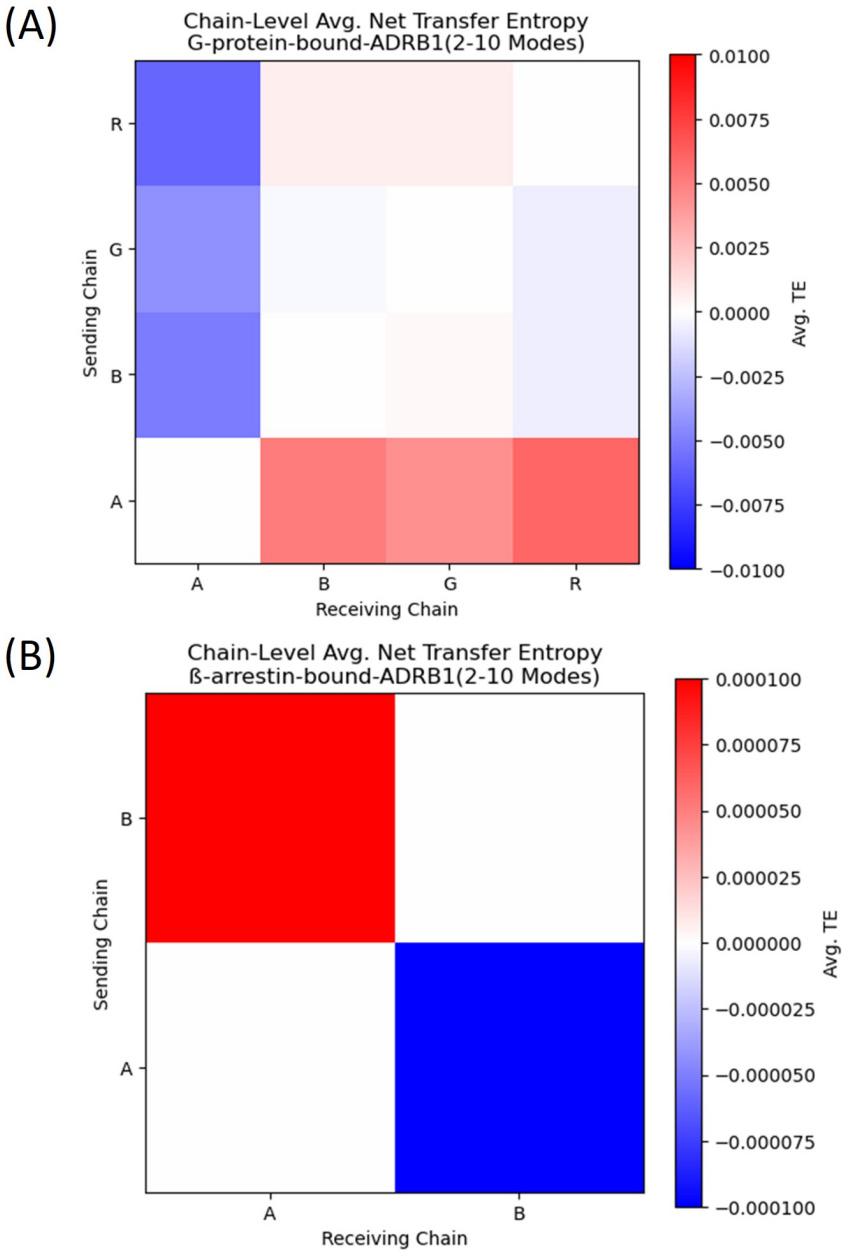

Figure 4.66. Chain-level Net transfer entropy (Net TE) analysis of ADRB1 for G protein– (A) and β-arrestin–bound (B) states in 2-10 mode subset.

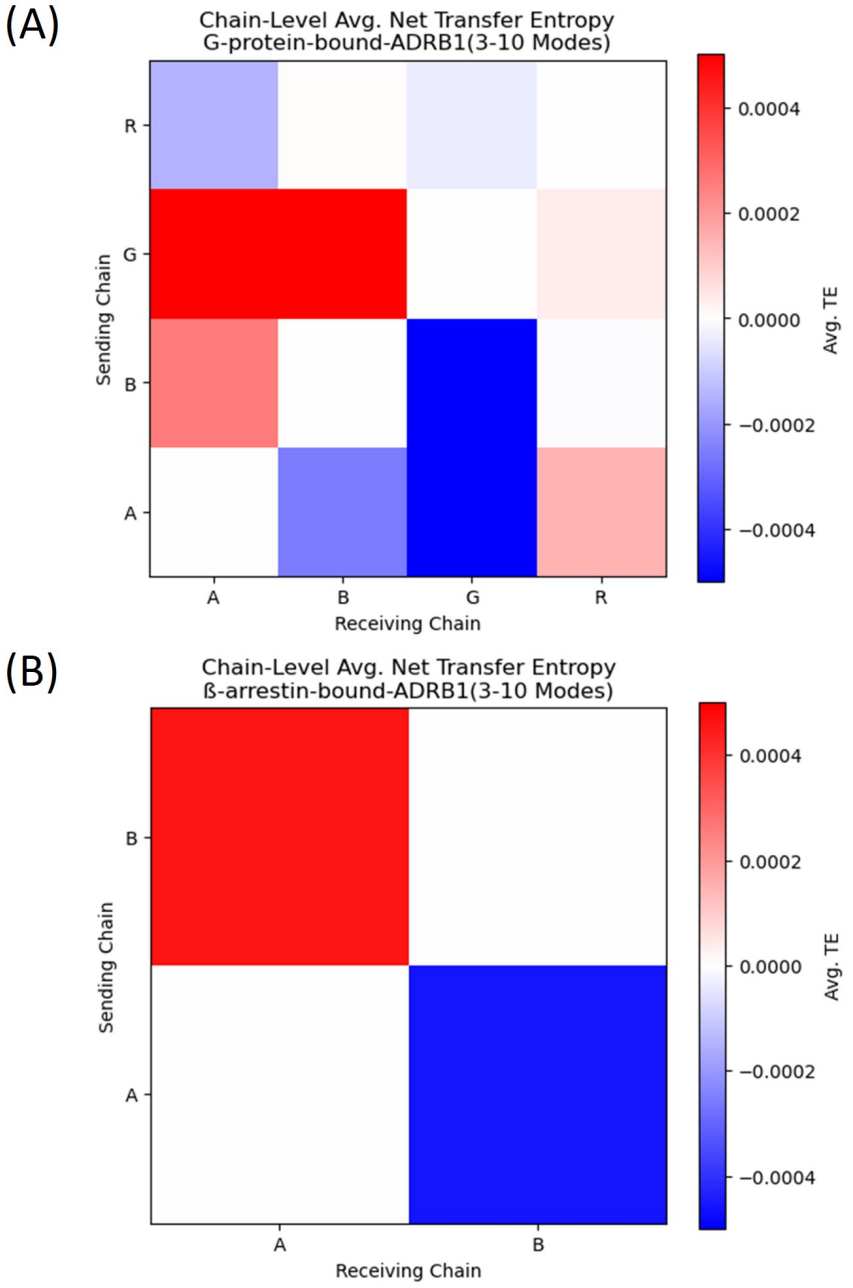

Figure 4.67. Chain-level Net transfer entropy (Net TE) analysis of ADRB1 for G protein– (A) and β-arrestin–bound (B) states in 3-10 mode subset.

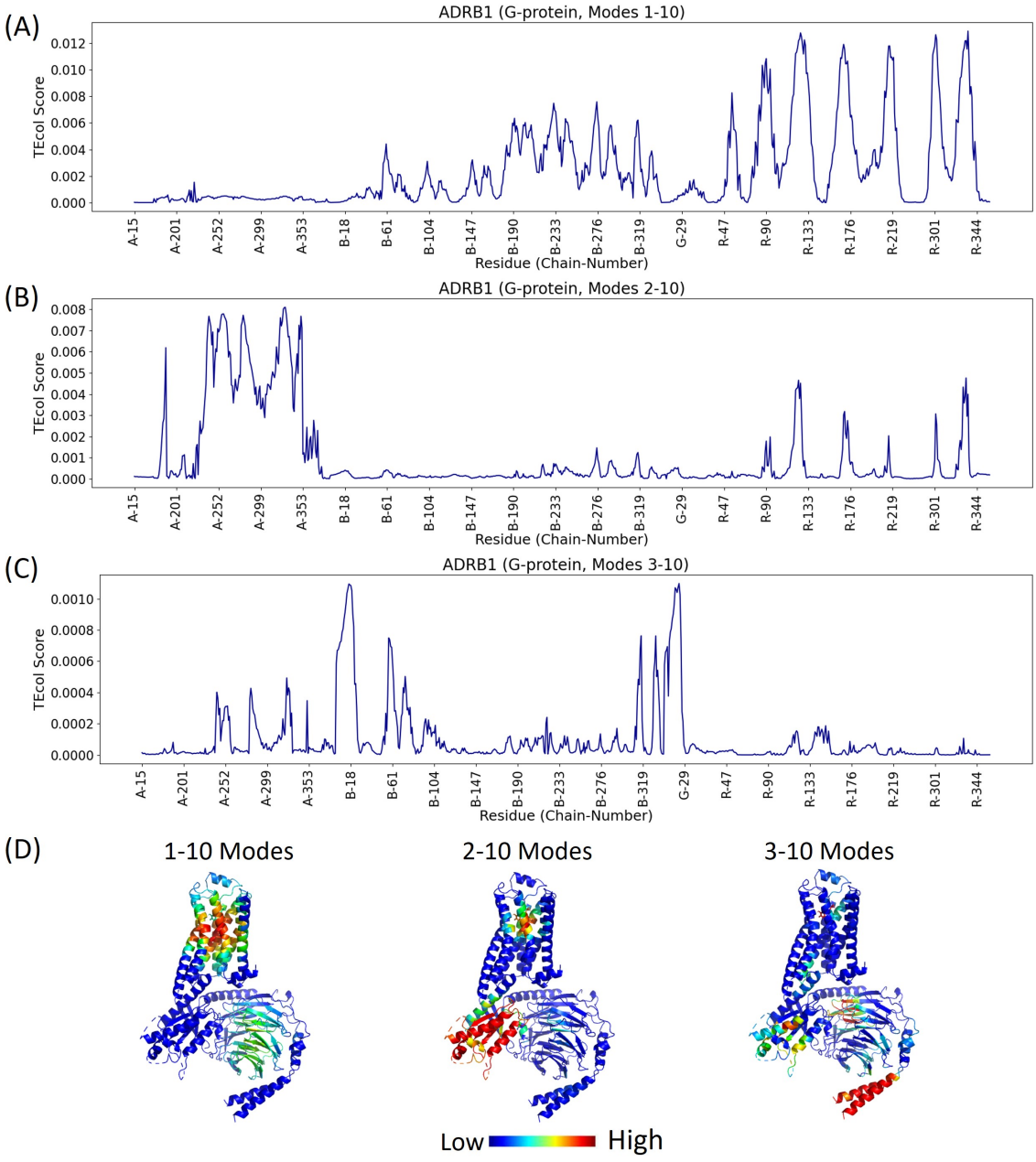

Figure 4.68. TEcol scores and structural mapping of information source residues for the G protein–bound state in ADRB1. Panels (A–C) show TEcol scores per residue, calculated using mode ranges 1–10, 2–10, and 3–10, respectively. Panel D display TEcol scores for the β-arrestin–bound state using the same mode ranges. (D) Structures color-mapped by TEcol score.

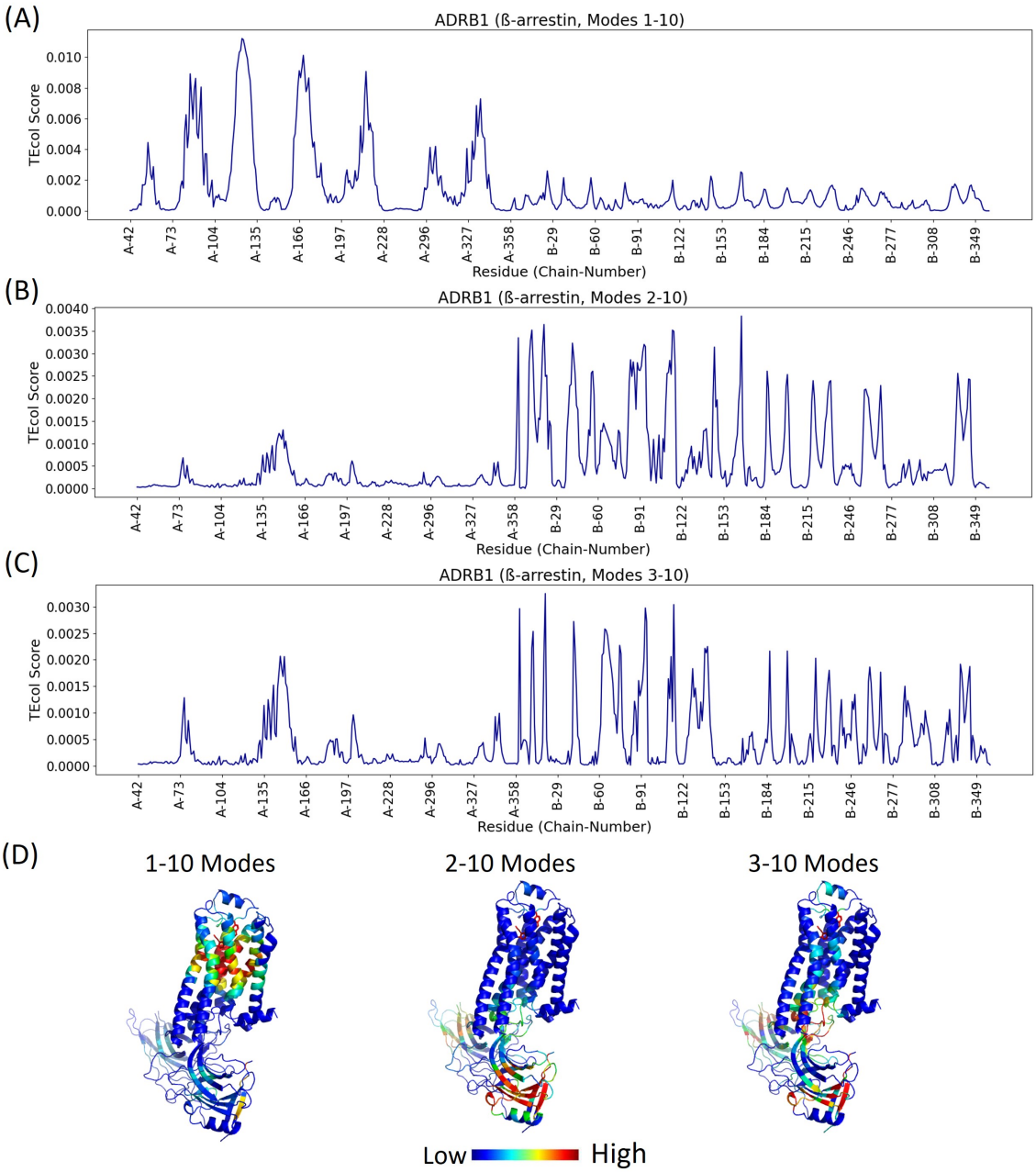

Figure 4.69. TEcol scores and structural mapping of information source residues for the β-arrestin state in ADRB1. Panels (A–C) show TEcol scores per residue, calculated using mode ranges 1–10, 2–10, and 3–10, respectively. Panel D display TEcol scores for the β-arrestin–bound state using the same mode ranges. (D) Structures color-mapped by TEcol score.

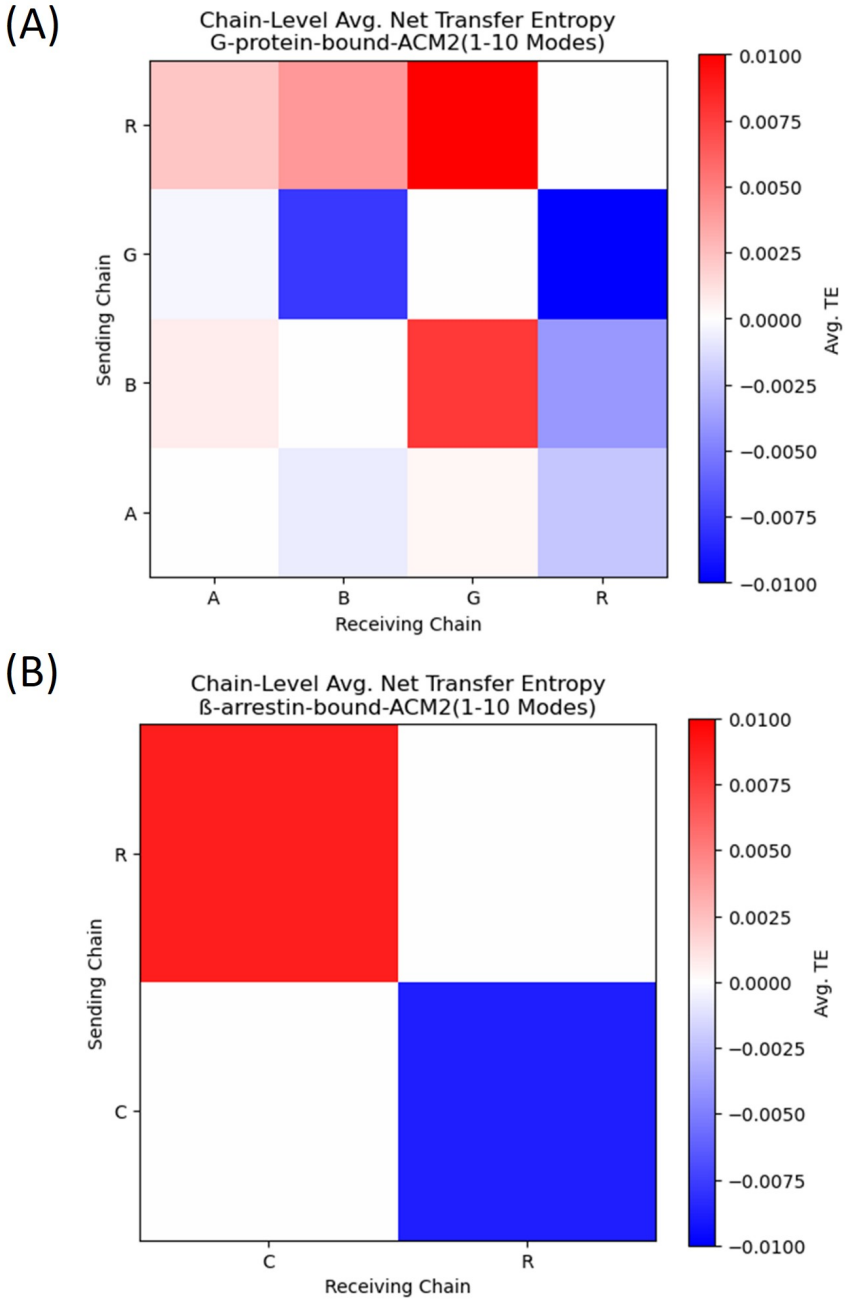

Figure 4.70. Chain-level Net transfer entropy (Net TE) analysis of ACM2 for G protein– (A) and β-arrestin–bound (B) states in 1-10 mode subset.

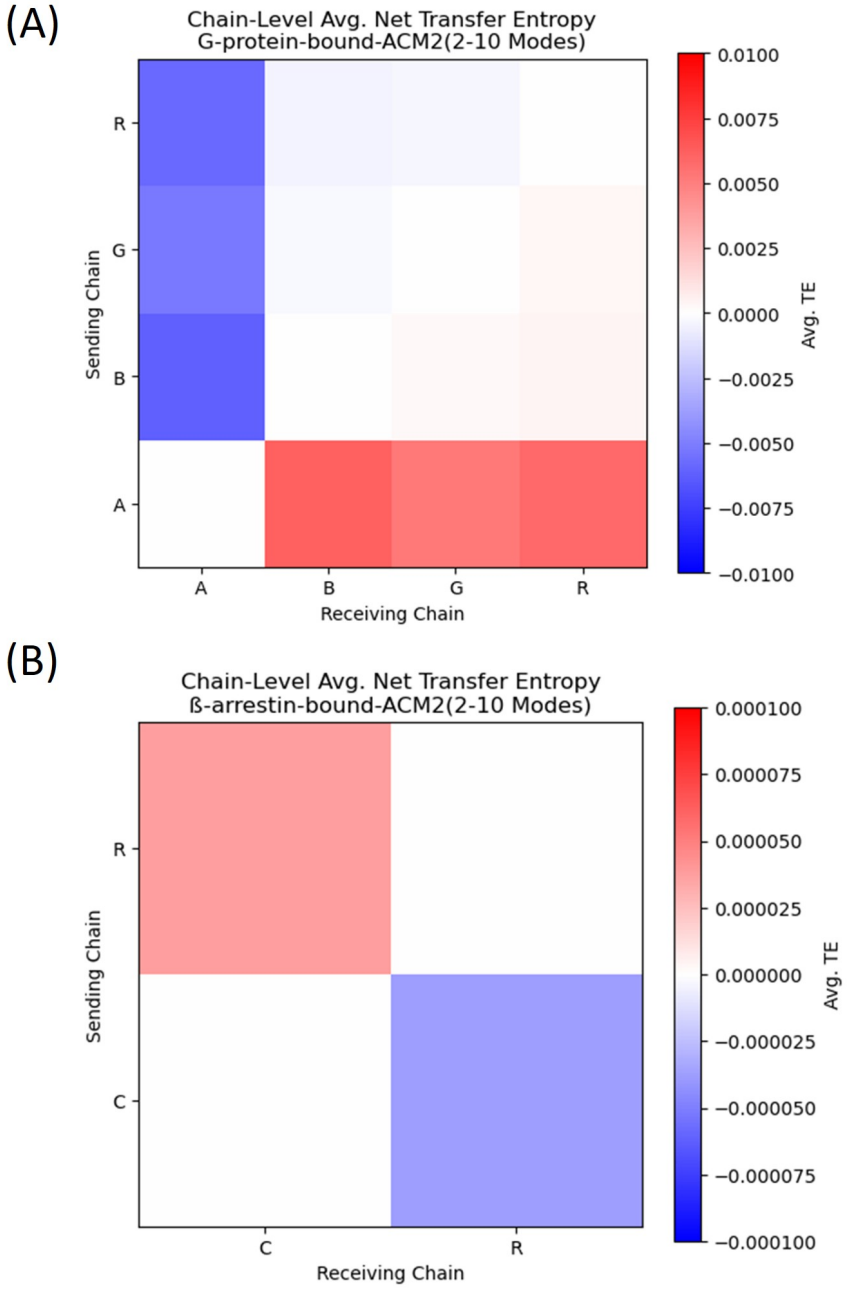

Figure 4.71. Chain-level Net transfer entropy (Net TE) analysis of ACM2 for G protein– (A) and β-arrestin–bound (B) states in 2-10 mode subset.

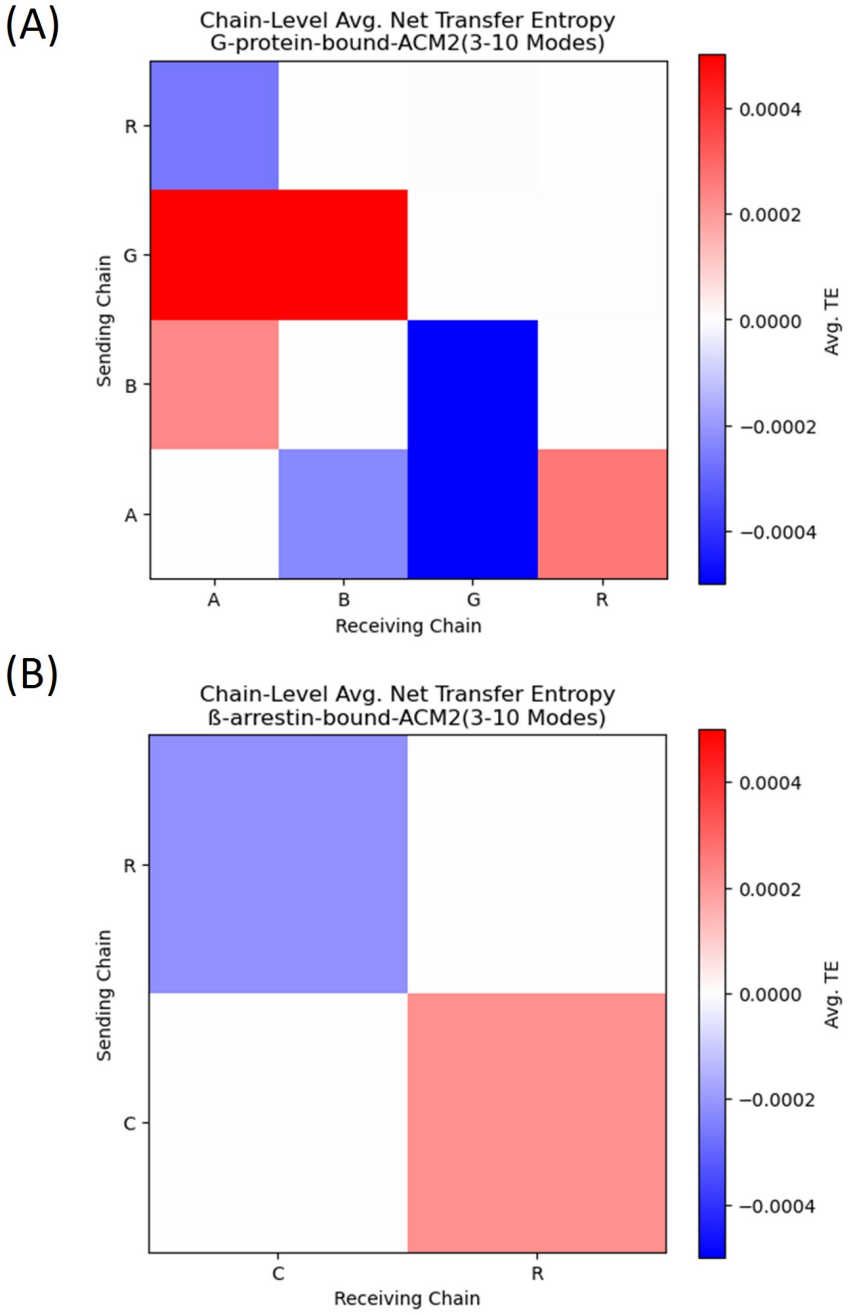

Figure 4.72. Chain-level Net transfer entropy (Net TE) analysis of ACM2 for G protein– (A) and β-arrestin–bound (B) states in 3-10 mode subset.

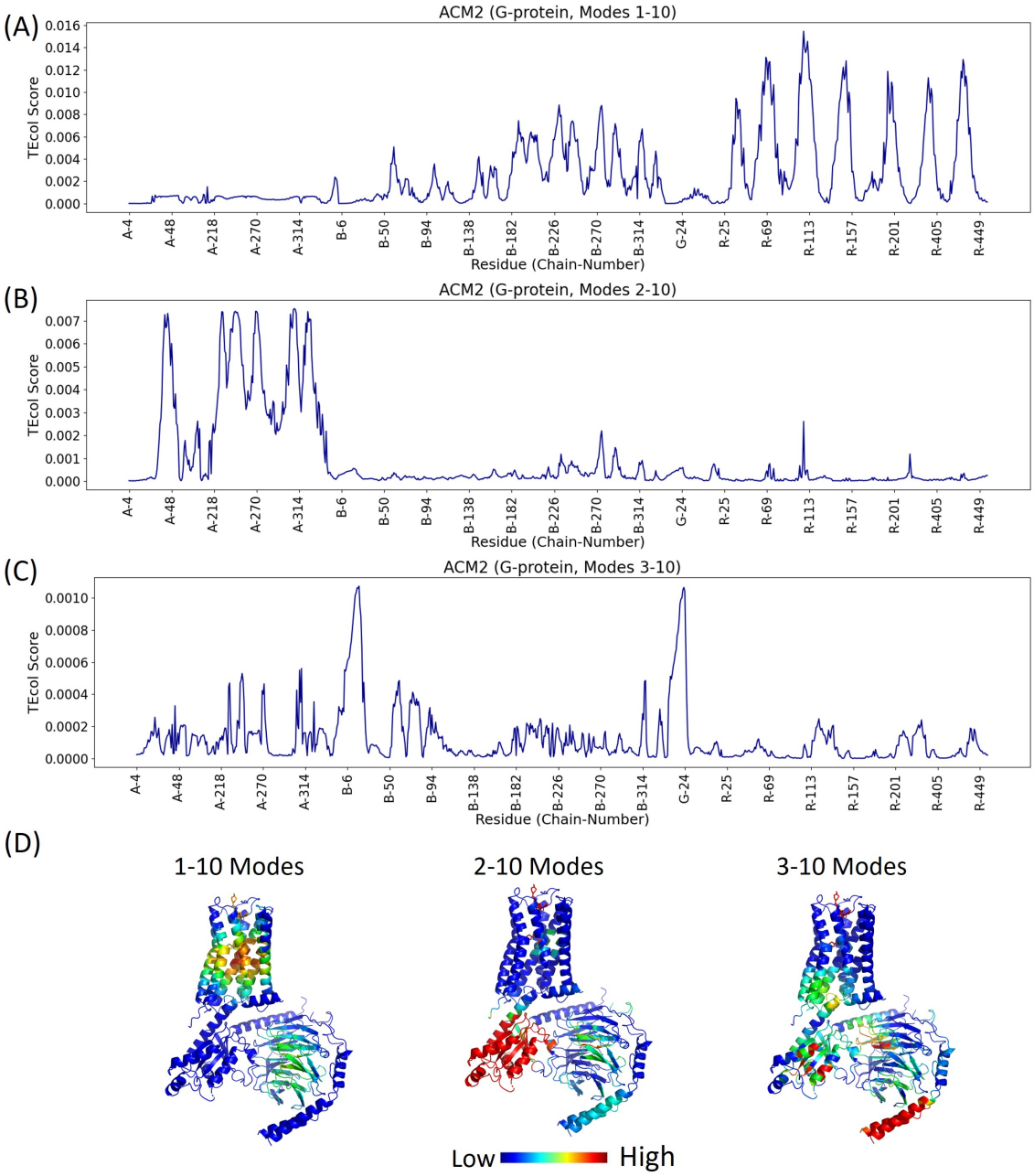

Figure 4.73. TEcol scores and structural mapping of information source residues for the G protein–bound state in ACM2. Panels (A–C) show TEcol scores per residue, calculated using mode ranges 1–10, 2–10, and 3–10, respectively. Panel D display TEcol scores for the β-arrestin–bound state using the same mode ranges. (D) Structures color-mapped by TEcol score.

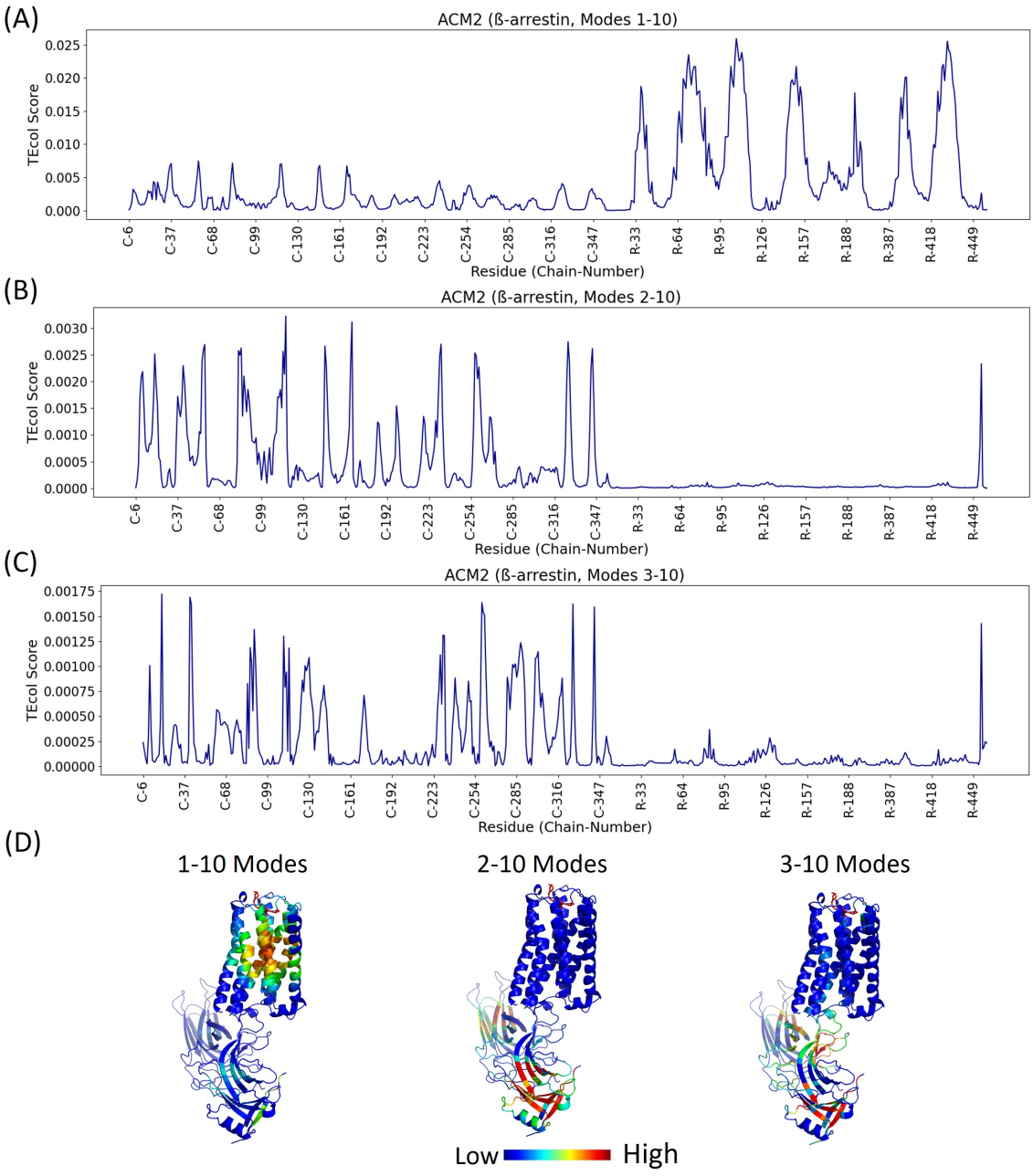

Figure 4.74. TEcol scores and structural mapping of information source residues for the β-arrestin state in ACM2. Panels (A–C) show TEcol scores per residue, calculated using mode ranges 1–10, 2–10, and 3–10, respectively. Panel D display TEcol scores for the β-arrestin–bound state using the same mode ranges. (D) Structures color-mapped by TEcol score.

4.2.5. Differential Coupling Score for Identifying Key Differential Couplings

To better capture the dynamic differences underlying biased signaling mechanisms, we have developed a Differential Coupling Score metric that integrates two complementary features: dynamic correlation changes and differences in information flow (see Methods for details). Specifically, we combined the absolute per-residue cross-correlation difference between G protein- and β-arrestin-targeting simulations, and absolute normalized difference in TEcol scores derived from GNM-TE analysis across multiple mode regimes (1–10, 2–10, and 3–10 modes). By combining these two components, the Differential Coupling Score highlights residues that undergo allosteric dynamics communication changes between different signaling outcomes. Residues with high Differential Coupling Scores represent potential "differential coupling regions" critical sites where structural rearrangements or shifts in allosteric flow might underlie the preferential engagement of distinct transducers.

Segment-level differential coupling score analysis of the 5HT2B receptor revealed that the most distinct region between the G protein- and β-arrestin-bound states is ICL2 (Figure 4.75). This region is known [14] to play a crucial role in transducing signals to both G proteins and β-arrestins, highlighting its central position in regulating downstream signaling. Importantly, ICL2 may also represent a potential site for ligand-induced biased signaling. Supporting this, previous structural studies have shown that positive allosteric modulators (PAMs) can bind to the ICL2 region in GPCRs such as the D1 dopamine receptor (DRD1) and the β2-adrenergic receptor (β2AR) [16, 153].

In addition to ICL2, TM3-EC and TM4-EC were identified as the two other regions showing the highest differential coupling between G protein- and β-arrestin-bound states. TM3-EC, located within the orthosteric ligand-binding region, exhibited significant dynamic changes, consistent with the idea that ligand engagement can alter the receptor's communication pathways. TM4-EC, although not directly involved in ligand binding, showed substantial differential coupling behavior as well. This region is known to undergo outward movement during receptor activation, and our findings

suggest that its dynamic role may differ depending on which signaling pathway is engaged. The high Differential Coupling Score of TM4-EC indicates that this region participates in modulating the receptor's overall allosteric network, even in the absence of direct ligand contact. Taken together, these results propose that TM4-EC, alongside TM3-EC, could serve as a novel target site for the development of biased ligands, offering an alternative strategy for fine-tuning receptor signaling.

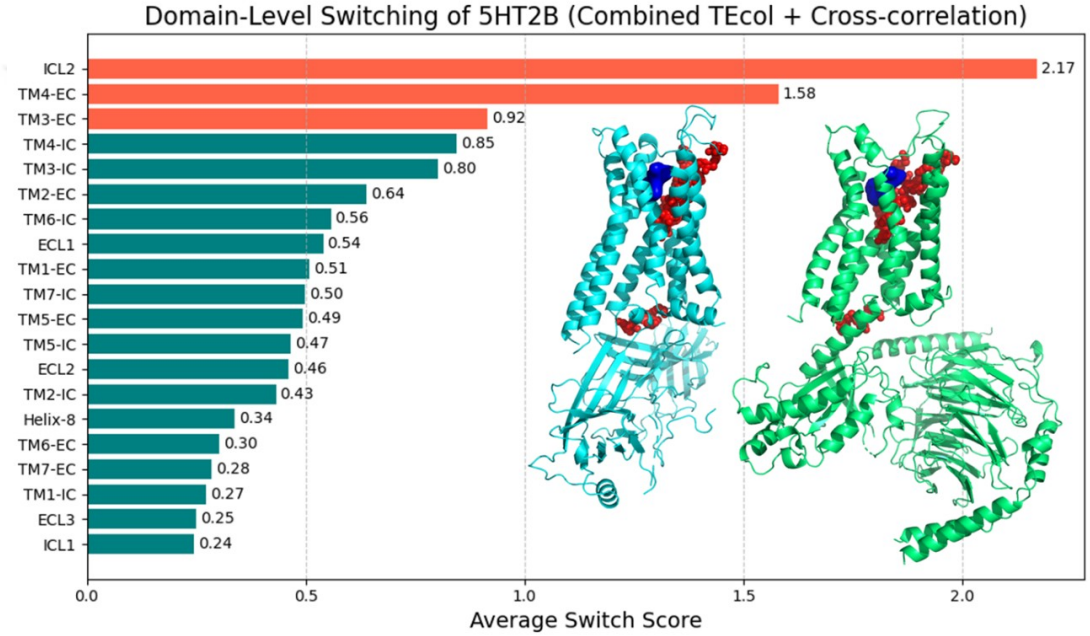

Figure 4.75. Segment-level differential coupling in 5HT2B between G protein- and β-arrestin-bound states. Bars show average differential coupling scores; top three segments (ICL2, TM4-EC, TM3-EC) are in red. These regions are mapped as red spheres on G protein-bound (green) and β-arrestin-bound (cyan) structures. LSD is shown as a blue surface.

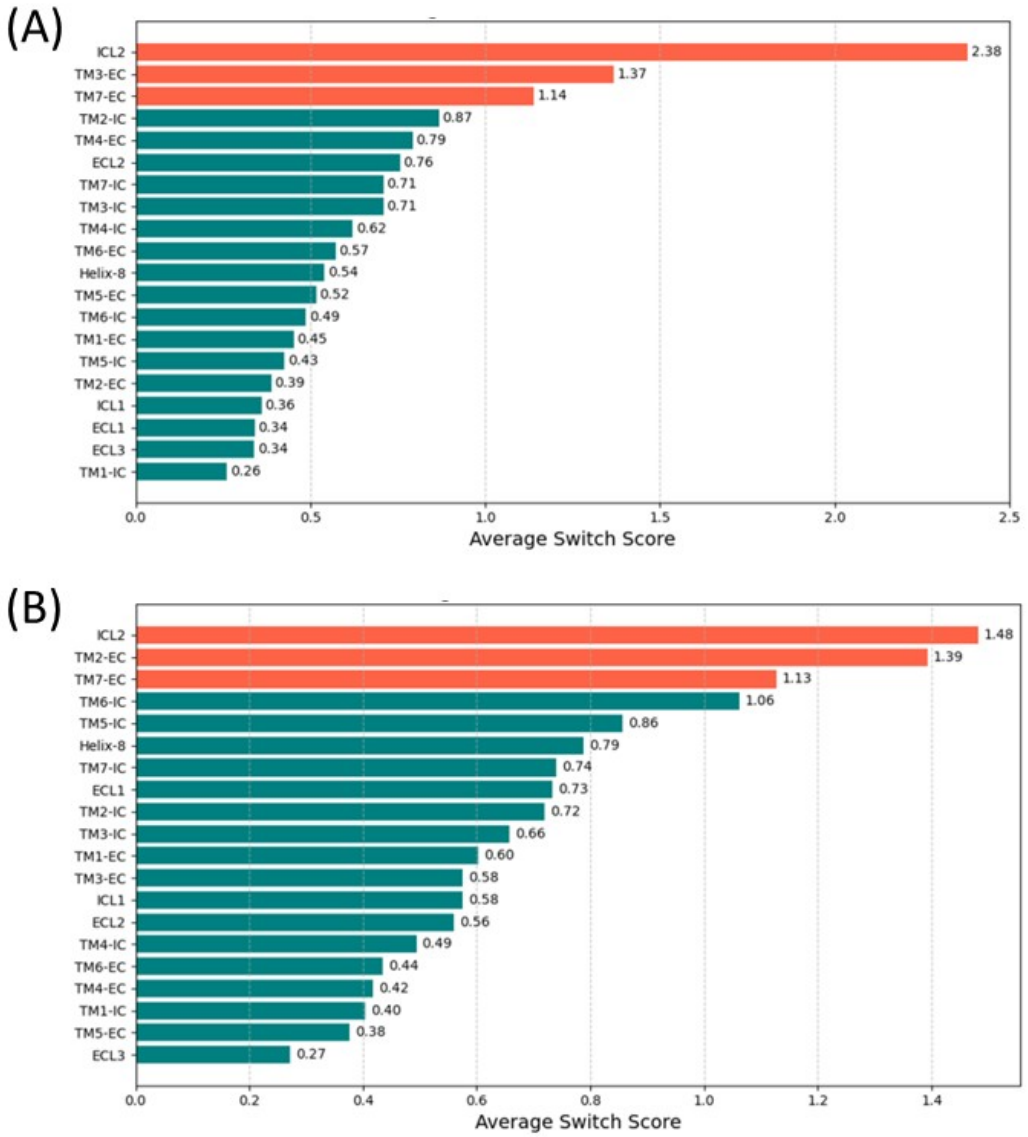

Figure 4.76. Segment-level differential coupling in other receptors between G protein- and β-arrestin-bound states. The average Differential Coupling Score (combining cross-correlation and TEcol differences) is plotted for each structural segments: (A) ADRB1 and (B) ACM2. In each case, the three segments exhibiting the highest differential coupling are highlighted with red bars.

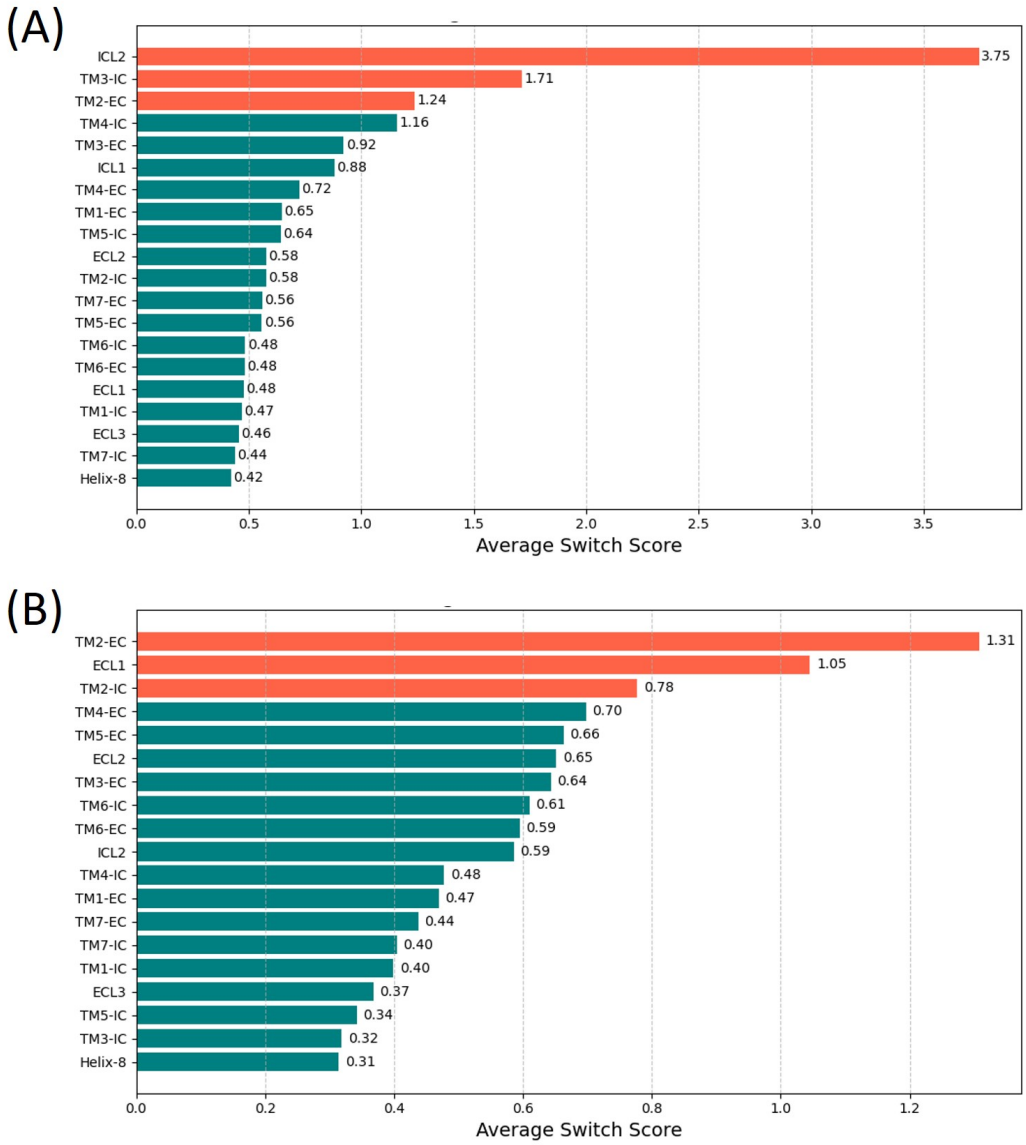

Figure 4.77. Segment-level differential coupling in other receptors between G protein- and β-arrestin-bound states. The average Differential Coupling Score (combining cross-correlation and TEcol differences) is plotted for each structural segments: (A) V2R, and (B) NTR1. In each case, the three segments exhibiting the highest differential coupling are highlighted with red bars.

Segment-level differential coupling analyses across different receptors reveal both conserved and receptor-specific patterns associated with biased signaling (4.75). For all five receptors analyzed — 5HT2B, ADRB1, ACM2, V2R, and NTR1 — ICL2 con-

sistently emerged as one of the top regions showing the highest differential coupling between G protein- and β-arrestin-bound states (Figure 4.75, Figure 4.76, 4.77). This observation highlights ICL2 as a dynamically critical region whose functional role is modulated depending on the recruited signaling protein, supporting previous studies proposing ICL2 as a key determinant in transducer coupling selectivity.

In ADRB1, TM3-EC and TM7-EC were identified among the top differential coupling regions, both of which correspond to ligand-binding sites (Figure 4.76A). Similarly, in ACM2, TM2-EC and TM7-EC showed prominent differential coupling, again mapping to ligand-binding regions (Figure 4.76B). This suggests that in these receptors, dynamic changes at the orthosteric binding pocket contribute significantly to biased signaling outcomes. Additionally, in V2R, differential coupling was observed in TM2-EC and TM3-IC (Figure 4.77A). While TM2-EC overlaps with the ligand-binding site, TM3-IC is known to undergo conformational changes that accommodate different signaling proteins, reflecting its dual role in G protein and β-arrestin coupling. For NTR1, differential coupling centered around TM2-EC, ECL1, and TM2-IC (Figure 4.77B). Notably, TM2-IC coincides with the binding site of the biased allosteric modulator SBI-553, which selectively promotes β-arrestin over Gαq coupling [54].

Collectively, these results suggest that while the specific structural segments undergoing dynamic rewiring vary among receptors, ICL2 stands out as a conserved switch region, making it a promising target for future biased ligand or allosteric modulator development across diverse GPCR families. These findings offer a structural and dynamic framework that could guide the design of biased ligands targeting specific GPCR pathways. We characterize apparent and latent conformational transition pathways in several members of Class A GPCRs, which streamline mechanistically key sites that are also attended by known highly conserved switches (PIF, DRY, NPxxY motifs, etc.). These sites may have the potential to become drug targets to modify the activation pathway with desired pharmaceutical properties. A portion of these results was presented at the EMBO conference Physics of Life under the title “Conformational Transition Pathways in GPCR Activation.”

4.3. Allostery and Activation in Class A GPCRs: Conserved and Divergent Features from Comparative Ensemble Analysis

In this part, we applied ANM-LD simulations to 25 Class A GPCRs, modeling 30 unique conformational transitions—including dual activation pathways for five receptors targeting both G protein- and β-arrestin-bound states—resulting in a comprehensive dynamic ensemble of 300 structures. This ensemble enabled a systematic investigation of receptor-, state-, ligand- and signaling protein-specific dynamic signatures. By incorporating intermediate conformations along activation pathways, we captured previously unresolved dynamic transitions and uncovered conserved and divergent allosteric features across the GPCR superfamily. Our findings shed light on how intrinsic dynamics govern state specificity, ligand selectivity and bias signaling offering a mechanistic framework that may inform structure-based drug design.

4.3.1. Overall Dynamics from Ensemble Analysis

The intermediate conformations obtained through ANM-LD simulations, along with the corresponding inactive and active state structures, were analyzed using the SignDy program to assess their structural and dynamic properties . Incorporating intermediate structures into the analysis enables a more comprehensive view of the evolutionary and dynamic relationships among class A GPCR family members and provides insights into their selectivity profiles.

To this end, we constructed an ensemble composed of 250 structures, including the inactive state, active state, and eight intermediate conformations for each of 25 GPCRs. For each receptor, one representative transition pathway was selected to avoid redundancy, and simulations targeting β-arrestin-bound states were excluded. The resulting ensemble was subjected to SignDy analysis to explore intrinsic dynamics and allosteric mechanisms across the receptor set. In this analysis, we examined three distinct mode subsets derived from elastic network models: global modes (the three slowest modes), low-frequency modes (modes 4–20), and high-frequency modes (the

10 fastest modes). These different dynamic regimes were compared to identify both conserved and divergent patterns of allosteric communication across receptor families, highlighting structural features that may underline functional selectivity. First, we analyzed the mean squared fluctuation (MSF) profiles corresponding to three distinct dynamic regimes. Figures 4.78 A,C and E display the average MSF profiles of residues across the ensemble for each mode regime (in blue), the variance among GPCR family members (dark blue shading), and the range of fluctuations indicated by their minima and maxima (light blue shading).Figure 4.78 B,D and F present the corresponding average MSF values mapped onto the reference structure, the M2 muscarinic receptor (PDB ID: 5ZK3) [132], which was used to align and organize the ensemble. In Figure 55G, the TM regions of the M2 receptor are shown as a wireframe model, with each TM segment represented with distinct color [154] and marked with these colors on the MSF plots, providing spatial context for the fluctuation patterns.

In the global mode regime (Figure 4.78 A-B), the most prominent fluctuations were observed in the ECLs, TM3, ICL2, and TM5. These findings align with the well-established functional roles of these regions. The ECLs are crucial for ligand recognition and serve as important mediators in initiating allosteric communication between the extracellular and intracellular domains [17], which correlates with the ECLs high mobility/flexibility in the global modes. On the intracellular side, the TM3–ICL2 interface and TM5 play a key role in G protein coupling, and their flexibility is likely necessary to accommodate the binding and engagement of signaling proteins [155].

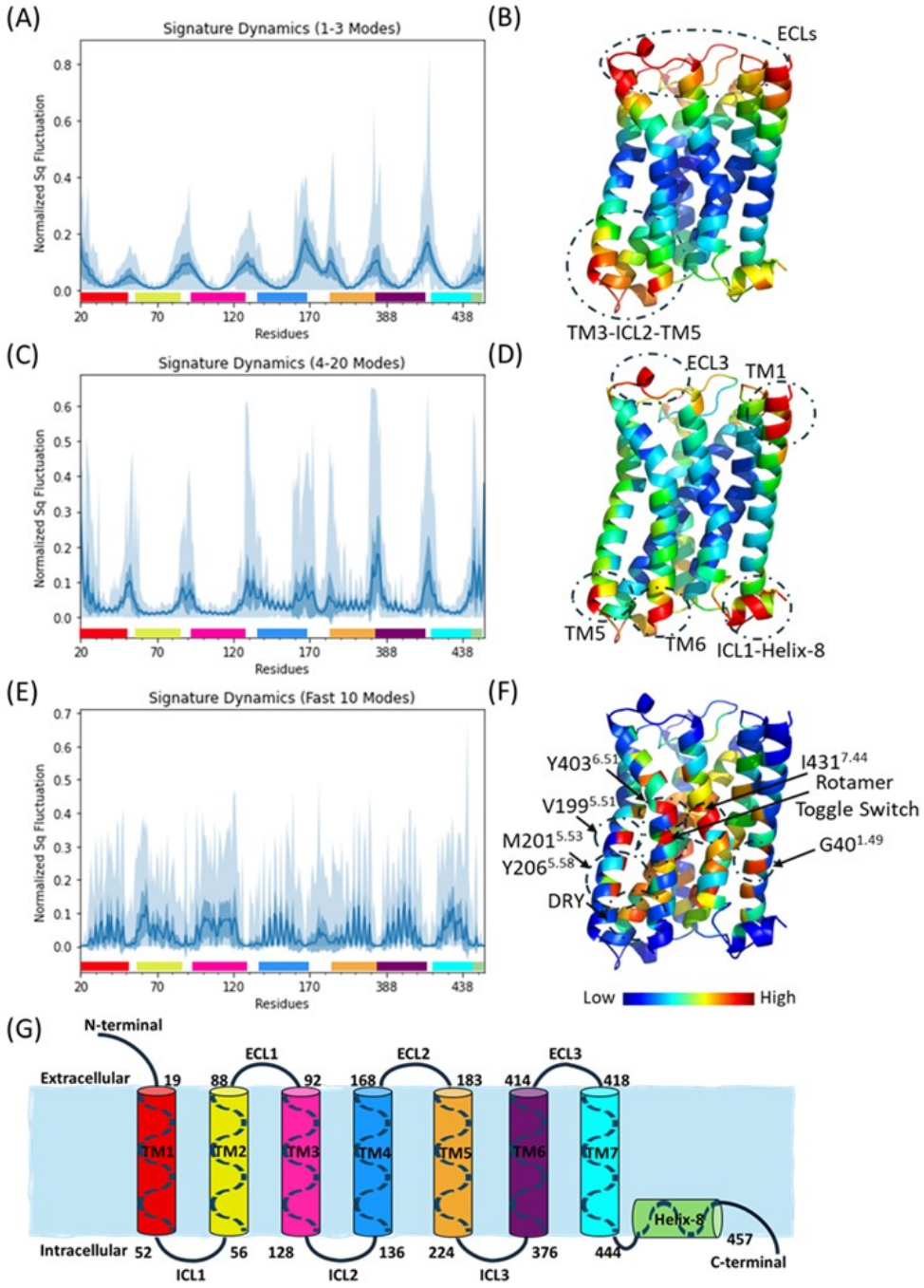

Figure 4.78. Mean squared fluctuation (MSF) analysis across the GPCR ensemble. (A, C, E) Average MSF profiles of residues for the global (A), low-frequency (C), and high-frequency (E) mode regimes. (B, D, F) Structural mapping of the corresponding average MSF values onto the reference structure.(G) Wireframe of M2 with color-coded TM segments for spatial reference.

In the low-frequency mode regime (Figure 4.78 C-D), ECL3 again exhibited pronounced flexibility, reinforcing its potential role in extracellular signal modulation. Additionally, the extracellular portion of TM1 displayed notable mobility, suggesting its involvement in ligand accommodation or entry. On the intracellular side, increased fluctuations were observed in ICL1, TM6, and Helix 8. Among these, the movement of TM6 is particularly significant, as it is a well-recognized hallmark of GPCR activation, undergoing a substantial outward displacement to facilitate G protein coupling [17, 21, 24]. Helix 8 is known to contribute to the stabilization of the receptor conformation and membrane anchoring, and its flexibility may reflect dynamic repositioning during activation [44]. Notably, TM5 continued to exhibit elevated fluctuations in this regime, indicating its sustained involvement in the dynamic rearrangement of the intracellular signaling interface.

In contrast, the high-frequency modes revealed a distinct set of dynamic regions, characterized by faster and more localized motions (Figure 4.78 E-F). These fluctuations were enriched around several conserved motifs and structurally important residues. Notably, elevated mobility was observed near the rotamer toggle switch, which is associated with conformational changes following ligand binding, and the DRY motif, which plays a key role in the transition from the inactive to active state through the disruption of the ionic lock [17]. These findings are consistent with previous work highlighting that while slow GNM modes reflect collective domain motions involved in global conformational transitions, fast modes can pinpoint local flexibility hotspots that often coincide with functionally critical residues [156]. Moreover, Ozbek et al. (2013) showed that high-frequency GNM modes are predictive of hot spot residues at protein interfaces, suggesting that the localized dynamics captured here may underlie conserved allosteric pathways or contribute to local structural adaptability required for receptor activation and effector coupling [157].

Additional fluctuations were detected in the vicinity of the PIF motif, specifically at V199$^{5.51}$, and near the sodium-binding site, I431$^{7.44}$ [24]. Y403$^{6.51}$, another residue exhibiting increased flexibility, lies adjacent to N404$^{6.52}$, a ligand-binding residue known

to undergo conformational changes in the N404Q$^{6.52}$ mutant, which has been associated with a partially active state [132, 158].

Other residues showing high fluctuations include G40$^{1.49}$, M201$^{5.53}$, and Y206$^{5.58}$ each with unclear functional roles but potentially involved in receptor dynamics and signaling. Their elevated mobility may indicate previously unrecognized contributions to GPCR function.

Next, to investigate collective domain motions and identify conformational variability across the GPCR ensemble, we performed an average cross-correlation analysis and calculated the standard deviation of cross-correlations. These analyses help uncover regions that act collectively across the family, as well as those that display variability in their dynamic behavior. Figure 4.79 presents the average cross-correlation maps computed for both the global and low-frequency mode regimes. In contrast, the high-frequency modes yielded minimal cross-correlated motions, with largely unstructured and weak correlations; therefore, high-frequency modes are excluded from the cross-correlation analysis.

In the global mode regime, the intracellular regions of the transmembrane helices (TMs), intracellular loops (ICLs), and Helix 8 exhibit strong mutual correlations, suggesting that these elements act in a coordinated manner to orchestrate the intracellular interface of GPCRs for signaling protein accommodation (Figure 4.80). When analyzing anticorrelated regions, we observed that the extracellular loops (ECL1–ECL3) display strong anticorrelations with the intracellular regions of several transmembrane helices—particularly TM2, TM4, TM5, TM6, and TM7—as well as with ICL1 and Helix 8. This pattern indicates that movements in the extracellular regions, often triggered by ligand binding, are mechanically coupled to conformational changes on the intracellular side (Figure 4.79). Such opposite-direction motions align with the well-established activation mechanism of class A GPCRs [24], in which extracellular ligand-induced perturbations propagate through the helical bundle to reorganize the cytoplasmic surface for G protein or β-arrestin engagement. This dynamic, seesaw-like

relationship between the ECLs and intracellular domains highlights the existence of long-range allosteric communication within the receptor and reinforces the active role of ECLs in initiating and modulating receptor activation.

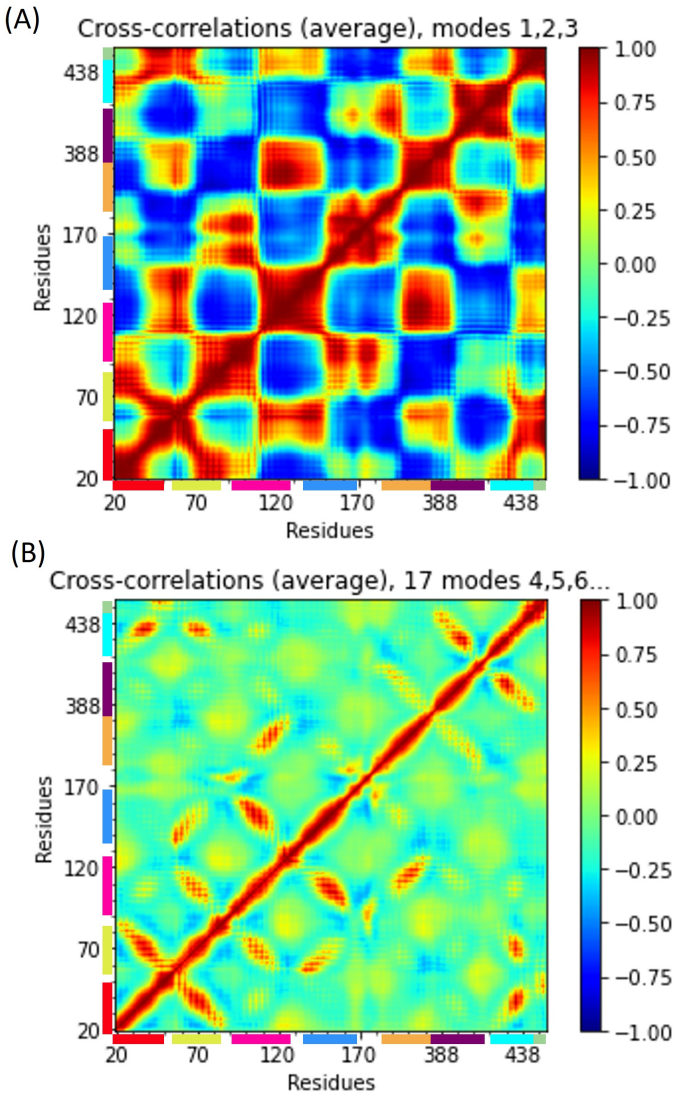

Figure 4.79. Cross-correlation analysis of collective motions across the GPCR ensemble. Average residue-level cross-correlation maps for the global (A) and low-frequency (B) mode regimes. Regions are colored according to the transmembrane segment color scheme shown in the wireframe representation in Figure 4.78.

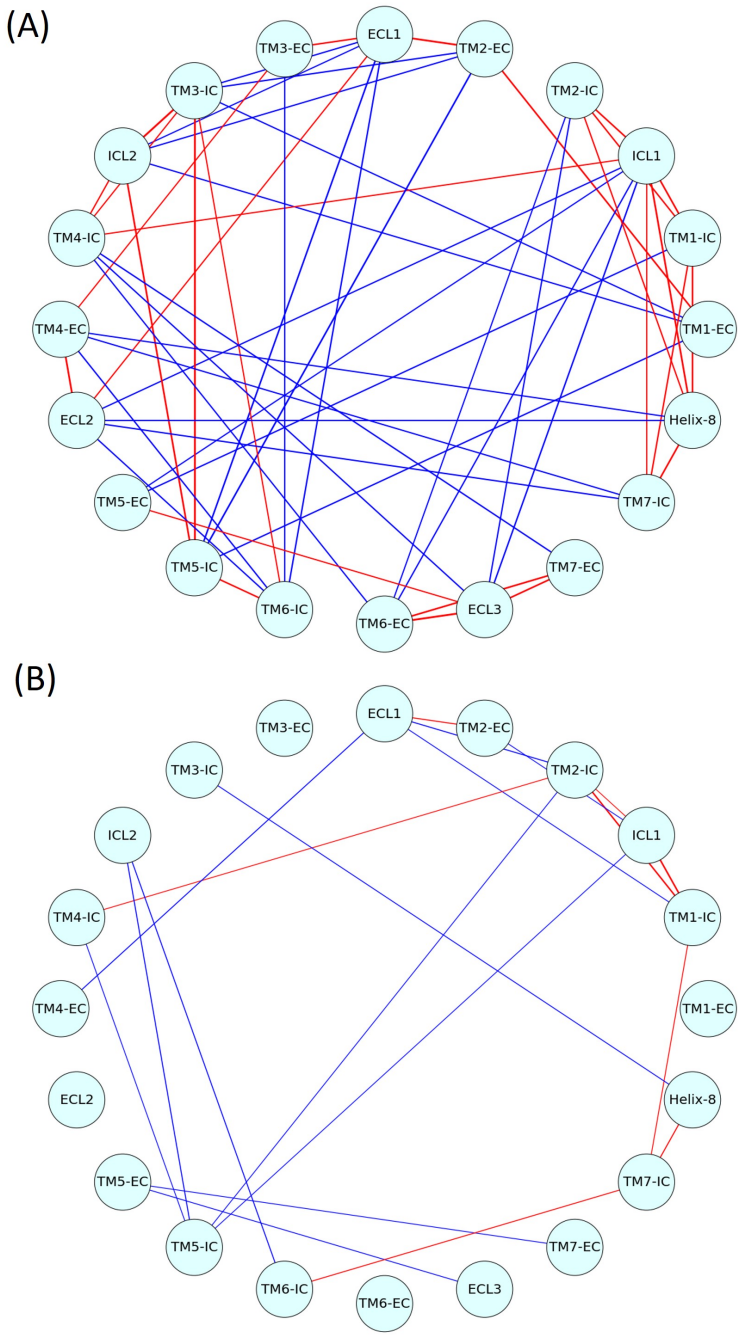

Figure 4.80. Segment-averaged cross-correlation networks derived from the global (A) and low-frequency (B) modes. In the global mode network, red edges indicate strong positive correlations (C≥0.60), and blue edges indicate strong anti-correlations (C≤–0.60). For the low-frequency mode network, a relaxed threshold is applied (C≥0.20 or C≤–0.20) due to reduced correlation strength.

In the low-frequency mode regime (Figures 4.79B- 4.80B), a series of correlated motions were observed among specific intracellular regions, suggesting the presence of a coordinated allosteric network on the cytoplasmic face of the receptor. Notably, TM4-IC was found to be correlated with TM2-IC, which in turn exhibited dynamic coupling with ICL1 and TM1-IC. This network extends further, as TM1-IC was correlated with TM7-IC, which itself showed coordinated motion with both Helix 8 and TM6-IC. The continuity of these correlations implies that the intracellular regions of TMs and loops do not act independently but instead operate as an integrated unit that may collectively adjust to accommodate intracellular signaling proteins such as G proteins or β-arrestins. These findings highlight the potential of low-frequency modes to capture subtle, yet functionally relevant, intrahelical communication pathways that support receptor activation and downstream signal transduction. A notable long-range anticorrelated interaction was observed between ECL1 and TM1-IC, suggesting that conformational changes in the extracellular loop may be mechanically coupled to opposing movements in the intracellular region of TM1, potentially contributing to the transmission of allosteric signals across the receptor.

The standard deviation maps of the cross-correlation matrices, presented in Figure 57, highlight the regions exhibiting the highest dynamic variability across the GPCR ensemble. These regions are further visualized on the reference structure to pinpoint their spatial and functional relevance. Among them, we identified a set of residues—N108$^{3.37}$, W148$^{4.50}$, F195$^{5.47}$, and N432$^{7.46}$—that display markedly variable allosteric behavior across receptor families in global modes (Figure 4.81 A-B). Notably, these residues are located just beneath the orthosteric binding site, positioning them strategically for modulating the transmission of ligand-induced signals to the intracellular face [132]. These residues are highlighted as dashed red rectangles in Figure 57A and as red spheres on the reference structure in Figure 4.81 B. Although key elements such as the rotamer toggle switch (W148$^{4.50}$) and the sodium-binding site (N432$^{7.46}$) are conserved across Class A GPCRs [21], our results reveal substantial variation in their dynamic behavior among receptor subtypes. This suggests that evolutionary conservation in sequence does not necessarily imply uniformity in motion or function. Their

variable flexibility may reflect receptor-specific adaptations in the allosteric network and could contribute to differences in activation pathways or signaling bias.

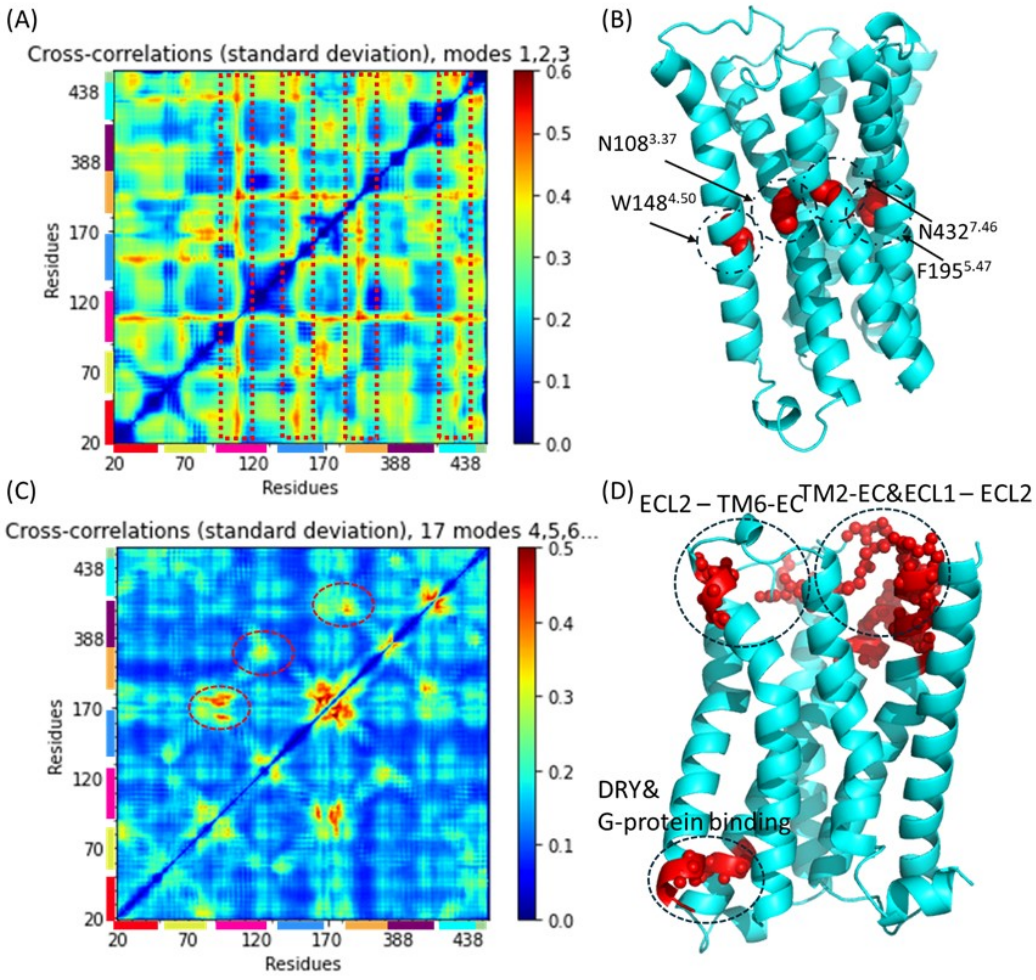

Figure 4.81. Variability in cross-correlation patterns across the GPCR ensemble. (A, C) Standard deviation maps of cross-correlation matrices for the global (A) and low-frequency (C) mode regimes. Colors follow TM segment scheme from Figure 4.78. (B, D) Structural mapping of the most variable residues onto the reference structure, corresponding to the global (B) and low-frequency (D) modes.

Analysis of variability in the low-frequency mode correlations (Figure 4.81C–D) reveals prominent differences across the extracellular loops, as well as the extracellular regions of TM2 and TM6. These regions are known to play key roles in ligand recogni-

tion and allosteric modulation, and their divergent dynamics suggest receptor-specific adaptations in how extracellular signals are received and transmitted. In addition, the DRY motif and the G protein binding interface exhibit substantial variation across the ensemble, indicating that differences in the flexibility of these critical intracellular regions may underlie the diverse signaling mechanisms employed by different GPCR family members. These findings highlight the potential role of dynamic divergence in shaping functional selectivity and signaling bias across the receptor superfamily.

4.3.2. State-Specific Dynamics

To investigate state-specific dynamic behaviors, we constructed three separate ensembles composed of inactive, active, and intermediate conformations. We then analyzed their square fluctuations across three distinct mode regimes—global, low-frequency, and high-frequency modes—using SignDy. These results are presented in 4.82, corresponding to the fluctuation profiles for each mode regime. The spatial distribution of fluctuations is further visualized by mapping them onto the receptor structure in 4.83 allowing for a direct comparison of dynamic features across different activation states.

The global and low-frequency mode regimes exhibit highly similar fluctuation patterns across different receptor states, indicating that these slower collective motions capture conserved, large-scale conformational rearrangements. Notably, fluctuations in TM4-EC and ECL2 are most pronounced in the intermediate ensemble, followed by the inactive ensemble (Figures 4.82A-4.83A). This suggests that in both the inactive and intermediate states, these regions remain more dynamically engaged in ligand-associated interactions, potentially modulating access to the orthosteric site.

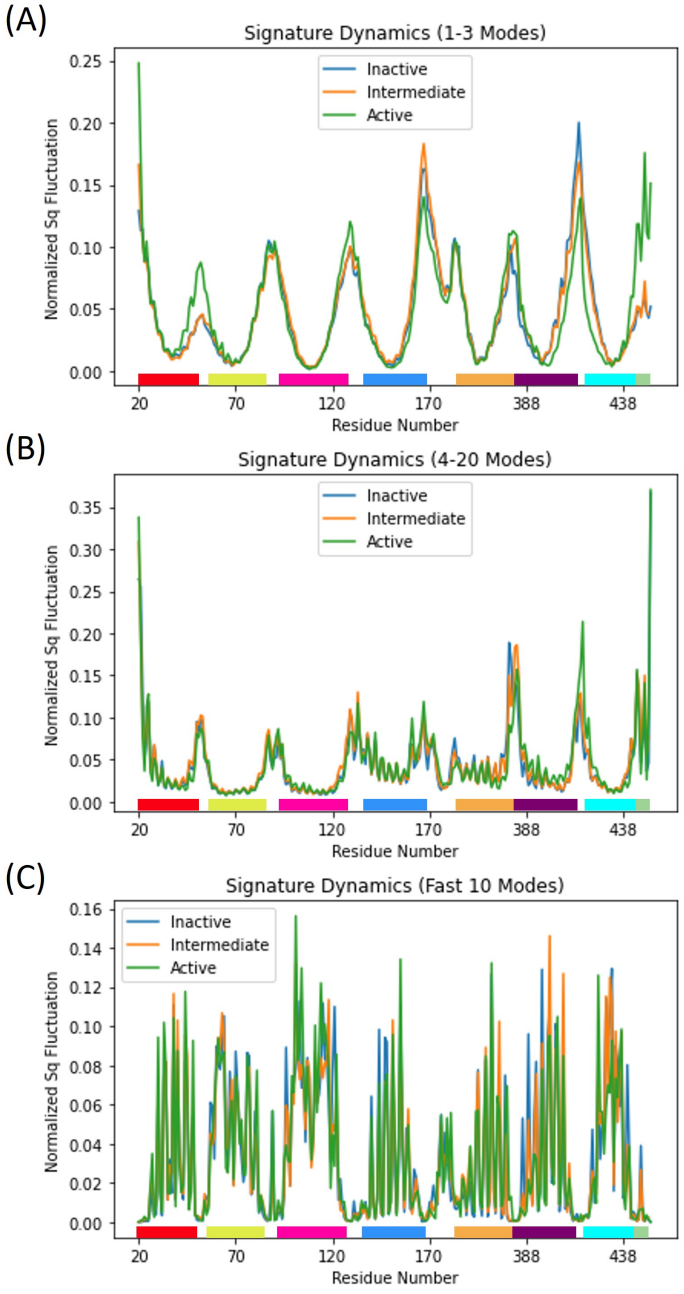

Figure 4.82. Fluctuation profiles of state-specific GPCR ensembles. Residue-level square fluctuations computed using SignDy for the global (A), low-frequency (B), and high-frequency (C) mode regimes across inactive, intermediate, and active ensembles. Regions are colored according to the transmembrane segment color scheme shown in the wireframe representation in Figure 4.78.

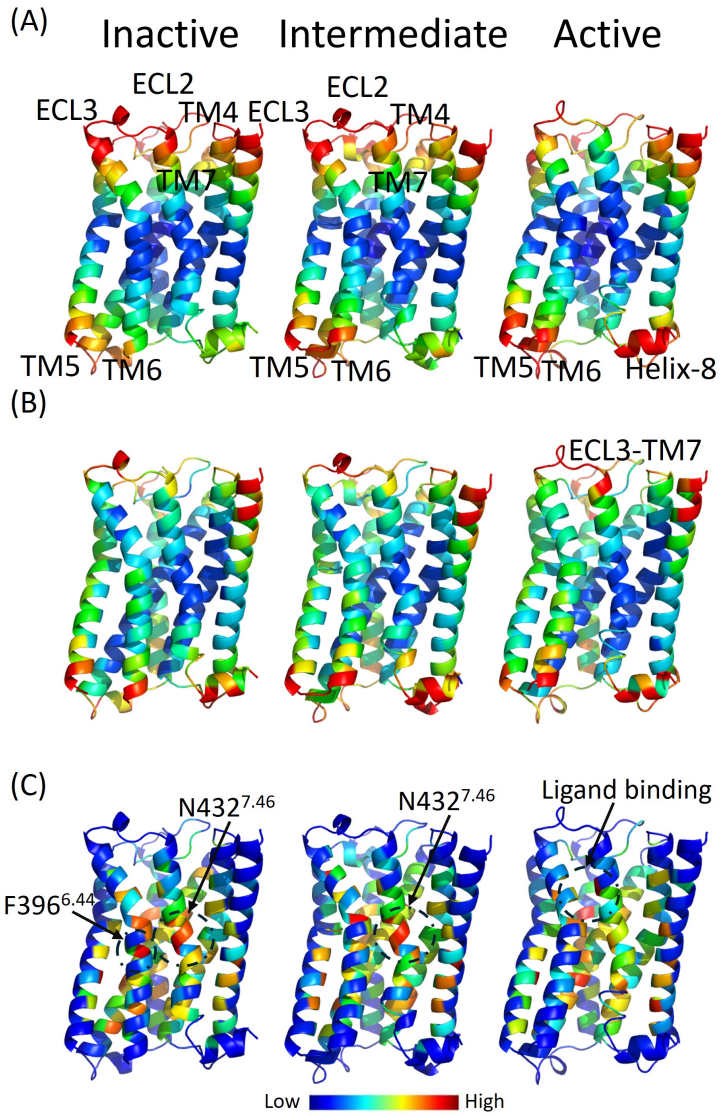

Figure 4.83. Structural mapping of the average fluctuations onto the M2 muscarinic receptor (PDB ID: 5ZK3) for the global (A), low-frequency (B), and high-frequency (C) mode regimes across inactive, intermediate, and active ensembles, providing spatial insight into the dynamic differences among activation states.

During activation, increased fluctuations are observed in TM5 and TM6 (Figures 4.82A-4.83A). These helices undergo the characteristic tilting motions required for activation in class A GPCRs, which facilitate the outward movement of TM6 and open the intracellular binding interface for G protein engagement [17, 21, 24, 28]. Addition-

ally, fluctuation in Helix 8 is also higher in the active ensemble. This may reflect its dynamic repositioning upon activation, where it adjusts to stabilize the active conformation, interact with the membrane environment, or accommodate intracellular signaling partners such as G proteins or β-arrestins. Interestingly, while the ECL3–TM7 region exhibits prominent fluctuations in the global mode regime of the inactive and intermediate ensembles, this dynamic feature shifts to lower-frequency modes in the active ensemble (Figures 4.82B-4.83B). In other words, what appears as a higher-order local flexibility in inactive states becomes part of a coordinated, low-frequency dynamic framework in the active state. This redistribution of motion may reflect the structural stabilization of the extracellular domain during activation, while still allowing functionally relevant flexibility through broader, more global conformational rearrangements.

Among the mode regimes, the high-frequency modes displayed the most pronounced differences between receptor states (Figures 4.82C-4.83C). Notably, the mobility of the PIF motif—specifically F396$^{6.44}$—decreases upon activation. This reduction in fluctuation is likely due to its role in stabilizing the active conformation; once the receptor transitions into the active state, the PIF motif adopts a tightly packed arrangement that supports the active intracellular interface and limits its flexibility.

The sodium-binding site (N432$^{7.46}$) also shows dynamic behavior, with the highest fluctuations observed in the intermediate ensemble and still significant mobility in the inactive state. As the receptor transitions through intermediate states and the sodium coordination network becomes destabilized, this region may exhibit higher local fluctuations before full activation locks it into a more rigid arrangement. Interestingly, the ligand-binding region demonstrates increased fluctuation in the active state. This enhanced mobility may reflect micro-adjustments that occur post-activation, possibly related to ligand unbinding, receptor reset, or conformational flexibility required for downstream signaling selectivity. Once the large-scale structural transition is completed, localized flexibility in the orthosteric pocket may become more pronounced as the receptor enters a more dynamic, signaling-competent state. Average cross-correlation differences were calculated for the global mode regime across the inactive,

intermediate, and active ensembles. To detect dynamic shifts between receptor states, pairwise cross-correlation differences were computed and visualized in Figure 4.84. In addition, segment-based average differences were calculated to highlight the most affected regions, as shown in Figure 4.85. Red edges indicate domain pairs with increased correlation, while blue edges denote decreased correlation in the ligand-specific ensemble. The thickness of edges reflects the magnitude of the correlation difference, with thicker edges indicating stronger effects.

Among the regions exhibiting the largest cross-correlation changes during activation, we observed an increase in coordination between extracellular regions, particularly ECL2, TM4-EC, TM5-EC, ECL1, and TM2-EC (Figures 4.84A- 4.85A). These results suggest that activation not only affects the intracellular coupling required for signaling protein recruitment but also reorganizes the extracellular interface—likely in response to ligand binding or release. One notable long-range dynamic interaction is observed between TM4-EC and Helix 8, indicating the presence of an extended allosteric pathway spanning from the extracellular surface to the intracellular tail.

Conversely, a decrease in correlation is observed between ICL1, ICL2, Helix 8, and other intracellular domains (Figures 4.84A- 4.85A). This loss of coordinated motion may reflect the structural rearrangements that accompany the opening of the intracellular cavity during activation. As the receptor transitions to an active state, these regions likely decouple dynamically to facilitate flexible accommodation of the signaling protein. The reduction in correlation could therefore be a mechanistic necessity, allowing the cytoplasmic face of the receptor to adopt diverse conformations for coupling specificity or biased signaling.

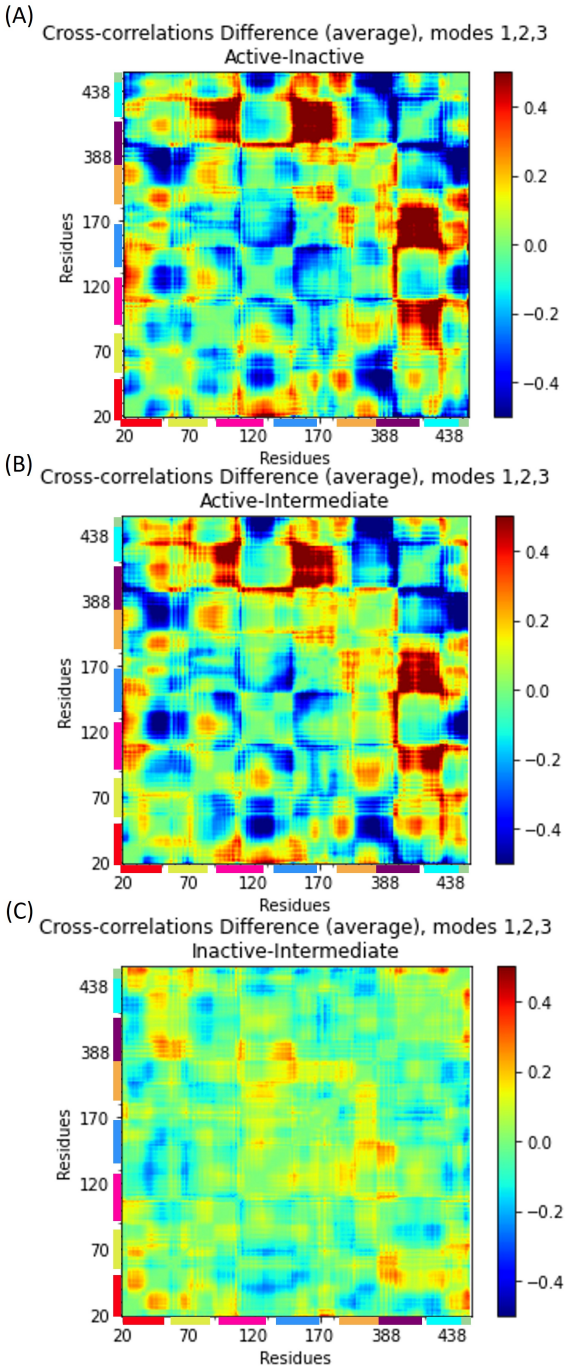

Figure 4.84. Cross-correlation differences between receptor states in the global mode regime. (A, B, C) Pairwise cross-correlation difference maps highlighting dynamic shifts between inactive vs. intermediate (A), intermediate vs. active (B), and inactive vs. active (C) ensembles. Regions are colored according to the transmembrane segment color scheme shown in the wireframe representation in Figure 4.78.

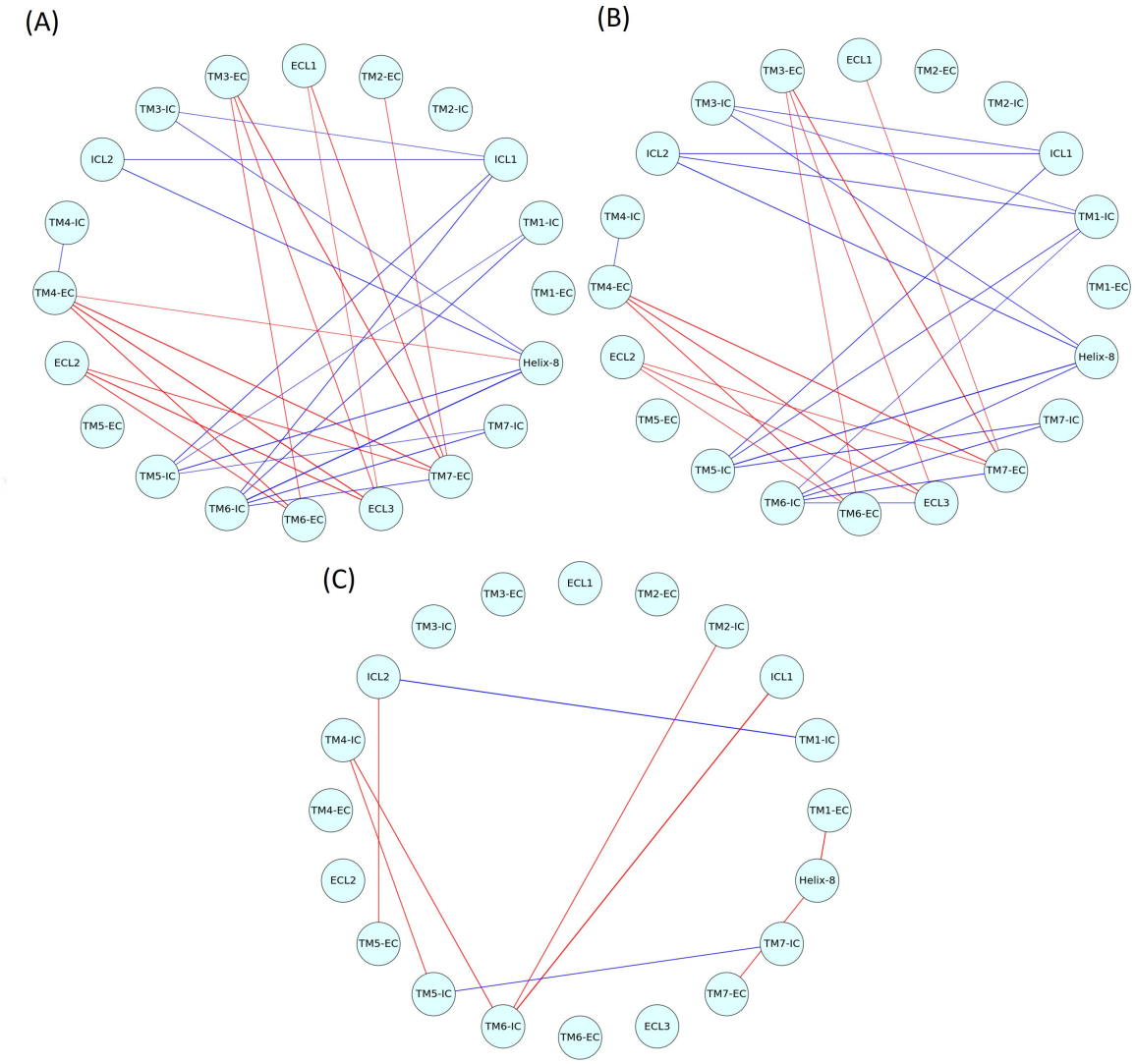

Figure 4.85. Segment-based average cross-correlation differences corresponding to dynamic shifts in global modes between inactive vs. intermediate (A), intermediate vs. active (B), and inactive vs. active (C) ensembles.

When comparing the active ensemble to the intermediate ensemble, we observe a notable decrease in correlations that are not as prominent in the inactive-to-active comparison (Figures 4.84B- 4.85B). Specifically, a reduction in correlation between ICL2 and TM1-IC is evident, suggesting a loosening of coordinated motion within the intracellular core during the transition from intermediate to fully active state.

Moreover, a long-range correlation between TM6-IC and ECL3 also diminishes in the active ensemble relative to the intermediate state (Figures 4.84B- 4.85B). This interaction may play a transient role during activation, possibly contributing to the structural alignment of transmembrane helices and loops. When comparing the inactive and intermediate ensembles, we observe a reduction in two key long-range interactions during the early stages of activation (Figures 4.84C- 4.85C). The first is a weakening of the dynamic coupling between ICL2 and TM5, both of which contribute to the intracellular surface that engages with signaling proteins. The loss of correlation in this region may reflect the structural rearrangement required to initiate the opening of the G protein binding cavity. The second involves a reduction in long-range correlations between Helix 8 and two extracellular regions: TM1-EC and TM7-EC. This suggests that, in the intermediate state, the allosteric bridge linking extracellular and intracellular ends of the receptor begins to loosen. Such decoupling may be a necessary step in preparing the receptor for full activation.

In the comparison of low-frequency modes across receptor states, an increase in correlation is observed between ECL1 and TM2-IC, as well as between ICL1 and TM2-IC during activation (Figures 4.86A- 4.87A). This suggests enhanced communication between extracellular and intracellular regions in early activation states, potentially reflecting the transmission of ligand-induced motions toward the cytoplasmic face. Additionally, the correlation between TM3-IC and TM6-IC—two regions bridged by the ionic lock in the inactive state—is reduced during activation (Figures 4.86A- 4.87A). This reduction is consistent with the known mechanism of GPCR activation, where disruption of the R3.50–E6.30 ionic lock increases the distance between these helices, weakening their dynamic coupling [17].

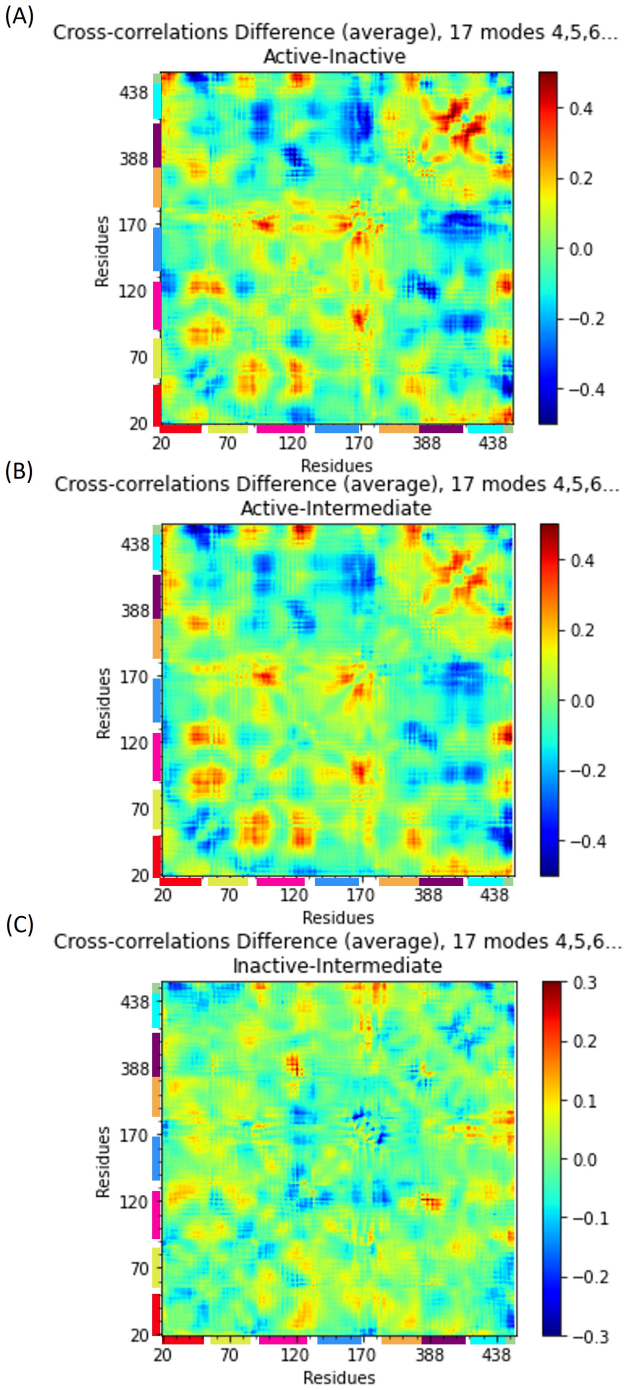

Figure 4.86. Cross-correlation differences between receptor states in the low frequency regime. (A, B, C) Pairwise cross-correlation difference maps highlighting dynamic shifts between inactive vs. intermediate (A), intermediate vs. active (B), and inactive vs. active (C) ensembles. Regions are colored according to the transmembrane segment color scheme shown in the wireframe representation in Figure 4.78.

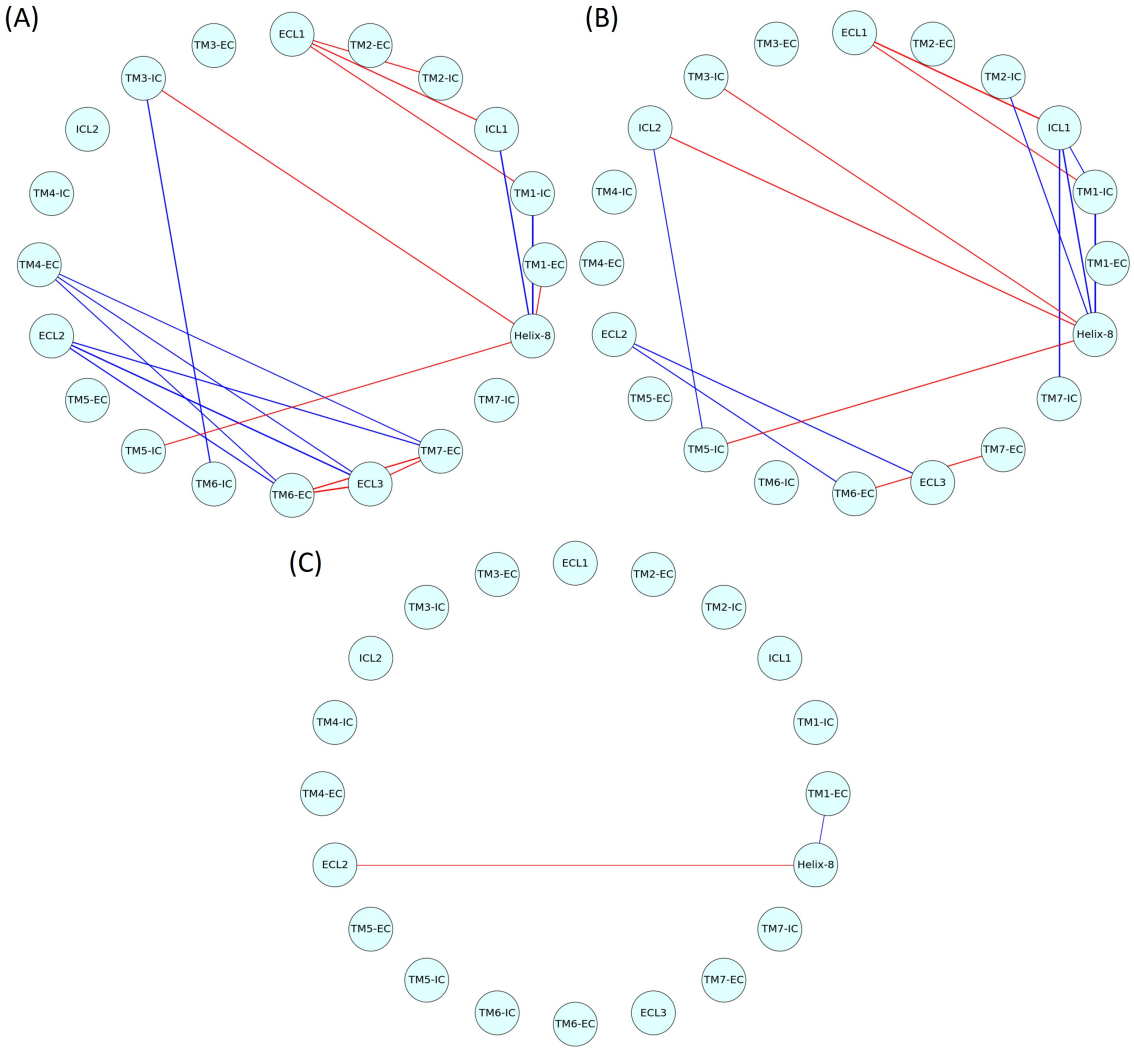

Figure 4.87. Segment-based average cross-correlation differences corresponding to dynamic shifts in low frequency modes between inactive vs. intermediate (A), intermediate vs. active (B), and inactive vs. active (C) ensembles.

When comparing the active and intermediate ensembles, we observe an increase in dynamic coupling between Helix 8 and several key intracellular regions, including TM3-IC, ICL2, and TM5-IC in the active state (Figures 4.86B- 4.87B). In contrast, a decrease in correlation is observed between Helix 8 and more peripheral intracellular elements such as ICL1 and TM1-IC. This shift may indicate a reorganization of allosteric communication, where Helix 8 transitions from interacting with early intermediates (e.g., TM1-IC) to forming more functionally relevant contacts with core

signaling regions during activation. When comparing the inactive and intermediate ensembles (Figures 4.86C- 4.87C), a decrease in correlation is observed between ECL2 and Helix 8, indicating a loss of long-range communication between the extracellular and intracellular ends of the receptor. Interestingly, at the same time, an increase in correlation is noted between Helix 8 and TM1-EC. This shift in interaction may reflect a reorganization of the allosteric network.

4.3.3. Ligand-Specific Dynamics

To explore how ligand type influences receptor dynamics, we categorized the full ensemble into five groups based on the chemical nature of the bound ligand: aminergic, peptide, nucleotide, lipid, and protein-bound GPCRs. Each group included 50 structures representing inactive, intermediate, and active conformational states. We analyzed the mean square fluctuation (MSF) profiles of each group using both global and low-frequency normal modes (Figure 4.88).

In the global mode regime, lipid-bound receptors exhibited higher flexibility in the ECL1 region (Figure 4.88A). This likely reflects the nature of their ligands, which insert laterally into the membrane and engage less directly with extracellular loops. In contrast, aminergic and peptide-bound receptors showed the lowest ECL1 fluctuations. This is especially notable in aminergic GPCRs, where small ligands bind deeply within the transmembrane core through a highly conserved orthosteric site, stabilizing nearby loop regions [15, 152].

The ECL2 region, which often acts as a dynamic lid over the orthosteric binding pocket [159,160], displayed the greatest flexibility in peptide- and protein-bound receptors (Figure 4.88A). These ligands typically require conformational rearrangements of ECL2 to achieve stable binding, consistent with their larger size and extended binding interfaces [3, 161]. Conversely, aminergic receptors again exhibited the lowest ECL2 mobility, consistent with their compact binding mode and minimal loop engagement.

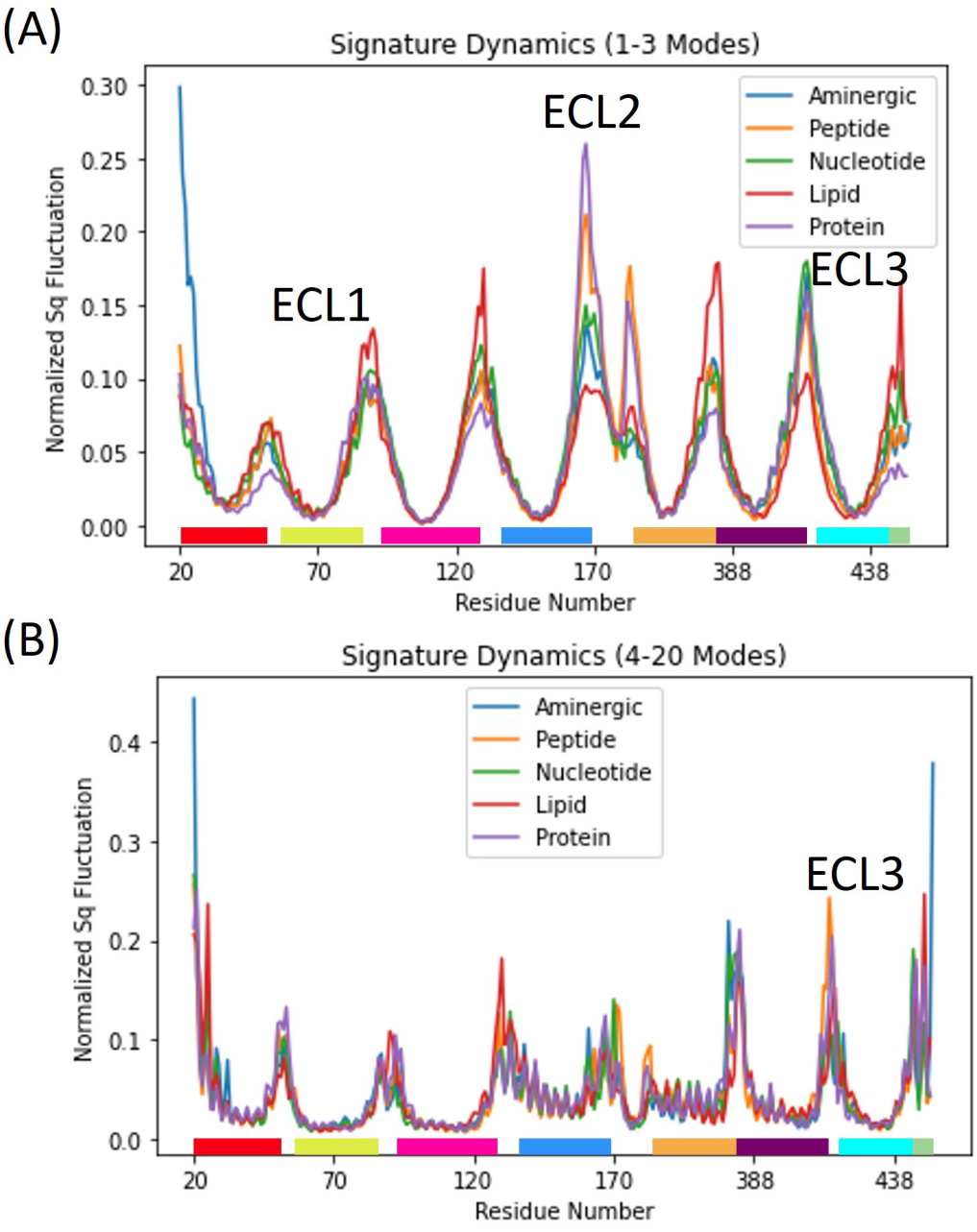

Figure 4.88. Fluctuation profiles of ligand-type–specific GPCR ensembles. Mean square fluctuation (MSF) profiles were computed for each group (aminergic, peptide, nucleotide, lipid, and protein-bound receptors) using the global (A) and low-frequency (B) mode regimes to reveal ligand-dependent dynamic signatures.Colors follow TM segment scheme from Figure 4.78.

In ECL3, fluctuations were highest in peptide- and protein-bound receptors (Figure 4.88A), likely due to the extended or polar nature of their ligands, which often interact with this extracellular loop [162]. Interestingly, in the low-frequency regime, overall MSF profiles across all five groups were more similar than in the global mode regime, suggesting a convergence of large-scale collective dynamics (Figure 4.88B). Peptide- and protein-bound receptors maintained higher ECL3 fluctuations, again aligning with trends seen in global modes, suggesting that the dynamic behavior of ECL3 may serve as a distinguishing feature for these ligand-bound receptors.

Figures 4.89 and 4.91 display heatmaps representing the average cross-correlation differences between each ligand-specific ensemble and the full GPCR ensemble for the global and low-frequency modes, respectively. These difference maps reveal which residue pairs become more or less dynamically coupled in the presence of specific ligand types. Notably, peptide- and protein-bound receptors exhibit more extensive global changes, particularly in extracellular regions, suggesting their ligands induce broader allosteric rearrangements.

To complement the residue-level heatmaps, Figures 4.90 and 4.92 present domain-based correlation networks summarizing inter-domain communication shifts for each ligand class. In these networks, red edges indicate increased correlations, and blue edges reflect reduced correlations relative to the full ensemble, with edge thickness representing the magnitude of change.

Across both dynamic regimes, lipid-bound receptors emerged as the most distinct group, exhibiting the largest deviations in inter-residue and inter-domain correlation patterns relative to the full ensemble. The most affected regions were primarily located on the extracellular side of the receptor, particularly within domains associated with ligand recognition and binding. Notably, ECL2, TM3-EC, ECL1, TM4-EC, and ECL3 showed consistent and ligand-specific alterations in their dynamic coupling with other receptor regions, highlighting their potential roles as modulatory hotspots in GPCR allostery.

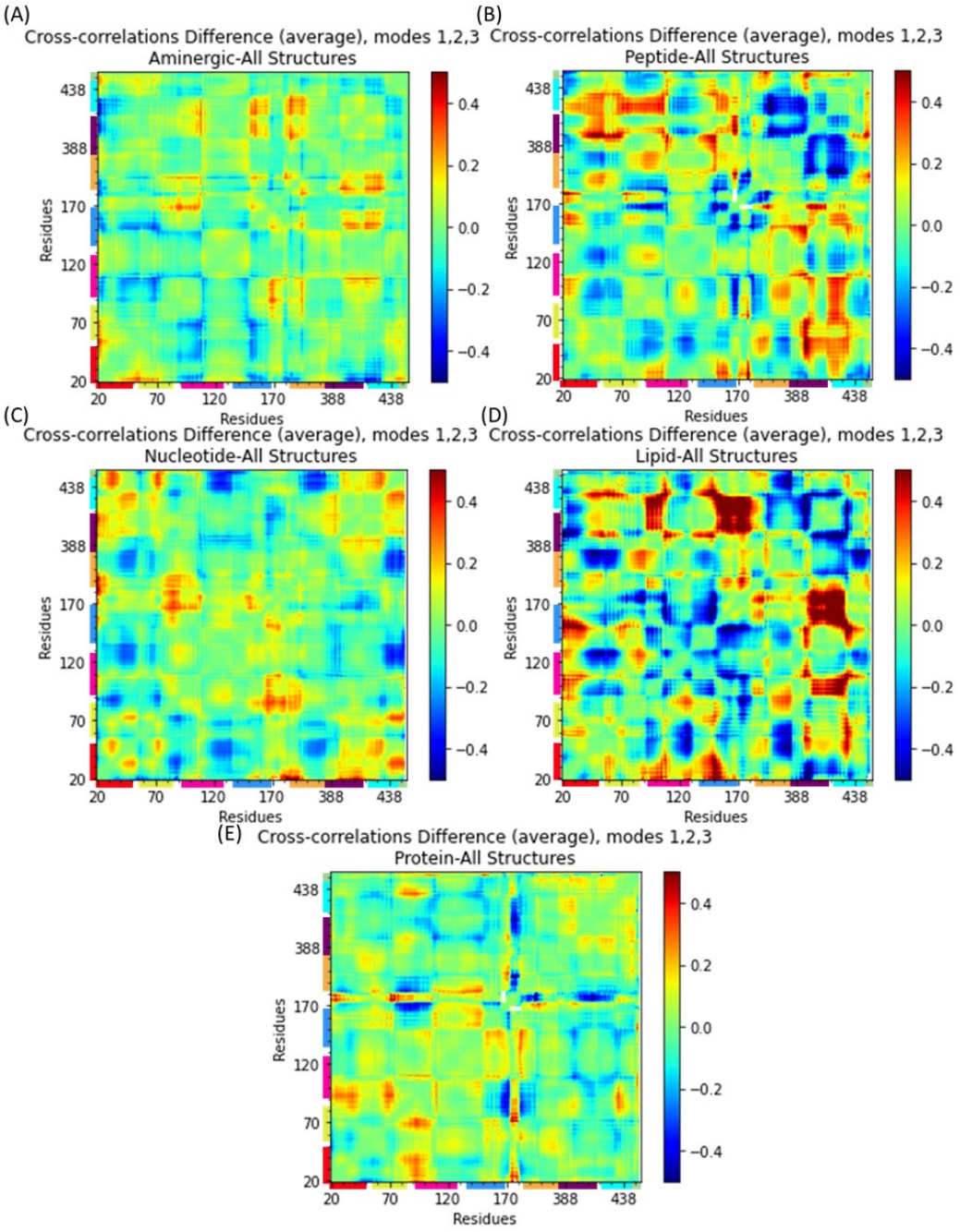

Figure 4.89. Ligand-type–specific cross-correlation differences in the global mode regime. (A–E) Heatmaps displaying the average cross-correlation differences between each ligand-bound ensemble—aminergic (A), peptide (B), nucleotide (C), lipid (D), and protein-bound and overall GPCR ensemble and (E). Colors follow TM segment scheme from Figure 4.78.

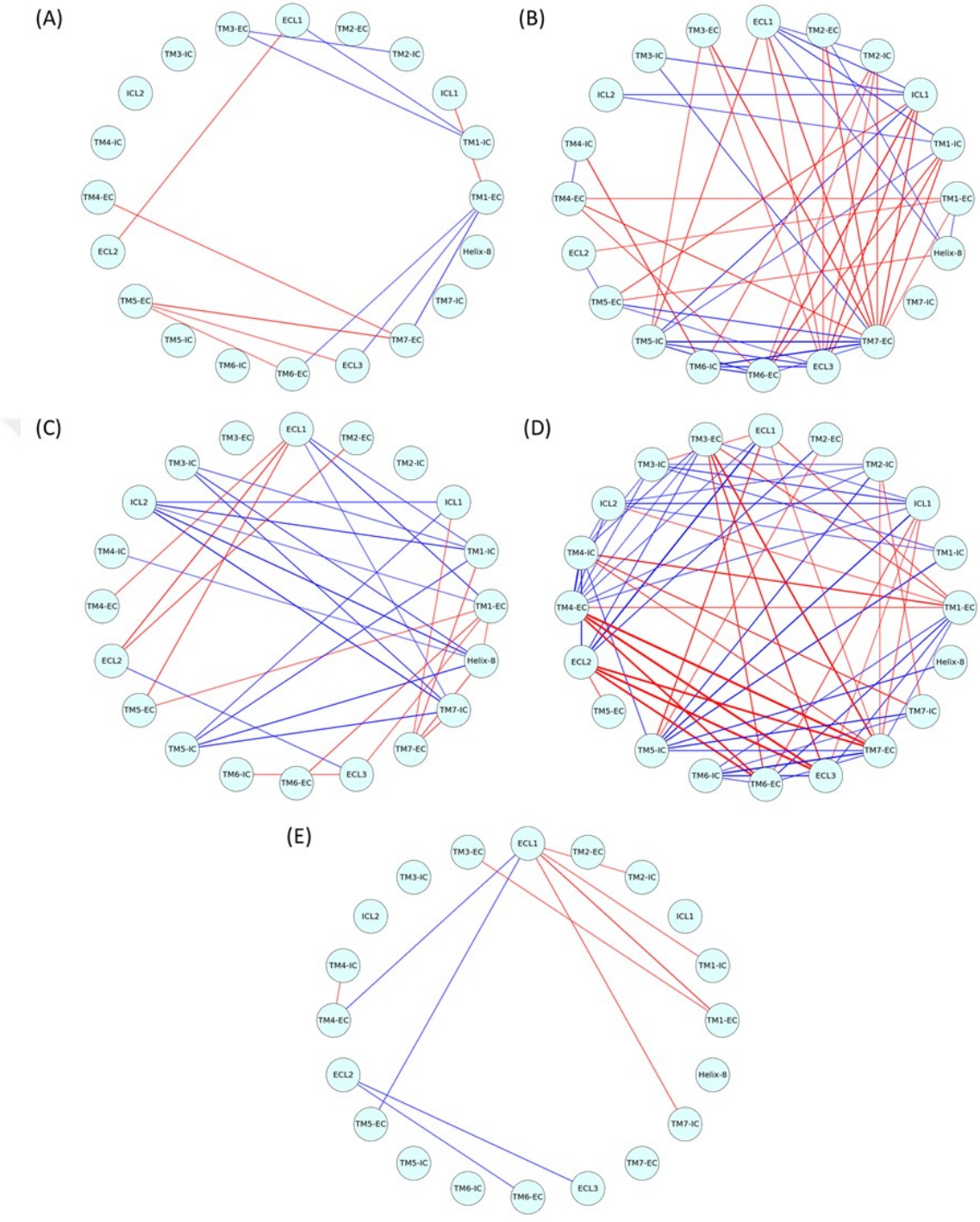

Figure 4.90. Ligand-type–specific correlation networks derived from global mode differences. Segment-based correlation difference networks are shown for each ligand-binding class: aminergic (A), peptide (B), nucleotide (C), lipid (D), and protein-bound (E).

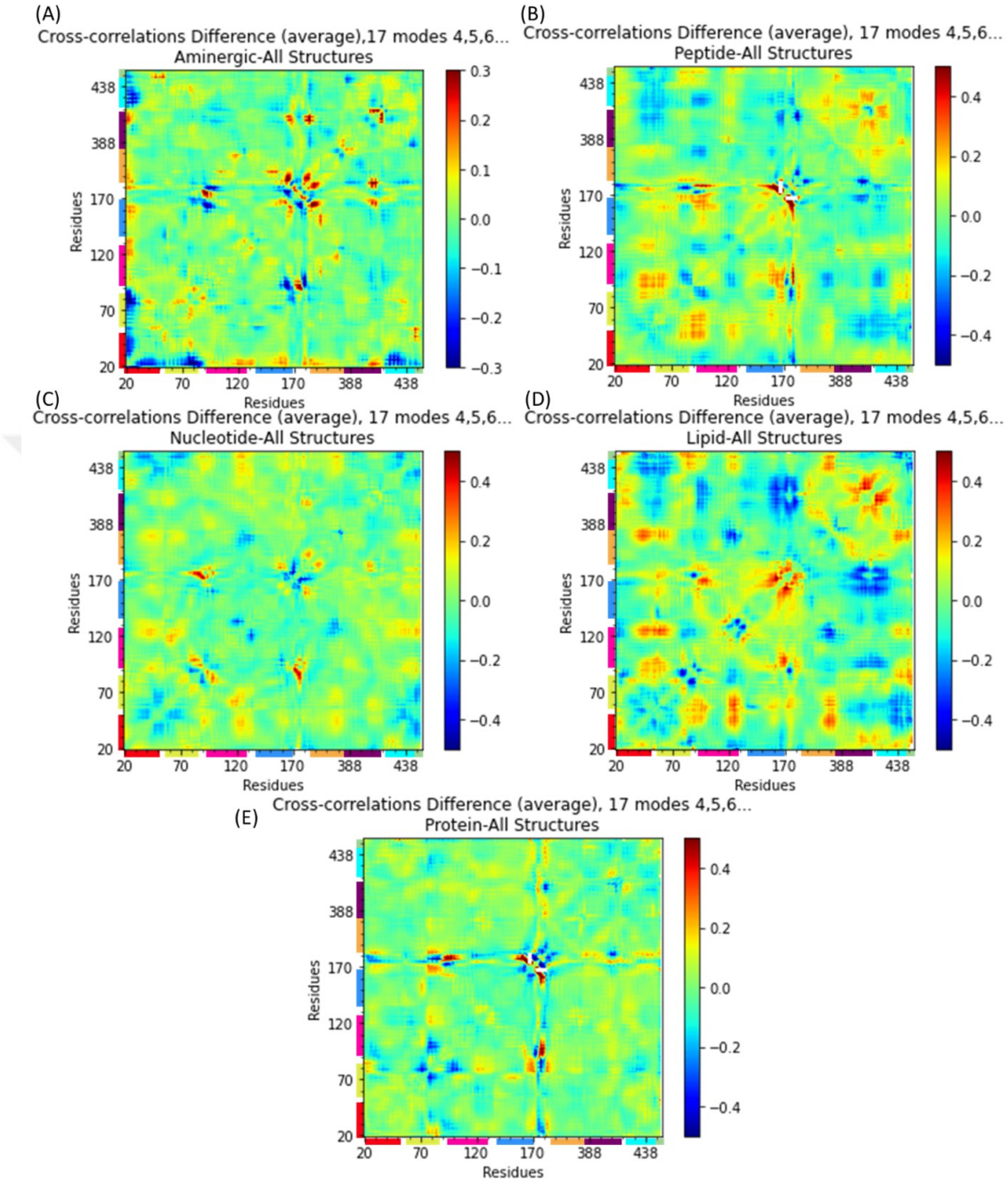

Figure 4.91. Ligand-type–specific cross-correlation differences in the low frequency mode regime. (A–E) Heatmaps displaying the average cross-correlation differences between each ligand-bound ensemble—aminergic (A), peptide (B), nucleotide (C), lipid (D), and protein-bound and overall GPCR ensemble and (E).

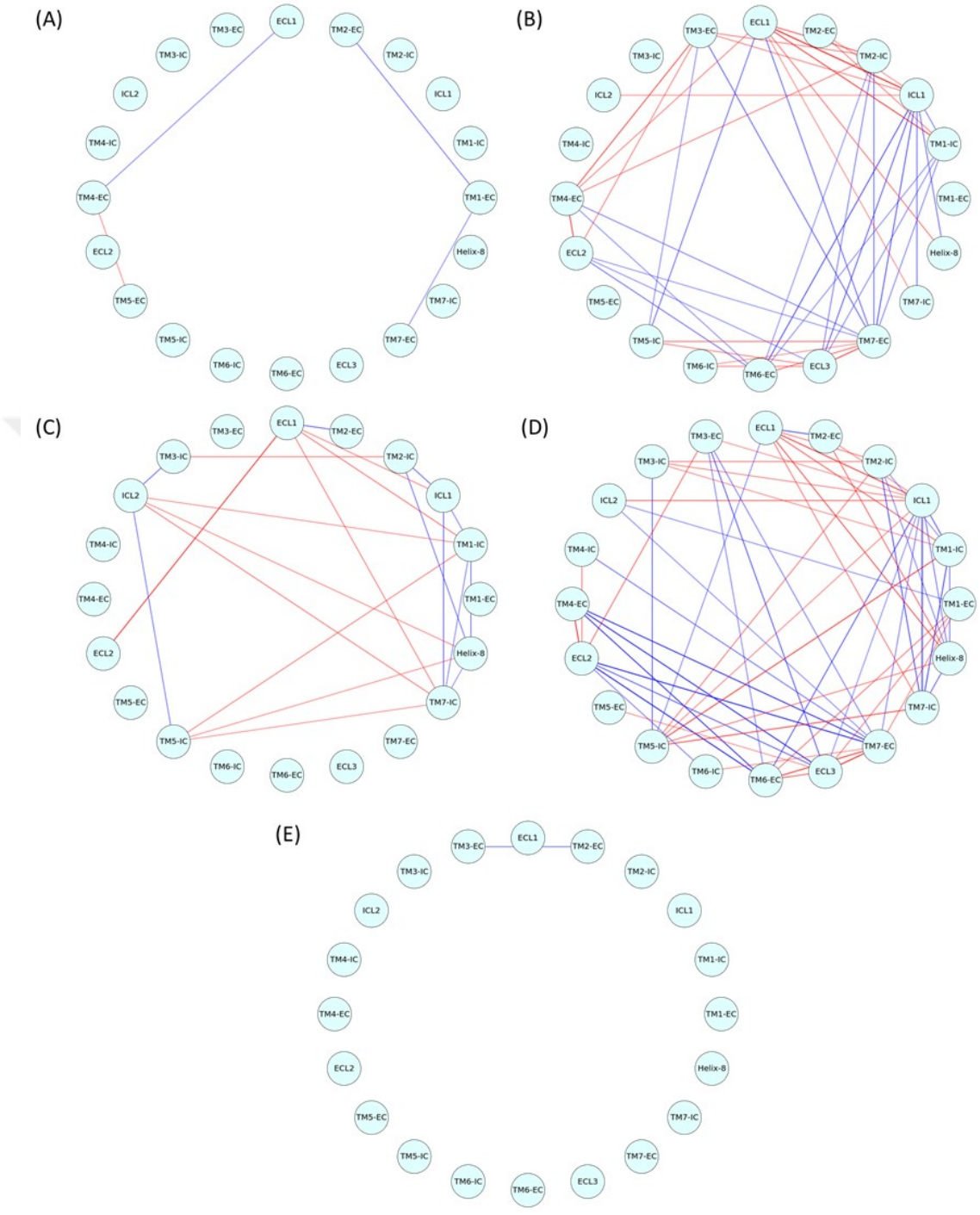

Figure 4.92. Ligand-type–specific correlation networks derived from low frequency mode differences. Segment-based correlation difference networks are shown for each ligand-binding class: aminergic (A), peptide (B), nucleotide (C), lipid (D), and protein-bound (E).

In aminergic receptors, cross-correlation analysis based on global modes revealed a notable reduction in dynamic coupling between extracellular and intracellular regions. Specifically, the TM3-EC region exhibited weakened correlations with TM2-IC and TM1-IC, and ECL1 displayed diminished interaction with TM1-IC (Figures 4.89A–4.90A). This pattern is consistent with the structural architecture of aminergic GPCRs, where small ligands bind deeply within the conserved orthosteric pocket formed by the transmembrane helices. Such deep insertion likely limits conformational propagation from extracellular loops to intracellular domains, thereby dampening long-range allosteric signaling. In the low-frequency regime, this behavior persisted, with reduced correlation across most extracellular regions—except for TM4-EC and TM5-EC, which maintained moderate connectivity (Figures 4.91A–4.92A). These helices are often involved in stabilizing the ligand-binding pocket and may serve as intermediate hubs for dynamic communication.

Peptide-bound receptors exhibited distinct and extensive dynamic rearrangements across both global and low-frequency mode regimes, reflecting the broad engagement of peptide ligands with the receptor architecture. In the global mode regime (Figures 4.89B–4.90B), we observed decreased correlations between ECL3 and TM7-EC with key intracellular regions including TM3-IC, TM5-IC, and TM6-IC, suggesting a decoupling of extracellular and intracellular motions. However, correlations increased among ECL3 and TM7-EC with TM3-EC, ECL1, TM2-EC, ICL1, TM1-IC, and TM1-EC, tighter coupling within the extracellular region, among adjacent transmembrane domains, and with the proximal intracellular interface. Notably, TM6-EC formed enhanced correlations with a network of domains spanning TM4-EC, TM1-IC, ICL1, and TM2-IC, forming an extended intracellular signaling hub. In the low-frequency modes, this pattern was partially reversed (Figures 4.91B–4.92B). Correlations involving ECL3 and TM7-EC with TM3-EC, ECL1, TM2-IC, ICL1, and TM1-IC decreased, while dynamic coupling intensified between TM5-IC, TM6-IC, and TM6-EC. The observation that this correlation pattern weakens in the global modes suggests that the associated motions may have shifted into slower collective dynamics—accompanied by reduced frequency and amplified amplitude, consistent with their dual-mode ligand binding

behavior. In this mechanism, peptide ligands typically engage both the transmembrane core and the extracellular loops simultaneously, allowing them to anchor deeply within the receptor while also modulating surface contacts that initiate allosteric transitions [162]. Helix 8 also demonstrated differential coupling behavior: in the global modes, its correlation with ECL1 and TM2-EC decreased while coupling with TM5-EC increased (Figures 4.89B–4.90B). Conversely, in low-frequency dynamics, Helix 8 regained correlation with ECL1 but lost coordination with ICL1 (Figures 4.91B–4.92B), highlighting its nuanced role in tuning the cytoplasmic surface of the receptor.

Nucleotide-bound receptors displayed distinct correlation changes across several regions, with the most prominent alterations localized to the TM7-EC (Figures 4.89C–4.90C). This finding is consistent with structural studies of receptors such as the adenosine A2A receptor (A2AR), where the orthosteric site lies adjacent to TM7-EC. Binding of nucleotide ligands is known to trigger an inward displacement of TM7 into the receptor core, reshaping the ligand-binding pocket and perturbing nearby dynamic couplings [28]. These conformational changes likely modulate long-range allosteric interactions with ICL1, TM1-IC, Helix 8, and TM7-IC, suggesting a signaling axis extending from the ligand-binding site toward the intracellular interface. In the global modes, we observed increased correlation between ECL2 and both ECL1 and TM2-EC, while correlation between ECL2 and ECL3 was reduced. Interestingly, in the low-frequency mode regime (Figures 4.91C–4.92C), the ECL2–ECL3 correlation was enhanced, suggesting that the collective motion coupling these regions may have shifted to slower, large-scale modes with reduced frequency and increased amplitude.

Lipid-bound GPCRs exhibited pronounced and spatially organized shifts in their dynamic correlation profiles compared to the full ensemble. Global mode analysis revealed significantly increased correlations within the extracellular regions, particularly among ECL2, ECL3, TM3-EC, TM4-EC, TM6-EC, and TM7-EC, and similarly strengthened correlations within the intracellular half across ICL1, ICL2, TM4-IC, and TM5-IC (Figures 4.89D–4.90D). These patterns suggest that lipid ligands promote enhanced intra-regional coherence without enforcing strong long-range coupling

between the extracellular and intracellular domains. This compartmentalized organization likely reflects the nature of lipid ligand engagement, which, as demonstrated in CB1 receptor structures bound to AM11542 and AM841, occurs deep within the transmembrane core and interacts predominantly with hydrophobic and aromatic residues across TM3, TM5, TM6, and TM7, as well as with ECL2—without extending fully into the orthosteric pocket [163].

Such binding geometry supports localized structural stabilization, leading to confined dynamic signatures. Notably, correlations between ECL3 and TM6-EC or between TM4-EC and intracellular domains (e.g., TM2-IC, ICL1) were reduced, suggesting that lipid ligands may restrict long-range allosteric communication across the membrane. Instead, lipid binding appears to foster side-specific concerted motions. In the low-frequency mode regime (Figures 4.91D–4.92D), this spatial segmentation remained evident. Helix 8 displayed enhanced dynamic coupling with ECL1, TM2-EC, and TM5-IC, implying its potential role in facilitating crosstalk at the intracellular-extracellular interface. Furthermore, TM5-IC showed increased correlations with TM2-IC, ICL1, and TM1-IC—forming an integrated intracellular signaling network—while its correlations with TM3-IC and ECL1 decreased. Interestingly, the correlated motions of TM4-EC and ECL2 with TM6-EC, ECL3 and TM7-EC observed in global modes diminished in the low-frequency regime, suggesting that these motions may be encoded in slower, large-amplitude dynamics specific to the global mode regime

Protein-bound GPCRs, despite their ligands being larger in size, often exhibit correlation changes predominantly in extracellular regions (Figure 4.89E-4.90E-4.91E-4.92E). This is because protein ligands generally interact mainly with the extracellular loops and N-terminal domain, without deeply penetrating the transmembrane core. As a result, the allosteric effects induced by protein ligands are more localized to the extracellular domain, with limited influence on the transmembrane helices and intracellular signaling interfaces.

4.3.4. Differential Dynamics Driven by G proteins and β-Arrestins

To better understand the molecular basis of biased signaling in GPCRs, we constructed a comparative ensemble that includes five receptor families, each represented by both G protein-bound and β-arrestin-bound structures. For each receptor, we incorporated one inactive state, eight intermediates (along the transition pathways toward both active states), and one fully active conformation, resulting in 10 structures per receptor and 50 structures per ensemble. Although the mean square fluctuation (MSF) profiles appeared similar between the two signaling ensembles, more pronounced differences emerged in the cross-correlation analyses based on global and low-frequency mode regimes (Figures 4.93). Domain-level correlation maps further illustrate these differences (Figures 4.94). Positive values indicate increased correlation in the β-arrestin–bound ensemble relative to the G protein–bound ensemble, while negative values reflect decreased correlation. Structural regions are colored according to the transmembrane segment color scheme shown in Figure 4.78. (B, D) Domain-based correlation difference networks for the global (B) and low-frequency (D) modes highlight the most significantly altered domain interactions. Red edges represent domain pairs with enhanced correlations in the β-arrestin–bound ensemble, while blue edges indicate decreased correlations.

Distinct dynamic signatures were observed between G protein- and β-arrestin-bound ensembles, particularly in the global and low-frequency mode regimes. In the global modes (Figures 4.93A-4.94A), β-arrestin-bound receptors exhibited enhanced correlations between TM6-EC and TM7-IC/Helix 8, and between ICL2 and TM3-EC, suggesting a unique interfacial dynamic architecture potentially tailored for β-arrestin engagement. Conversely, the G protein-bound ensemble showed stronger correlations between ICL2 and TM6-IC, and a broader coordination network linking TM3-EC with TM7-IC, Helix 8, TM1-EC, and TM1-IC. Notably,ECL1 in G protein-bound receptors displayed extensive long-range interactions with intracellular elements, including TM7-IC, Helix 8, TM1-EC, TM1-IC, and ICL1, suggesting its integral role in G protein-mediated allosteric propagation.

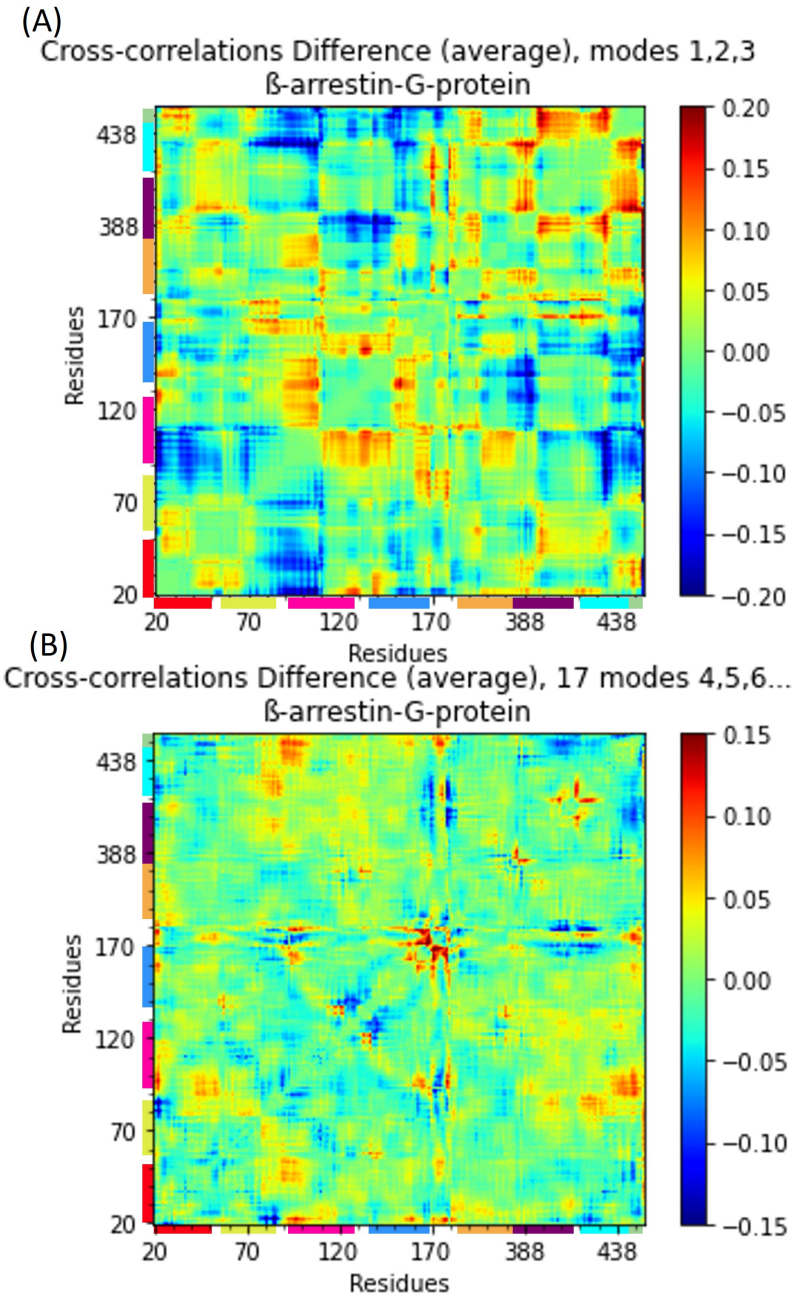

Figure 4.93. Signal protein–specific cross-correlation differences across global and low-frequency mode regimes. Heatmaps depicting the average cross-correlation differences between β-arrestin–bound and G protein–bound ensembles in the global (A) and low-frequency (B) mode regimes.

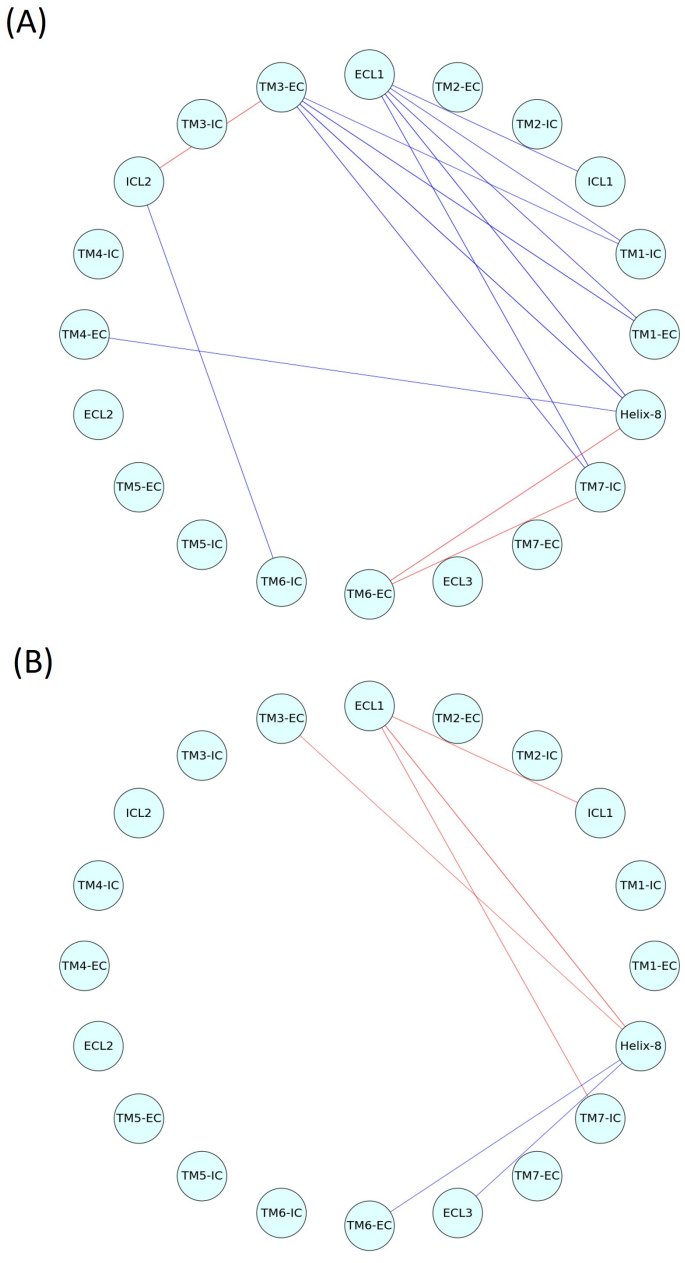

Figure 4.94. Signal protein–specific segment based correlation differences across global and low-frequency mode regimes. Segment-based correlation difference networks are shown for differences between β-arrestin–bound and G protein–bound ensembles in the global (A) and low-frequency (B) mode regimes.

In the low-frequency mode regime (Figures 4.93B-4.94B), these distinctions shifted. β-arrestin-bound receptors showed increased correlations between Helix 8 and TM3-

EC/ECL1, as well as between ECL1 and both TM7-IC and ICL1, indicating a reorganization of communication toward the extracellular-transducer interface. Interestingly, the correlation between Helix 8 and TM6-EC/ECL3, as well as between TM7-IC and ECL1, prominent in the G protein-bound global modes, diminished in this regime, suggesting that this motion has transitioned into slower, collective dynamics characteristic of the global mode regime. This shift supports the idea of mode redistribution, where allosteric coupling shifts across frequency domains depending on the signaling context.

Importantly, Helix 8 and TM7-IC consistently demonstrated mode- and pathway-dependent coupling shifts across the ensembles, reinforcing its established role in biased signaling [27]. Together, these findings highlight unique allosteric architectures for G protein and β-arrestin signaling, offering mechanistic insight into the structural encoding of signaling bias. The distinctions between GPCRs bound to varying ligands and those engaged with different partner proteins help elucidate the dynamic codes underlying biased signaling—particularly the modulatory role of the conserved rotamer toggle switch and the pathway-specific behavior of Helix 8—potentially guiding the development of more selective and effective therapeutic strategies. These results were presented at the EMBO Workshop: Computational Structural Biology under the title "Signature Dynamics of Activation Transition Pathways in GPCRs".

4.4. Additional Works

4.4.1. Computational and experimental mapping of the allosteric network of two manganese ABC transporters

This work, recently published in Protein Science, presents an integrative computational and experimental approach to decipher the allosteric communication mechanisms in two manganese ABC importers: Streptococcus pneumoniae PsaBC and Bacillus anthracis MntBC, both of which are essential for bacterial virulence [145]. Transition metals such as Mn^2+, Fe^2 + /3+, and Zn^2+ serve as critical enzymatic cofactors across all domains of life. However, their limited availability in host environments has

driven the evolution of high-affinity uptake systems in pathogenic bacteria. PsaBC and MntBC are representative members of this class of importers, sharing a conserved homodimeric architecture consisting of a transmembrane domain (TMD) connected to a cytoplasmic nucleotide-binding domain (NBD). Due to the slow transport cycle and large size of these complexes, conventional molecular dynamics simulations are often inadequate for capturing long-range, functionally relevant motions. To overcome this, we applied a computationally efficient framework that combines Gaussian Network Model (GNM) analysis with information-theoretic Transfer Entropy (TE) calculations, enabling the identification of dynamic couplings and directional allosteric communication pathways within these complexes. Our predictions were strongly supported by experimental validation. Based on the computational identification of "allosteric hotspots," we introduced 10 single-point mutations and assessed their functional impact in vitro. Strikingly, the experimental results were in excellent agreement with the TE-based predictions, confirming the functional relevance of the predicted allosteric sites.

The analysis revealed key allosteric communication hubs located along the transmembrane translocation pathway, within the coupling helices that mediate TMD-NBD interactions, and at the ATP-binding motifs. We further uncovered a distinct pattern of inter-domain information flow: robust bi-directional communication was observed between the two TMDs, while transmission from NBDs to TMDs was unidirectional and asymmetric—originating from one NBD and targeting the TMD of the opposite protomer. Notably, NBD–NBD allosteric coupling was minimal in both systems. These findings highlight a unique allosteric signature that differentiates transition metal ABC importers from other members of the ABC transporter superfamily, suggesting their classification as a distinct functional subclass. Moreover, this study provides the first comprehensive mapping of conformational dynamics in these virulence-associated importers, offering novel insights for structure-based drug discovery targeting bacterial metal uptake systems. To acquire the allosteric "footprint" of Streptococcus pneumoniae PsaBC, we employed GNM-TE analysis using the experimentally resolved inward-facing conformation (PDB ID: 7KYP; [164]). The analysis focused on the 10 slowest

modes derived from the Gaussian Network Model (GNM), which collectively capture the most functionally relevant, global-scale motions of the system. To quantify allosteric signaling, we calculated TEcol scores for each residue, which integrate both the magnitude of net Transfer Entropy (netTE)—reflecting how much information is transmitted—and the collectivity of information transfer—i.e., how broadly this signal is distributed across the structure. Residues with TEcol scores exceeding twice the mean TEcol score and twice the average peak prominence were designated as "allosteric hotspots".

Using these stringent criteria, we identified 31 residues as information source residues, located across both the transmembrane domains (TMDs) and nucleotide-binding domains (NBDs) (Figure 4.95a,b) [145]. Within the TMDs, the highest TEcol scores were associated with residues forming the transmembrane permeation pathway, while in the NBDs, the top-scoring residues were located near the ATP-binding sites, suggesting functional relevance of these allosteric hotspots in both substrate translocation and ATP-driven conformational cycling.

To evaluate the predictive power of GNM-TE, we compared our computationally identified hotspots with previously validated functionally essential residues. According to experimental findings [164], eight residues (Asp46, His50, Phe121, and Phe124 from each protomer) have been shown to play critical roles in metal coordination and gating. Notably, five of these eight essential residues exactly overlapped with the predicted allosteric hotspots (Figure 4.95b [145], red spheres), suggesting a high degree of predictive fidelity.

To determine whether this overlap occurred by chance, we performed a statistical test: 100,000 sets of 31 randomly distributed residues were generated, and the number of exact matches with the eight functionally essential residues was computed for each set. The GNM-TE-based prediction of five matches significantly outperformed random expectation, which had a mean match count of only 0.25 ($p = 2.7 \times 10^{-11}$; Figure 4.95c) [145].

Further analysis expanded the criteria for matching to include spatial proximity—residues located within 4Åor 7Åof functionally essential residues. Under these relaxed conditions, all eight essential residues were found to be either direct GNM-TE peaks or within the first or second coordination shell of identified peaks (Figure 4.95d,e) [145]. This further strengthens the case for the functional relevance of GNM-TE hotspots and highlights the method's ability to uncover biologically meaningful allosteric communication pathways.

The results presented thus far were obtained using the 10 slowest GNM modes which represent the full dynamic spectrum of PsaBC (Figure 4.96) [145]. However, during the calculations, the large entropic contribution of the slowest modes may overshadow that of the next slowest modes, which might hold significant functional relevance [165]. To address this issue, one approach is to recompute the analysis while excluding the slowest GNM mode(s). This approach has proven effective in identifying important functional sites within a dataset of allosteric proteins [144] and in the homologous human ABC transporter, CFTR [37].

Replication of the calculations after excluding the slowest GNM mode revealed that the coupling helices emerge as prominent allosteric peaks (Figure 68a). Located at the interface between the nucleotide-binding domains (NBDs) and transmembrane domains (TMDs), the coupling helices are known to play a critical role in allosteric transmission, linking ATP binding and hydrolysis at the NBDs to conformational changes in the TMDs [36, 166–169].

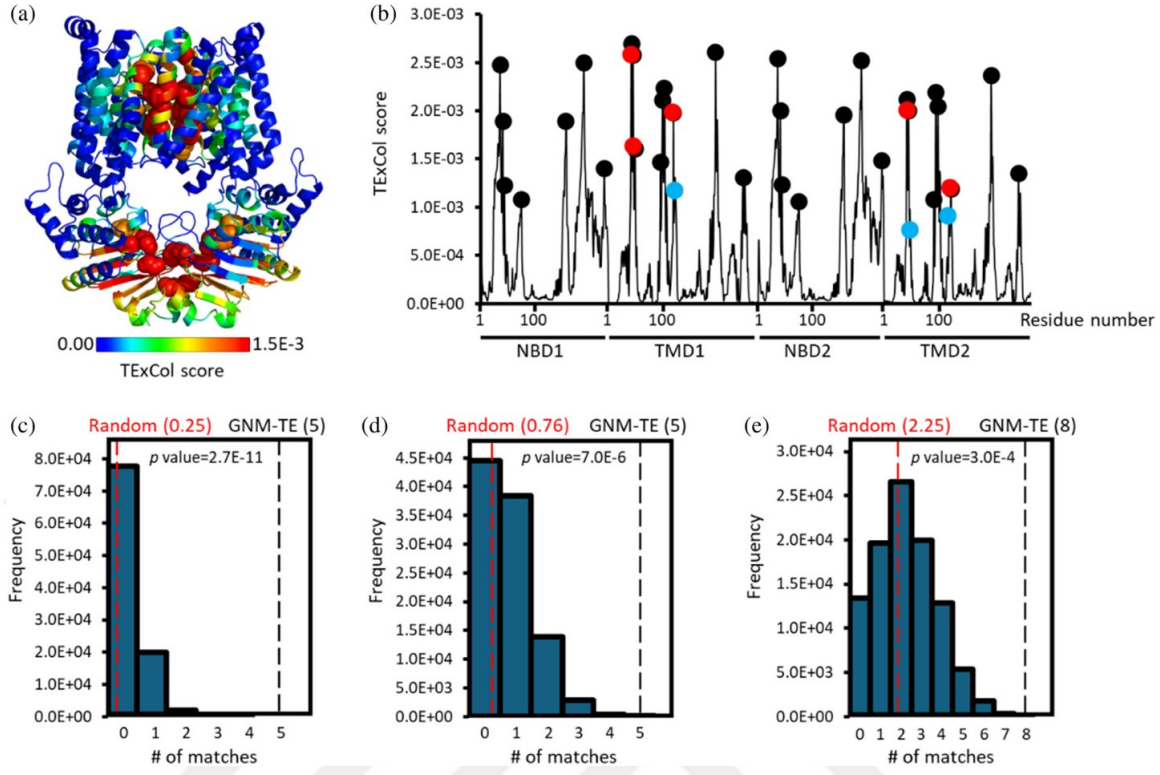

Figure 4.95. TEcol-colored structure with peak residues as spheres. (b) TEcol profile with 31 peaks; red/cyan circles indicate exact or $\leq 4\mathring{A}$ matches to essential residues. (c–e) Randomization analysis confirms statistical significance against 100,000 random sets.

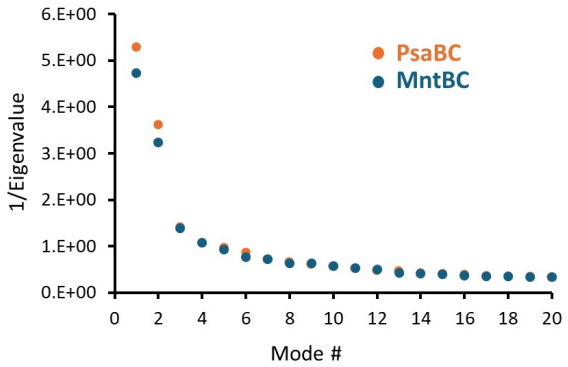

Figure 4.96. Relative contribution in 1/Eigenvalue of the slow modes of PsaBC and MntBC to the overall dynamics as a function of mode number.

Notably, akin to the results obtained with PsaBC, the GNM-TE predictions of MntBC demonstrated significant accuracy compared to random allocation, whether evaluating exact matches or first- or second-coordination sphere interactions. Based on GNM-TE predictions, we generated 11 de novo point mutations targeting transmembrane residues that lacked obvious functional annotations. Experimental assays revealed that 8 out of 10 mutations introduced at computationally predicted allosteric hotspots abolished MntBC activity under manganese-supplemented conditions, while a control mutation at a low-scoring residue had no functional effect. These findings demonstrate excellent concordance between computational predictions and experimental results, reinforcing the reliability of TEcol scores in identifying functionally critical allosteric sites. We propose that GNM-TE represents a computationally efficient and accessible alternative to conventional molecular dynamics simulations for probing functional dynamics in large membrane proteins. From a biological perspective, this study provides novel insights into structure–function relationships in active transporters, highlighting a distinct allosteric wiring in manganese ABC importers and supporting the broader consensus that protein structure underlies and constrains biological function.

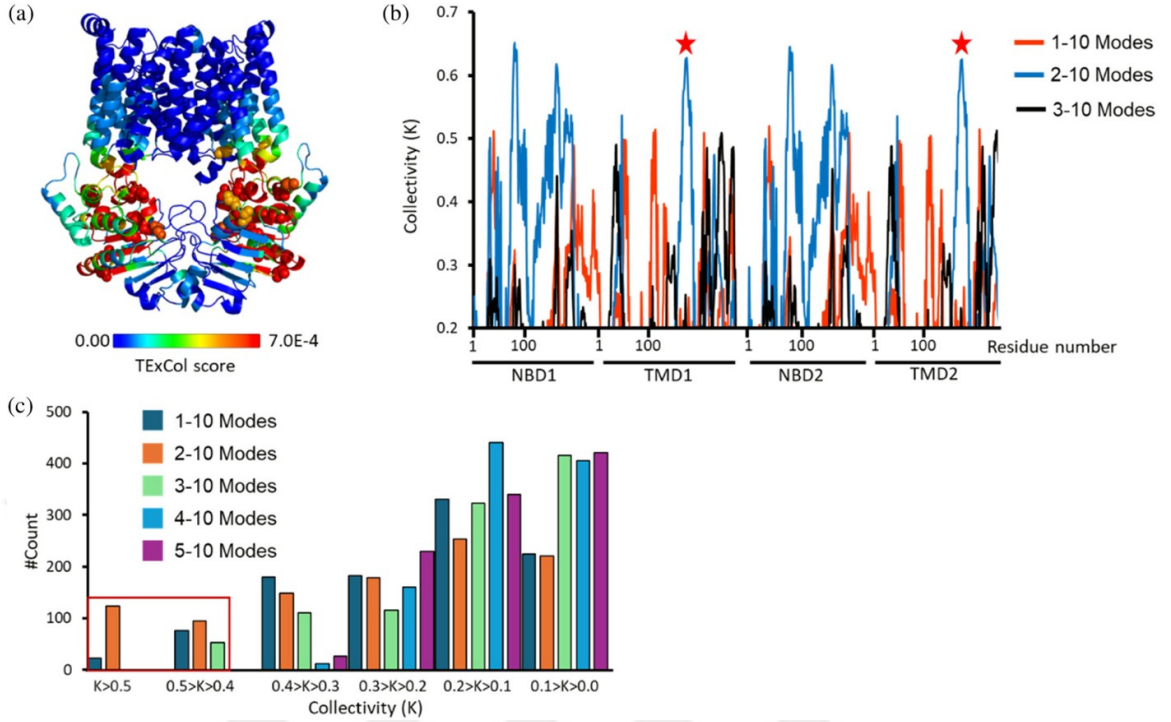

Figure 4.97. Allosteric peaks and collectivity across mode ranges in PsaBC. (a) TEcol-colored structure with peaks shown as spheres, computed following exclusion of the slowest mode. (b) Shown are the collectivity values (K) for all residues of PsaBC across different mode ranges, red stars mark coupling helices. (c) Distribution of K values across mode subsets.

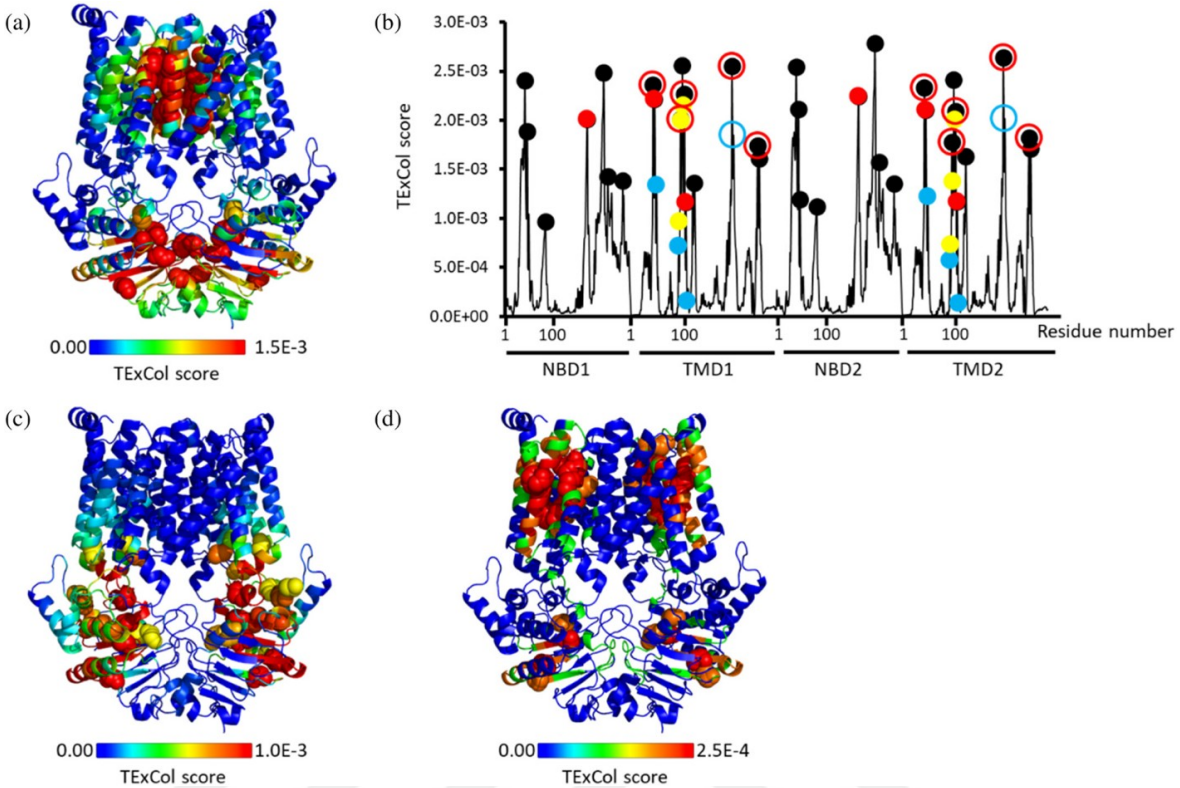

Figure 4.98. Correlation between allosteric hotspots in MntBC and functionally essential residues. (a) TEcol-colored structure with peak residues as spheres. (b) TEcol profile with 35 peaks; colored circles indicate overlap or proximity to functional residues. (c) and (d) same as A, only the computations were performed after exclusion of the first slowest mode (c) or the two slowest modes (d).

4.4.2. ANM-LD Path Web Server: A Framework for Predicting Conformational Transitions and Allosteric Interactions

The ANM-LD Path web server is a user-friendly computational platform that implements the Anisotropic Network Model–guided Langevin Dynamics (ANM-LD) simulation protocol, a hybrid method designed to efficiently predict conformational transition pathways between experimentally resolved protein states. This approach integrates coarse-grained normal mode analysis with all-atom stochastic simulations in implicit solvent, enabling the generation of physically plausible transition trajectories.

The platform accepts user-submitted PDB files of two end states representing a functional conformational change and outputs all-atom transition trajectories reconstructed via the intrinsic dynamics of slowest ANM modes. These trajectories are energy-minimized and propagated via Langevin dynamics to capture the stochastic yet functionally guided nature of protein motion. The resulting paths allow for the identification of key collective motions and mechanistically critical residues that facilitate conformational transitions, with implications for understanding allostery and functional regulation in proteins.

In this work, I contributed to the backend development of the server by automating the analysis workflow and integrating GPU acceleration to optimize computational performance. To validate the server's performance and versatility, I tested its capabilities on five biologically relevant systems with known conformational transitions: Adenylate Kinase (ADK), Sarcoplasmic/Endoplasmic Reticulum Calcium ATPase (SERCA), Calmodulin (CaM), Human Transferrin, and the D-Ribose-Binding Protein. These case studies demonstrated the robustness of the platform in predicting transition pathways across diverse protein architectures and functional mechanisms.

The web server and accompanying methodology are being prepared for publication: Aykac Fas, B., Akbas Buz, Z. E., Kutlu, Y., Duman, O., and Haliloglu, T. ANM-LD Path: A Computational Framework for Predicting Conformational Transition Pathways and Allosteric Interactions, to be submitted, 2025.

4.4.2.1. Adenylate kinase (ADK). Adenylate kinase (ADK) plays a central role in nucleotide metabolism by catalyzing the reversible transfer of a phosphate group between two adenosine diphosphate (ADP) molecules to generate one adenosine triphosphate (ATP) and one adenosine monophosphate (AMP). This reaction is essential for maintaining cellular energy balance and the equilibrium of adenine nucleotides. Due to its pronounced conformational changes during catalysis, ADK has long served as a model system for studying allosteric regulation, enzymatic mechanisms, and conformational dynamics. Moreover, ADK has emerged as a potential therapeutic target in diseases

such as cancer and epilepsy [170]. Figure 4.99 illustrates the conformational transition captured by the ANM-LD simulation for ADK. Panel A shows the structural alignment of the inactive (PDB ID: 4AKE) and active (PDB ID: 1AKE) states, revealing a significant conformational change with an initial RMSD of 7.18 Å. Panel B presents the simulation trajectory, depicting the gradual decrease in RMSD across simulation cycles and highlighting the contribution of specific ANM modes. The RMSD steadily decreases throughout the simulation, ultimately reaching a final value of approximately 1 Å. This outcome demonstrates the ANM-LD Path method's ability to effectively capture and refine the transition between functionally distinct conformational states of ADK.

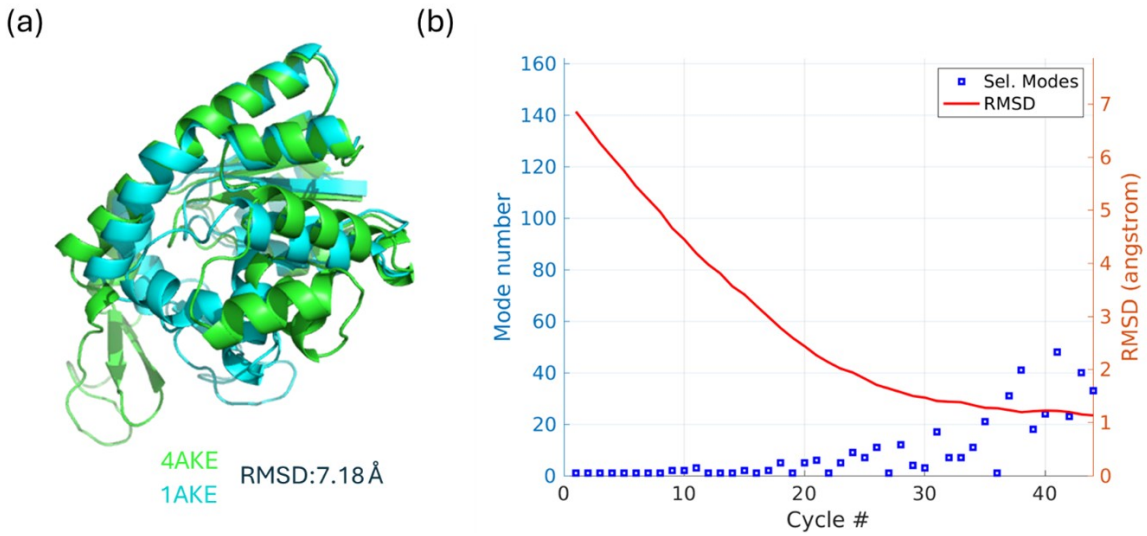

Figure 4.99. ANM-LD simulation results for adenylate kinase (AdK). (a) Alignment of the inactive (PDB ID: 4AKE) and active (PDB ID: 1AKE) states of AdK, with an initial RMSD of 7.18 Å.(b) Progression of the ANM-LD simulation, showing mode numbers and RMSD versus cycles. The RMSD decreases to approximately 1 Å, reflecting the convergence of the transition pathway toward the active state.

4.4.2.2. The Sarcoplasmic / Endoplasmic Reticulum Calcium ATPase (SERCA). The Sarcoplasmic / Endoplasmic Reticulum Calcium ATPase (SERCA) is an essential

transmembrane protein belonging to the P-type ATPase family. It actively transports calcium ions from the cytoplasm into the sarcoplasmic or endoplasmic reticulum (SR/ER), a process driven by ATP hydrolysis. This function is vital for maintaining intracellular calcium homeostasis and supports numerous physiological processes, including muscle contraction, signal transduction, and calcium storage. SERCA undergoes a well-characterized cycle of conformational transitions between two major states, which have been resolved in high-resolution crystal structures. These structures have made SERCA a valuable model for investigating the mechanistic basis of ion transport in P-type ATPases [171, 172].

Figure 4.100 presents the results of the ANM-LD simulation applied to SERCA. Panel A shows the structural alignment of the inactive state (PDB ID: 1SU4) and the active state (PDB ID: 1T5S), which initially exhibit a substantial conformational difference with an RMSD of 13.55 Å. Panel B illustrates the simulation trajectory, detailing the gradual reduction in RMSD and the evolving contributions of ANM modes across cycles. By the end of the simulation, the RMSD decreases to approximately 3.5 Å, indicating a refined alignment and a successful reconstruction of the transition pathway. These results highlight the capability of the ANM-LD method to capture large-scale conformational shifts in membrane proteins such as SERCA.

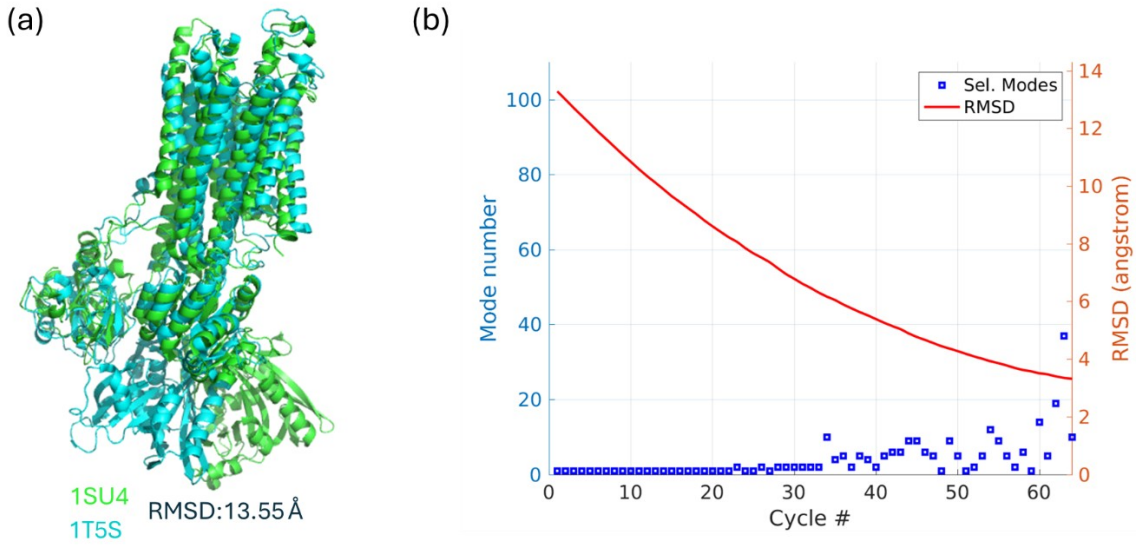

Figure 4.100. ANM-LD simulation results for the SERCA protein. (a) Alignment of the inactive (PDB ID: 1SU4) and active (PDB ID: 1T5S) states of the SERCA protein, with an initial RMSD of 13.55 Å. (b) Simulation progression showing mode numbers and RMSD versus cycles. The RMSD decreases to approximately 3.5 Å, illustrating the convergence of the transition pathway toward the active state.

4.4.2.3. Calmodulin (CaM). Calmodulin (CaM) is a highly conserved, calcium-binding protein that plays a central role in regulating a wide range of cellular functions. Acting as both a calcium sensor and signal transducer, CaM interacts with numerous target proteins in a calcium-dependent manner to modulate processes such as gene expression, muscle contraction, metabolism, and cell division. Its ability to translate intracellular calcium fluctuations into specific functional responses makes it a critical component of calcium signaling networks. Owing to its versatility and dynamic nature, CaM has been widely studied as a model system for understanding protein–protein interactions and calcium-mediated conformational transitions [173, 174].

Figure 4.101 displays the ANM-LD simulation results for calmodulin, capturing the transition between its inactive (PDB ID: 1CFD) and active (PDB ID: 1CLL) conformations. Panel A illustrates the initial alignment between the two states, with a

starting RMSD of 10.8 Å. Panel B shows the simulation trajectory, highlighting both the mode contributions and the reduction in RMSD over time. The RMSD decreases steadily throughout the simulation and converges to a final value of approximately 2.3 Å. This result demonstrates the effectiveness of ANM-LD in reconstructing the conformational transition and refining the alignment between structurally distinct states of CaM.

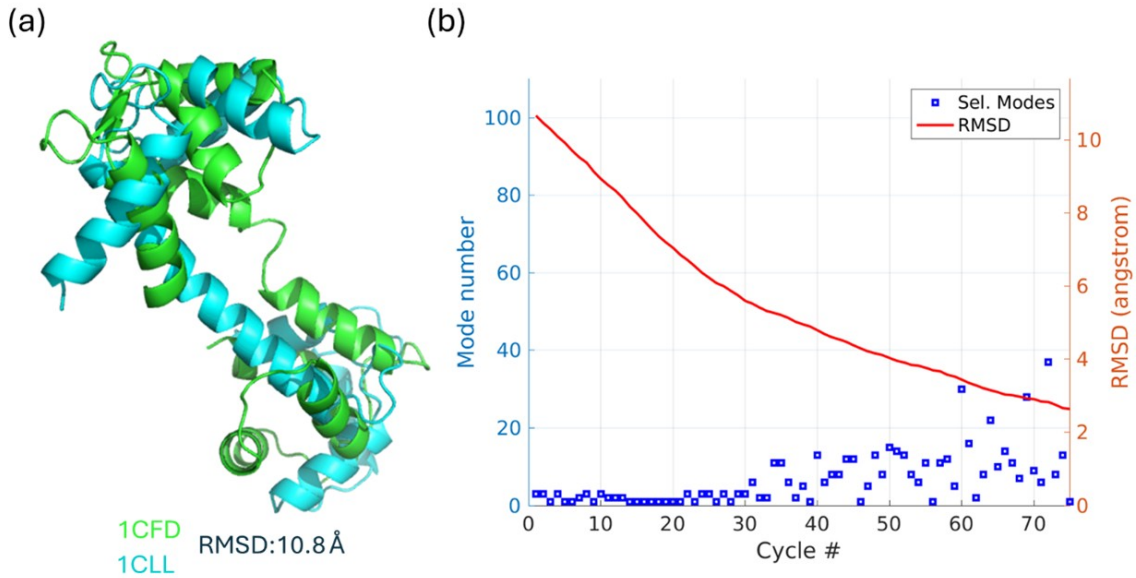

Figure 4.101. ANM-LD simulation results for calmodulin. (a) Alignment of the inactive (PDB ID: 1CFD) and active (PDB ID: 1CLL) states of calmodulin, with an initial RMSD of 10.8 Å. (b) Simulation progression showing mode numbers and RMSD versus cycles. The RMSD decreases to approximately 2.3 Å, demonstrating the convergence of the transition pathway toward the active state.

4.4.2.4. Human Transferrin. Human transferrin is a glycoprotein primarily responsible for the transport of iron through the bloodstream to various tissues. This process is vital for maintaining systemic iron homeostasis and ensuring the availability of iron for essential cellular functions, including electron transport, DNA replication, and hemoglobin synthesis. Synthesized predominantly in the liver and circulating in the

plasma, transferrin plays a key role in regulating iron levels and preventing iron toxicity. Due to its clinical relevance, human transferrin is extensively studied in the context of diagnostics, therapeutic targeting, and understanding iron metabolism-related diseases [175, 176]. Figure 4.102 presents the ANM-LD simulation results for human transferrin, depicting the transition between its inactive (PDB ID: 1BP5) and active (PDB ID: 1A8E) conformations. Panel A shows the initial structural alignment between these states, with a starting RMSD of 6.70 Å. Panel B illustrates the simulation trajectory, highlighting the contributions of ANM modes and the reduction of RMSD across cycles. The RMSD decreases steadily throughout the simulation, ultimately reaching a final value of approximately 1 Å. These results confirm the ability of the ANM-LD framework to accurately reconstruct the conformational transition pathway and refine the alignment between distinct functional states of human transferrin.

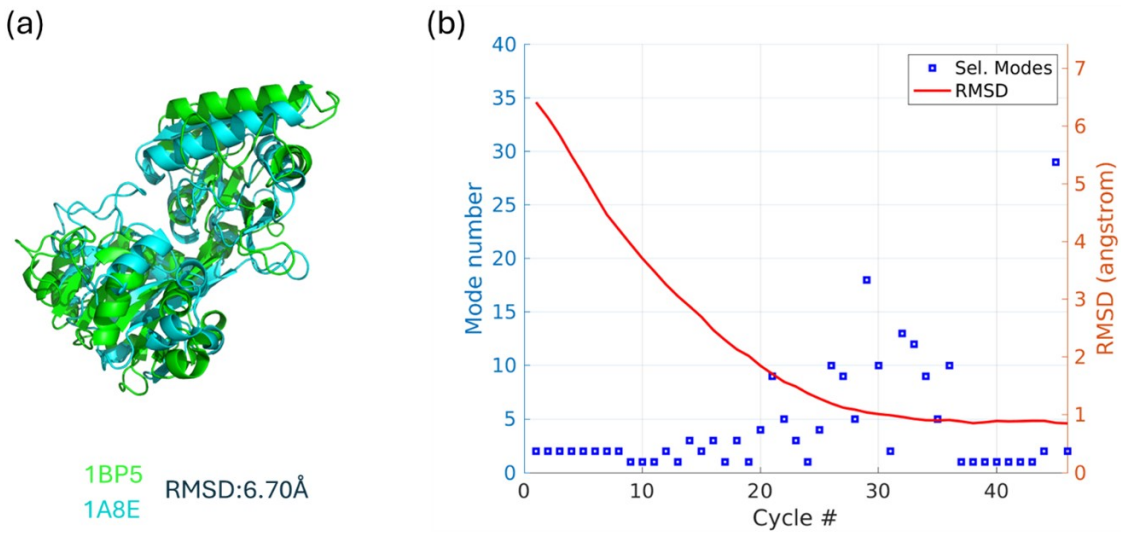

Figure 4.102. ANM-LD simulation results for human transferrin. (a) Alignment of the inactive (PDB ID: 1BP5) and active (PDB ID: 1A8E) states of human transferrin, with an initial RMSD of 6.70 Å. (b) Simulation progression showing mode numbers and RMSD versus cycles. The RMSD decreases to approximately 1 Å, demonstrating the successful convergence of the transition pathway toward the active state.

4.4.2.5. D-Ribose-Binding Protein. The D-ribose-binding protein is a periplasmic protein essential for the high-affinity uptake and utilization of D-ribose—a five-carbon sugar crucial for energy production, metabolic processes, and nucleoside biosynthesis. It functions as a component of the ATP-binding cassette (ABC) transport system in bacteria, facilitating the translocation of D-ribose across the cell membrane. As a key player in bacterial nutrient acquisition, the D-ribose-binding protein contributes directly to metabolic regulation and cellular survival. Its structural and functional significance has made it a subject of interest in microbiology, structural biology, and antimicrobial drug development [177, 178].

Figure 4.103 illustrates the ANM-LD simulation results for the D-ribose-binding protein, capturing the conformational transition between its inactive (PDB ID: 1URP) and active (PDB ID: 2DRI) forms. Panel A depicts the initial structural alignment between the two states, which exhibit an RMSD of 4.06 Å. Panel B shows the simulation trajectory, highlighting both the evolving contributions of ANM modes and the progressive reduction in RMSD across cycles. The simulation successfully models the transition, with the RMSD converging to a final value of approximately 1 Å. These findings underscore the effectiveness of the ANM-LD framework in resolving conformational transitions even in compact and highly dynamic bacterial transport proteins.

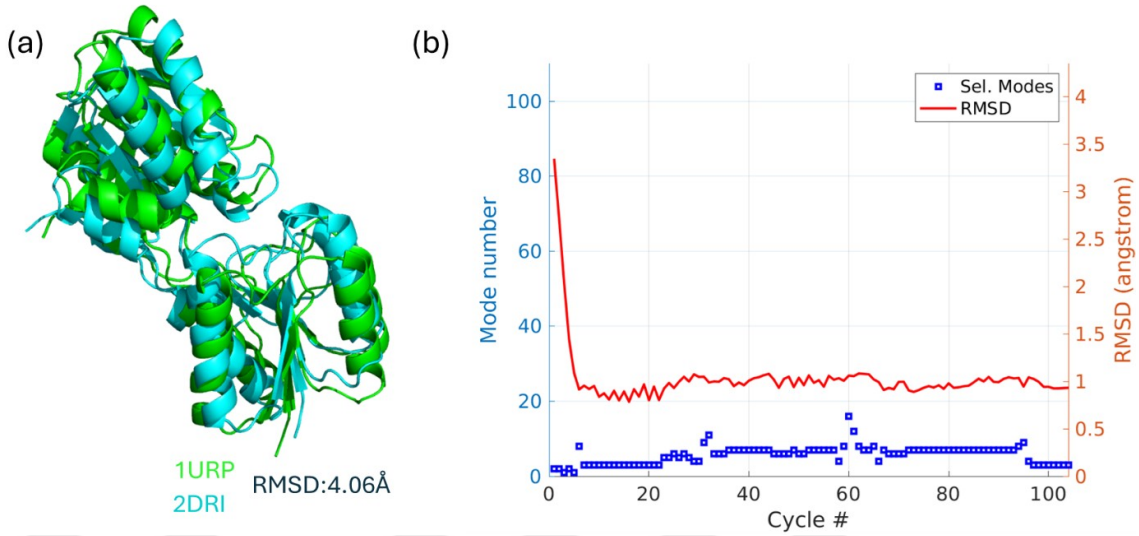

Figure 4.103. ANM-LD simulation results for D-ribose-binding protein. (a) Alignment of the inactive (PDB ID: 1URP) and active (PDB ID: 2DRI) states of the D-ribose-binding protein, with an initial RMSD of 4.06 Å. (b) Simulation progression showing mode numbers and RMSD versus cycles.

4.4.3. Understanding the Role of Factor V in the Coagulation Cascade and the Impact of Mutations on Its Dynamics

Factor V (FV) is a glycoprotein that plays a dual role in the coagulation cascade, acting as both a procoagulant and an anticoagulant depending on its activation state. In its inactive form (PDB ID: 7KVE), FV circulates as a procofactor and becomes activated upon cleavage by thrombin, producing Factor Va (FVa, PDB ID: 7KXY) [179]. Once activated, FVa functions as a critical cofactor in the prothrombinase complex by associating with Factor Xa (FXa), catalyzing the conversion of prothrombin into thrombin. This complex exhibits a remarkably high turnover rate, converting thousands of prothrombin molecules per minute [180–182].

FVa is inactivated through proteolytic cleavage at three arginine residues—R306, R506, and R679—by the activated protein C (APC)–protein S complex, yielding Factor Vai (PDB ID: 1SDD), which exhibits anticoagulant activity [183]. In this role,

Factor Vai cooperates with APC and protein S to maintain regulatory feedback within the coagulation cascade. Notably, APC can efficiently cleave R506 without protein S, whereas cleavage at R306 is significantly enhanced in the presence of protein S. Subsequent cleavage at R679, located at the C-terminal region of the A2 domain, results in full inactivation of FVa. Protein S, although functionally critical, is not homologous to coagulation factors or APC and is instead a vitamin K-dependent protein [182]. Functionally important residues are demonstrated in Figure 4.104.

The significance of FV lies in its involvement in both the intrinsic and extrinsic pathways of the coagulation process. Mutations or defects in FV may lead to divergent clinical outcomes, ranging from thrombosis (e.g., deep vein thrombosis, ischemic stroke) to excessive bleeding, depending on how they affect its activation or inactivation pathways [179, 184].For instance, the well-known FV Leiden mutation (R506Q) impairs inactivation by APC and is a common cause of hereditary thrombophilia. On the other hand, excessive tissue factor expression in malignancies can drive thrombotic events via the extrinsic pathway. Bleeding disorders can also arise due to deficiencies in other clotting factors, such as Factor VIII (Hemophilia A), Factor IX (Hemophilia B), or Factor VII (extrinsic pathway) [185]. In addition to the Leiden mutation, we examined two newly identified patient-specific mutations: G563A and Y2021C. These mutations were discovered in individuals with unexplained coagulation abnormalities (Figure 4.104B). Intriguingly, despite markedly reduced FV activity in the patient carrying the G563A mutation—normally associated with a bleeding phenotype—the individual exhibited no clinical signs of bleeding. Instead, a prothrombotic tendency was observed. Similarly, the Y2021C variant was associated with an increased risk of clot formation.

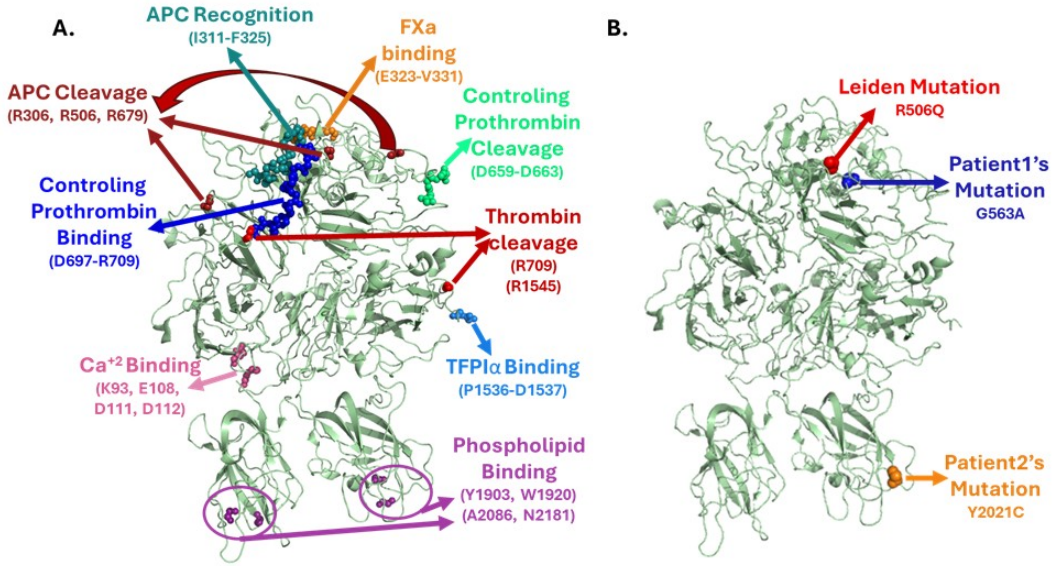

Figure 4.104. Representation of human Factor V with A) important sites B) mutation points.

To investigate the structural and dynamic consequences of these mutations, we conducted molecular dynamics (MD) simulations of wild-type FV (PDB ID: 7KVE), the R506Q (Leiden), G563A, and Y2021C variants. Additionally, we employed GNM to evaluate the potential alterations in collective dynamics induced by these mutations.

All MD simulations were performed using the AMBER 22 software suite with the ff19SB force field and included explicit solvent representation. Simulations were conducted at 310 K for 500 ns on a high-performance computing cluster equipped with Intel Xeon processors and NVIDIA GPUs. Three independent trajectories were generated for each variant to ensure statistical robustness.

Figure 4.105 presents the RMSD analysis of wild-type Factor V and its three mutant variants (R506Q, G563A, and Y2021C) over the course of 500 ns molecular dynamics simulations. Panel A displays the time-dependent evolution of RMSD calculated using the entire structure, reflecting the overall structural stability and conformational flexibility of each system. While all variants reached stable trajectories after an ini-

tial equilibration phase, differences in fluctuation amplitude and convergence behavior were observed among the mutants. Panel B summarizes the mean RMSD values with standard deviations calculated over the equilibrated interval (250–500 ns), providing a quantitative measure of structural deviation from the starting conformation. Notably, the G563A and Y2021C mutants exhibited slightly higher RMSD values compared to the wild type, suggesting mutation-induced alterations in structural dynamics. These differences may reflect changes in the global conformational landscape and functional behavior of Factor V variants.

To explore the global dynamics of Factor V and assess the impact of clinically relevant mutations, we performed a series of analyses integrating Gaussian Network Model (GNM) calculations and cross-correlation evaluations. Global individual modes were computed using both the crystal structure of Factor V (PDB ID: 7KVE) and an averaged Kirchhoff connectivity matrix derived from the ensemble of conformations sampled during the 250–500 ns interval of MD simulations for the wild type and mutant forms.

The slowest GNM modes of the crystal structure highlight functionally critical residues located at or near hinge sites—defined as minima in the mode shape profiles. Notably, residues involved in calcium binding, TFPIα interaction, APC cleavage and recognition, as well as residues important for prothrombin binding and cleavage, all reside within 7 Å of hinge points in the dominant global modes (Figure 4.106). Among these, the R506 residue (associated with the Leiden mutation), G563 (identified in Patient 1), and residues governing prothrombin binding were found to be hinge residues or hinge neighbors in the fourth slowest mode. This observation suggests that perturbations at these positions may propagate long-range effects across the protein's structure due to their dynamic centrality.

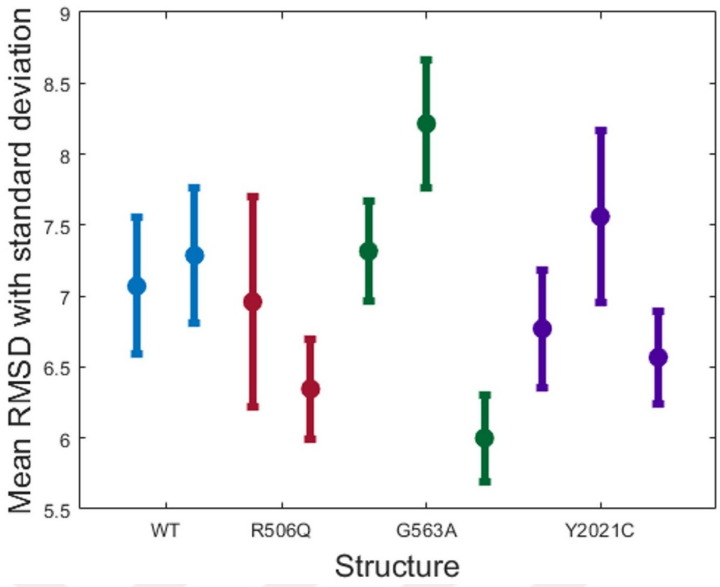

Figure 4.105. RMSD analysis of Factor V wild-type and mutant variants over the course of 500 ns molecular dynamics simulations. Mean RMSD values with standard deviations computed over the 250–500 ns interval, representing the equilibrated phase of the simulation for each system.

To further examine the distal C1 and C2 domains, a focused GNM analysis was carried out on residues D1878–Y2196. The seven slowest modes of this region (Figure 4.107) again revealed that functionally important residues—including phospholipid binding sites—and the Y2021C mutation (identified in Patient 2) are located at or near hinge points across several modes (3rd through 7th). This localization underscores their potential role in modulating domain-specific mobility and allosteric interactions relevant to membrane association.

To assess how mutations alter the intrinsic dynamic behavior of Factor V, GNM mode shapes (1–10) were recalculated using MD-derived ensembles for the wild-type, R506Q, G563A, and Y2021C variants (Figure 4.108).

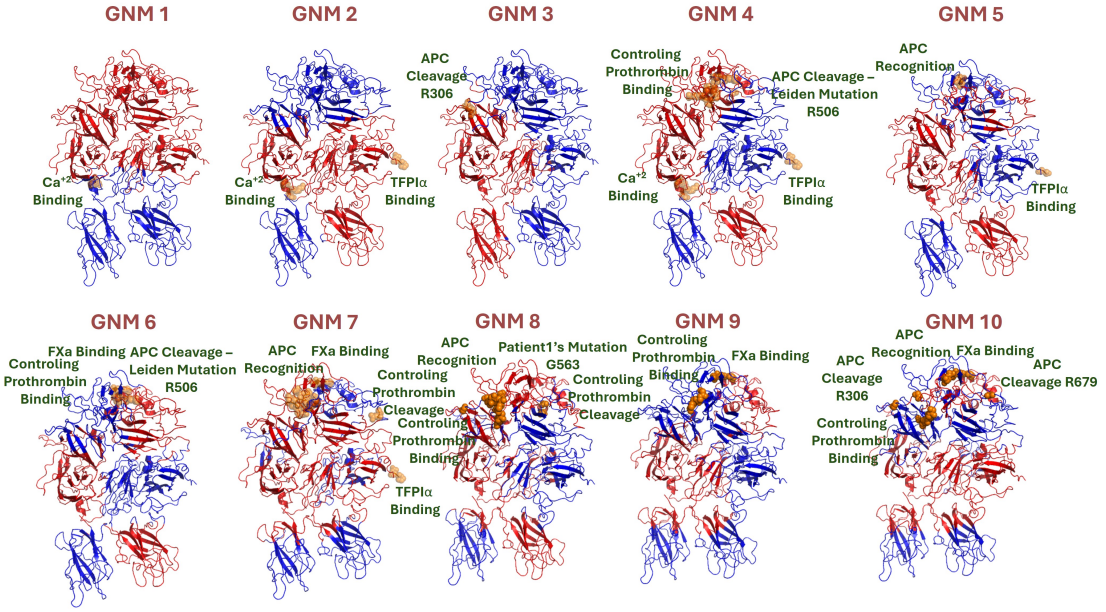

Figure 4.106. Residue correlations of seven slowest GNM modes in color-coded ribbon diagram of the factor V (functionally important regions/residues in the cutoff distance of 7 Å to hinge residues demonstrated as orange spheres).

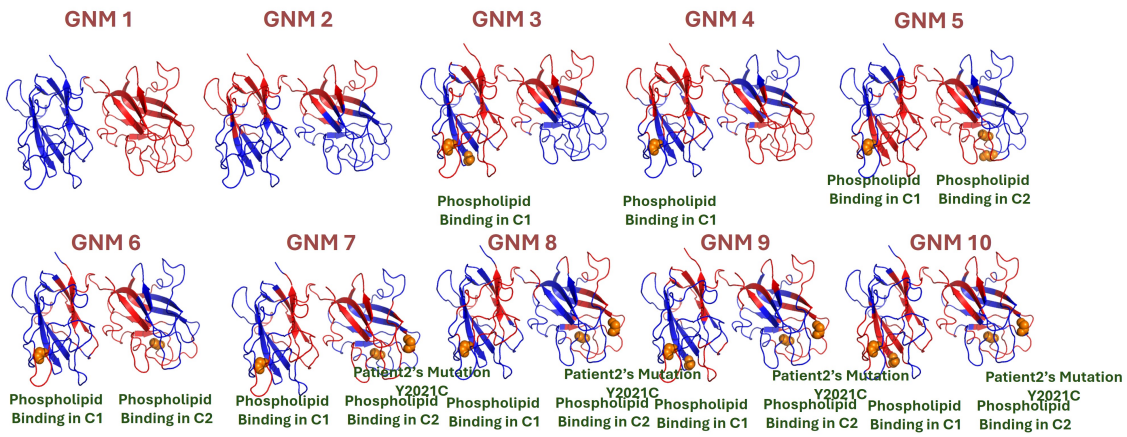

Figure 4.107. Residue correlations of seven slowest GNM modes in color-coded ribbon diagram of the C1 and C2 region of factor V (functionally important regions/residues in the cutoff distance of 7 Å to hinge residues demonstrated as orange spheres).

R506Q (Leiden mutation): A significant reduction in correlation was observed between the calcium-binding site and the A1 domain, suggesting disrupted allosteric regulation that may compromise calcium binding and subsequent activation efficiency. Additional correlation losses were observed between residues E1567–I1581 and E1608 (of unknown function) and the A3 region, possibly affecting A3's stability and its interaction with the C1 domain. The A2-A3–C1 interdomain correlations were also diminished, indicating weakened structural coordination in the prothrombinase complex assembly.

G563A (Patient 1): This mutation led to correlation losses within the A2 domain at residues P283, T466, and D513—all previously uncharacterized, but now implicated in maintaining A2 integrity. N641 also showed loss of correlation with A2, B, and A3 domains. Moreover, residue Q1576 (unknown function) lost correlations with A1, A2, B, and A3, indicating impaired coupling across large portions of the molecule. These findings point to a broad destabilization of interdomain dynamics caused by the G563A substitution. Y2021C (Patient 2): This mutant exhibited similar correlation losses at P283, T466, and N641 as seen in G563A, suggesting shared effects on A2, B, and A3 dynamics. However, Y2021C uniquely disrupted correlations between the A1 and A2 domains, indicating reduced interdomain communication. Most notably, this mutant showed a pronounced correlation loss between the A3 domain and the C1-C2 regions—areas essential for phospholipid binding—potentially impairing membrane localization and procoagulant activity.

Overall, these analyses reveal that each mutation introduces unique allosteric disruptions in Factor V. The spatial alignment of mutation sites with dynamically central regions (hinges or hinge neighbors), together with the observed losses in correlated motion, supports the hypothesis that these mutations impair the long-range communication required for proper Factor V function—either by affecting activation, membrane association, or participation in the prothrombinase complex.

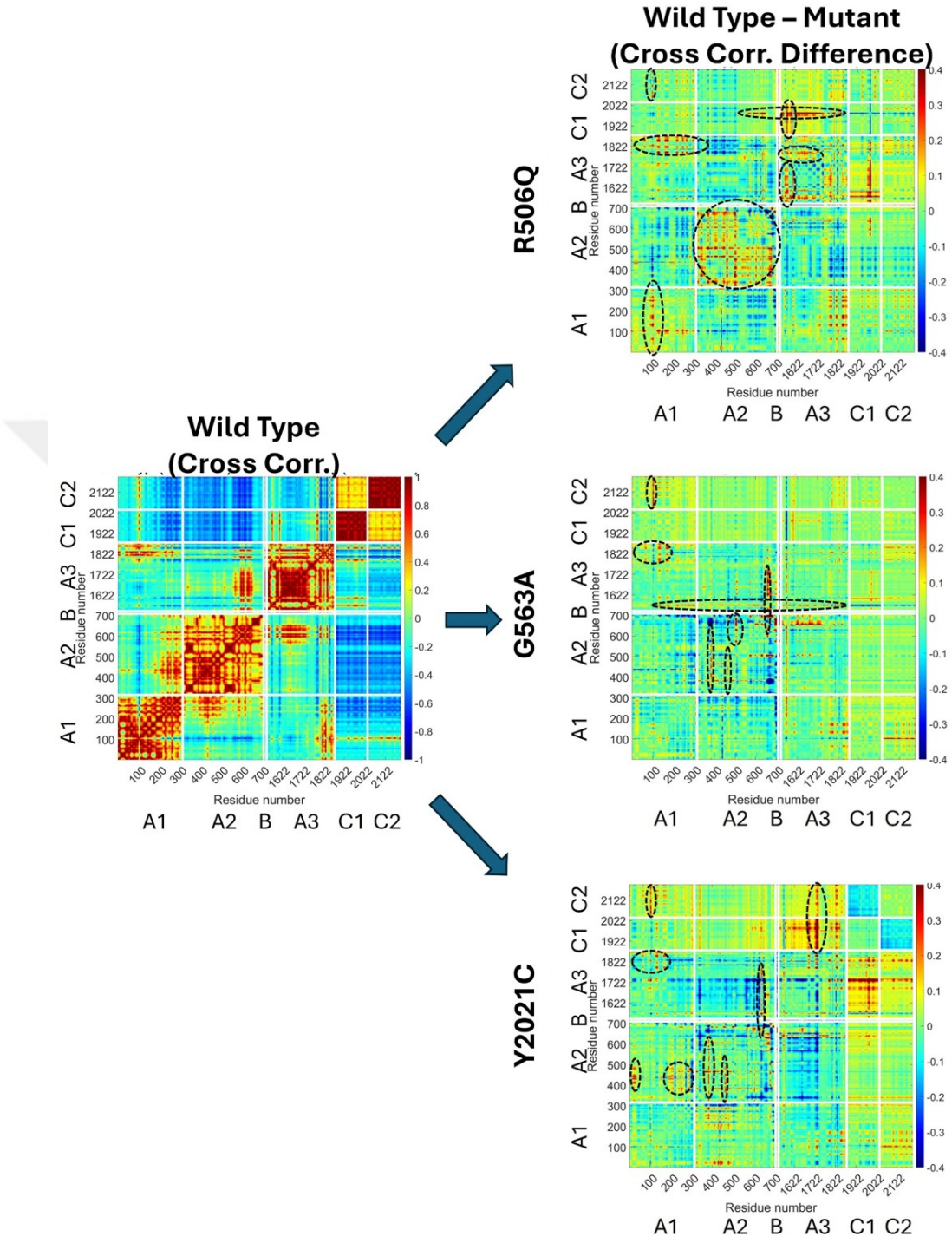

Figure 4.108. Comparison of the dynamic behavior of wild-type and mutant Factor V, calculated using the average Kirchhoff matrix from snapshots taken between 250-500 ns, focusing on modes 1-10.

5. CONCLUSIONS AND RECOMMENDATIONS

5.1. Conclusion

This thesis presents a comprehensive computational investigation of G protein-coupled receptor (GPCR) dynamics, focusing on the structural underpinnings of activation, biased signaling, and selective signal transduction. By leveraging elastic network models and enhanced coarse-grained dynamics through the Anisotropic Network Model–Langevin Dynamics (ANM-LD) framework [35–37], we simulated conformational transitions across 25 Class A GPCRs and constructed a dynamic ensemble that captures the intermediate states along activation pathways. These intermediates, validated using key collective variables such as TM6 tilt and TM7 shift, exhibit hallmark features of GPCR activation and provide physically and biologically meaningful representations of the conformational landscape [31, 32].

In the first section, the ANM-LD simulations successfully modeled 30 distinct transition pathways, including dual transitions toward both G protein and β-arrestin bound states for five receptors. The co-vibrational mode analysis [38] revealed that while early low-frequency dynamics may be dominated by β-arrestin transitions, G protein-bound pathways align more closely with the global collective motions of the receptor, especially in higher co-vibrational modes. This distinction offers insight into the differential dynamical encoding of signaling pathways at the level of normal mode spectra.

The second section focused on mechanistic insights into biased signaling, analyzing five receptors with experimentally resolved G protein and β-arrestin bound active states, along with their transition pathways obtained in Section 4.1. Analysis of the key ANM modes driving the transition pathways revealed specific hinge residues facilitate differential coupling to G proteins and β-arrestins. While core motifs like the PIF motif, sodium-binding site, and rotamer toggle switch [3] acted as conserved dy-

namic pivots, G protein-selective transitions involved distinct hinge regions, notably the DRY and NPxxY motifs [186], highlighting alternative pathways underlying biased signaling in 5HT2B. GNM-TE analysis showed that in the 1–10 mode subset, both G protein– and β-arrestin–bound complexes exhibit strong receptor-driven information flow originating from the orthosteric ligand binding site [187], underscoring the receptor's central role in initiating signaling. A newly developed metric, the Differential Coupling Score, systematically integrated correlation and information flow differences to uncover structural segments mediating pathway-selective coupling. Notably, the identified regions were found to overlap with known biased ligand binding sites reported in the literature [16, 54]. These results reinforce the idea that signaling bias arises from a reorganization of long-range allosteric networks rather than localized structural changes alone.

In the third section, we extended the analysis to a comparative ensemble-level evaluation across all 25 modeled receptors, yielding 300 conformations spanning inactive, intermediate, and active states. Using the SignDy tool [39], the ensemble was analyzed to identify conserved allosteric scaffolds and divergent motion patterns linked to receptor state, ligand type, and effector engagement. Cross-correlation analyses revealed a coordinated redistribution of extracellular and intracellular interactions during activation, including a seesaw-like coupling between ECL1–ECL3 and cytoplasmic domains, and significant shifts in Helix 8 and TM7-IC dynamics between signaling states. Ligand-specific differences were also observed: while aminergic receptors displayed compact dynamics centered on the core binding site, peptide- and protein-bound receptors exhibited enhanced flexibility in loop regions, and lipid-bound receptors showed localized dynamic segregation with minimal long-range coupling. Comparative ensemble analysis in G protein– versus β-arrestin–bound ensembles highlight that Helix 8 and TM7-IC consistently act as flexible dynamic hubs, exhibiting pathway-specific coupling profiles that shift across mode regimes [27]. Together, these findings demonstrate that ligand type and diversity of signal protein modulates not only local conformational changes but also the global dynamic architecture of GPCRs, shaping the receptor's allosteric potential and bias profile [15, 74].

The fourth section of this thesis highlights the generalizability of the developed computational framework. In collaboration with experimental teams, we applied GNM-TE to study two homologous manganese ABC transporters. The predicted allosteric hotspots aligned closely with experimental mutation data across multiple validation sets and accuracy levels, confirming the utility of GNM-TE as an efficient and biologically accurate method for identifying functional residues [145]. Additionally, contributions were made to the development and testing of the ANM-LD Path server, including the integration of GPU-accelerated simulation and automated analysis for large-scale protein transition modeling. Case studies involving ADK, SERCA, CaM, and other systems demonstrated the broad applicability and robustness of the platform. Finally, we investigated the dynamic consequences of disease-relevant mutations in Factor V, revealing that R506Q, G563A, and Y2021C variants disrupt information flow and coupling between key domains involved in cofactor function and anticoagulant activity, offering structural insights into coagulation disorders of genetic origin.

Overall, this thesis advances our understanding of how intrinsic protein dynamics orchestrate GPCR activation, signaling bias, and functional selectivity. By integrating coarse-grained simulations, dynamic mode analysis, and information-theoretic metrics, we establish a scalable, generalizable framework to forecast and elucidate the transition pathways from inactive to active receptor states. A key novelty of this work lies in the use of computationally generated intermediate structures, which bridge static experimental conformations and reveal the continuous landscape of conformational change. In this way, we can decipher allosteric mechanisms in a dynamic and mechanistically interpretable manner—capturing transient states and signaling-relevant motions that are inaccessible to current structural techniques. These insights illuminate the underlying principles governing allosteric regulation and the temporal-spatial orchestration of intracellular signals. Beyond fundamental contributions to GPCR biology, the findings lay a foundation for drug design strategies—enabling the development of biased ligands and allosteric modulators that precisely tune receptor responses with subtype- and pathway-specific selectivity.

5.2. Recommandation

Building on the insights gained from this study, future work should aim to integrate experimental validation with the computationally identified dynamic hotspots and transition pathways to strengthen their physiological relevance. Expanding the conformational modeling to include additional GPCR classes and ligand types—such as class B, C, and F receptors, or biased allosteric modulators—could further generalize the framework developed here. Moreover, combining coarse-grained approaches like ANM-LD with enhanced atomistic simulations or machine learning models may help resolve finer-scale conformational subtleties and predict signaling outcomes with higher precision. Finally, incorporating mutational data and clinically relevant variants will be essential to translating structural dynamics into actionable strategies for the design of pathway-selective ligands and allosteric drugs targeting GPCRs.

REFERENCES

1. Trzaskowski, B., D. Latek, S. Yuan, U. Ghoshdastider, A. Debinski and S. Filipek, "Action of Molecular Switches in GPCRs—Theoretical and Experimental Studies", *Current Medicinal Chemistry*, Vol. 19, No. 8, pp. 1090–1109, 2012.

2. Geppetti, P., N. A. Veldhuis, T. Lieu and N. W. Bunnett, "G Protein-Coupled Receptors: Dynamic Machines for Signaling Pain and Itch", *Neuron*, Vol. 88, No. 4, pp. 635–649, 2015.

3. Hauser, A. S., M. M. Attwood, M. Rask-Andersen, H. B. Schiöth and D. E. Gloriam, "Trends in GPCR Drug Discovery: New Agents, Targets and Indications", *Nature Reviews Drug Discovery*, Vol. 16, No. 12, pp. 829–842, 2017.

4. Chan, H. S., Y. Li, T. Dahoun, H. Vogel and S. Yuan, "New Binding Sites, New Opportunities for GPCR Drug Discovery", *Trends in Biochemical Sciences*, Vol. 44, No. 4, pp. 312–330, 2019.

5. Insel, P. A., K. Sriram, M. W. Gorr, S. Z. Wiley, A. Michkov, C. Salmerón and A. M. Chinn, "GPCRomics: An Approach to Discover GPCR Drug Targets", *Trends in Pharmacological Sciences*, Vol. 40, No. 6, pp. 378–387, 2019.

6. Congreve, M., C. de Graaf, N. A. Swain and C. G. Tate, "Impact of GPCR Structures on Drug Discovery", *Cell*, Vol. 181, No. 1, pp. 81–91, 2020.

7. Lorente, J. S., A. V. Sokolov, G. Ferguson, H. B. Schiöth, A. S. Hauser and D. E. Gloriam, "GPCR Drug Discovery: New Agents, Targets and Indications", *Nature Reviews Drug Discovery*, Vol. 1, pp. 1–22, 2025.

8. Wingert, B., P. Doruker and I. Bahar, "Activation and Speciation Mechanisms in Class A GPCRs", *Journal of Molecular Biology*, Vol. 434, No. 17, p. 167690, 2022.

9. Shukla, A. K., G. Singh and E. Ghosh, "Emerging Structural Insights into Biased GPCR Signaling", *Trends in Biochemical Sciences*, Vol. 39, No. 12, pp. 594–602, 2014.

10. Zhou, X. E., K. Melcher and H. E. Xu, "Understanding the GPCR Biased Signaling through G Protein and Arrestin Complex Structures", *Current Opinion in Structural Biology*, Vol. 45, pp. 150–159, 2017.

11. Slosky, L. M., M. G. Caron and L. S. Barak, "Biased Allosteric Modulators: New Frontiers in GPCR Drug Discovery", *Trends in Pharmacological Sciences*, Vol. 42, No. 4, pp. 283–299, 2021.

12. Seyedabadi, M., M. Gharghabi, E. V. Gurevich and V. V. Gurevich, "Structural Basis of GPCR Coupling to Distinct Signal Transducers: Implications for Biased Signaling", *Trends in Biochemical Sciences*, Vol. 47, No. 7, pp. 570–581, 2022.

13. Fan, L. and S. Wang, "Biased GPCR Signaling: Possible Mechanisms and Therapeutic Applications", *Biochemistry*, Vol. 64, No. 6, pp. 1180–1192, 2025.

14. Powers, A. S., A. Khan, J. M. Paggi, N. R. Latorraca, S. Souza, J. Di Salvo, J. Lu, S. M. Soisson, J. M. Johnston, A. B. Weinglass and R. O. Dror, "A Non-Canonical Mechanism of GPCR Activation", *Nature Communications*, Vol. 15, No. 1, p. 9938, 2024.

15. Venkatakrishnan, A. J., X. Deupi, G. Lebon, C. G. Tate, G. F. Schertler and M. M. Babu, "Molecular Signatures of G-Protein-Coupled Receptors", *Nature*, Vol. 494, No. 7436, pp. 185–194, 2013.

16. Zhang, M., T. Chen, X. Lu, X. Lan, Z. Chen and S. Lu, "G Protein-Coupled Receptors (GPCRs): Advances in Structures, Mechanisms and Drug Discovery", *Signal Transduction and Targeted Therapy*, Vol. 9, No. 1, p. 88, 2024.

17. Latorraca, N. R., A. J. Venkatakrishnan and R. O. Dror, "GPCR Dynamics:

Structures in Motion", *Chemical Reviews*, Vol. 117, No. 1, pp. 139–155, 2017.

18. Kato, H. E., Y. Zhang, H. Hu, C.-M. Suomivuori, F. M. N. Kadji, J. Aoki, K. Krishna Kumar, R. Fonseca, D. Hilger, W. Huang, N. R. Latorraca, A. Inoue, R. O. Dror, B. K. Kobilka and G. Skiniotis, "Conformational Transitions of a Neurotensin Receptor 1–Gi1 Complex", *Nature*, Vol. 572, No. 7767, pp. 80–85, 2019.

19. Maeda, S., Q. Qu, M. J. Robertson, G. Skiniotis and B. K. Kobilka, "Structures of the M1 and M2 Muscarinic Acetylcholine Receptor/G-Protein Complexes", *Science*, Vol. 364, No. 6440, pp. 552–557, 2019.

20. Yin, W., Z. Li, M. Jin, Y.-L. Yin, P. W. De Waal, K. Pal, Y. Yin, X. Gao, Y. He, J. Gao, X. Wang, Y. Zhang, H. Zhou, K. Melcher and H. E. Xu, "A Complex Structure of Arrestin-2 Bound to a G Protein-Coupled Receptor", *Cell Research*, Vol. 29, No. 12, pp. 971–983, 2019.

21. Zhou, Q., D. Yang, M. Wu, Y. Guo, W. Guo, L. Zhong, X. Cai, A. Dai, W. Jang, E. I. Shakhnovich, Z.-J. Liu, R. C. Stevens, N. A. Lambert, M. M. Babu, M.-W. Wang and S. Zhao, "Common Activation Mechanism of Class A GPCRs", *Elife*, Vol. 8, p. e50279, 2019.

22. Lee, Y., T. Warne, R. Nehmé, S. Pandey, H. Dwivedi-Agnihotri, M. Chaturvedi, P. C. Edwards, J. García-Nafría, A. G. W. Leslie, A. K. Shukla and C. G. Tate, "Molecular Basis of β-Arrestin Coupling to Formoterol-Bound β1-Adrenoceptor", *Nature*, Vol. 583, No. 7818, pp. 862–866, 2020.

23. Staus, D. P., H. Hu, M. J. Robertson, A. L. W. Kleinhenz, L. M. Wingler, W. D. Capel, N. R. Latorraca, R. J. Lefkowitz and G. Skiniotis, "Structure of the M2 Muscarinic Receptor–β-Arrestin Complex in a Lipid Nanodisc", *Nature*, Vol. 579, No. 7798, pp. 297–302, 2020.

24. Wang, J., T. Hua and Z. J. Liu, "Structural Features of Activated GPCR Signaling Complexes", *Current Opinion in Structural Biology*, Vol. 63, pp. 82–89, 2020.

25. Karnam, P. C., S. A. Vishnivetskiy and V. V. Gurevich, "Structural Basis of Arrestin Selectivity for Active Phosphorylated G Protein-Coupled Receptors", *International Journal of Molecular Sciences*, Vol. 22, No. 22, p. 12481, 2021.

26. Zhou, F., C. Ye, X. Ma, W. Yin, T. I. Croll, Q. Zhou, X. He, X. Zhang, D. Yang, P. Wang, H. E. Xu, M.-W. Wang and Y. Jiang, "Molecular Basis of Ligand Recognition and Activation of Human V2 Vasopressin Receptor", *Cell research*, Vol. 31, No. 8, pp. 929–931, 2021.

27. Cao, C., X. Barros-Álvarez, S. Zhang, K. Kim, M. A. Dämgen, O. Panova, C. M. Suomivuori, J. F. Fay, X. Zhong, B. E. Krumm, R. H. Gumpper, A. B. Seven, M. J. Robertson, N. J. Krogan, R. Hüttenhain, D. E. Nichols, R. O. Dror, G. Skiniotis and B. L. Roth, "Signaling Snapshots of a Serotonin Receptor Activated by the Prototypical Psychedelic LSD", *Neuron*, Vol. 110, No. 19, pp. 3154–3167, 2022.

28. Cheng, L., F. Xia, Z. Li, C. Shen, Z. Yang, H. Hou, S. Sun, Y. Feng, X. Yong, X. Tian, H. Qin, W. Yan and Z. Shao, "Structure, Function and Drug Discovery of GPCR Signaling", *Molecular Biomedicine*, Vol. 4, No. 1, p. 46, 2023.

29. Weis, W. I. and B. K. Kobilka, "The Molecular Basis of G Protein-Coupled Receptor Activation", *Annual Review of Biochemistry*, Vol. 87, No. 1, pp. 897–919, 2018.

30. Latorraca, N. R., J. K. Wang, B. Bauer, R. J. L. Townshend, S. A. Hollingsworth, J. E. Olivieri, H. E. Xu, M. E. Sommer and R. O. Dror, "Molecular Mechanism of GPCR-Mediated Arrestin Activation", *Nature*, Vol. 557, No. 7705, pp. 452–456, 2018.

31. Zou, Y., J. Ewalt and H. L. Ng, "Recent Insights from Molecular Dynamics Simulations for G Protein-Coupled Receptor Drug Discovery", *International Journal of Molecular Sciences*, Vol. 20, No. 17, p. 4237, 2019.

32. Rodríguez-Espigares, I., M. Torrens-Fontanals, J. K. S. Tiemann, D. Aranda-García, J. M. Ramírez-Anguita, T. M. Stepniewski, N. Worp, A. Varela-Rial, A. Morales-Pastor, B. Medel-Lacruz, G. Pándy-Szekeres, E. Mayol, T. Giorgino, J. Carlsson, X. Deupi, S. Filipek, M. Filizola, J. C. Gomez-Tamayo, Gonzalez, H. Gutiérrez-de Terán, M. Jiménez-Rosés, W. Jespers, J. Kapla, G. Khelashvili, P. Kolb, D. Latek, M. Marti-Solano, P. Matricon, M. T. Matsoukas, P. Miszta, M. Olivella, L. Perez-Benito, D. Provasi, S. Ríos, I. R. Torrecillas, J. Sallander, A. Sztyler, S. Vasile, H. Weinstein, U. Zachariae, P. W. Hildebrand, G. De Fabritiis, F. Sanz, D. E. Gloriam, A. Cordomi, R. Guixà-González and J. Selent, "GPCRmd Uncovers the Dynamics of the 3D-GPCRome", *Nature Methods*, Vol. 17, No. 8, pp. 777–787, 2020.

33. Vilardaga, J. P., M. Bünemann, C. Krasel, M. Castro and M. J. Lohse, "Measurement of the Millisecond Activation Switch of G Protein–Coupled Receptors in Living Cells", *Nature Biotechnology*, Vol. 21, No. 7, pp. 807–812, 2003.

34. Grushevskyi, E. O., T. Kukaj, R. Schmauder, A. Bock, U. Zabel, T. Schwabe, K. Benndorf and M. J. Lohse, "Stepwise Activation of a Class C GPCR Begins with Millisecond Dimer Rearrangement", *Proceedings of the National Academy of Sciences*, Vol. 116, No. 20, pp. 10150–10155, 2019.

35. Yang, M., N. Livnat Levanon, B. Acar, B. Aykac Fas, G. Masrati, J. Rose, N. Ben-Tal, T. Haliloglu, Y. Zhao and O. Lewinson, "Single-Molecule Probing of the Conformational Homogeneity of the ABC Transporter BtuCD", *Nature Chemical Biology*, Vol. 14, No. 7, pp. 715–722, 2018.

36. Acar, B., J. Rose, B. A. Fas, N. Ben-Tal, O. Lewinson and T. Haliloglu, "Distinct Allosteric Networks Underlie Mechanistic Speciation of ABC Transporters",

Structure, Vol. 28, No. 6, pp. 651–663, 2020.

37. Ersoy, A., B. Altintel, N. L. Levanon, N. Ben-Tal, T. Haliloglu and O. Lewinson, "Computational Analysis of Long-Range Allosteric Communications in CFTR", *Elife*, Vol. 12, p. RP88659, 2023.

38. Kolossváry, I., "A Fresh Look at the Normal Mode Analysis of Proteins: Introducing Allosteric Co-Vibrational Modes", *JACS Au*, Vol. 4, No. 4, pp. 1303–1309, 2024.

39. Zhang, S., H. Li, J. M. Krieger and I. Bahar, "Shared Signature Dynamics Tempered by Local Fluctuations Enables Fold Adaptability and Specificity", *Molecular Biology and Evolution*, Vol. 36, No. 9, p. 2053–2068, 2019.

40. Zhang, S., J. M. Krieger, Y. Zhang, C. Kaya, B. Kaynak, K. Mikulska-Ruminska, P. Doruker, H. Li and I. Bahar, "ProDy 2.0: Increased Scale and Scope after 10 Years of Protein Dynamics Modelling with Python", *Bioinformatics*, Vol. 37, No. 20, pp. 3657–3659, 2021.

41. Attwood, T. K. and J. B. C. Findlay, "Fingerprinting G-Protein-Coupled Receptors", *Protein Engineering*, Vol. 7, No. 2, pp. 195–203, 1994.

42. Pándy-Szekeres, G., J. Caroli, A. Mamyrbekov, A. A. Kermani, G. M. Keserű, A. J. Kooistra and D. E. Gloriam, "GPCRdb in 2023: State-Specific Structure Models Using AlphaFold2 and New Ligand Resources", *Nucleic Acids Research*, Vol. 51, No. D1, pp. D395–D402, 2023.

43. Sadler, F., N. Ma, M. Ritt, Y. Sharma, N. Vaidehi and S. Sivaramakrishnan, "Autoregulation of GPCR Signalling through the Third Intracellular Loop", *Nature*, Vol. 615, No. 7953, pp. 734–741, 2023.

44. Huynh, J., W. G. Thomas, M. I. Aguilar and L. K. Pattenden, "Role of Helix 8 in G Protein-Coupled Receptors Based on Structure–Function Studies on the Type

1 Angiotensin Receptor", *Molecular and Cellular Endocrinology*, Vol. 302, No. 2, pp. 118–127, 2009.

45. White, K. L., M. T. Eddy, Z.-G. Gao, G. W. Han, T. Lian, A. Deary, N. Patel, K. A. Jacobson, V. Katritch and R. C. Stevens, "Structural Connection between Activation Microswitch and Allosteric Sodium Site in GPCR Signaling", *Structure*, Vol. 26, No. 2, pp. 259–269.e5, 2018.

46. Hauser, A. S., A. J. Kooistra, C. Munk, F. M. Heydenreich, D. B. Veprintsev, M. Bouvier, M. M. Babu and D. E. Gloriam, "GPCR Activation Mechanisms Across Classes and Macro/Microscales", *Nature Structural & Molecular Biology*, Vol. 28, No. 11, pp. 879–888, 2021.

47. Ballesteros, J. A. and H. Weinstein, "Integrated Methods for the Construction of Three-Dimensional Models and Computational Probing of Structure–Function Relations in G Protein-Coupled Receptors", *Methods in Neurosciences*, Vol. 25, pp. 366–428, 1995.

48. Hedderich, J. B., M. Persechino, K. Becker, F. M. Heydenreich, T. Gutermuth, M. Bouvier, M. Bünemann and P. Kolb, "The Pocketome of G-Protein-Coupled Receptors Reveals Previously Untargeted Allosteric Sites", *Nature Communications*, Vol. 13, No. 1, p. 2567, 2022.

49. Flock, T., A. S. Hauser, N. Lund, D. E. Gloriam, S. Balaji and M. M. Babu, "Selectivity Determinants of GPCR–G-Protein Binding", *Nature*, Vol. 545, No. 7654, pp. 317–322, 2017.

50. Smith, J. S., R. J. Lefkowitz and S. Rajagopal, "Biased Signalling: From Simple Switches to Allosteric Microprocessors", *Nature Reviews Drug Discovery*, Vol. 17, No. 4, pp. 243–260, 2018.

51. Jean-Charles, P.-Y., S. Kaur and S. K. Shenoy, "G Protein–Coupled Receptor

Signaling through β-Arrestin–Dependent Mechanisms", *Journal of Cardiovascular Pharmacology*, Vol. 70, No. 3, pp. 142–158, 2017.

52. Thomsen, A. R. B., "GPCRs and β-Arrestins—An On-Off Relationship", *Cell Research*, Vol. 33, No. 11, pp. 819–820, 2023.

53. Thomsen, A. R. B., B. Plouffe, T. J. Cahill, 3rd, A. K. Shukla, J. T. Tarrasch, A. M. Dosey, A. W. Kahsai, R. T. Strachan, B. Pani, J. P. Mahoney, L. Huang, B. Breton, F. M. Heydenreich, R. K. Sunahara, G. Skiniotis, M. Bouvier and R. J. Lefkowitz, "GPCR-G Protein-β-Arrestin Super-Complex Mediates Sustained G Protein Signaling", *Cell*, Vol. 166, No. 4, pp. 907–919, 2016.

54. Sun, D., X. Li, Q. Yuan, Y. Wang, P. Shi, H. Zhang, T. Wang, W. Sun, S. Ling, Y. Liu, J. Lai, W. Xie, W. Yin, L. Liu, H. E. Xu and C. Tian, "Molecular Mechanism of the Arrestin-Biased Agonism of Neurotensin Receptor 1 by an Intracellular Allosteric Modulator", *Cell Research*, Vol. 35, pp. 1–12, 2025.

55. Kenakin, T. and A. Christopoulos, "Signalling Bias in New Drug Discovery: Detection, Quantification and Therapeutic Impact", *Nature Reviews Drug Discovery*, Vol. 12, No. 3, pp. 205–216, 2013.

56. González-Maeso, J., N. V. Weisstaub, M. Zhou, P. Chan, L. Ivic, R. Ang, A. Lira, M. Bradley-Moore, Y. Ge, Q. Zhou, S. C. Sealfon and J. A. Gingrich, "Hallucinogens Recruit Specific Cortical 5-HT(2A) Receptor-Mediated Signaling Pathways to Affect Behavior", *Neuron*, Vol. 53, No. 3, pp. 439–452, 2007.

57. Schmid, C. L., K. M. Raehal and L. M. Bohn, "Agonist-Directed Signaling of the Serotonin 2A Receptor Depends on β-Arrestin-2 Interactions in Vivo", *Proceedings of the National Academy of Sciences*, Vol. 105, No. 3, pp. 1079–1084, 2008.

58. Rodriguiz, R. M., J. J. Nadler, S. S. Moy, J. N. Crawley, J. L. Silverman and J. N.

Crawley, "Behavioral Phenotyping Assays for Genetic Mouse Models of Neurodevelopmental, Neurodegenerative, and Psychiatric Disorders", *Current Protocols in Neuroscience*, Vol. 97, No. 1, p. e104, 2021.

59. Kossatz, S., J. D. Smith, A. H. Lee, Y. Chen, M. T. Johnson and L. Wang, "Advanced Insights into GPCR Signaling Pathways", *Journal of Molecular Pharmacology*, Vol. 95, No. 2, pp. 123–135, 2024.

60. Bohn, L. M., R. J. Lefkowitz and M. G. Caron, "Enhanced Morphine Analgesia in Mice Lacking Beta-Arrestin 2", *Science*, Vol. 286, No. 5449, pp. 2495–2498, 1999.

61. Raehal, K. M., J. K. L. Walker and L. M. Bohn, "Morphine Side Effects in Beta-Arrestin 2 Knockout Mice", *Journal of Pharmacology and Experimental Therapeutics*, Vol. 314, No. 3, pp. 1195–1201, 2005.

62. Barak, L. S., R. H. Oakley, S. A. Laporte and M. G. Caron, "Molecular Determinants Underlying the Formation of Stable Intracellular G Protein-Coupled Receptor-β-Arrestin Complexes after Receptor Endocytosis", *Journal of Biological Chemistry*, Vol. 276, No. 22, pp. 19452–19460, 2001.

63. Hernandez, L. M., K. L. Pierce, L. M. Luttrell and R. J. Lefkowitz, "Regulation of G Protein-Coupled Receptor Signaling: Functional Implications and Therapeutic Opportunities", *Journal of Clinical Investigation*, Vol. 111, No. 3, pp. 317–324, 2003.

64. Balabanian, K., B. Lagane, S. Infantino, K. Y. C. Chow, J. Harriague, B. Moepps, F. Arenzana-Seisdedos, M. Thelen and F. Bachelerie, "The Chemokine SDF-1/CXCL12 Binds to and Signals through the Orphan Receptor RDC1 in T Lymphocytes", *Journal of Biological Chemistry*, Vol. 280, No. 42, pp. 35760–35766, 2005.

65. Hopkins, A. L. and C. R. Groom, "The Druggable Genome", *Nature Reviews Drug Discovery*, Vol. 1, No. 9, pp. 727–730, 2002.

66. Ozbabacan, S. A., A. Gursoy, O. Keskin and R. Nussinov, "Conformational Ensembles, Signal Transduction and Residue Hot Spots: Application to Drug Discovery", *Current Opinion in Drug Discovery & Development*, Vol. 13, No. 5, pp. 527–537, 2010.

67. Engin, H. B., A. Gursoy, R. Nussinov and O. Keskin, "Network-Based Strategies Can Help Mono- and Poly-Pharmacology Drug Discovery: A Systems Biology View", *Current Pharmaceutical Design*, Vol. 20, No. 8, pp. 1201–1207, 2014.

68. Wingler, L. M. and R. J. Lefkowitz, "Conformational Basis of G Protein-Coupled Receptor Signaling Versatility", *Trends in Cell Biology*, Vol. 30, No. 9, pp. 736–747, 2020.

69. Cao, A.-M., R. B. Quast, F. Fatemi, P. Rondard, J.-P. Pin and E. Margeat, "Allosteric Modulators Enhance Agonist Efficacy by Increasing the Residence Time of a GPCR in the Active State", *Nature Communications*, Vol. 12, No. 1, p. 5426, 2021.

70. Shen, S., C. Zhao, C. Wu, S. Sun, Z. Li, W. Yan and Z. Shao, "Allosteric Modulation of G Protein-Coupled Receptor Signaling", *Frontiers in Endocrinology*, Vol. 14, p. 1137604, 2023.

71. Jumper, J., R. Evans, A. Pritzel, T. Green, M. Figurnov, O. Ronneberger, K. Tunyasuvunakool, R. Bates, A. Žídek, A. Potapenko, A. Bridgland, C. Meyer, S. A. A. Kohl, A. J. Ballard, A. Cowie, B. Romera-Paredes, S. Nikolov, R. Jain, J. Adler, T. Back, S. Petersen, D. Reiman, E. Clancy, M. Zielinski, M. Steinegger, M. Pacholska, T. Berghammer, S. Bodenstein, D. Silver, O. Vinyals, A. W. Senior, K. Kavukcuoglu, P. Kohli and D. Hassabis, "Highly Accurate Protein Structure Prediction with AlphaFold", *Nature*, Vol. 596, No. 7873, pp. 583–589, 2021.

72. Krishna, R., J. Wang, W. Ahern, P. Sturmfels, P. Venkatesh, I. Kalvet, G. R. Lee, F. S. Morey-Burrows, I. Anishchenko, I. R. Humphreys, R. McHugh, D. Vafeados, X. Li, G. A. Sutherland, A. Hitchcock, C. N. Hunter, A. Kang, E. Brackenbrough, A. K. Bera, M. Baek, F. DiMaio and D. Baker, "Generalized Biomolecular Modeling and Design with RoseTTAFold All-Atom", *Science*, Vol. 384, No. 6693, p. eadl2528, 2024.

73. Abramson, J., J. Adler, J. Dunger, R. Evans, T. Green, A. Pritzel, O. Ronneberger, L. Willmore, A. J. Ballard, J. Bambrick, S. W. Bodenstein, D. A. Evans, C.-C. Hung, M. O'Neill, D. Reiman, K. Tunyasuvunakool, Z. Wu, A. Žemgulytė, E. Arvaniti, C. Beattie, O. Bertolli, A. Bridgland, A. Cherepanov, M. Congreve, A. I. Cowen-Rivers, A. Cowie, M. Figurnov, F. B. Fuchs, H. Gladman, R. Jain, Y. A. Khan, C. M. R. Low, K. Perlin, A. Potapenko, P. Savy, S. Singh, A. Stecula, A. Thillaisundaram, C. Tong, S. Yakneen, E. D. Zhong, M. Zielinski, A. Žídek, V. Bapst, P. Kohli, M. Jaderberg, D. Hassabis and J. M. Jumper, "Accurate Structure Prediction of Biomolecular Interactions with AlphaFold 3", *Nature*, Vol. 618, No. 7965, pp. 590–596, 2024.

74. Aranda-García, D., T. M. Stepniewski, M. Torrens-Fontanals, A. García-Recio, M. Lopez-Balastegui, B. Medel-Lacruz, A. Morales-Pastor, A. Peralta-García, M. Dieguez-Eceolaza, D. Sotillo-Nuñez, T. Ding, M. Drabek, C. Jacquemard, J. Jakowiecki, W. Jespers, M. Jiménez-Rosés, V. Jun-Yu-Lim, A. Nicoli, U. Orzel, A. Shahraki, J. K. S. Tiemann, V. Ledesma-Martin, F. Nerín-Fonz, S. Suárez-Dou, O. Canal, G. Pándy-Szekeres, J. Mao, D. E. Gloriam, E. Kellenberger, D. Latek, R. Guixà-González, H. Gutiérrez-de Terán, I. G. Tikhonova, P. W. Hildebrand, M. Filizola, M. M. Babu, A. Di Pizio, S. Filipek, P. Kolb, A. Cordomi, T. Giorgino, M. Marti-Solano and J. Selent, "Large Scale Investigation of GPCR Molecular Dynamics Data Uncovers Allosteric Sites and Lateral Gateways", *Nature Communications*, Vol. 16, No. 1, p. 2020, 2025.

75. Han, Y., J. R. D. Dawson, K. R. DeMarco, K. C. Rouen, K. Ngo, S. Bekker, V. Yarov-Yarovoy, C. E. Clancy, Y. K. Xiang, S.-H. Ahn and I. Vorobyov, "Molec-

ular Simulations Reveal Intricate Coupling Between Agonist-Bound β-Adrenergic Receptors and G Protein", *IScience*, Vol. 28, No. 2, p. 111741, 2025.

76. Dror, R. O., D. H. Arlow, P. Maragakis, T. J. Mildorf, A. C. Pan, H. Xu, D. W. Borhani and D. E. Shaw, "Activation Mechanism of the β2-Adrenergic Receptor", *Proceedings of the National Academy of Sciences of the United States of America*, Vol. 108, No. 46, pp. 18684–18689, 2011.

77. Inan, T., M. Yuce, A. D. MacKerell Jr and O. Kurkcuoglu, "Exploring Druggable Binding Sites on the Class A GPCRs Using the Residue Interaction Network and Site Identification by Ligand Competitive Saturation", *ACS Omega*, Vol. 9, No. 38, pp. 40154–40171, 2024.

78. Maria-Solano, M. A. and S. Choi, "Dynamic Allosteric Networks Drive Adenosine A1 Receptor Activation and G-Protein Coupling", *Biophysical Journal*, Vol. 122, No. 3, p. 31a, 2023.

79. Miao, Y., S. E. Nichols, P. M. Gasper, V. T. Metzger and J. A. McCammon, "Activation and Dynamic Network of the M2 Muscarinic Receptor", *Proceedings of the National Academy of Sciences of the United States of America*, Vol. 110, No. 27, pp. 10982–10987, 2013.

80. Masson, J., M. B. Emerit, M. Hamon and M. Darmon, "Serotonergic Signaling: Multiple Effectors and Pleiotropic Effects", *Wiley Interdisciplinary Reviews: Membrane Transport and Signaling*, Vol. 1, No. 6, pp. 685–713, 2012.

81. Diaz, S. L., S. Doly, N. Narboux-Nême, S. Fernández, P. Mazot, S. M. Banas, K. Boutourlinsky, I. Moutkine, A. Belmer, A. Roumier and L. Maroteaux, "5-HT2B Receptors Are Required for Serotonin-Selective Antidepressant Actions", *Molecular Psychiatry*, Vol. 17, No. 2, pp. 154–163, 2012.

82. Zhang, Y. and Y. Wang, "The Dual Roles of Serotonin in Antitumor Immunity",

Pharmacological Research, Vol. 205, p. 107255, 2024.

83. Trinh-Minh, T., C. Tran-Manh, A. Györfi, N. Dickel, C. Liebel, X. Zhou, J. Wang, M. Kunz, H. Arozenius, L. Pettersson, S. Lindgren, C. Wenglén and J. H. W. Distler, "Antifibrotic Effects of Specific Targeting of the 5-Hydroxytryptamine 2B Receptor (5-HT2BR) in Murine Models and Ex Vivo Models of Scleroderma Skin", *Arthritis & Rheumatology*, Vol. 76, No. 5, pp. 1234–1245, 2025.

84. Taylor, M. R. G., "Pharmacogenetics of the Human Beta-Adrenergic Receptors", *The Pharmacogenomics Journal*, Vol. 7, No. 1, pp. 29–37, 2007.

85. Motiejunaite, J., L. Amar and E. Vidal-Petiot, "Adrenergic Receptors and Cardiovascular Effects of Catecholamines", *Annales d'Endocrinologie*, Vol. 82, No. 3-4, pp. 193–197, 2021.

86. Cherezov, V., D. M. Rosenbaum, M. A. Hanson, S. G. F. Rasmussen, F. S. Thian, T. S. Kobilka, H.-J. Choi, P. Kuhn, W. I. Weis, B. K. Kobilka and R. C. Stevens, "High-Resolution Crystal Structure of an Engineered Human β2-Adrenergic G Protein–Coupled Receptor", *Science*, Vol. 318, No. 5854, pp. 1258–1265, 2007.

87. Rosenbaum, D. M., S. G. Rasmussen and B. K. Kobilka, "The Structure and Function of G-Protein-Coupled Receptors", *Nature*, Vol. 459, No. 7245, pp. 356–363, 2009.

88. Chien, E. Y. T., W. Liu, Q. Zhao, V. Katritch, G. W. Han, M. A. Hanson, L. Shi, A. H. Newman, J. A. Javitch, V. Cherezov and R. C. Stevens, "Structure of the Human Dopamine D3 Receptor in Complex with a D2/D3 Selective Antagonist", *Science*, Vol. 330, No. 6007, pp. 1091–1095, 2010.

89. Xu, P., S. Huang, B. E. Krumm, Y. Zhuang, C. Mao, Y. Zhang, Y. Wang, X. P. Huang, Y. Liu, X. He, H. Li, W. Yin, Y. Jiang, B. L. Roth and H. E. Xu, "Structural Genomics of the Human Dopamine Receptor System", *Cell Research*,

Vol. 33, No. 8, pp. 604–616, 2023.

90. Kitabgi, P., "Targeting Neurotensin Receptors with Agonists and Antagonists for Therapeutic Purposes", *Current Opinion in Drug Discovery & Development*, Vol. 5, No. 5, pp. 764–776, 2002.

91. Carraway, R. E. and A. M. Plona, "Involvement of Neurotensin in Cancer Growth: Evidence, Mechanisms and Development of Diagnostic Tools", *Peptides*, Vol. 27, No. 10, pp. 2445–2460, 2006.

92. Sánchez, M. L. and R. Coveñas, "The Neurotensinergic System: A Target for Cancer Treatment", *Current Medicinal Chemistry*, Vol. 29, No. 18, pp. 3231–3260, 2022.

93. Pinkerton, A. B., S. Peddibhotla, F. Yamamoto, L. M. Slosky, Y. Bai, P. Maloney, P. Hershberger, M. P. Hedrick, B. Falter, R. J. Ardecky, L. H. Smith, T. D. Y. Chung, M. R. Jackson, M. G. Caron and L. S. Barak, "Discovery of β-Arrestin Biased, Orally Bioavailable, and CNS Penetrant Neurotensin Receptor 1 (NTR1) Allosteric Modulators", *Journal of Medicinal Chemistry*, Vol. 62, No. 17, pp. 8357–8363, 2019.

94. Robben, J. H., M. L. A. Kortenoeven, M. Sze, C. Yae, G. Milligan, V. M. J. Oorschot, J. Klumperman, N. V. A. M. Knoers and P. M. T. Deen, "Intracellular Activation of Vasopressin V2 Receptor Mutants in Nephrogenic Diabetes Insipidus by Nonpeptide Agonists", *Proceedings of the National Academy of Sciences*, Vol. 106, No. 29, pp. 12195–12200, 2009.

95. Higuchi, S., H. Ohtsu, H. Suzuki, H. Shirai, G. D. Frank and S. Eguchi, "Angiotensin II Signal Transduction through the AT1 Receptor: Novel Insights into Mechanisms and Pathophysiology", *Clinical Science*, Vol. 112, No. 8, pp. 417–428, 2007.

96. Mehta, P. K. and K. K. Griendling, "Angiotensin II Cell Signaling: Physiological and Pathological Effects in the Cardiovascular System", *American Journal of Physiology-Cell Physiology*, Vol. 292, No. 1, pp. C82–C97, 2007.

97. Lino, C. A. and M. L. Barreto-Chaves, "Beta-Arrestins in the Context of Cardiovascular Diseases: Focusing on Angiotensin II Type 1 Receptor (AT1R)", *Cellular Signalling*, Vol. 92, p. 110253, 2022.

98. Béguin, C., D. N. Potter, J. A. DiNieri, T. A. Munro, M. R. Richards, T. A. Paine, L. Berry, Z. Zhao, B. L. Roth, W. Xu, L.-Y. Liu-Chen, W. A. J. Carlezon and B. M. Cohen, "N-Methylacetamide Analog of Salvinorin A: A Highly Potent and Selective κ-Opioid Receptor Agonist with Oral Efficacy", *The Journal of Pharmacology and Experimental Therapeutics*, Vol. 324, No. 1, pp. 188–195, 2008.

99. Snyder, S. H. and G. W. Pasternak, "Historical Review: Opioid Receptors", *Trends in Pharmacological Sciences*, Vol. 24, No. 4, pp. 198–205, 2003.

100. Martini, L. and J. L. Whistler, "The Role of Mu Opioid Receptor Desensitization and Endocytosis in Morphine Tolerance and Dependence", *Current Opinion in Neurobiology*, Vol. 17, No. 5, pp. 556–564, 2007.

101. Boom, M., M. Niesters, E. Sarton, L. Aarts, T. W. Smith and A. Dahan, "Non-Analgesic Effects of Opioids: Opioid-Induced Respiratory Depression", *Current Pharmaceutical Design*, Vol. 18, No. 37, pp. 5994–6004, 2012.

102. Jacobson, K. A. and Z. G. Gao, "Adenosine Receptors as Therapeutic Targets", *Nature Reviews Drug Discovery*, Vol. 5, No. 3, pp. 247–264, 2006.

103. Dunwiddie, T. V. and S. A. Masino, "The Role and Regulation of Adenosine in the Central Nervous System", *Annual Review of Neuroscience*, Vol. 24, pp. 31–55, 2001.

104. Morelli, M., A. R. Carta and P. Jenner, "Adenosine A2A Receptors and Parkin-

son's Disease", *Adenosine receptors in Health and Disease*, Vol. 193, pp. 589–615, 2009.

105. Cai, H., Y. Xu, S. Guo, X. He, J. Sun, X. Li, C. Li, W. Yin, X. Cheng, H. Jiang, H. E. Xu, X. Xie and Y. Jiang, "Structures of Adenosine Receptor A2BR Bound to Endogenous and Synthetic Agonists", *Cell Discovery*, Vol. 8, No. 1, p. 140, 2022.

106. Sun, Y. and P. Huang, "Adenosine A2B Receptor: From Cell Biology to Human Diseases", *Frontiers in Chemistry*, Vol. 4, p. 37, 2016.

107. Gao, Z. G., A. Inoue and K. A. Jacobson, "On the G Protein-Coupling Selectivity of the Native A2B Adenosine Receptor", *Biochemical Pharmacology*, Vol. 151, pp. 201–213, 2018.

108. Li, B., S. Han, M. Wang, Y. Yu, L. Ma, X. Chu, Q. Tan, Q. Zhao and B. Wu, "Structural Insights into Signal Transduction of the Purinergic Receptors P2Y1R and P2Y12R", *Protein & Cell*, Vol. 14, No. 5, pp. 382–386, 2023.

109. Guzman, M., "Cannabinoids: Potential Anticancer Agents", *Nature Reviews Cancer*, Vol. 3, No. 10, pp. 745–755, 2003.

110. Kendall, D. and S. Alexander, *Cannabinoid Pharmacology*, Vol. 80 of *Handbook of Experimental Pharmacology*, Academic Press, Cambridge, MA, 2017.

111. Liu, H., R. N. V. K. Deepak, A. Shiriaeva, C. Gati, A. Batyuk, H. Hu, U. Weierstall, W. Liu, L. Wang, V. Cherezov, H. Fan and C. Zhang, "Molecular Basis for Lipid Recognition by the Prostaglandin D2 Receptor CRTH2", *Proceedings of the National Academy of Sciences*, Vol. 118, No. 32, p. e2102813118, 2021.

112. Oguma, T., K. Asano and A. Ishizaka, "Role of Prostaglandin D2 and Its Receptors in the Pathophysiology of Asthma", *Allergology International*, Vol. 57, No. 4, pp. 307–312, 2008.

113. Fan, H., S. Chen, X. Yuan, S. Han, H. Zhang, W. Xia, Y. Xu, Q. Zhao and B. Wu, "Structural Basis for Ligand Recognition of the Human Thromboxane A2 Receptor", *Nature Chemical Biology*, Vol. 15, No. 1, pp. 27–33, 2019.

114. McIntyre, T. M., A. V. Pontsler, A. R. Silva, A. St. Hilaire, Y. Xu, J. C. Hinshaw, G. A. Zimmerman, K. Hama, J. Aoki, H. Arai and G. D. Prestwich, "Identification of an Intracellular Receptor for Lysophosphatidic Acid (LPA): LPA Is a Transcellular PPARγ Agonist", *Proceedings of the National Academy of Sciences*, Vol. 100, No. 1, pp. 131–136, 2003.

115. Chrencik, J. E., C. B. Roth, M. Terakado, H. Kurata, R. Omi, Y. Kihara, D. Warshaviak, S. Nakade, G. Asmar-Rovira, M. Mileni, H. Mizuno, M. T. Griffith, C. Rodgers, G. W. Han, J. Velasquez, J. Chun, R. C. Stevens and M. A. Hanson, "Crystal Structure of Antagonist Bound Human Lysophosphatidic Acid Receptor 1", *Cell*, Vol. 161, No. 7, pp. 1633–1643, 2015.

116. Suzuki, S., K. Tanaka, A. Kamegawa, K. Nishikawa, H. Suzuki, A. Oshima and Y. Fujiyoshi, "Structural Insights into the Engagement of Lysophosphatidic Acid Receptor 1 with Different G Proteins", *Journal of Structural Biology*, Vol. 217, No. 1, p. 108164, 2025.

117. Chen, H., Y. Qin, M. Chou, J. G. Cyster and X. Li, "Transmembrane Protein CD69 Acts as an S1PR1 Agonist", *Elife*, Vol. 12, p. e88204, 2023.

118. Watters, J. R., H. G. Wang, S. S. Sung, T. P. Loughran and X. Liu, "Targeting Sphingosine-1-Phosphate Receptors in Cancer", *Anti-Cancer Agents in Medicinal Chemistry*, Vol. 11, No. 9, pp. 810–817, 2011.

119. Shao, Z., Q. Shen, B. Yao, C. Mao, L.-N. Chen, H. Zhang, D.-D. Shen, C. Zhang, W. Li, X. Du, F. Li, H. Ma, Z.-H. Chen, H. E. Xu, S. Ying, Y. Zhang and H. Shen, "Identification and Mechanism of G Protein-Biased Ligands for Chemokine Receptor CCR1", *Nature Chemical Biology*, Vol. 18, No. 3, pp. 264–271, 2022.

120. Dhaiban, S., M. Al-Ani, N. M. Elemam and A. A. Maghazachi, "Targeting Chemokines and Chemokine Receptors in Multiple Sclerosis and Experimental Autoimmune Encephalomyelitis", *Journal of Inflammation Research*, Vol. 13, pp. 619–633, 2020.

121. Lopalco, L., "CCR5: From Natural Resistance to a New Anti-HIV Strategy", *Viruses*, Vol. 2, No. 2, pp. 574–600, 2010.

122. Korbecki, J., K. Kojder, D. Simińska, R. Bohatyrewicz, I. Gutowska, D. Chlubek and I. Baranowska-Bosiacka, "CC Chemokines in a Tumor: A Review of Pro-Cancer and Anti-Cancer Properties of the Ligands of Receptors CCR1, CCR2, CCR3, and CCR4", *International Journal of Molecular Sciences*, Vol. 21, No. 21, p. 8412, 2020.

123. Wen, Y., Y. Xia, X. Yang, H. Li and Q. Gao, "CCR8: A Promising Therapeutic Target Against Tumor-Infiltrating Regulatory T Cells", *Trends in Immunology*, Vol. 46, pp. 153–165, 2025.

124. Cheng, Y., X. L. Ma, Y. Q. Wei and X. W. Wei, "Potential Roles and Targeted Therapy of the CXCLs/CXCR2 Axis in Cancer and Inflammatory Diseases", *Biochimica et Biophysica Acta (BBA)-Reviews on Cancer*, Vol. 1871, No. 2, pp. 289–312, 2019.

125. Lazennec, G., K. Rajarathnam and A. Richmond, "CXCR2 Chemokine Receptor–A Master Regulator in Cancer and Physiology", *Trends in Molecular Medicine*, Vol. 30, No. 1, pp. 37–55, 2024.

126. Sitaru, S., A. Budke, R. Bertini and M. Sperandio, "Therapeutic Inhibition of CXCR1/2: Where Do We Stand?", *Internal and Emergency Medicine*, Vol. 18, No. 6, pp. 1647–1664, 2023.

127. Qin, L., I. Kufareva, L. G. Holden, C. Wang, Y. Zheng, C. Zhao, G. Fenalti,

H. Wu, G. W. Han, V. Cherezov, R. Abagyan, R. C. Stevens and T. M. Handel, "Crystal Structure of the Chemokine Receptor CXCR4 in Complex with a Viral Chemokine", *Science*, Vol. 347, No. 6226, pp. 1117–1122, 2015.

128. Saotome, K., L. L. McGoldrick, J.-H. Ho, T. F. Ramlall, S. Shah, M. J. Moore, J. H. Kim, R. Leidich and M. C. Franklin, "Structural Insights into CXCR4 Modulation and Oligomerization", *Nature Structural & Molecular Biology*, Vol. 32, pp. 315–325, 2024.

129. Busillo, J. M. and J. L. Benovic, "Regulation of CXCR4 Signaling", *Biochimica et Biophysica Acta (BBA)-Biomembranes*, Vol. 1768, No. 4, pp. 952–963, 2007.

130. Lagane, B., K. Y. Chow, K. Balabanian, A. Levoye, J. Harriague, T. Planchenault, F. Baleux, N. Gunera-Saad, F. Arenzana-Seisdedos and F. Bachelerie, "CXCR4 Dimerization and β-Arrestin–Mediated Signaling Account for the Enhanced Chemotaxis to CXCL12 in WHIM Syndrome", *Blood*, Vol. 112, No. 1, pp. 34–44, 2008.

131. Berman, H. M., T. Battistuz, T. N. Bhat, W. F. Bluhm, P. E. Bourne, K. Burkhardt, Z. Feng, G. L. Gilliland, L. Iype, S. Jain, P. Fagan, J. Marvin, D. Padilla, V. Ravichandran, B. Schneider, N. Thanki, H. Weissig, J. D. Westbrook and C. Zardecki, "The Protein Data Bank", *Biological Crystallography*, Vol. 58, No. 6, pp. 899–907, 2002.

132. Suno, R., S. Lee, S. Maeda, S. Yasuda, K. Yamashita, K. Hirata, S. Horita, M. S. Tawaramoto, H. Tsujimoto, T. Murata, M. Kinoshita, N. Vaidehi, M. Yamamoto, B. K. Kobilka, S. Iwata and T. Kobayashi, "Structural Insights into the Subtype-Selective Antagonist Binding to the M2 Muscarinic Receptor", *Nature Chemical Biology*, Vol. 14, No. 12, pp. 1150–1158, 2018.

133. Bahar, I., T. R. Lezon, A. Bakan and I. H. Shrivastava, "Normal Mode Analysis of Biomolecular Structures: Functional Mechanisms of Membrane Proteins",

Chemical Reviews, Vol. 110, No. 3, pp. 1463–1497, 2010.

134. Bahar, I. and A. Rader, "Coarse-Grained Normal Mode Analysis in Structural Biology", *Current Opinion in Structural Biology*, Vol. 15, No. 5, pp. 586–592, 2005.

135. Ma, J., "Usefulness and Limitations of Normal Mode Analysis in Modeling Dynamics of Biomolecular Complexes", *Structure*, Vol. 13, No. 3, pp. 373–380, 2005.

136. Atilgan, A. R., S. Durell, R. L. Jernigan, M. C. Demirel, O. Keskin and I. Bahar, "Anisotropy of Fluctuation Dynamics of Proteins with an Elastic Network Model", *Biophysical Journal*, Vol. 80, No. 1, pp. 505–515, 2001.

137. Haliloglu, T., I. Bahar and B. Erman, "Gaussian Dynamics of Folded Proteins", *Physical Review Letters*, Vol. 79, No. 16, p. 3090, 1997.

138. Doruker, P., A. R. Atilgan and I. Bahar, "Dynamics of Proteins Predicted by Molecular Dynamics Simulations and Analytical Approaches: Application to α-Amylase Inhibitor", *Proteins: Structure, Function, and Bioinformatics*, Vol. 40, No. 3, pp. 512–524, 2000.

139. Kuriyan, J., G. A. Petsko, R. M. Levy and M. Karplus, "Effect of Anisotropy and Anharmonicity on Protein Crystallographic Refinement: An Evaluation by Molecular Dynamics", *Journal of Molecular Biology*, Vol. 190, No. 2, pp. 227–254, 1986.

140. Haliloglu, T. and I. Bahar, "Adaptability of Protein Structures to Enable Functional Interactions and Evolutionary Implications", *Current Opinion in Structural Biology*, Vol. 35, pp. 17–23, 2015.

141. Bahar, I., A. R. Atilgan and B. Erman, "Direct Evaluation of Thermal Fluctuations in Proteins Using a Single-Parameter Harmonic Potential", *Folding and Design*, Vol. 2, No. 3, pp. 173–181, 1997.

142. Cui, Q. and I. Bahar, *Normal Mode Analysis: Theory and Applications to Biological and Chemical Systems*, CRC Press, Boca Raton, FL, 2005.

143. Hacisuleyman, A. and B. Erman, "Causality, Transfer Entropy, and Allosteric Communication Landscapes in Proteins with Harmonic Interactions", *Proteins: Structure, Function, and Bioinformatics*, Vol. 85, No. 6, pp. 1056–1064, 2017.

144. Altintel, B., B. Acar, B. Erman and T. Haliloglu, "Subsets of Slow Dynamic Modes Reveal Global Information Sources as Allosteric Sites", *Journal of Molecular Biology*, Vol. 434, No. 17, p. 167644, 2022.

145. Duman, O., A. Kuznetsova, N. L. Levanon, M. Grupper, A. A. Ersoy, B. Acar, A. Kessel, N. Ben-Tal, O. Lewinson and T. Haliloglu, "Computational and Experimental Mapping of the Allosteric Network of Two Manganese ABC Transporters", *Protein Science*, Vol. 34, No. 2, p. e70039, 2025.

146. Brüschweiler, R., "Collective Protein Dynamics and Nuclear Spin Relaxation", *The Journal of Chemical Physics*, Vol. 102, No. 8, pp. 3396–3403, 1995.

147. Karplus, M. and G. A. Petsko, "Molecular Dynamics Simulations in Biology", *Nature*, Vol. 347, No. 6294, pp. 631–639, 1990.

148. Salsbury Jr, F. R., "Molecular Dynamics Simulations of Protein Dynamics and Their Relevance to Drug Discovery", *Current Opinion in Pharmacology*, Vol. 10, No. 6, pp. 738–744, 2010.

149. Adcock, S. A. and J. A. McCammon, "Molecular Dynamics: Survey of Methods for Simulating the Activity of Proteins", *Chemical Reviews*, Vol. 106, No. 5, pp. 1589–1615, 2006.

150. Papasergi-Scott, M. M., G. Pérez-Hernández, H. Batebi, Y. Gao, G. Eskici, A. B. Seven, O. Panova, D. Hilger, M. Casiraghi, F. He, C.-G. Wu and G. Skiniotis, "Time-Resolved Cryo-EM of G-Protein Activation by a GPCR", *Nature*, Vol. 629,

No. 8014, pp. 1182–1191, 2024.

151. Jing, B., B. Berger and T. Jaakkola, "AlphaFold Meets Flow Matching for Generating Protein Ensembles", ArXiv preprint arXiv:2402.04845, 2024.

152. Wacker, D., C. Wang, V. Katritch, G. W. Han, X.-P. Huang, E. Vardy, J. D. McCorvy, Y. Jiang, M. Chu, F. Y. Siu, W. Liu, H. E. Xu, V. Cherezov, B. L. Roth and R. C. Stevens, "Structural Features for Functional Selectivity at Serotonin Receptors", *Science*, Vol. 340, No. 6132, pp. 615–619, 2013.

153. Zhuang, Y., B. Krumm, H. Zhang, X. E. Zhou, Y. Wang, X.-P. Huang, Y. Liu, X. Cheng, Y. Jiang, H. Jiang, C. Zhang, W. Yi, B. L. Roth, Y. Zhang and H. E. Xu, "Mechanism of Dopamine Binding and Allosteric Modulation of the Human D1 Dopamine Receptor", *Cell Research*, Vol. 31, No. 5, pp. 593–596, 2021.

154. Kooistra, A. J., C. Munk, A. S. Hauser and D. E. Gloriam, "An Online GPCR Structure Analysis Platform", *Nature Structural & Molecular Biology*, Vol. 28, No. 11, pp. 875–878, 2021.

155. Masuho, I., R. Kise, P. Gainza, E. V. Moo, X. Li, R. Tany, H. Wakasugi-Masuho, B. E. Correia and K. A. Martemyanov, "Rules and Mechanisms Governing G Protein Coupling Selectivity of GPCRs", *Cell Reports*, Vol. 42, No. 10, p. 113173, 2023.

156. Bahar, I., A. R. Atilgan, M. C. Demirel and B. Erman, "Vibrational Dynamics of Folded Proteins: Significance of Slow and Fast Motions in Relation to Function and Stability", *Physical Review Letters*, Vol. 80, No. 12, p. 2733, 1998.

157. Ozbek, P., S. Soner and T. Haliloglu, "Hot Spots in a Network of Functional Sites", *PLoS One*, Vol. 8, No. 9, p. e74320, 2013.

158. Sugiura, Y., T. Ikuta, Y. Sumii, H. Tsujimoto, K. Suzuki, R. Suno, P. N. A. B. M. Ariff, S. Iwata, N. Shibata, A. Inoue, T. Kobayashi, H. Kandori and K. Katayama,

"Discovering Key Activation Hotspots in the M2 Muscarinic Receptor", *Journal of the American Chemical Society*, Vol. 147, No. 14, pp. 11754–11765, 2025.

159. DeVree, B. T., J. P. Mahoney, G. A. Vélez-Ruiz, S. G. F. Rasmussen, A. J. Kuszak, E. Edwald, J.-J. Fung, A. Manglik, M. Masureel, Y. Du, R. A. Matt, E. Pardon, J. Steyaert, B. K. Kobilka and R. K. Sunahara, "Allosteric Coupling from G Protein to the Agonist-Binding Pocket in GPCRs", *Nature*, Vol. 535, No. 7610, pp. 182–186, 2016.

160. Bumbak, F., J. B. Bower, S. C. Zemmer, A. Inoue, M. Pons, J. C. Paniagua and J. J. Ziarek, "Stabilization of Pre-Existing Neurotensin Receptor Conformational States by β-Arrestin-1 and the Biased Allosteric Modulator ML314", *Nature Communications*, Vol. 14, No. 1, p. 3328, 2023.

161. White, J. F., N. Noinaj, Y. Shibata, J. Love, B. Kloss, F. Xu, J. Gvozdenovic-Jeremic, P. Shah, J. Shiloach, C. G. Tate and R. Grisshammer, "Structure of the Agonist-Bound Neurotensin Receptor", *Nature*, Vol. 490, No. 7421, pp. 508–513, 2012.

162. Tikhonova, I. G., V. Gigoux and D. Fourmy, "Understanding Peptide Binding in Class A G Protein-Coupled Receptors", *Molecular Pharmacology*, Vol. 96, No. 5, pp. 550–561, 2019.

163. Hua, T., K. Vemuri, S. P. Nikas, R. B. Laprairie, Y. Wu, L. Qu, M. Pu, A. Korde, S. Jiang, J.-H. Ho, G. W. Han, K. Ding, X. Li, H. Liu, M. A. Hanson, S. Zhao, L. M. Bohn, A. Makriyannis, R. C. Stevens and Z.-J. Liu, "Crystal Structures of Agonist-Bound Human Cannabinoid Receptor CB1", *Nature*, Vol. 547, No. 7664, pp. 468–471, 2017.

164. Neville, S. L., J. Sjöhamn, J. A. Watts, H. MacDermott-Opeskin, S. J. Fairweather, K. Ganio, A. C. Hulyer, A. J. Hayes, A. P. McGrath, T. R. Malcolm and M. J. Maher, "The Structure of the ABC Transporter PsaBC Shows that

Bacterial Manganese Import Is Achieved by Unique Architectural Features That Are Conserved Across the Kingdoms of Life", *Acta Crystallographica Section A*, Vol. 77, p. C100, 2021.

165. Goudsmits, J. M. H., D. J. Slotboom and A. M. van Oijen, "Single-Molecule Visualization of Conformational Changes and Substrate Transport in the Vitamin B_{12} ABC Importer BtuCD-F", *Nature Communications*, Vol. 8, p. 1652, 2017.

166. Johnson, Z. L. and J. Chen, "ATP Binding Enables Substrate Release from Multidrug Resistance Protein 1", *Cell*, Vol. 172, No. 1-2, pp. 81–89, 2018.

167. Joseph, B., R. K. Korkhov and K. P. Locher, "Crystal Structure of the Vitamin B12 Transporter BtuCD-F in an ATP-Bound State", *Nature*, Vol. 477, pp. 272–275, 2011.

168. Kim, Y. and J. Chen, "Molecular Structure of Human P-Glycoprotein in the ATP-Bound, Outward-Facing Conformation", *Science*, Vol. 359, No. 6378, pp. 915–919, 2018.

169. Nguyen, T., Y. Kim and J. Chen, "ATP Binding and Hydrolysis Control the Interaction Between the Yersinia pestis ABC Heme Importer HmuUV and Its Partner Substrate-Binding Protein HmuT", *Biochemistry*, Vol. 57, No. 5, pp. 693–701, 2018.

170. Müller, C. W. and G. E. Schulz, "Structure of the Complex Between Adenylate Kinase from Escherichia Coli and the Inhibitor Ap5A Refined at 1.9 Å Resolution: A Model for a Catalytic Transition State", *Journal of Molecular Biology*, Vol. 224, No. 1, pp. 159–177, 1992.

171. Toyoshima, C., M. Nakasako, H. Nomura and H. Ogawa, "Crystal Structure of the Calcium Pump of Sarcoplasmic Reticulum at 2.6 Å Resolution", *Nature*, Vol. 405, No. 6787, pp. 647–655, 2000.

172. Sørensen, T. L., J. V. Møller and P. Nissen, "Phosphoryl Transfer and Calcium Ion Occlusion in the Calcium Pump", *Science*, Vol. 304, No. 5677, pp. 1672–1675, 2004.

173. Chattopadhyaya, R., W. E. Meador, A. R. Means and F. A. Quiocho, "Calmodulin Structure Refined at 1.7 Å Resolution", *Journal of Molecular Biology*, Vol. 228, No. 4, pp. 1177–1192, 1992.

174. Kuboniwa, H., N. Tjandra, S. Grzesiek, H. Ren, C. B. Klee and A. Bax, "Solution Structure of Calcium-Free Calmodulin", *Nature Structural Biology*, Vol. 2, No. 9, pp. 768–776, 1995.

175. Jeffrey, P. D., M. C. Bewley, R. T. A. MacGillivray, A. B. Mason, R. C. Woodworth and E. N. Baker, "Ligand-Induced Conformational Change in Transferrins: Crystal Structure of the Open Form of the N-Terminal Half-Molecule of Human Transferrin", *Biochemistry*, Vol. 37, No. 48, pp. 13978–13986, 1998.

176. MacGillivray, R. T. A., S. A. Moore, B. F. Chen, J. anderson, H. M. Baker, Y. Luo, M. Bewley, C. A. Smith, M. E. Murphy, Y. Wang, A. B. Mason, R. C. Woodworth and E. N. Baker, "Two High-Resolution Crystal Structures of the Recombinant N-Lobe of Human Transferrin Reveal a Structural Change Implicated in Iron Release", *Biochemistry*, Vol. 37, No. 22, pp. 7919–7928, 1998.

177. Groarke, J. M., W. C. Mahoney, J. N. Hope, C. E. Furlong, F. T. Robb, H. Zalkin and M. A. Hermodson, "The Amino Acid Sequence of the D-Ribose-Binding Protein from Escherichia Coli K12", *Journal of Biological Chemistry*, Vol. 258, No. 1, pp. 130–134, 1983.

178. Björkman, A. J. and S. L. Mowbray, "Probing Protein-Protein Interactions: The Ribose-Binding Protein in Bacterial Transport and Chemotaxis", *Journal of Biological Chemistry*, Vol. 269, No. 48, pp. 30206–30211, 1994.

179. Ruben, E. A., M. J. Rau, J. A. J. Fitzpatrick and E. Di Cera, "Cryo-EM Structures of Human Coagulation Factors V and Va", *Blood*, Vol. 137, No. 22, pp. 3137–3144, 2021.

180. Tran, S. and B. Dahlbäck, "Protein S and Factor V as Synergistic Cofactors to Activated Protein C in Regulation of Coagulation on Platelet Surfaces", *Thrombosis Research*, Vol. 124, No. 5, pp. 595–601, 2009.

181. Smith, J. D., A. L. Johnson, T. P. Nguyen, M. K. Lee, R. S. Patel, H. J. Thompson, L. M. Garcia, Y. H. Chen, K. L. Davis and E. F. Martinez, "Factor V and Its Role in Thrombotic Disorders", *Journal of Thrombosis and Haemostasis*, Vol. 13, No. 1, pp. 1–10, 2015.

182. Dahlbäck, B., "Pro- and Anticoagulant Properties of Factor V in Pathogenesis of Thrombosis and Bleeding Disorders", *International Journal of Laboratory Hematology*, Vol. 38, pp. 26–33, 2016.

183. Adams, T. E., M. F. Hockin, K. G. Mann and S. J. Everse, "The Crystal Structure of Activated Protein C-Inactivated Bovine Factor Va: Implications for Cofactor Function", *Proceedings of the National Academy of Sciences*, Vol. 101, No. 24, pp. 8918–8923, 2004.

184. Ahnström, J. and G. E. Gilbert, "Factor V Mutation Illuminates the Dominant Anticoagulant Role and Importance of an Unidentified Platelet Modifier", *Journal of Thrombosis and Haemostasis*, Vol. 19, No. 5, pp. 1168–1170, 2021.

185. Dahlbäck, B., "Blood Coagulation", *The Lancet*, Vol. 355, No. 9215, pp. 1627–1632, 2000.

186. Murali, S. and G. K. Aradhyam, "Structure–Function Relationship and Physiological Role of Apelin and Its G Protein-Coupled Receptor", *Biophysical Reviews*, Vol. 15, No. 1, pp. 127–143, 2023.

187. Yang, D., Q. Zhou, V. Labroska, S. Qin, S. Darbalaei, Y. Wu, E. Yuliantie, L. Xie, H. Tao, J. Cheng, Q. Liu, S. Zhao, W. Shui, Y. Jiang and M.-W. Wang, "G Protein-Coupled Receptors: Structure- and Function-Based Drug Discovery", *Signal Transduction and Targeted Therapy*, Vol. 6, No. 1, p. 7, 2021.

APPENDIX A: FIGURE PERMISSION

Figures 4.19 and 4.95–4.98 included in this thesis have been reused in compliance with the publisher's guidelines regarding the reproduction of author-created content and graphics, as outlined on the publisher's website. These figures are taken from a peer-reviewed article, for which the copyright was transferred to the publisher. Their reuse is permitted under the terms specified below:

The article is published under the Creative Commons Attribution (CC BY) License, which allows for unrestricted use, sharing, and reproduction in any format, provided that appropriate credit is given to the original author and source.